# POTENTIAL APPLICATION OF 2D CARBON MATERIALS IN SILICON HETEROJUNCTION SOLAR CELLS

A Thesis Submitted
In Partial Fulfilment of the Requirements
for the Degree of

### **DOCTOR OF PHILOSOPHY**

by

NAIMA (2K20/PHDAP/01)

**Under the Supervision of** 

DR. PAWAN KUMAR TYAGI
Associate Professor
Department of Applied Physics

**Delhi Technological University** 

PROF. VINOD SINGH
Professor
Department of Applied Physics
Delhi Technological University



**Department of Applied Physics** 

DELHI TECHNOLOGICAL UNIVERSITY
(Formerly Delhi College of Engineering)
Shahbad Daulatpur, Main Bawana Road, Delhi-110042, India

OCTOBER, 2025

© DELHI TECHNOLOGICAL UNIVERSITY-2025 ALL RIGHTS RESERVED

## **DEDICATION**

This dissertation is dedicated to my beloved parents and supportive brothers.

#### **ACKNOWLEDGEMENT**

First and foremost, I thank the Almighty for granting me the fortitude and resilience required to navigate these years of commitment and hard work. This acknowledgement is a small but heartfelt token of appreciation for all those who supported and guided me along this journey.

I sincerely thank my supervisors, **Dr. Pawan Kumar Tyagi & Prof. Vinod Singh (HoD)**, for their excellent mentorship and invaluable, continuous support, which helped me navigate the complex aspects of this research. I am deeply appreciative of their insightful advice, constructive feedback, and constant encouragement, which have all contributed to the successful completion of my thesis. Their mentorship not only enriched my academic development but also taught me invaluable lessons that extend beyond the realm of research. I am truly fortunate to have had the privilege to work under their guidance, and I will carry forward the lessons they have imparted with immense respect and gratitude. For all of this and more, I am sincerely thankful and will always remain deeply indebted to them.

My sincere thanks also go to **Prof. Prateek Sharma**, Hon'ble Vice-Chancellor, DTU, for providing a marvellous research environment and ample research facilities to conduct this research. I extend my sincere gratitude to **Prof. Rinku Sharma**, Dean (Academic-PG), DTU, and **Prof. A. S. Rao**, Former Head of the Department of Applied Physics, DTU, along with all the faculty and staff members, for their support and cooperation throughout my research journey.

I am immensely grateful to my seniors, **Dr. Kamlesh Patel**, **Dr. Vinay Kumar** and **Dr. Priya Pradeep Kumar**, who stood by me unwaveringly, serving as pillars of support through every high and low. Their support and companionship have undoubtedly left a lasting impression on me, for which I am immensely thankful. I am grateful to my labmates, **Mr. Jasveer Singh**, **Mr. Ramesh Kulriya**, **Ms. Shivani**, **Mr. Hemendra Singh**, **Ms. Nisha Singh**, **Mr. Bharat Bhushan**, **and Mr. Dedraj Yadav** for their enthusiasm, fresh perspectives, and willingness to assist whenever needed. Your energy and curiosity have been a wonderful source of motivation.

I extend my heartfelt thanks to my close friend Ms. Shilpa Rana for her unwavering support, encouragement, and companionship. Your presence has been a true source of

strength and positivity throughout this journey. Thank you for standing by me through every high and low, for cheering on my successes, and for lifting my spirits whenever I felt overwhelmed. Furthermore, I would like to sincerely thank my friends for their support and encouragement at DTU, including **Dr. Sakshi Verma, Mrs. Megha Narwan, Mr. Sunil, Ms. Sheetal, Dr. Priyanka, Mr. Hemant Arrora, and Ms. Ankita Dahiya** and outside DTU including **Mrs. Damini Arora, Mrs. Megha Bhaduriya and Ms. Khushi Sharma** for their unwavering technical guidance, valuable suggestions, and support throughout this journey. I am incredibly fortunate to have friends like you, and I will always cherish the memories we've created together during this journey.

I am profoundly grateful to my father, Mr. Abdul Karim, and my mother, Mrs. Bano, who mean the world to me and have always given me the freedom to follow my path. I deeply admire them for their selfless love, care, sacrifices, and unwavering support in shaping my life. I also extend my sincere gratitude to my brothers, Mr. Nadeem Tyagi and Mr. Naim Tyagi, for their belief in me, their unwavering support and their constant kindness and understanding. They have always encouraged me to think beyond the ordinary and strive for excellence, pushing me to step outside my comfort zone and explore new horizons. Their infectious laughter and lighthearted presence have been a source of comfort, brightening my challenging Ph.D. journey and offering moments of joy and innocence. I dedicate this achievement to their boundless encouragement and love. I would also like to acknowledge my two wonderful sisters-in-law, Anjum and Fatima, for their constant encouragement, kindness, and support.

Lastly, I want to acknowledge the tiniest, most joyful members of my family, my nephews, **Arhaan, Izhaan, Hasan** and niece, **Enaya**. Though too young to understand what a thesis is, their innocent laughter, playful chaos, and unconditional affection brought balance and light to even the most stressful days. Thank you for being a source of pure happiness throughout this journey.

78.7	-	•		
N	1	1	111	
/ V	"	L	11	•

Date:

#### DELHI TECHNOLOGICAL UNIVERSITY



(Govt. of National Capital Territory of Delhi) Shahbad Daulatpur, Bawana Road, Delhi-110042

#### **CANDIDATE'S DECLARATION**

I, Ms. Naima (2K20/PHDAP/01), hereby declare that the work which is being presented in the thesis entitled "Potential application of 2D carbon materials in silicon heterojunction solar cells" in partial fulfillment of the requirements for the award of the Degree of Doctor of Philosophy, submitted in the Department of Applied Physics, Delhi Technological University is an authentic record of my own work carried out during the period from August 2020 to July 2025 under the supervision of <u>Dr. Pawan Kumar Tyagi & Prof. Vinod Singh, Department of Applied Physics, Delhi Technological University</u>. The matter presented in the thesis has not been submitted by me for the award of any other degree of this or any other Institute.

Candidate's Signature

This is to certify that the student has incorporated all the corrections suggested by the examiners in the thesis and the statement made by the candidate is correct to the best of our knowledge.

Dr. Pawan Kumar Tyagi

**Prof. Vinod Singh** 

(Supervisor)

(Joint-Supervisor)

Dr. Fouran Singh

(External Examiner)

Scientist-G, Inter-University Accelator Centre, New Delhi -110067

#### DELHI TECHNOLOGICAL UNIVERSITY



(Govt. of National Capital Territory of Delhi) Shahbad Daulatpur, Bawana Road, Delhi-110042

#### **CERTIFICATE BY THE SUPERVISOR**

Certified that Ms. Naima (2K20/PHDAP/01) has carried out her research work presented in this thesis entitled "Potential application of 2D carbon materials in silicon heterojunction solar cells" for the award of Doctor of Philosophy from Department of Applied Physics, Delhi Technological University, Delhi, under my supervision. The thesis embodies results of original work, and studies are carried out by the student herself and the contents of the thesis do not form the basis for the award of any other degree to the candidate or to anybody else from this or any other University/Institution.

Dr. Pawan K. Tyagi

(Supervisor)
Associate Professor
Department of Applied Physics
Delhi Technological University
Delhi-110042, India

**Prof. Vinod Singh** 

(Joint-Supervisor)
Professor and HoD
Department of Applied Physics
Delhi Technological University
Delhi-110042, India

Date:

#### **ABSTRACT**

As the world moves toward more sustainable energy systems, photovoltaic technologies are becoming vital in supplying the increasing electricity demand. Silicon-based solar cells remain the most popular among PV technologies because of their advanced technology, scalability, high efficiency, and long-term dependability. Nevertheless, in order to address the challenges of mounting worldwide energy consumption and the limitations imposed within conventional device structures, further power conversion efficiency advancement is anticipated. In this regard, the integration of two-dimensional materials with silicon-based heterojunction solar cells represents a promising strategy to transcend existing performance barriers.

In this thesis, AFORS-HET simulation software is used to numerically investigate the feasibility of the integration of diamane, a recently synthesized 2D diamond-like allotrope of carbon, into silicon-based solar cell designs. Diamane is reported to be a promising material for advanced photovoltaic applications because of its wide and tunable bandgap, excellent optical properties, and higher carrier mobility. The objective of this thesis is to meticulously investigate the integration of doped diamane as a promising material to be used as the emitter and back surface field (BSF) layers in silicon-based heterojunction solar cells.

The application of n-type diamane as an emitter layer in an ITO/n-Diamane/p-cSi/Ag heterostructure solar cell is investigated in the first section of the study. A maximum power conversion efficiency (PCE) of 16.84% was attained at 300 K by layer's parameter optimization. To validate its practical applicability, the structure was simulated using commercially available silicon substrates that are commercially accessible, resulting in an efficiency of 10.41%. The analysis also revealed that as the diamane thickness increased, efficiency slightly decreased, highlighting the importance of precise thickness control. After that, an advanced HIT structure, Gr/n-Dn/a-Si: H(i)/p-c-Si/Ag, is modelled. Here, graphene with zero absorption loss is used as the transparent conducting oxide (TCO). The optimized cell delivered a record efficiency of 31.2%, surpassing structures that utilized traditional ITO electrodes. The results highlight their

unique compatibility and practical synergy by demonstrating that the Gr/Dn interface of carbon materials could serve as both an emitter and a TCO, respectively. In order to further enhance device performance, doped diamane was used as an efficient electron/hole collection layer. The modelled structure is Gr/n-Dn/a-Si: H(i)/p-c-Si/p-Dn/Au. Specifically, the n-type and p-type diamane layers are used as the emitter and BSF layers of the cell, respectively. For the fully optimized configuration, which accounts for absorption losses at the front contact, a conversion efficiency of 27.88% is achieved, with a short-circuit current density (J<sub>SC</sub>) of 49.3 mA/cm<sup>2</sup>, open-circuit voltage (V<sub>OC</sub>) of 691.1 mV, and fill factor (FF) of 81.83%. A comprehensive analysis is also conducted on the influence of front surface texturing angle and associated optical losses, providing insights into light exposure angle to enhance photovoltaic performance. The study further presents a detailed simulation of BSFHJ and BSFHIT solar cells, incorporating passivation strategies and precise control over material bandgaps and thicknesses. The simulated structures, Gr/n-Dn/p-c-Si/p-Dn/Au and Gr/n-Dn/a-Si: H(i)/p-c-Si/a-Si: H(i)/p-Dn/Au, achieved efficiencies of 26.86% and 29.38%, respectively. For the BSFHJ cell, optimal performance was obtained with an n-diamane emitter (thickness 1.36 nm, bandgap 1.4 eV) and a p-diamane BSF layer (2.04 nm, 1.6 eV). In contrast, the BSFHIT structure reached optimum efficiency using much thinner diamane layers (0.34 nm), with band gaps of 1.6 eV (n-type) and 1.3 eV (p-type). The ideal c-Si thickness was found to be 80 µm for BSFHJ and 35 µm for BSFHIT, indicating potential for material savings and enhanced sustainability, albeit with associated fabrication challenges for ultra-thin wafers. Key performance parameters, including Voc, Jsc, FF, J-V characteristics, and spectral response, were analyzed in detail, confirming that the integration of both passivation and BSF layers substantially improves device efficiency.

Finally, we explored a cell design with SiO<sub>2</sub>/Si<sub>3</sub>N<sub>4</sub> passivation layers on the emitter layer, resulting in the structure Gr/Si<sub>3</sub>N<sub>4</sub>/SiO<sub>2</sub>/n-Dn/p-c-Si/p-Dn/Au. A high current density of 54.53 mA/cm<sup>2</sup> and an efficiency of 30.59% were attained in this optimized design. To illustrate the superior effectiveness of diamane-based structured solar cells, a traditional PERC structure with a-Si for both emitter and BSF layers was also simulated, which yielded an efficiency of 24.01%. In order to further identify the most efficient design, a

comparison study of each simulated configuration was carried out. Among these structures, the passivated emitter layer BSFHIT structure was found to be more efficient, with the highest efficiency of 30.69%. This confirms the practical utility and commercial significance of the proposed 2D carbon material-based solar cells.

In summary, the present work confirms that doped diamane is a multifunctional material for high-efficiency silicon photovoltaics. The possibility of developing a new class of carbon-integrated solar cell design is being offered. This happened as a result of graphene's ability to work as a transparent conducting electrode and diamene's dual use as an emitter and BSF layer. These findings pave the way towards the development of high-performance, sustainable solar systems based on 2D carbon materials, providing a strong theoretical basis for future demonstrations and commercial applications.

#### LIST OF PUBLICATIONS

#### **Publications in Peer-Reviewed Journals (Included in Thesis)**

- 1. Naima, Pawan K. Tyagi, Vinod Singh, "N-type diamane: An effective emitter layer in crystalline silicon heterojunction solar cell", Carbon Trends, 9 (2022) 100209. (I.F. 3.9)
- Naima, Pawan K. Tyagi, Vinod Singh, "Potential application of novel graphene/diamane interface in silicon-based heterojunction with intrinsic thin layer solar cell", Computational Materials Science 226 (2023) 112252. (I.F. 3.3)
- 3. Naima, Pawan K. Tyagi, Vinod Singh, "Doped diamane: An efficient electron/hole collection layer in HIT solar cell", Materials Science and Engineering B 310 (2024) 117754. (I.F. 4.6)
- **4.** Naima, Pawan K. Tyagi, Vinod Singh, "Potential application of p-type diamane as back surface field layer in silicon-based heterojunction solar cells", **Semicond.** Sci. Technol. 39 (2024) 125021 (17pp). (I.F. 2.1)

#### Communicated

 Naima, Mohamed Alla, Vinod Singh, "Potential application of diamane and graphene in silicon-based heterojunction solar cells" Diamond and Related Materials (I.F. 5.1) (Under review)

#### **Publications in Conference**

- Naima, Pawan K. Tyagi, Vinod Singh, "Affinity Optimization of Commercially Available Crystalline-Silicon Heterojunction Solar Cell by Using AFORS-HET Software", Recent Advances in Nanotechnology, Springer Proceedings in Materials, 28 (2022) 111-115.
- Naima, Pawan K. Tyagi, Vinod Singh, "Effect of temperature variation on the performance of HIT solar cell", Springer's Proceedings in Physics (2023) (Accepted).

#### **Publications in Peer-Reviewed Journals (Not Included in Thesis)**

- 1. H. El-assib, Naima, et al. "High-performance optimization of Cs<sub>2</sub>CuSbCl<sub>6</sub>-based lead-free double perovskite solar cells with >27% efficiency", Renewable Energy, 239 (2025) 122092. (I.F. 9.1)
- 2. H. El-Assib, M. Alla, S. Tourougui, M. Mohammed, S. Dar, Y. Labghough, M. Alla, Naima, M. Rouchdi, B. Fares, "Electron extraction layer-Driven performance enhancement in CaHfSe<sub>3</sub> Photovoltaics", RSC Advances, 15 (2025) 35859. (I.F. 4.6)

#### **Conference Contributions-Poster/Oral**

- 1. Naima, Pawan K. Tyagi, Vinod Singh "Affinity Optimization of Commercially Available Crystalline-Silicon Heterojunction Solar Cell by Using AFORS-HET Software" at International Conference on Nanotechnology: Opportunities & Challenges (ICNOC 2022) held in Department of Applied Sciences and Humanities Faculty of Engineering and Technology, Jamia Millia Islamia, New Delhi, from 28th-29th Nov, 2022.
- 2. Naima, Pawan K. Tyagi, Vinod Singh "Effect of optical band gap of the emitter layer on the efficiency of the silicon heterojunction photovoltaic cell" at International Union of Materials Research Society International Conference in Asia 2022 (IUMRS-ICA-2022) held in IIT Jodhpur, from 19th to 23rd December 2022.
- **3.** Naima, Pawan K. Tyagi, Vinod Singh "Effect of temperature variation on the performance of HIT solar cell" at International Conference on Atomic, Molecular, Material, Nano and Optical Physics with Applications (ICAMNOP–2023) held in Delhi Technological University, from 20<sup>th</sup>-22<sup>nd</sup> Dec, 2023.
- **4.** Naima, Pawan K. Tyagi, Vinod Singh "Graphene–Diamane Interfaces for Enhanced Silicon Solar Cell Performance" at International Conference on Innovations, Advances in Material Science for Sustainable Goals (IAMSSG–2025) held in JECRC University Jaipur (India), from 29<sup>th</sup>-31<sup>nd</sup> Oct, 2025.

#### TABLE OF CONTENTS

Ackr	owledge	ment	i
Can	didate's l	Declaration	iii
Cert	ificate		iv
Abst	ract		<i>v</i>
List	of Public	ations	viii
Tabl	e of conte	ents	x
List	of Tables		xiv
List	of Figure	25	xvi
List	of Abbre	viations	xxiv
Cha	pter 1:	Introduction	1-22
1.1	Backg	round and Motivation /Overview	2
1.2	Solar (	Cells for Solar Energy Harvesting	4
	1.2.1	Working Principle of Solar Cells	4
	1.2.2	Types of Solar Cells	9
1.3	Silicon	Heterojunction and HIT Solar Cells	10
	1.3.1	Carrier-Selective Contacts: Trends and Limitations	12
1.4	2D Ca	arbon Materials in Photovoltaics	15
	1.4.1	Graphene and Its Derivatives	15
	1.4.2	Carbon Nanotubes (CNTs)	16
	1.4.3	Graphdiyne (GDY)	16
1.5	Resea	rch Challenges	17
1.6	Resea	rch Gap	18
	1.6.1	Research Objectives	18
	1.6.2	Overview of Thesis	19
Refe	rences		19
Cha	pter 2:	Literature Review	23-35
2 1	Introd	luction	24

2.2		entional ations	Electron/Hole				their26
	2.2.1	Doped Am	norphous Silicon (a	ı-Si:H)			26
			Metal Oxides (TM				
	2.2.3	Other Eme	erging Materials				27
2.3	Desira	ble Proper	ties for Carrier-Se	lective Layers.			28
	2.3.1 H	Electronic 1	Requirements				28
	2.3.2	Optical Red	quirements				28
	2.3.3 7	Thermal an	d Chemical Stabil	ity		•••••	28
	2.3.4	Interfacial	Passivation				29
	2.3.5 \$	Scalability	and Process Comp	atibility			29
2.4	Diama	ne: A Pror	mising 2D Carbon	Material			29
	2.4.1 \$	Structural a	and Electronic Proj	perties			30
	2.4.2 (	Optical and	Mechanical Chara	cteristics			31
	2.4.3 F	abrication	Challenges and Re	esearch Directi	ons		32
2.5	Scope	of the pres	sent work				32
Refe	rences						35
Cha	pter 3:	crystalli	ion of N-type di ne silico	n he	terojunction	1	solar
3.1	Intro	duction					37
3.2	Device	ce structur	e and simulation d	etails			41
3.3	Resu	lts and disc	cussion				46
	3.3.1	Optimiz	ation of n-type dia	mane layer par	rameters	•••••	46
	3.3.2	-	ration and simuers		•		
	3.3.3	-	response, q		•	-	
3.4	Sumr	nary					60
Refe	rences						61
Cha	pter 4:	0	nce of novel g	-			
		heteroju	nction with intri	nsic thin laye	er (HIT) sola	ar cell	.62-89

4.1	Introduction63		
4.2	Simulation and structural details and junction formation66		
	4.2.1	Simulation and structural details	66
	4.2.2	Junction formation	72
4.3	Result	ts and discussion	73
	4.3.1	Optimization of diamane layer	73
	4.3.2	Optimization of a-Si: H(i) layer	77
	4.3.3	Optimization of p-cSi layer	79
	4.3.4	Optimization of the TCE (graphene) parameters	82
	4.3.5	Optimization and simulation of front and back material	
4.4	Summ	nary	88
Refere	ences		89
Chap		Doped diamane: an efficient electron/hole collection l	•
5.1	Introd	luction	91
5.2	Struct	tural Model and Junction Formation95	
5.3	Results and Discussion		
	5.3.1	Evaluation of Approach	99
	5.3.2	Fabrication Details	100
	5.3.3	Optimization of Emitter Layer	101
	5.3.4	Optimization of BSF Layer	105
	5.3.5	Optimization of Buffer layer	107
	5.3.6	Optimization of Active Layer	109
5.4	Summ	nary	113
Refere	ences		114
Chap		Significance of passivating c-Si layer in silicon heteroj solar cells	
6.1	Introd	luction	116
6.2	Simul	ation model and junction formation	122
6.3	Result	ts and Discussion	127
	6.3.1	Fabrication Details	127

	6.3.2	Optimisation of the Thickness of the n-Dn, p-Dn, and p-cSi HJBSF and HITBSF Cell	
	6.3.3	Optimisation of the Bandgap of the Emitter and BSF Layer and HITBSF Cells	
	6.3.4	Optimisation of the Thickness and Bandgap of the Front and Layers of a-Si: H(i) in HITBSF Cell	
	6.3.5	Spectral Response, J-V Curve and Quantum Efficiency of HITBSF Cell	
6.4	Summ	nary	145
Refer	ences		146
Chaj		Influence of passivation layer (SiO <sub>2</sub> /Si <sub>3</sub> N <sub>4</sub> ) emplo commercially available silicon cell	solar
7.1	Introd	uction	148
7.2	Struct	ure and simulation details	154
7.3	_	y Band Diagram and Carrier Dynamics	
7.4	Result	ts and Discussion	157
	7.4.1	Optimization of carrier lifetime in active layer	157
	7.4.2	Optimization of thickness of p-type c-Si	158
	7.4.3	Optimization of the doping concentration of the BSF layer	159
	7.4.4	Optimization of the thickness of the BSF layer	160
	7.4.5	Optimization of the thickness of the emitter layer	161
	7.4.6	Optimization of the doping concentration of the emitter layer	r162
7.5	Summ	nary	165
Refer	ences		166
Chap	oter 8: (	Conclusion, Future Scope and Social Impact	170-173
8.1		usion	
8.2	Future	e Scope and Social Impact	173
Publ	ication	Proofs	174
		Vitae	

#### LIST OF TABLES

<b>Table 3.1:</b>	Information of the parameters used as front and back contact in the designed solar cell.	40
<b>Table 3.2:</b>	Ranges of other parameters chosen for the simulation.	42
<b>Table 3.3:</b>	Overview of the variables of the finest simulated solar cell.	57
<b>Table 4.1:</b>	List of parameters used as front and back contacts.	66
<b>Table 4.2:</b>	List of the range of values of parameters used.	67
<b>Table 4.3:</b>	List of parameters used at interfaces.	70
<b>Table 4.4:</b>	List of initially taken values of parameters.	72
<b>Table 4.5:</b>	Crystalline silicon based solar cells.	84
Table 5.1:	List of models applied at different interfaces between the layers used in the structure of designed solar cell investigated in this report.	93
<b>Table 5.2:</b>	Values of parameters of front and back contacts used in the designed solar cell investigated in this work.	96
<b>Table 5.3:</b>	List of initial set of values of parameters used for different layers before optimization.	97
<b>Table 6.1:</b>	List of the intial values of all parameters used for performing the simulation in HJBSF cell.	121
<b>Table 6.2:</b>	List of the initial parameter values of all layers used for performing simulation over HITBSF cell.	121

<b>Table 6.3:</b>	Values of parameters of front and back contacts used in the designed solar cells (both HJBSF & HITBSF) investigated in this work.	122
<b>Table 6.4:</b>	Optimum values of the simulated parameters of layers, n-Dn, p-Dn, p-cSi and front/back passivation layers of HJBSF and HITBSF cell.	123
<b>Table 6.5:</b>	Values of performance parameters of the optimal cells; HJBSF cell & HITBSF cell at the optimized values of all the parameters as tabluated in Table 6.1, 6.3 and 6.4.	137
Table 6.6:	Comparison and details solar cells based on crystalline silicon [10, 16, 69–74]	140
<b>Table 7.1:</b>	The parameters of the front and rear contacts utilised in the solar cell design were examined in this study.	153
<b>Table 7.2:</b>	Initial parameter values for various layers prior to optimisation.	154
<b>Table 7.3:</b>	The results obtained after analysing previously reported cell with and without passivation along with newly simulated cells with and without passivation.	160

#### LIST OF FIGURES

Fig. 1.1	Various renewable and sustainable source of energy present in		
	surrounding.		
<b>Fig. 1.2</b>	A diagram showing the photovoltaic effect	5	
	[http://www.ecogreenelectrical.com/solar.htm].		
Fig. 1.3	A diagram showing structure of PV cell	5	
	[https://www.geeksforgeeks.org/photovoltaic-cell/].		
Fig. 1.4	Band diagram of an idealized solar cell structure at the a) open-	6	
	circuit and b) short-circuit conditions.		
Fig. 1.5	Schematic representation of an isolated p-type and n-type	7	
	semiconductor and corresponding band diagrams.		
Fig. 1.6	Formation of a space-charge region at the p-n junction due to	7	
	carrier diffusion and built-in electric field.		
Fig. 1.7	The equivalent circuit of photovoltaic cell	8	
	[https://www.geeksforgeeks.org/photovoltaic-cell/].		
Fig. 1.8	J-V characteristics of a p-n junction in the dark and under	8	
	illumination .		
Fig. 1.9	Layered structure of (a) HJT, and (b) HIT.		
Fig. 1.10	Schematic representation of the heterojunction silicon (HIT)		
	solar cell structure.		
Fig. 1.11	Flowchart for the organisation of the thesis.	18	
Fig. 2.1	Various applications of diamane in optoelectronic devices.	29	
Fig. 2.2	Atomic structures of (a) graphane and (b) diamane, and (c) the	30	
	mechanism of the diamane nucleus formation on the initial		
	graphene bilayer.		
Fig. 2.3	The block diagram summarizing the key methods used for the	32	
	fabrication of diamanes.		
T1 0.4		•	
Fig. 3.1	(a) Schematic diagram of the simulated structure, (b) Schematic	39	
	diagram under forward biasing just after the formation of		

heterojunction showing the transportation of electrons and holes.  $\Phi_{Dn} \ , \ \Phi_{Si} \ \text{and} \ \chi_{Dn} \ , \ \chi_{Si} \ \text{are the diamane and Si work function and}$  the diamane and silicon affinity, respectively.

- Fig. 3.2 Graphic representation of the performance of designed cell after optimization of different variables of n-diamane, (a, b)  $N_D$  (cm<sup>-3</sup>) donor concentration, (c, d)  $N_C$  / $N_V$  effective conduction/valence band density, (e, f) bandgap  $E_g$  (eV), (g, h)  $\chi$  (eV) electron affinity, (i, j) dielectric constant  $\epsilon_r$ , and (k, l) layer numbers. After fixing the variables of p-cSi at some constant values like:  $N_A = 1 \times 10^{16}$  cm<sup>-3</sup>,  $N_C/N_V = 3 \times 10^{19}$  cm<sup>-3</sup>,  $\chi = 4.05$  eV, and layer thickness = 100  $\mu$ m. Remaining variables of both p-cSi and n-Dn are mentioned in Table 3.2.
- Fig. 3.3 Graphic representation of the performance of the designed cell after simulation of different variables of p-crystalline Si wafer, (a, b)  $N_A$  (cm<sup>-3</sup>), (c, d)  $N_C/N_V$  (cm<sup>-3</sup>), (e-f)  $\chi$  (eV), (g, h) wafer thickness ( $\mu$ m), (i, j) layer number of n-Dn at best optimized values of p-cSi wafer and (k, l) thickness of Si layer at commercially available values of parameters p-cSi wafer, whereas the values of parameters of n-Dn are kept at their best optimized values i.e.,  $N_D=1\times 10^{18}$  cm<sup>-3</sup>,  $N_C/N_V=1\times 10^{19}$  cm<sup>-3</sup>,  $E_g=2.05$  eV,  $\chi=4.4$  eV,  $\mu_n=2732$  cm<sup>2</sup>V<sup>-1</sup>s<sup>-1</sup> and  $\mu_p=1565$  cm<sup>2</sup>V<sup>-1</sup>s<sup>-1</sup>.
- Fig. 3.4 Wavelength dependency of (a) SR, (b) EQE and (c) IQE of the best simulated solar cell at single layer n-Dn/p-cSi (  $\eta=8\%$ ,  $\eta=16.84\%$  with  $N_A=7\times 10^{18}$  cm<sup>-3</sup>,  $N_C/N_V=1\times 10^{19}$  cm<sup>-3</sup> for 100  $\mu$ m p-cSi and efficiency = 10.41% with  $N_A=5\times 10^{16}$  cm<sup>-3</sup>,  $N_V=1.04\times 10^{19}$  cm<sup>-3</sup> and  $N_C=2.8\times 10^{19}$  cm<sup>-3</sup> at 100  $\mu$ m p-cSi).
- Fig. 3.5 Dependency of the optimized cell response with temperature variation at  $\eta = 16.84\%$ . (a) efficiency and fill factor, (b)  $V_{OC}$  and  $J_{SC}$ .

47

52

56

- **Fig. 4.1** (a) Schematic of the designed HIT module. (b) Energy band diagram for the designed HIT structure showing separation of charges at the interfaces.
- Fig. 4.2 Simulation of diamane layer by keeping the parameters of remaining layers at values given in Table 4.4. (a and b) optimization of  $N_D$  (cm<sup>-3</sup>), (c and d) optimization of  $N_C$  (cm<sup>-3</sup>), (e and f) optimization of  $E_g$  (eV), (g and h) optimization of  $\chi$  (eV), (i and j) optimization of  $\varepsilon_r$ , (k and l) optimization of layer numbers of diamane by keeping its other parameters at optimum set of values.
- Fig. 4.3 Simulation of a-Si: H (i) at optimized diamane and other layers at the previous set of values (Table 4.4). (a and b) optimization of  $N_{\text{C}}/N_{\text{V}}$  (cm<sup>-3</sup>), (c and d) optimization of  $E_{\text{g}}$  (eV), (e and f) optimization of thickness (nm).
- Fig. 4.4 Simulation of p-csi layer at optimized diamane as well as a-si: 79 H (i) layer. (a and b) optimization of  $N_A$  (cm<sup>-3</sup>), (c and d) optimization of  $N_V$  (cm<sup>-3</sup>), (e and f) optimization of  $\chi$  (eV), (g and h) optimization of thickness ( $\mu$ m), (i and j) optimization of layer numbers of diamane at fully optimized cell, (k and l) optimization of thickness (nm) of a-Si: H (i) again at fully optimized cell.
- Fig. 4.5 Simulation of graphene (TCE) at optimized cell. (a and b) 82 optimization of layer numbers, (c and d) optimization of  $\varphi$  (ev) at single layer graphene, (e and f) optimization of  $\varphi$  (ev) of graphene layer by taking commercially available values of pcsi layer. (g and h) thickness of pcsi layer at single layer graphene with  $\varphi = 4.31$  eV (other parameters of pcsi layer are at practically available set of values).
- **Fig. 4.6** Simulation of front as well as back contact surfaces for final optimized cell. (a and b) optimization of the work function (eV) of ITO at thickness 80 nm, (c and d) optimization of work

function (eV) of Al (front contact) at thickness 80 nm, (e and f) $$
optimization of work function (eV) of Ag (back contact) at
thickness 10 µm.

- **Fig. 5.1** (a) Schematic depicting the structure of the HIT solar cell under AM 1.5 G light that was simulated. (b) Simulated energy band diagram of the proposed HIT structure as generated by the software.
- Fig. 5.2 Results obtained for optimising the emitter layer (n-Dn) (a & 101 b) optimization of  $N_D$  within the range  $1 \times 10^{16}$  cm<sup>-3</sup>  $2 \times 10^{20}$  cm<sup>-3</sup>, (c & d) optimization of  $Nc/N_V$  within the range  $6 \times 10^{17}$  cm<sup>-3</sup>  $7 \times 10^{21}$  cm<sup>-3</sup>, (e & f) optimization of  $E_g$  within 3.2 eV 4.1 eV, (g & h) optimization of  $\chi$  in the range 3.2 eV 4.1 eV, (i & j) optimization of  $E_g$  in the range 4 11. (k & l) Optimization of the number of layers of n-Dn from 1 to 7.
- **Fig. 5.3** Results obtained for the optimization of BSF (p-Dn) (a & b) 106 optimization of  $N_A$  within the range  $1 \times 10^{16}$  cm<sup>-3</sup>  $1 \times 10^{21}$  cm<sup>-3</sup>, (c & d) optimization of  $N_C/N_V$  within the range  $1 \times 10^{12}$  cm<sup>-3</sup>  $9 \times 10^{21}$  cm<sup>-3</sup>, (e & f) optimization of  $E_g$  within 0.8 eV 1.8 eV, (g & h) optimization of  $\chi$  in the range 3.6 eV 4.5 eV, (i & j) optimization of  $\varepsilon_r$  in the range 4 11. (k & l) Optimization of the number of layers of p-Dn from 1 7.
- **Fig. 5.4** Results obtained for the optimization of buffer layer a-Si: H(i) 107 (a&b) optimization of Nc/N<sub>V</sub> within  $1\times10^{21}$  cm<sup>-3</sup>  $3\times10^{21}$  cm<sup>-3</sup>, (c & d) optimization of E<sub>g</sub> within the range 1.6 eV 1.7 eV, (e & f) optimization of thickness of a-Si: H(i) within the range 3 nm 10 nm.
- Fig. 5.5 Results obtained for the optimization of active layer p-cSi (a & 107 b) optimization of  $N_A$  within  $2 \times 10^{16}$  cm<sup>-3</sup>  $1.5 \times 10^{19}$  cm<sup>-3</sup>, (c & d) optimization of  $N_C/N_V$  within the range  $2.5 \times 10^{19}$  cm<sup>-3</sup>  $9 \times 10^{21}$  cm<sup>-3</sup>, (e & f) optimization of thickness of p-cSi layer within the range 30  $\mu$ m to 300  $\mu$ m.

- Fig. 5.6 (a & b) Results obtained for the optimization of the angle at which texturing is done (texturing angle). (c & d) Results obtained for the optimization of absorption loss at the front contact (single layer graphene) while taking the texturing angle at 90°.
- **Fig. 6.1**. Schematic of the designed HJBSF (a) and HITBSF (b) cells. 121 The band bending diagram showing the separation of charges at the hetero-interfaces for the HJ (c) and HIT (d) cell.
- Fig. 6.2 Optimization of the thickness of the emitter layer of HJBSF cell showing the variation of  $V_{OC}$ ,  $J_{SC}$  (a), and FF,  $\eta$  (b), respectively. Optimization of the thickness of the emitter layer of HITBSF cell showing the variation of  $V_{OC}$ ,  $J_{SC}$  (c), and FF,  $\eta$  (d), respectively, with layer numbers of n-type diamane, acting as the emitter layer.
- Fig. 6.3 Optimization of the thickness of BSF layer of HJ cell showing the variation of  $V_{OC}$ ,  $J_{SC}$  (a) and FF,  $\eta$  (b), respectively. Optimization of the thickness of BSF layer of HIT cell showing the variation of  $V_{OC}$ ,  $J_{SC}$  (c) and FF,  $\eta$  (d), respectively with layer numbers of p-type diamane, acting as the BSF layer.
- Fig. 6.4 Optimization of the thickness of active layer (p-cSi) in the range from 15 to 80  $\mu$ m for HJBSF cell showing the variation of  $V_{OC}$ ,  $J_{SC}$  (a) and FF,  $\eta$  (b), respectively. Optimization of the thickness of active layer (p-cSi) in the range from 15 to 35  $\mu$ m for HITBSF cell showing the variation of  $V_{OC}$ ,  $J_{SC}$  (c) and FF,  $\eta$  (d), respectively.
- Fig. 6.5 Optimization of the bandgap of emitter layer (n-Dn) of HJBSF cell showing the variation of  $V_{OC}$ ,  $J_{SC}$  (a) and FF,  $\eta$  (b), respectively in the range from 0.8 eV to 1.4 eV. Optimization of the bandgap of emitter layer of HITBSF cell in the range from 0.8 eV to 1.4 eV, showing the variation of  $V_{OC}$ ,  $J_{SC}$  (c) and FF,  $\eta$  (d), respectively.

- Fig. 6.6 Optimization of the bandgap of BSF layer (p-Dn) of HJBSF 132 cell showing the variation of  $V_{OC}$ ,  $J_{SC}$  (a) and FF,  $\eta$  (b), respectively in the range from 1.2 eV to 1.9 eV. Optimization of the bandgap of BSF layer of HITBSF cell in the range from 1.2 eV to 1.9 eV, showing the variation of  $V_{OC}$ ,  $J_{SC}$  (c) and FF,  $\eta$  (d), respectively.
- Fig. 6.7 Optimization of the thickness of front intrinsic a-Si: H layer in 133-134 the range from 3 nm to 10 nm for HITBSF solar cell showing the variation of  $V_{OC}$ ,  $J_{SC}$  (a) and FF,  $\eta$  (b), respectively. Optimization of the thickness of back intrinsic a-Si: H layer in the range from 3 nm to 10 nm for HITBSF solar cell, showing the variation of  $V_{OC}$ ,  $J_{SC}$  (c) and FF,  $\eta$  (d), respectively.
- Fig. 6.8 Optimization of the bandgap of front intrinsic a-Si: H layer in the range from 1.6 eV to 1.72 eV for HITBSF solar cell showing the variation of  $V_{OC}$ ,  $J_{SC}$  (a) and FF,  $\eta$  (b), respectively. Optimization of the bandgap of back intrinsic a-Si: H layer in the range from 1.6 eV to 1.72 eV for the same HITBSF cell, showing the variation of  $V_{OC}$ ,  $J_{SC}$  (c) and FF,  $\eta$  (d), respectively.
- Fig. 6.9 J-V characteristics of the best optimised HJBSF cell ( $\eta=138$  26.86%) (a) and Wavelength dependency of (b) SR in the range (300 nm–1200 nm) at 80  $\mu$ m p-cSi wafer. J-V characteristics of the best optimised HITBSF cell ( $\eta=29.38\%$ ) (c) and Wavelength dependency of (d) SR in the range (300 nm–1200 nm) at 35  $\mu$ m p-cSi wafer.
- **Fig. 6.10** (a) IQE and (b) EQE of the best simulated HJBSF solar cell ( $\eta = 139$  26.86%) at 80  $\mu$ m p-cSi wafer in the range of wavelength from 300 nm to 1200 nm. (c) IQE and (d) EQE of the best simulated HIJBSF solar cell (29.38%) at 35  $\mu$ m p-cSi wafer in the same range of wavelength from 300 nm to 1200 nm.

- **Fig. 7.1** (a) The structure of the proposed designed cell with a 151 passivated emitter. (b) The energy band diagram of the fully simulated cell was generated by the software.
- Fig. 7.2 (a & b) The effect of variation of carrier lifetime (τ) of the pc-Si layer (active layer) on the performance parameters of the
  designed cell. (c & d) The effect of thickness (μm) of the active
  layer (p-c-Si) on the performance parameters of the designed
  cell.
- Fig. 7.3 (a & b) The effect of variation of carrier lifetime (τ) of the pc-Si layer (active layer) on the performance parameters of the
  designed cell. (c & d) The effect of thickness (μm) of the active
  layer (p-c-Si) on the performance parameters of the designed
  cell.
- Fig. 7.4 (a & b) The effect of variation of thickness (nm) of the emitter layer (n-Dn) on the performance parameters of the designed cell. (c & d) The effect of variation of doping concentration  $(N_D)$  of the emitter layer (n-Dn) on the performance parameters of the designed cell.
- Fig. 7.5 shows the I-V characteristics of optimized HJ solar cells: (a) 161 ITO/n-Dn/p-cSi/Au; A simple HJ design with ITO as TCE and n-Dn as the emitter, achieving 17.17% PCE. (b) Gr/n-Dn/p-cSi/Au Replacing ITO with graphene improves PCE to 23.05%. (c) Gr/n-Dn/p-cSi/p-Dn/Au; Adding a p-Dn as BSF, boosts PCE to 26.86%. (d) Gr/Si<sub>3</sub>N<sub>4</sub>/SiO<sub>2</sub>/n-Dn/p-cSi/p-Dn/Au; Emitter passivation with Si<sub>3</sub>N<sub>4</sub>/SiO<sub>2</sub> raises PCE to 30.59%.
- Fig. 7.6

  I-V characteristics of optimized HIT solar cells: (a) Gr/n-Dn/aSi:H(i)/p-cSi/Au; Simple HIT design with single-sided passivation, achieving 26.19% PCE. (b) Gr/n-Dn/a-Si:H(i)/p-cSi/a-Si:H(i)/Au; Double-sided passivated c-Si layer slightly improves PCE to 26.20%. (c) Gr/n-Dn/a-Si:H(i)/p-cSi/p-Dn/Au; Adding a p-Dn BSF to single-sided passivated HIT

boosts PCE to 27.57%. (d) Gr/n-Dn/a-Si:H(i)/p-cSi/a-Si:H(i)/p-Dn/Au; Fully passivated c-Si with BSF further increases PCE to 29.38%.

I-V characteristics of optimized HIT solar cells with passivated Fig. 7.7 164 emitter: Gr/Si<sub>3</sub>N<sub>4</sub>/SiO<sub>2</sub>/n-Dn/a-Si:H(i)/p-cSi/Au; (a) Passivated emitter with Si<sub>3</sub>N<sub>4</sub>/SiO<sub>2</sub> enhances PCE to 26.94%. (b) Gr/Si<sub>3</sub>N<sub>4</sub>/SiO<sub>2</sub>/n-Dn/a-Si:H (i)/p-cSi/a-Si:H(i)/Au; Fully passivated c-Si layer with emitter passivation improves PCE to 28.15%. (c)  $Gr/Si_3N_4/SiO_2/n-Dn/a-Si:H(i)/p-cSi/p-Dn/Au;$ Adding a p-Dn BSF to single-sided passivated HIT with passivation boosts **PCE** to 28.73%. emitter (d)  $Gr/Si_3N_4/SiO_2/n-Dn/a-Si:H(i)/p-cSi/a-Si:H(i)/p-Dn/Au;$  Fully optimized HIT with passivated emitter achieves 30.69% PCE.

#### LIST OF ABBREVIATIONS

Acronyms	Meaning
PV	Photovoltaic
SHJ	Silicon Heterojunction
HIT	Heterojunction with Intrinsic Thin-layer
2D	Two-Dimensional
BSF	Back Surface Field
PCE	Power Conversion Efficiency
SR	Spectral Response
FF	Fill Factor
Voc	Open circuit voltage
$J_{ m SC}$	Short circuit current density
Mono-Si	Monocrystalline Silicon
Poly-Si	Polycrystalline Silicon
CdTe	Cadmium Telluride
CIGS	Copper Indium Gallium Selenide
a-Si: H(i)	Intrinsic Hydrogenated Amorphous Silicon
CSCs	Carrier-selective Contacts
OPVs	Organic Photovoltaics
DSSCs	Dye-Sensitized Solar Cells
НЈТ	Heterojunction Technology
MoOx	Molybdenum Oxide

VOx Vanadium Oxide

TiOx Titanium Oxide

ZnO Zinc Oxide

MoS<sub>2</sub> Molybdenum Disulfide

XRD X-ray diffraction

FTIR Fourier transform infrared spectroscopy

FESEM Field-emission scanning electron microscopy

XPS X-ray photoelectron spectroscopy

AFM Atomic force microscopy

PECVD Plasma-Enhanced Chemical Vapor Deposition

ALD Atomic Layer Deposition

CNTs Carbon Nanotubes

GDY Graphdiyne

TCEs Transparent Conductive Electrodes

TCO Transparent Conductive Oxide

ITO Indium Tin Oxide

GO Graphene Oxide

RGO Reduced Graphene Oxide

SHJ Silicon Heterojunction

MoO<sub>3</sub> Molybdenum Trioxide

UV Ultraviolet

TMOs Transition Metal Oxides

CSLs Carrier-selective layers

CBO Conduction Band Offset

VBO Valence Band Offset

DFT Density Functional Theory

XPS X-ray Photoelectron Spectroscopy

TEM Transmission Electron Microscopy

AFORS-HET Automat FOR Simulation of Heterojunction

PLD Pulsed Layer Deposition

SEM Scanning Electron Microscopy

AFM Atomic Force Microscopy

TLM Transmission Line Model

EHP Electron-Hole Pair

EQE External Quantum Efficiencies

IQE Internal Quantum Efficiencies

IBC Interdigitated Back Contacts

CuSCN Copper (I) Thiocyanate

TMDs Transition Metal Dichalcogenides

NIR Near Infrared

PERC Passivated Emitter Rear Cell

HBC Heterojunction Back Contact

AR Anti-Reflective

AM Air Mass

## CHAPTER 1

#### **INTRODUCTION**

This chapter provides a comprehensive review of energy harvesting technologies, with a focus on their diverse applications and ability to meet rising energy demands. It provides a thorough analysis of solar energy harvesting methods, with a particular emphasis on silicon heterojunction solar cells. It also highlights the critical need for reducing dependency on fossil fuels and the contribution of cutting-edge solar technology to the development of renewable energy in the future. This chapter explores the fundamental principles, current challenges, and recent advancements in energy harvesting, laying the foundations for a future that is more sustainable and energy-efficient. The chapter also reviews strategies for enhancing solar cell efficiency, including material selection, structural optimization, and integrated design approaches adopted in the past. It concludes by outlining the research's objectives, which are focused on the design of high-performance solar cells, and providing an overview of the thesis structure.

#### 1.1 Background and Motivation/Overview

The growing global energy demand, driven by rapid technological progress and an increasing population, has prompted both scientific and industrial communities to pursue sustainable and renewable energy solutions. The overreliance on non-renewable resources, particularly fossil fuels, has led to environmental degradation and resource depletion, highlighting the urgent need for alternative energy generation methods [1]. Energy harvesting offers a promising path forward by capturing and converting naturally available ambient energy, such as solar, wind, hydro, geothermal, and biomass, into usable electrical power [2]. Fig. 1.1 illustrates various types of renewable energy harvesting sources available in our environment. These renewable energy sources are widely available and easy to obtain in our day-to-day lives. Wind energy converts the kinetic energy of moving air into electricity using wind turbines. However, wind energy is geographically and meteorologically dependent, requiring specific site conditions such as consistent wind speeds and open landscapes [3]. Hydropower relies on the potential energy of stored or flowing water, typically in the form of dams or run-of-river systems. While hydropower is efficient and capable of providing baseload power, its environmental consequences, such as ecosystem disruption, displacement of communities, and alteration of river dynamics, limit its sustainability in certain contexts [4]. Geothermal energy exploits the heat stored beneath the Earth's surface to produce electricity and provide direct heating. It offers a stable and continuous power supply with low emissions and a minimal land footprint. However, geothermal development is also constrained by geographical limitations, because it is only feasible in regions with significant tectonic or volcanic activity [5]. Biomass energy, generated from organic materials such as agricultural waste, wood, and biofuels, is a flexible and dispatchable energy source. It can be used for electricity generation, heating, and transportation. While biomass is considered renewable when managed sustainably, it raises important concerns about land use, deforestation, air quality, and carbon neutrality [6]. Another abundant energy source in the environment that remains unaffected by external conditions is solar energy. It is one of the most widely recognised and utilized renewable resources, consistently available during daylight hours and easily converted into electricity using photovoltaic (PV) cells or solar thermal systems [7]. As the most abundant and widely distributed renewable source, solar energy is well-suited for both centralised and

decentralised applications. Over the past few decades, advancements in technology have significantly improved its efficiency and reduced costs, enhancing its economic viability [8]. Its silent operation, low maintenance, and adaptability to various built environments make solar energy a key component of a sustainable energy future [7].



Fig. 1.1 Various renewable and sustainable sources of energy present in the surroundings.

In this context, the present thesis explores innovative strategies to enhance the performance of silicon heterojunction (SHJ) and HIT solar cells by introducing a novel two-dimensional (2D) carbon material as an alternative to conventional doped amorphous silicon layers. The research centres on investigating this material's potential as both the emitter and BSF or hole-selective contact layer, to address key limitations such as parasitic absorption, interface recombination, and thermal instability.

A significant emphasis of this study is placed on the simulation and comparative analysis of various SHJ and HIT device architectures, incorporating the novel 2D material into different configurations to optimize energy band alignment, carrier selectivity, and light absorption. Through detailed numerical simulations, the thesis evaluates the influence of structural and material modifications on photovoltaic parameters such as Voc, Jsc, FF,

and overall PCE. The primary objective of this work is to achieve a maximum possible solar cell efficiency by systematically designing, modelling, and refining high-performance device structures. This research contributes to the advancement of next-generation solar technologies by offering a pathway toward scalable, stable, and environmentally sustainable photovoltaic solutions with industry-leading performance potential.

#### 1.2 Solar Cells for Solar Energy Harvesting

The global transition to sustainable energy has positioned solar energy as a leader among renewable energy technologies. Among the several methods for harnessing and converting solar energy, solar cells, PV cells, represent the most direct and efficient way. Solar cells immediately transform sunlight into electricity through the photovoltaic effect, providing a clean, renewable, and progressively economical energy source [9].

#### 1.2.1 Working Principle of Solar Cells

Solar cells operate on the photovoltaic effect, generating a potential difference at a junction between two materials when exposed to radiation [9]. This process involves three key steps: the generation of charge carriers through photon absorption, the separation of these carriers at the junction, and their collection at the terminals [9]. A typical solar cell comprises an absorber layer that efficiently absorbs incident radiation, creating electron-hole pairs [9]. Semi-permeable membranes are attached to both sides of the absorber, selectively allowing only one type of charge carrier to pass through [9,10]. For efficient solar cell design, charge carriers must reach these membranes, requiring diffusion lengths greater than the absorber's thickness [9]. Fig. 1.2 and Fig. 1.3 portray the photoelectric effect and the structure of a PV cell.

In c-Si solar cells, a moderately-doped p-type c-Si is used as an absorber (active) layer [9]. A thin, highly-doped n-type layer forms the electron membrane on the top side, while a highly-doped p-type serves as the hole membrane on the back side [9]. This asymmetry in the electronic structure of the n-type and p-type semiconductors is the basic requirement for photovoltaic energy conversion. Fig. 1.4 shows a schematic band diagram of an illuminated idealised solar cell structure with an absorber and the semi-permeable membranes at two conditions: a) open-circuit and b) short-circuit conditions.

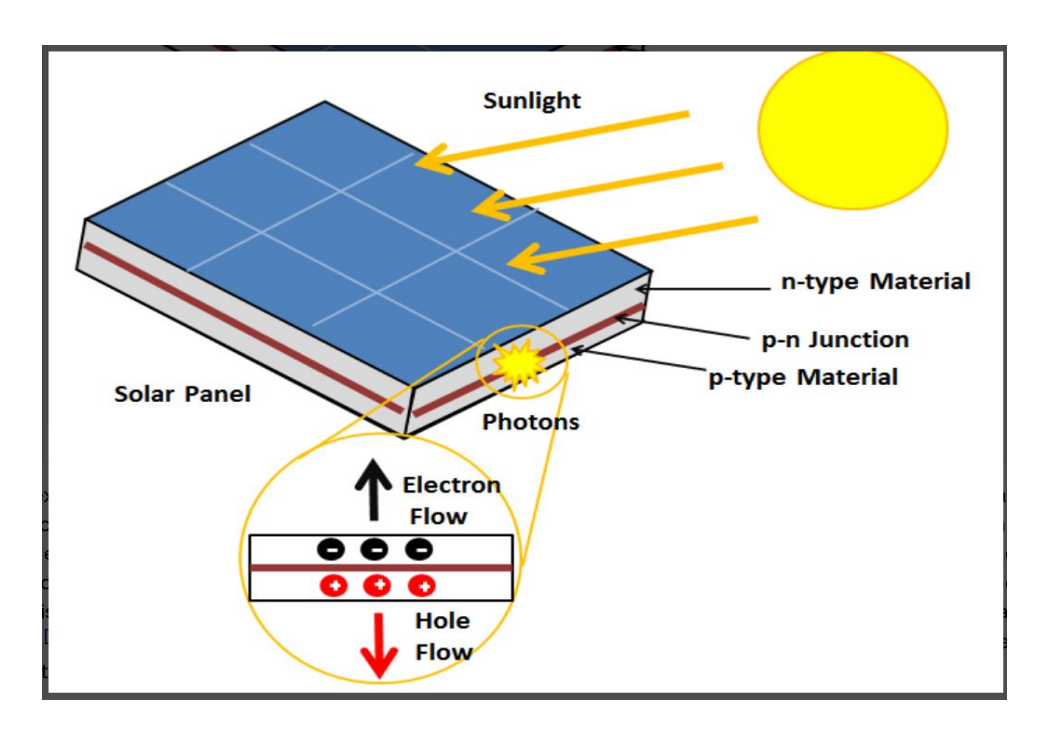


**Fig. 1.2** A diagram showing the photovoltaic effect [http://www.ecogreenelectrical.com/solar.htm].

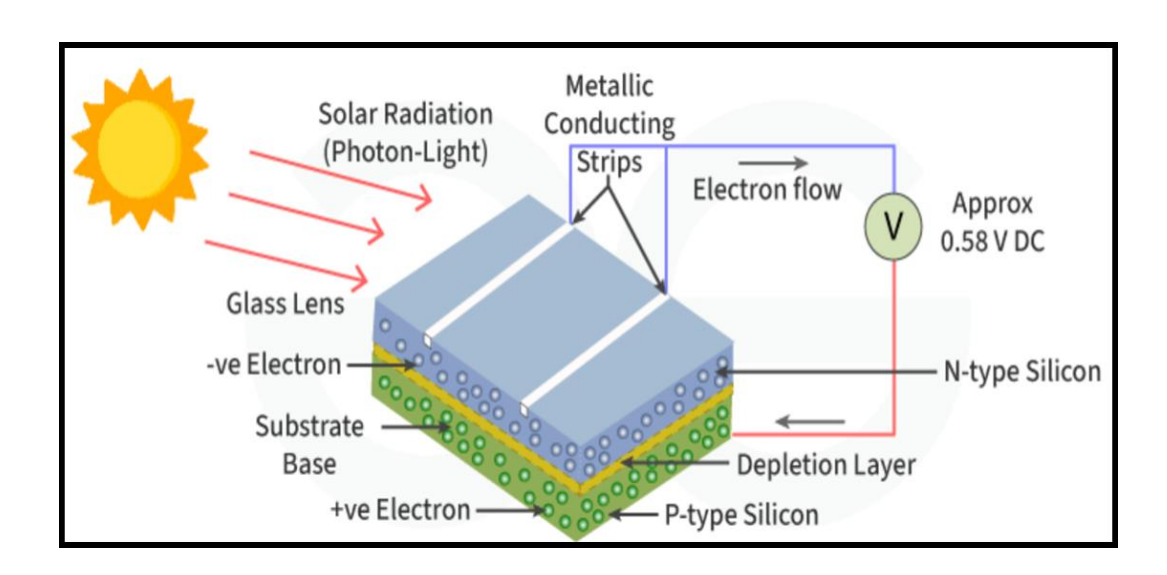


**Fig. 1.3** A diagram showing the structure of a PV cell [https://www.geeksforgeeks.org/photovoltaic-cell/].

The quasi-Fermi level for electrons,  $E_{FC}$ , and the quasi-Fermi level for holes,  $E_{FV}$ , are used to describe the illuminated state of the solar cell. The energy difference between the

quasi-Fermi levels is a measure of the efficient conversion of the energy of radiation into electrochemical energy.

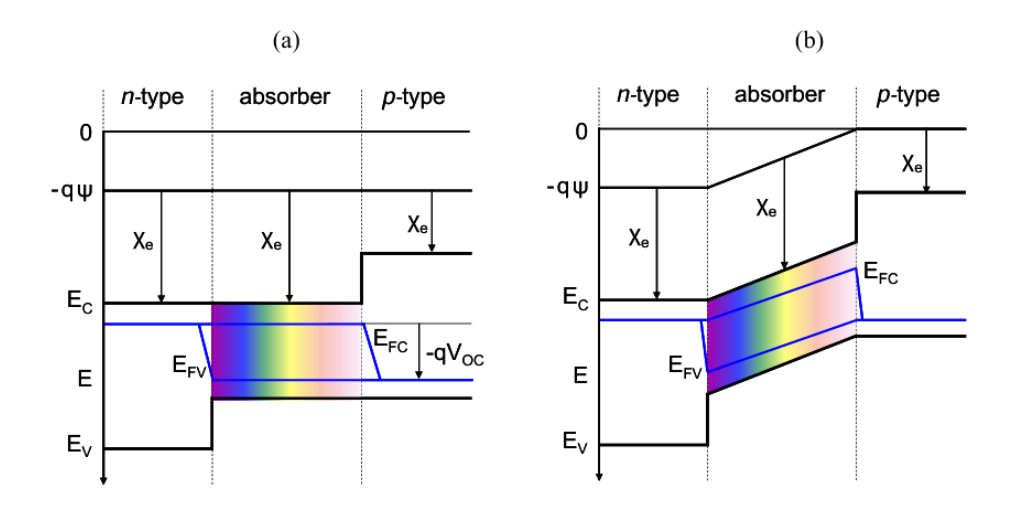


Fig. 1.4 Band diagram of an idealized solar cell structure at the a) open-circuit and b) short-circuit conditions [9].

P-N junctions, critical for solar cells, form at the interfaces between the c-Si p-type absorber and the highly-doped n-type and p-type membranes [9]. Fig. 1.5 shows schematically isolated pieces of a p-type and an n-type semiconductor and their corresponding band diagrams. In both isolated pieces, the charge neutrality is maintained. When a p-type and n-type semiconductor are joined, electrons diffuse from the n-type to the p-type side, and holes from the p-type to the n-type side due to concentration differences. This movement depletes the region near the junction of mobile charge carriers, creating a depletion region with fixed ionized donor and acceptor atoms. This region holds a space charge, while areas outside remain electrically neutral and are called quasi-neutral regions. The formation of this region is schematically illustrated in Fig. 1.6. The internal electric field within these junctions facilitates the separation of photogenerated electron-hole pairs, preventing their recombination and contributing to energy conversion [9]. The equivalent circuit of a photovoltaic cell is shown in Fig. 1.7. The performance of solar cells is characterized by parameters such as Jsc, Voc, and FF [9]. The parameters can be derived from the illuminated J-V characteristic, as depicted in Fig. 1.8. Jsc represents the current flowing through the external circuit when the cell's electrodes are short-circuited, ideally equaling the photo-generated current density (J<sub>ph</sub>) [9].  $V_{OC}$  is the voltage at which no current flows, where the dark current compensates for the photo-current, can be calculated as [9].

$$V_{OC} = \frac{kT}{q} \ln \left( \frac{J_{ph}}{J_0} + 1 \right) \tag{1.1}$$

The FF is the ratio between the maximum power deliverable by a solar cell and the product of Voc and Jsc [9].

$$FF = \frac{J_{mp}V_{mp}}{J_{SC}V_{OC}}$$
 (1.2)

$$\eta = \frac{P_m}{P_{in}} = \frac{J_{mp}V_{mp}}{P_{in}} = \frac{J_{SC}V_{OC}FF}{P_{in}}$$
(1.3)

These parameters determine the conversion efficiency  $(\eta)$ , calculated as the ratio between the generated maximum power and the incident power [9].

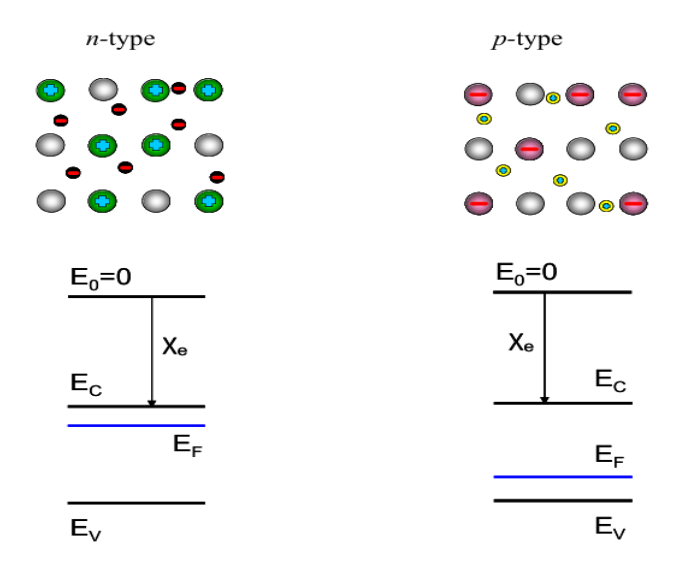
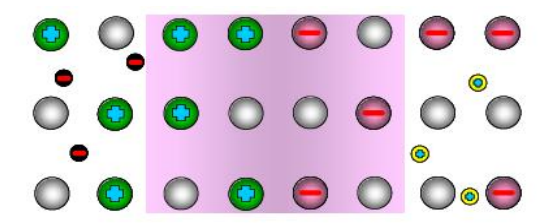
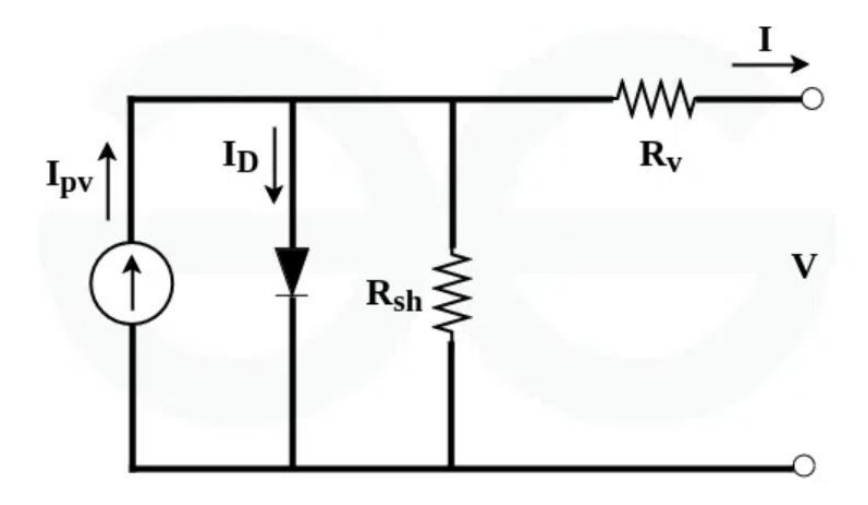


Fig. 1.5 Schematic representation of an isolated p-type and n-type semiconductor and corresponding band diagrams [9].



**Fig. 1.6** Formation of a space-charge region at the p—n junction due to carrier diffusion and built-in electric field [9].



**Fig. 1.7** The equivalent circuit of a photovoltaic cell [https://www.geeksforgeeks.org/photovoltaic-cell/].

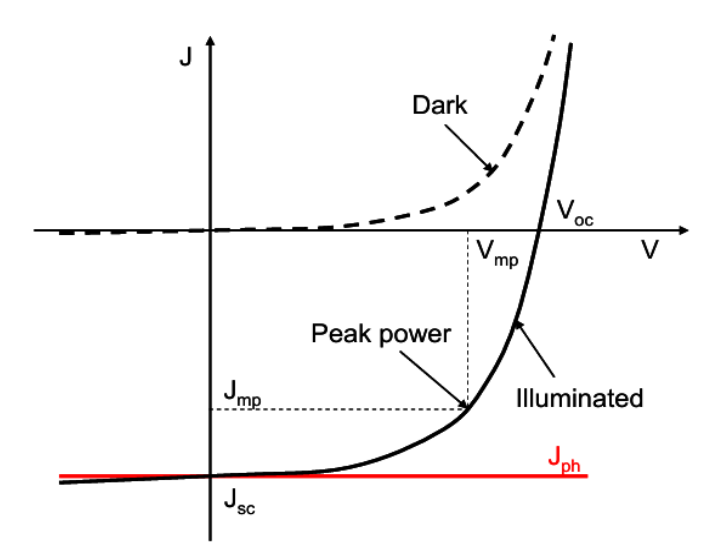


Fig. 1.8 J-V characteristics of a p-n junction in the dark and under illumination [9].

#### 1.2.2 Types of Solar Cells

#### **First-Generation Solar Cells**

These are based on c-Si and dominate the commercial market due to mature technology and high efficiency.

• **Monocrystalline Silicon (mono-Si):** High efficiency (>24%), long lifespan, but expensive [11,12].

• Polycrystalline Silicon (poly-Si): Lower cost, slightly lower efficiency (17–20%) [12].

#### **Second-Generation Solar Cells**

Known as thin-film solar cells, these offer lower manufacturing costs and flexibility, but generally lower efficiency.

- Cadmium Telluride (CdTe): High absorption coefficient, moderate efficiency (~22%) [12].
- Copper Indium Gallium Selenide (CIGS): Good performance under low-light conditions, flexible substrates [12].
- Amorphous Silicon (a-Si): Low cost, low efficiency ( $\sim$ 10%) [12].

#### **Third-Generation Solar Cells**

These are research-focused, aiming for higher efficiency and lower cost by incorporating novel materials and device architectures.

- **Perovskite Solar Cells:** High efficiency (more than 25%), tunable bandgap, solution processable [13].
- Organic Photovoltaics (OPVs): Lightweight, flexible, low-cost fabrication, but stability issues [14].
- Quantum Dot Solar Cells: Size-tunable properties, potential for multi-exciton generation [15].
- **Dye-Sensitized Solar Cells (DSSCs):** Inspired by photosynthesis, suitable for indoor use [15].

Silicon-based solar cells dominate the PV market due to their mature manufacturing processes and cost-effectiveness. Despite their widespread adoption, conventional silicon solar cells face challenges such as high-temperature processing requirements and efficiency limitations. Emerging technologies aim to address these issues by introducing new materials and cell architectures.

#### 1.3 Silicon Heterojunction and HIT Solar Cells

HJ silicon solar cells, also referred to as heterojunction technology (HJT) solar cells, merge the beneficial properties of c-Si and hydrogenated amorphous silicon (a-Si: H). This hybrid architecture enables high-efficiency photovoltaic conversion using reduced amounts of silicon and significantly lower processing temperatures, typically not exceeding 200–250 °C, compared to conventional diffusion-based silicon solar cell technologies [16]. The first heterojunction solar cells were developed in the 1990s by Sanyo, achieving an initial efficiency of approximately 12% [17]. Since then, HJT has undergone substantial advancements, with continuous improvements in design, materials, and fabrication processes leading to record-breaking efficiencies surpassing 26%, the highest reported for all-silicon solar cell technologies [18-21]. Due to these merits, HJT has emerged as one of the most promising candidates for large-scale PV applications.

According to the theoretical work of Shockley and Queisser, the efficiency limit for a single p-n junction solar cell is 33.7% [22]. More specific calculations for silicon-based solar cells estimate a practical efficiency ceiling of around 29.4% [23-24]. These theoretical boundaries have served as benchmarks for research and innovation in silicon photovoltaics, motivating the development of novel structures like HJT. In the earliest versions of HJT devices, a thin layer of p-type a-Si: H was deposited on an n-type crystalline silicon wafer to form the heterojunction [17]. This configuration achieved an efficiency of 12.3% with the a-Si: H layer thickness around 10 nm. Further advancements revealed that incorporating an intrinsic (i-type) a-Si: H layer between the doped a-Si: H and c-Si significantly reduced interface defect densities, leading to improvements in open-circuit voltage, short-circuit current, and fill factor. This HIT structure reached an efficiency of 14.8%, with the optimal intrinsic layer thickness in the range of 6–7 nm. Sanyo further enhanced the design by texturing the c-Si surface to improve light absorption, especially at low incidence angles. Although the exact texturing parameters were not disclosed, the use of hydrogen plasma treatment before a-Si: H deposition was noted. Additionally, an n-type a-Si: H layer was applied to the rear surface to create a back electric field or BSF, pushing the efficiency up to 18.1% for 1 cm<sup>2</sup> cell samples. Fig. 1.9 is the cross-sectional diagram of silicon-based HJ and HIT solar cells. Subsequent research focused on optimizing the deposition conditions of a-Si: H to enhance surface passivation. A major milestone was reported when Tsunomura et al. (2009) fabricated a

high-efficiency HJT cell with an area of 100.5 cm<sup>2</sup> [25]. Improvements in the heterointerface quality, grid design, and optical management played a key role. Later that year, Sanyo presented another advanced HJT device featuring a 98 μm-thick wafer and a 100.3 cm<sup>2</sup> area. In 2014, Panasonic achieved a new record efficiency for HJT cells using high-quality monocrystalline wafers [26].

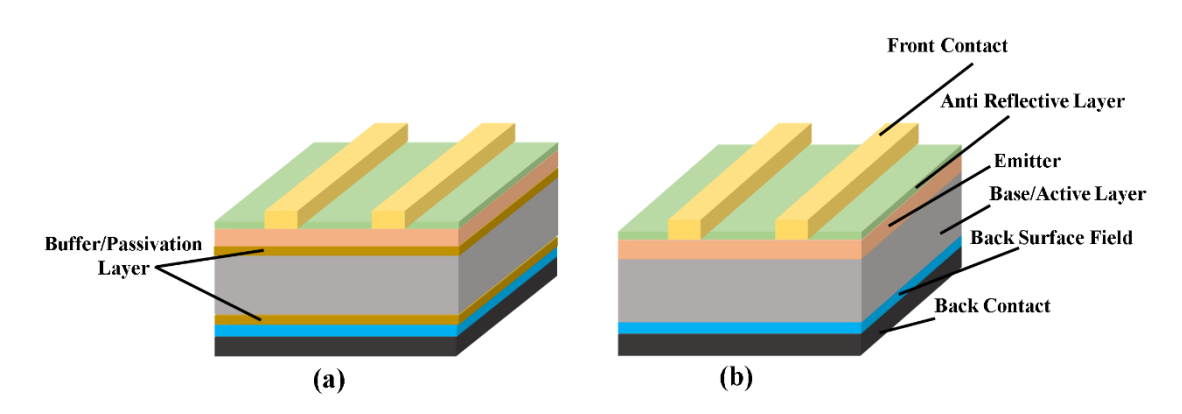


Fig. 1.9 Layered structure of (a) HJT, and (b) HIT.

The core principle behind heterojunction solar cells lies in forming p—n junctions between materials with dissimilar band gaps. A critical component of HJT design is the insertion of a wide-bandgap semiconductor layer between the active region and the metal contacts. This layer enhances voltage output by reducing carrier recombination at the interfaces [27-28]. According to the information mentioned above, we can say that a-Si: H, with its larger bandgap compared to c-Si and the ability to be doped n-type or p-type, is especially suitable as a buffer layer in such devices [29]. The a-Si: H/c-Si heterojunction concept dates back to 1974, when V. Fuss *et. al* conducted the earliest investigations [30]. Initial work on surface passivation using a-Si: H followed shortly after [31]. In 1983, a tandem solar cell based on an a-Si/c-Si configuration was reported [32]. Sanyo began commercializing heterojunction cells in the 1970s, using p-type boron-doped a-Si: H as the emitter on n-type wafers. These early devices achieved modest efficiencies (~14%) due to high parasitic currents and low fill factors [33].

A breakthrough came with the introduction of intrinsic a-Si: H layers between the doped emitter and the crystalline silicon, dramatically reducing interface defect states and improving carrier lifetimes. This HIT structure, first achieving 14.8% efficiency ([17],

p. 3521), was later refined further. By applying an additional intrinsic layer to the rear surface, a new design reached a record efficiency of 18% ([17], underscoring the significance of interface engineering in heterojunction solar cells.

#### 1.3.1 Carrier-Selective Contacts: Trends and Limitations

Carrier-selective contacts (CSCs) are essential elements in the architecture of high-efficiency silicon HJ solar cells. These contacts allow for the selective extraction of either electrons or holes while blocking the opposite type of carrier, significantly minimizing recombination losses at the interfaces. By enabling efficient carrier separation and collection, CSCs contribute to the high Voc and overall conversion efficiency observed in HJ solar technologies [34-35]. The typical HIT solar cell features a sandwich-like structure composed of five primary layers: a front p-type a-Si: H layer, a front intrinsic a-Si: H layer, a central n-type c-Si wafer, a rear intrinsic a-Si: H layer, and a rear heavily doped n-type a-Si: H layer as shown in Fig. 1.10. The front p-type a-Si: H layer forms a p—n heterojunction with the c-Si wafer, facilitating charge separation. On the rear side, the heavily doped n-type a-Si: H layer functions as a BSF, creating an energy barrier that prevents minority carrier recombination. The thin intrinsic a-Si: H layers at both interfaces play a vital role in passivating the surface states of the c-Si, thereby enhancing Voc and FF, and ultimately improving the overall device performance [37–40].

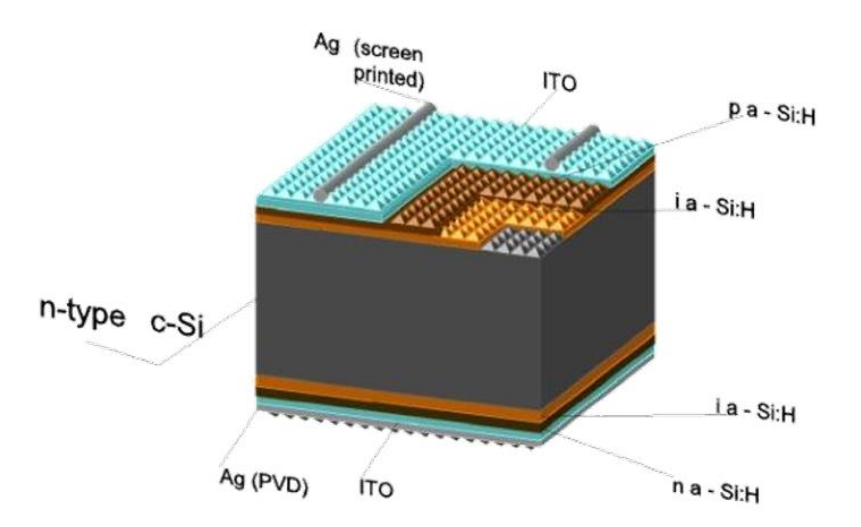


Fig. 1.10 Schematic representation of the heterojunction silicon (HIT) solar cell structure [36].

#### **Trends in Carrier-Selective Contact Development**

Silicon heterojunction solar cells have emerged as a leading photovoltaic technology, achieving record-breaking efficiencies through sophisticated carrier-selective contact structures. These contacts fundamentally transform light-absorbing semiconductors into high-performance photovoltaic devices by enabling efficient separation and collection of photogenerated carriers [41]. Recent developments in carrier-selective contacts have propelled SHJ technology to demonstrate certified power conversion efficiencies exceeding 26.8%, positioning them as a dominant force in next-generation solar cell architectures [42]. The development of CSCs in silicon HJ solar cells has seen exciting progress in recent years. The evolution from traditional doped silicon contacts to advanced dopant-free alternatives represents a paradigm shift that addresses fundamental limitations while opening new pathways for enhanced performance, simplified processing, and improved thermal stability. The primary focus has been on boosting transparency, minimizing optical and electrical losses, and improving the quality of interface passivation. Several key trends are shaping the future of this technology:

- Exploring New Materials: Researchers are looking beyond traditional doped a-Si: H and experimenting with wide-bandgap materials like transition metal oxides. Materials such as molybdenum oxide (MoOx) and vanadium oxide (VOx) show promise as hole-selective contacts, while titanium oxide (TiOx) and zinc oxide (ZnO) are being used for electron-selective contacts [41, 43-46]. These alternatives are attractive because they offer better transparency and help reduce unwanted light absorption, which can otherwise limit solar cell performance.
- Integration of 2D and Nanostructured Materials: Ultra-thin materials like graphene and molybdenum disulfide (MoS<sub>2</sub>) are gaining attention for their unique properties. Thanks to their atomically thin nature, adjustable work functions, and excellent charge transport capabilities, these materials are strong candidates for next-generation carrier-selective contacts. They hold potential for reducing recombination and enhancing overall efficiency in a lightweight, low-loss design.
- Emphasizing Low-Temperature Processing: One of the major advantages of HJ solar cells is that they can be manufactured at relatively low temperatures, typically below 250 °C [47]. This is beneficial not only for saving energy during

production but also for making it easier to work with flexible substrates or temperature-sensitive materials, paving the way for new applications like flexible or lightweight solar panels.

Improving Deposition Techniques: Techniques like plasma-enhanced chemical
vapour deposition (PECVD), atomic layer deposition (ALD), and sputtering are
being fine-tuned to achieve better control over film thickness, uniformity, and
doping. These advancements are crucial for producing cleaner interfaces with
fewer defects, which directly translates to better performance and longer-lasting
solar cells.

#### 1.4 2D Carbon Materials in Photovoltaics

The integration of 2D carbon materials into silicon HJ solar cells represents a cutting-edge strategy to overcome several inherent limitations of conventional contact materials. Allotropes such as graphene, carbon nanotubes (CNTs), and graphdiyne (GDY) exhibit outstanding electrical, optical, and mechanical properties, making them highly effective when applied as carrier-selective contacts, emitter layers, hole-selective layers, or (TCEs) transparent conductive electrodes [48-51].

These materials' atomically thin structures, tunable work functions, and high carrier mobilities contribute to improved interface quality, reduced recombination losses, and enhanced light absorption. Their incorporation into SHJ architectures has demonstrated significant potential for boosting both the efficiency and long-term stability of solar cells.

Recent advancements underscore this potential: graphene oxide/silicon heterojunctions have achieved efficiencies of up to 18.8%, CNT/Si solar cells have reached ~22% efficiency with encapsulation, and graphdiyne-based perovskite cells have attained 21.4% [51]. These improvements address critical challenges in traditional SHJ designs, such as interfacial recombination and parasitic optical losses, while also enabling low-temperature, scalable fabrication processes.

#### 1.4.1 Graphene and Its Derivatives

Graphene, a single layer of sp<sup>2</sup>-hybridized carbon atoms arranged in a hexagonal lattice, is widely studied as a transparent conductive electrode in SHJ solar cells. Its high

conductivity and transmittance (~97%) make it a compelling alternative to indium tin oxide (ITO). Moreover, its flexibility and chemical stability make it ideal for next-generation solar cells, including flexible and wearable photovoltaics [48-49].

Graphene can also be functionalized to serve additional roles. For instance, graphene oxide (GO) has been utilized to modify the interface between amorphous silicon and crystalline silicon, improving passivation and reducing interface trap densities. Experimental demonstrations have reported PCE as high as 18.8% in GO/Si heterojunction cells. Furthermore, graphene-based heterostructures have been explored for dual roles as both transparent electrodes and carrier-selective layers, simplifying device architecture while enhancing performance [52].

#### 1.4.2 Carbon Nanotubes (CNTs)

CNTs, cylindrical nanostructures composed of rolled graphene sheets, have shown promise as hole-selective contact materials due to their high work function and excellent hole mobility. Their unique 1D structure facilitates efficient charge transport, while their flexibility and solution processability allow low-temperature deposition, compatible with SHJ fabrication protocols. CNT/Si solar cells have achieved efficiencies exceeding 22% under encapsulated conditions, primarily by improving charge collection and minimizing contact resistance [53]. These structures benefit from strong interfacial bonding with silicon and enhanced light trapping due to CNTs' nanostructured morphology. Additionally, CNT films can be tuned in thickness and doping level to serve as TCEs or selective contact layers depending on device requirements.

#### 1.4.3 Graphdiyne (GDY)

Graphdiyne, a newer member of the carbon allotrope family, features a mix of sp and sp<sup>2</sup> hybridized carbon atoms with extended  $\pi$ -conjugation. Its natural semiconducting behaviour and tunable band gap ( $\sim$ 0.46–1.22 eV) enable its application in both charge transport and light absorption layers. GDY has been incorporated into perovskite and silicon solar cell architectures as an interfacial layer to enhance charge separation and minimize recombination. In one study, graphdiyne-based interlayers in perovskite solar cells yielded a PCE of 21.01%, demonstrating excellent interface passivation and moisture resistance [54]. Its potential integration into SHJ cells is of growing interest,

especially as a passivating hole-selective layer due to its inherent asymmetry in electron and hole transport.

The use of 2D carbon materials in SHJ solar cells addresses several critical limitations:

- Enhanced Surface Passivation: Atomically smooth 2D interfaces minimize surface defect states and improve open-circuit voltage.
- Tunable Work Function: Enables formation of energy-aligned carrier-selective contacts without requiring heavy doping.
- **Reduced Parasitic Absorption**: High optical transmittance preserves photon flux reaching the active silicon layer.

Common integration strategies include transferring pre-synthesized 2D layers via wet or dry transfer techniques, in situ CVD, and solution-based processing. Challenges include ensuring uniform coverage over large areas, minimizing interfacial contamination, and achieving strong adhesion with underlying silicon layers.

#### 1.5 Research Challenges

The integration of 2D carbon materials into SHJ solar cells presents a promising route to improving efficiency, flexibility, and cost-effectiveness, but it is not without considerable research challenges and limitations. One of the foremost barriers is the scalability of material synthesis. Although CVD allows for the fabrication of high-quality graphene, the process of transferring these films onto silicon substrates often introduces defects and contamination that degrade performance [55-56]. Furthermore, roll-to-roll production methods for rGO, while scalable, are hindered by high sheet resistance values often exceeding 200  $\Omega$ /sq, which limits electrical conductivity and efficiency [57]. For CNTs, synthesis typically yields a mixture of metallic and semiconducting tubes, necessitating complex and costly post-growth sorting to ensure device functionality [58]. Interface engineering remains another critical challenge. Unpassivated silicon surfaces exhibit high surface recombination velocities (SRV >1,000 cm/s), which significantly reduce opencircuit voltage ( $V_{\rm OC}$  <0.6 V) in graphene/Si solar cells unless additional passivation strategies, such as thin interfacial oxide layers, are implemented [59]. Similarly, CNT/Si interfaces suffer from Fermi-level pinning, which limits carrier selectivity and

necessitates the use of interlayers such as MoO₃ to reduce contact resistance to as low as 5 mΩ·cm² [60]. Work function tuning and band alignment also pose significant limitations, as precise energy level alignment is critical for efficient carrier extraction. While 2D materials like graphene and MoS₂ can have their work functions adjusted, it is still difficult to achieve reliable and large-scale doping or chemical modification needed to control their properties consistently [61]. Deposition and integration techniques are further limited by compatibility issues with existing low-temperature SHJ processing (≤250 °C), with many 2D materials requiring specialized handling or protection from ambient degradation. Stability and degradation of 2D materials under operational conditions also raise concerns. Graphene can oxidize under ambient exposure, and other materials like black phosphorus degrade rapidly without encapsulation [62].

Finally, standardization, reproducibility, and long-term reliability present persistent obstacles. Variability in material quality, device fabrication, and performance metrics impedes commercial translation and requires the development of industry-wide benchmarks for 2D carbon-based SHJ technologies. Addressing these challenges requires a multidisciplinary effort combining materials science, interface engineering, process optimization, and economic modelling to fully unlock the potential of 2D carbon materials in next-generation silicon photovoltaics.

#### 1.6 Research gap

The motivation behind this research stems from the pressing need to develop high-efficiency, cost-effective, and scalable solar cell technologies. Traditional silicon-based photovoltaics, despite their commercial success, face fundamental challenges such as intrinsic efficiency limits and high recombination losses. The integration of advanced nanomaterials such as diamane may offer an opportunity to address these challenges and enhance solar cell efficiency beyond current limits. A systematic investigation into the role of this 2D carbon material in various solar cell architectures could further optimize its potential for advanced PV applications.

#### 1.6.1 Research Objectives

The main objectives of the present thesis work are:

- To investigate the potential of diamane as an emitter layer in silicon heterojunction solar cells
- ❖ To design and develop a high-efficiency HIT cell incorporating graphene as a TCE and diamane as an emitter layer
- ❖ To investigate the potential of diamane as an effective BSF layer for enhancing charge carrier selectivity and minimizing recombination losses
- ❖ To evaluate the impact of surface passivation on c-Si and its influence on improving overall device performance and efficiency
- To analyze the impact of a passivating emitter layer on overall solar cell performance

#### 1.6.2 Overview of Thesis

The arrangement of the various thesis chapters is shown in a flowchart, which is illustrated in Fig. 1.11.

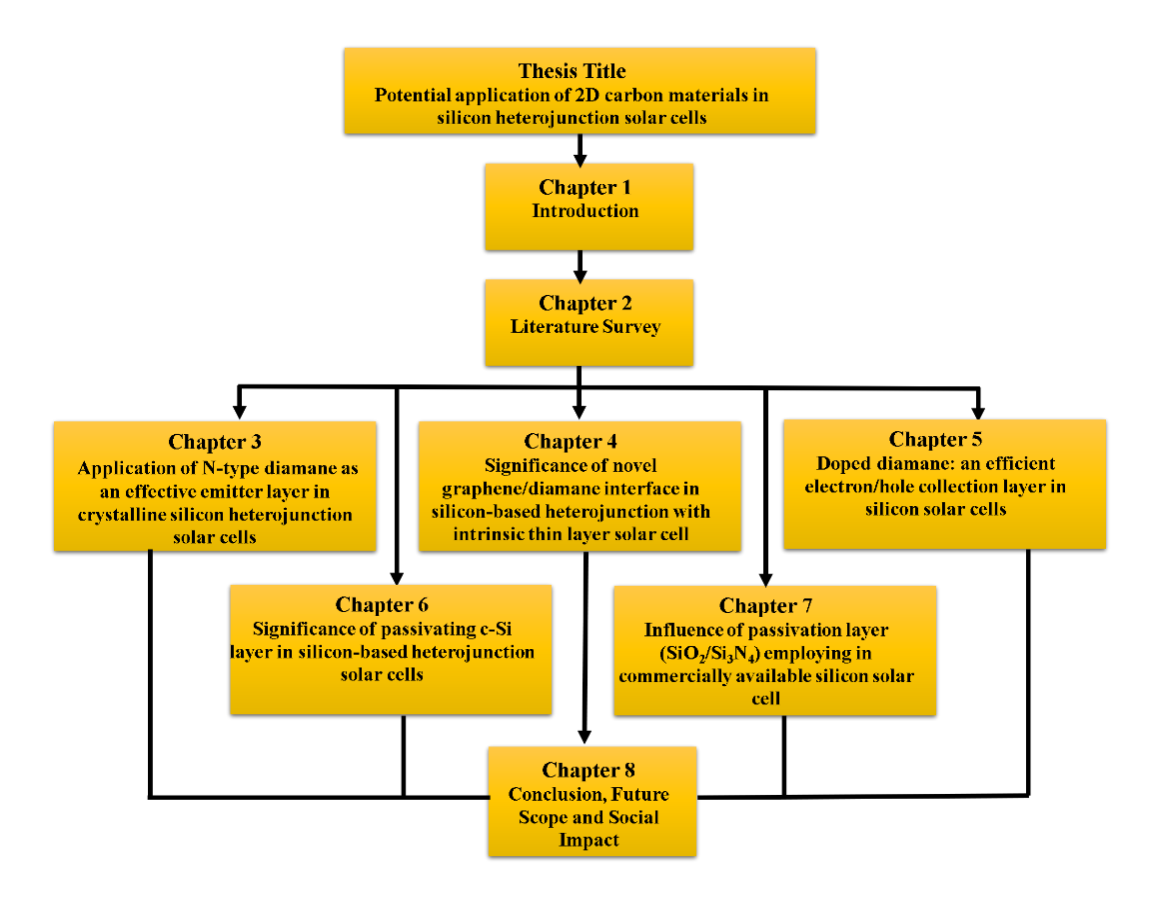


Fig. 1.11 Flowchart for the organisation of the thesis.

#### REFERENCES

- [1] Denchak, M., NRDC. 2022. Fossil Fuels: The Dirty Facts. https://www.nrdc.org/stories/fossil-fuels-dirty-facts.
- [2] Khaligh, A. and Onar, O.C., 2017. Energy harvesting: solar, wind, and ocean energy conversion systems. CRC press.
- [3] Duranay, Z.B., Güldemir, H. and Coşkun, B., 2024. The Role of Wind Turbine Siting in Achieving Sustainable Energy Goals. Processes, 12, 12, pp.2900.
- [4] Anderson, D., Moggridge, H., Warren, P. and Shucksmith, J., 2015. The impacts of 'run-of-river'hydropower on the physical and ecological condition of rivers. *Water and Environment Journal*, 29, 2, pp.268-276.
- [5] Igwe, C.I., 2021. Geothermal energy: a review. Int. J. Eng. Res. Technol.(IJERT), 10, 3, pp.655-661.
- [6] Ali, F., Dawood, A., Hussain, A., Alnasir, M.H., Khan, M.A., Butt, T.M., Janjua, N.K. and Hamid, A., 2024. Fueling the future: Biomass applications for green and sustainable energy. *Discover Sustainability*, *5*, 1, pp.156.
- [7] Weliwaththage, S.R. and Arachchige, U.S.P.R., 2020. Solar energy technology. *Journal of Research Technology and Engineering*, 1, 3, pp.67-75.
- [8] Maka, A.O. and Alabid, J.M., 2022. Solar energy technology and its roles in sustainable development. *Clean Energy*, 6, 3, pp.476-483.
- [9] TU Delft OpenCourseWare, n.d. *Reading 4: Solar cell operational principles*. [online] Available at: https://ocw.tudelft.nl [Accessed 23 Jun. 2025].
- [10] Wiirfel, P., 2005. Physics of solar cells. *Université Karlsruhe*.
- [11] Osborne, M., 2020. JinkoSolar Large-Area N-type Monocrystalline Silicon Solar Cell Reaches Record High Efficiency of 24.79%. *ed: PVTech*, July, 20.
- [12] Bayod-Rújula, A.A., 2019. Solar photovoltaics (PV). In *Solar hydrogen production*. Academic Press, pp. 237-295.
- [13] Bhattarai, S., Mhamdi, A., Hossain, I., Raoui, Y., Pandey, R., Madan, J., Bouazizi, A., Maiti, M., Gogoi, D. and Sharma, A., 2022. A detailed review of perovskite solar cells: Introduction, working principle, modelling, fabrication techniques, future challenges. *Micro and Nanostructures*, 172, 1, pp.207450.
- [14] Li, G., Zhu, R. and Yang, Y., 2012. Polymer solar cells. *Nature photonics*, 6, 3, pp.153-161.
- [15] Song, Y. and Zhu, W., 2024. Application of nanomaterials in solar cell. In *MATEC Web of Conferences*. EDP Sciences, 404, pp. 03007.
- [16] Dunlop, E.D., Emery, K., Green, M.A., Hishikawa, Y. and Warta, W., 2014. Solar Cell Efficiency Tables (Version 43). *Progress in Photovoltaics: Research and Applications*, 22, 1, pp.1-9.
- [17] Tanaka, M., Taguchi, M., Matsuyama, T., Sawada, T., Tsuda, S., Nakano, S., Hanafusa, H. and Kuwano, Y., 1992. Development of new a-Si/c-Si heterojunction solar cells: ACJ-HIT (artificially constructed junction-heterojunction with intrinsic thin-layer). *Japanese journal of applied physics*, 31, 11R, pp.3518.
- [18] Green, M.A., Emery, K., Hishikawa, Y. and Warta, W. (2009), Solar cell efficiency tables (version 33). *Prog. Photovolt: Res. Appl.*, 17, 1, pp. 85-94.
- [19] Green, M.A., Emery, K., Hishikawa, Y. and Warta, W. (2011), Solar cell efficiency tables (version 37). *Prog. Photovolt: Res. Appl.*, 19, 1, pp. 84-92.
- [20] Green M. A., Emery K., Hishikawa Y., Warta W., and Dunlop E. D. (2014) Solar cell efficiency tables (Version 45), *Prog. Photovolt: Res. Appl.*, 23, 1, pp. 1–9.
- [21] Yoshikawa, K., Kawasaki, H., Yoshida, W., Irie, T., Konishi, K., Nakano, K., Uto, T., Adachi, D., Kanematsu, M., Uzu, H. and Yamamoto, K., 2017. Silicon heterojunction solar cell with interdigitated back contacts for a photoconversion efficiency over 26%. *Nature energy*, 2, 5, pp.1-8.

- [22] Shockley, W. and Queisser, H., 2018. Detailed balance limit of efficiency of p-n junction solar cells. *Renewable energy*. Routledge, 2, pp.35-54.
- [23] Richter, A., Hermle, M. and Glunz, S.W., 2013. Reassessment of the limiting efficiency for crystalline silicon solar cells. *IEEE journal of photovoltaics*, 3, 4, pp.1184-1191.
- [24] Martin, A., 2013. Solar Cell Efficiency Tables (version 41). *Prog. Photovolt: Res. Appl.*, 21, 1, pp.1-11.
- [25] Tsunomura, Y., Yoshimine, Y., Taguchi, M., Baba, T., Kinoshita, T., Kanno, H., Sakata, H., Maruyama, E. and Tanaka, M., 2009. Twenty-two percent efficiency HIT solar cell. *Solar Energy Materials and Solar Cells*, 93, 6-7, pp.670-673.
- [26] Masuko, K., Shigematsu, M., Hashiguchi, T., Fujishima, D., Kai, M., Yoshimura, N., Yamaguchi, T., Ichihashi, Y., Mishima, T., Matsubara, N. and Yamanishi, T., 2014. Achievement of more than 25% conversion efficiency with crystalline silicon heterojunction solar cell. *IEEE journal of photovoltaics*, 4, 6, pp.1433-1435.
- [27] Yablonovitch, E., Gmitter, T., Swanson, R.M. and Kwark, Y.H., 1985. A 720 mV open circuit voltage SiO x: c-Si: SiO x double heterostructure solar cell. *Applied Physics Letters*, 47, 11, pp.1211-1213.
- [28] Chuchvaga, N., Zholdybayev, K., Aimaganbetov, K., Zhantuarov, S. and Serikkanov, A., 2023. Development of hetero-junction silicon solar cells with intrinsic thin layer: a review. *Coatings*, 13, 4, pp.796.
- [29] Spear, W.E. and Le Comber, P.G., 1975. Substitutional doping of amorphous silicon. *Solid state communications*, 17, 9, pp.1193-1196.
- [30] Fuhs, W., Niemann, K. and Stuke, J., 1974, May. Heterojunctions of amorphous silicon and silicon single crystals. In *AIP conference proceedings*. American Institute of Physics, 20, pp.345-350.
- [31] Pankove, J.I. and Tarng, M.L., 1979. Amorphous silicon as a passivant for crystalline silicon. *Applied Physics Letters*, 34, 2, pp.156-156.
- [32] Hamakawa, Y., Fujimoto, K., Okuda, K., Kashima, Y., Nonomura, S. and Okamoto, H., 1983. New types of high efficiency solar cells based on a-Si. *Applied Physics Letters*, 43, 7, pp.644-646.
- [33] Taguchi, M., 2021. Development history of high efficiency silicon heterojunction solar cell: from discovery to practical use. *ECS Journal of Solid State Science and Technology*, 10, 2, pp.025002.
- [34] Wang, G., Zhang, C., Sun, H., Huang, Z. and Zhong, S., 2021. Understanding and design of efficient carrier-selective contacts for solar cells. *AIP Advances*, 11, 11, pp. 115026.
- [35] Ibarra Michel, J., Dréon, J., Boccard, M., Bullock, J. and Macco, B., 2023. Carrier-selective contacts using metal compounds for crystalline silicon solar cells. *Progress in Photovoltaics: Research and Applications*, 31, 4, pp.380-413.
- [36] Chuchvaga, N.A., Zhilina, D.V., Zhantuarov, S.R., Tokmoldin, S.Z., Terukov, E.I. and Tokmoldin, N.S., 2018, March. Study and optimization of heterojunction silicon solar cells. In *Journal of Physics: Conference Series*. IOP Publishing, 993, pp. 012039.
- [37] Tucci, M., Della Noce, M., Bobeico, E., Roca, F.D., de Cesare, G. and Palma, F., 2004. Comparison of amorphous/crystalline heterojunction solar cells based on n-and p-type crystalline silicon. *Thin Solid Films*, 451, pp.355-360.
- [38] Voz, C., Munoz, D., Fonrodona, M., Martin, I., Puigdollers, J., Alcubilla, R., Escarré, J., Bertomeu, J. and Andreu, J., 2006. Bifacial heterojunction silicon solar cells by hot-wire CVD with open-circuit voltages exceeding 600 mV. *Thin solid films*, 511, 5, pp.415-419.
- [39] Xu, Y., Hu, Z., Diao, H., Cai, Y., Zhang, S., Zeng, X., Hao, H., Liao, X., Fortunato, E. and Martins, R., 2006. Heterojunction solar cells with n-type nanocrystalline silicon emitters on p-type c-Si wafers. *Journal of Non-Crystalline Solids*, 352, 9-20, pp.1972-1975.
- [40] Kleider, J.P., Chouffot, R., Gudovskikh, A.S., i Cabarrocas, P.R., Labrune, M., Ribeyron, P.J. and Brüggemann, R., 2009. Electronic and structural properties of the amorphous/crystalline silicon interface. *Thin Solid Films*, 517, 23, pp.6386-6391.

- [41] Oener, S.Z., Cavalli, A., Sun, H., Haverkort, J.E., Bakkers, E.P. and Garnett, E.C., 2018. Charge carrier-selective contacts for nanowire solar cells. *Nature Communications*, *9*, 1, pp.3248.
- [42] Lin, H., Yang, M., Ru, X., Wang, G., Yin, S., Peng, F., Hong, C., Qu, M., Lu, J., Fang, L. and Han, C., 2023. Silicon heterojunction solar cells with up to 26.81% efficiency achieved by electrically optimized nanocrystalline-silicon hole contact layers. *Nature Energy*, 8, 8, pp.789-799.
- [43] Battaglia, C., Yin, X., Zheng, M., Sharp, I.D., Chen, T., McDonnell, S., Azcatl, A., Carraro, C., Ma, B., Maboudian, R. and Wallace, R.M., 2014. Hole selective MoO x contact for silicon solar cells. *Nano letters*, 14, 2, pp.967-971.
- [44] Bivour, M., Temmler, J., Steinkemper, H. and Hermle, M., 2015. Molybdenum and tungsten oxide: High work function wide band gap contact materials for hole selective contacts of silicon solar cells. *Solar Energy Materials and Solar Cells*, 142, pp.34-41.
- [45] Fernández, S., Torres, I. and Gandía, J.J., 2022. Sputtered ultrathin TiO2 as electron transport layer in silicon heterojunction solar cell technology. *Nanomaterials*, 12, 14, pp.2441.
- [46] He, J., Cao, P., Zhang, P., Meng, F., Xie, A. and Gao, P., 2024. Vanadium Oxide Hole-Selective Contact for Crystalline Silicon Solar Cells. *ACS Applied Energy Materials*, 7, 23, pp.11218-11224.
- [47] Morvillo, P., Diana, R., Mucci, A., Bobeico, E., Ricciardi, R. and Minarini, C., 2015. Influence of annealing treatments on solution-processed ZnO film deposited on ITO substrate as electron transport layer for inverted polymer solar cells. *Solar Energy Materials and Solar Cells*, 141, pp.210-217.
- [48] Liu, Z., Lau, S.P. and Yan, F., 2015. Functionalized graphene and other two-dimensional materials for photovoltaic devices: device design and processing. *Chemical Society Reviews*, 44, 15, pp.5638-5679.
- [49] Bellani, S., Bartolotta, A., Agresti, A., Calogero, G., Grancini, G., Di Carlo, A., Kymakis, E. and Bonaccorso, F., 2021. Solution-processed two-dimensional materials for next-generation photovoltaics. *Chemical Society Reviews*, 50, 21, pp.11870-11965.
- [50] Chen, J., Wan, L., Li, H., Yan, J., Ma, J., Sun, B., Li, F. and Flavel, B.S., 2020. A polymer/carbon-nanotube ink as a boron-dopant/inorganic-passivation free carrier selective contact for silicon solar cells with over 21% efficiency. *Advanced Functional Materials*, 30, 38, pp.2004476.
- [51] Li, J., Jiu, T., Chen, S., Liu, L., Yao, Q., Bi, F., Zhao, C., Wang, Z., Zhao, M., Zhang, G. and Xue, Y., 2018. Graphdiyne as a host active material for perovskite solar cell application. *Nano letters*, 18, 11, pp.6941-6947.
- [52] Gao, Q., Yan, J., Wan, L., Zhang, C., Wen, Z., Zhou, X., Li, H., Li, F., Chen, J., Guo, J. and Song, D., 2022. High-efficiency graphene-oxide/silicon solar cells with an organic-passivated interface. *Advanced Materials Interfaces*, 9, 24, pp.2201221.
- [53] Yan, J., Zhang, C., Li, H., Yang, X., Wan, L., Li, F., Qiu, K., Guo, J., Duan, W., Lambertz, A. and Lu, W., 2021. Stable organic passivated carbon nanotube–silicon solar cells with an efficiency of 22%. *Advanced science*, 8, 20, pp.2102027.
- [54] Li, J., Jiu, T., Chen, S., Liu, L., Yao, Q., Bi, F., Zhao, C., Wang, Z., Zhao, M., Zhang, G. and Xue, Y., 2018. Graphdiyne as a host active material for perovskite solar cell application. *Nano letters*, 18, 11, pp.6941-6947.
- [55] Lee, W.C., Tsai, M.L., Chen, Y.L. and Tu, W.C., 2017. Fabrication and analysis of chemically-derived graphene/pyramidal Si heterojunction solar cells. *Scientific reports*, 7, 1, pp.46478.
- [56] Singh, E. and Nalwa, H.S., 2015. Stability of graphene-based heterojunction solar cells. *Rsc Advances*, 5, 90, pp.73575-73600.
- [57] Gomez De Arco, L., Zhang, Y., Schlenker, C.W., Ryu, K., Thompson, M.E. and Zhou, C., 2010. Continuous, highly flexible, and transparent graphene films by chemical vapor deposition for organic photovoltaics. *ACS nano*, 4, 5, pp.2865-2873.

- [58] Murakami, T., Nakatsuji, H., Inada, M., Matoba, Y., Umeyama, T., Tsujimoto, M., Isoda, S., Hashida, M. and Imahori, H., 2012. Photodynamic and photothermal effects of semiconducting and metallic-enriched single-walled carbon nanotubes. *Journal of the American Chemical Society*, 134, 43, pp.17862-17865.
- [59] Tune, D.D., Blanch, A.J., Krupke, R., Flavel, B.S. and Shapter, J.G., 2014. Nanotube film metallicity and its effect on the performance of carbon nanotube–silicon solar cells. *physica status solidi (a)*, 211, 7, pp.1479-1487.
- [60] Geier, M.L., McMorrow, J.J., Xu, W., Zhu, J., Kim, C.H., Marks, T.J. and Hersam, M.C., 2015. Solution-processed carbon nanotube thin-film complementary static random access memory. *Nature nanotechnology*, 10, 11, pp.944-948.
- [61] Giovannetti, G.A.K.P.A., Khomyakov, P.A., Brocks, G., Karpan, V.V., van den Brink, J. and Kelly, P.J., 2008. Doping graphene with metal contacts. *Physical review letters*, 101, 2, pp.026803.
- [62] Galceran, R., Gaufres, E., Loiseau, A., Piquemal-Banci, M., Godel, F., Vecchiola, A., Bezencenet, O., Martin, M.B., Servet, B., Petroff, F. and Dlubak, B., 2017. Stabilizing ultrathin black phosphorus with in-situ-grown 1 nm-Al<sub>2</sub>O<sub>3</sub> barrier. *Applied Physics Letters*, 111, 24, pp. 243101.

## CHAPTER 2

#### LITERATURE REVIEW

This chapter reviews the potential of 2D carbon materials, particularly diamane, as carrier-selective contacts in SHJ solar cells. It begins by outlining the limitations of conventional materials like doped amorphous silicon, including parasitic absorption and poor thermal stability. The key requirements for efficient contact layers, such as high transparency, mobility, tunable bandgap, and effective passivation are discussed, followed by a survey of alternatives like TMOs and organic layers. The focus then shifts to diamane, a sp³-hybridized carbon film with superior electrical and thermal properties. Simulation studies highlight diamane's effectiveness as both emitter and BSF layers, demonstrating its potential to enhance efficiency and scalability in SHJ and HIT architectures. The chapter concludes by defining the scope of the current research aimed at optimizing diamane-based solar cell designs.

#### 2.1. Introduction

Silicon-based solar cells continue to dominate the global PV market, primarily due to their technological maturity, cost competitiveness, and high efficiency [1]. Among the various silicon-based architectures, SHJ and HIT solar cells stand out. These designs leverage c-Si wafers in combination with thin-film layers to improve surface passivation and carrier selectivity. Recent advancements have significantly enhanced the PCE of SHJ devices, with certified records surpassing 26%, such as the 26.81% efficiency achieved by Longi Green Energy in 2022 [2]. Despite these promising developments, SHJ and HIT solar cells still face several critical challenges that hinder further efficiency improvements and limit their large-scale commercial adoption. One of the primary bottlenecks lies in the use of conventional doped a-Si: H layers for electron and hole-selective contacts. These layers often exhibit drawbacks such as high parasitic optical absorption, limited thermal stability, and relatively poor carrier mobility.

To overcome these limitations, recent research has increasingly focused on the integration of novel materials, particularly low-dimensional nanostructures, into SHJ architectures. Among these, 2D carbon-based materials, including graphene, CNTs, and the recently synthesized diamane, have attracted considerable attention. These materials offer unique advantages such as high electrical conductivity, tunable band gaps, mechanical flexibility, and atomically thin profiles, making them strong candidates for next-generation carrier-selective contact layers.

This chapter presents a critical review of the current landscape of carrier-selective contacts in SHJ solar cells, with a particular focus on 2D carbon materials. It examines the limitations of traditional approaches, outlines the key characteristics required for effective carrier-selective layers, and explores the potential of diamane as a novel contact material. The discussion ultimately situates this research within the broader efforts to develop more efficient, scalable, and durable solar cell technologies.

# 2.2 Conventional Electron/Hole Collection Materials and Their Limitations

#### 2.2.1 Doped Amorphous Silicon (a-Si: H)

In most commercial SHJ solar cells, intrinsic and doped a-Si: H layers serve as the passivating and carrier-selective layers, respectively. Typically, n-type a-Si: H is employed for electron collection, while p-type a-Si: H facilitates hole extraction. These layers are commonly deposited using PECVD at relatively low temperatures (~200– 300 °C), making them compatible with both c-Si wafers and flexible substrates [3]. Although doped a-Si: H layers provide reasonable surface passivation and are compatible with established low-temperature fabrication processes, they suffer from several intrinsic drawbacks that limit the overall performance of SHJ solar cells. One of the primary issues is parasitic absorption, as the relatively narrow bandgap of a-Si: H (~1.7 eV) leads to significant absorption in the visible and near-infrared regions of the spectrum [4]. This reduces the amount of light that reaches the c-Si absorber layer, thereby lowering the Jsc. In addition, doped a-Si: H films are characterized by high defect densities, typically in the range of  $10^{16}$  to  $10^{18}$  cm<sup>-3</sup>, which increase interface recombination losses and negatively impact the Voc [5]. Another challenge is their limited thermal and UV stability; prolonged exposure to thermal cycling and UV irradiation can lead to material degradation, posing a risk to long-term device reliability [4]. Furthermore, the low carrier mobility of doped a-Si: H, generally between 1 and 10 cm<sup>2</sup>/V·s, contributes to higher series resistance and reduces the FF, ultimately constraining the power conversion efficiency of the device. Collectively, these limitations impose constraints on both the maximum achievable power conversion efficiency and the operational durability of SHJ solar cells.

#### 2.2.2 Transition Metal Oxides (TMOs)

To address the inherent limitations of doped a-Si: H layers, considerable research has been directed toward TMOs as alternative, dopant-free carrier-selective contacts in SHJ solar cells. Materials such as MoO<sub>x</sub>, WO<sub>x</sub>, and V<sub>2</sub>O<sub>x</sub> have emerged as promising candidates, particularly for hole-selective applications, due to their intrinsically high work functions, typically exceeding 5.5 eV. This property allows for favourable energy level alignment with the valence band of c-Si, thereby enhancing hole extraction [6-9]. Despite these advantages, several critical challenges persist. TMOs are prone to interfacial instability due to potential diffusion or chemical interactions with adjacent

layers, which can degrade contact quality over time. Moreover, many TMOs exhibit poor lateral (in-plane) electrical conductivity, contributing to higher series resistance and reduced fill factor in devices. Their environmental sensitivity also poses concerns, as prolonged exposure to light and humidity can lead to material degradation and compromised long-term stability [10,11]. Despite these limitations, SHJ solar cells incorporating TMO-based hole-selective contacts have demonstrated power conversion efficiencies exceeding 22.5% [11]. While these results are encouraging, challenges related to stability, scalability, and integration into commercial manufacturing processes must still be resolved before TMOs can be widely adopted in industrial SHJ architectures.

#### 2.2.3 Other Emerging Materials

Beyond TMOs, several other emerging materials have been explored as potential carrier-selective layers in SHJ solar cells, each offering unique advantages and facing distinct challenges. Doped ZnO, for example, has been investigated due to its excellent transparency and electrical conductivity. However, its practical application is hindered by its susceptibility to degradation in acidic or humid environments, which raises concerns regarding long-term stability. Organic materials, particularly poly(3,4-ethylenedioxythiophene): poly(styrenesulfonate) (PEDOT: PSS), have also been used as hole-selective contacts [12]. These materials are attractive for their solution-processability and compatibility with flexible substrates, but they typically suffer from moisture sensitivity and limited thermal stability, which can impact device durability. Another notable candidate is nanocrystalline silicon oxide (nc-SiOx: H), which offers lower optical absorption compared to doped a-Si: H, along with improved environmental stability [13]. However, achieving uniform and reproducible deposition of nc-SiOx: H remains technically challenging due to its complex fabrication requirements.

#### 2.3 Desirable Properties for Carrier-Selective Layers

Carrier-selective layers (CSLs) are critical components in SHJ solar cells, as they enable the efficient extraction of the majority carriers, electrons or holes, while simultaneously blocking the flow of minority carriers. To perform this dual function

effectively, these layers must meet a comprehensive set of criteria encompassing electronic, optical, thermal, interfacial, and processing-related properties.

#### 2.3.1 Electronic Requirements

From an electronic standpoint, one of the key requirements for CSLs is proper energy band alignment with the underlying c-Si. For electron-selective contacts, a large conduction band offset (CBO) is desirable to block holes. In contrast, hole-selective contacts benefit from a significant valence band offset (VBO) to impede electron flow. Additionally, the work function of the contact material should align appropriately with the c-Si band edges, ideally below 4.0 eV for electron-selective layers and above 5.2 eV for hole-selective ones. High carrier mobility is equally essential to facilitate rapid and efficient transport of majority carriers through the contact with minimal electrical resistance [7,8,12]

#### 2.3.2 Optical Transparency

To ensure maximum light absorption by the c-Si absorber, optical losses within the CSL must be minimized. This can be achieved by selecting materials with wide optical bandgaps, typically greater than 3 eV, which help to reduce parasitic absorption in the visible range [14]. High optical transparency, especially over the 300–1100 nm wavelength range, is also crucial, with transmission ideally exceeding 90%. Furthermore, minimizing the refractive index mismatch between adjacent layers can reduce Fresnel reflections at interfaces, further improving light management within the device [15].

#### 2.3.3 Thermal and Chemical Stability

Since CSLs must withstand both fabrication and long-term operational conditions, their thermal and chemical stability is of paramount importance. Materials should retain their structural and functional integrity under processing temperatures in the range of 200–300 °C [16,17]. Moreover, they must be chemically inert, exhibiting strong resistance to oxidation, corrosion, and degradation when exposed to environmental stressors such as moisture, air, or UV radiation.

#### 2.3.4 Interfacial Passivation

Effective interfacial passivation is critical for reducing recombination losses at the c-Si/contact interface. This requires a low interface defect density (Dit), ideally below  $10^{11} \, \text{cm}^{-2} \text{eV}^{-1}$ , to suppress Shockley-Read-Hall recombination. Minimal Fermi-level pinning is also desirable, as it allows for predictable Schottky barrier heights and more efficient carrier selectivity [18-20].

#### 2.3.5 Scalability and Process Compatibility

Finally, for CSLs to be practicable in commercial production, they must be compatible with scalable and cost-effective fabrication techniques. Low-temperature processing, preferably below 250 °C, is advantageous for integration with existing silicon-based technologies [21-24]. Solution-processable materials are especially attractive due to their potential for large-area, low-cost manufacturing. In addition, mechanical flexibility is an increasingly valuable attribute for emerging applications such as bifacial and flexible solar modules, where traditional rigid materials may fall short.

#### 2.4 Diamane: A Promising 2D Carbon Material

Diamane, a recent addition to the family of two-dimensional carbon materials, has emerged as a particularly intriguing candidate for next-generation solar cell technologies [25-31]. It is synthesized through the chemical functionalization of bilayer graphene, commonly by hydrogenation or fluorination, which transforms the carbon atoms from sp<sup>2</sup> to sp<sup>3</sup> hybridization [30]. This structural change gives rise to a diamond-like, atomically thin material that exhibits an exceptional combination of electronic, optical, and mechanical properties [25]. Unlike graphene, which is a zero-bandgap semimetal, diamane features a wide and tunable bandgap (ranging from 0 to 5.7 eV), along with impressive mechanical stiffness, high thermal conductivity, and significantly improved chemical stability [28, 32-35]. These properties make it particularly attractive for use as a carrier-selective material in SHJ solar cells. While research on diamane is still in its early stages, its combination of electronic tunability and physical robustness makes it a promising material for future photovoltaic applications, as shown in Fig. 2.1.

#### 2.4.1 Structural and Electronic Properties

Diamane is typically synthesized by exposing bilayer graphene to a hydrogen or fluorine plasma, which induces interlayer bonding and converts the carbon atoms to sp<sup>3</sup> hybridization, shown in Fig. 2.1 [37-38]. This modification results in a two-dimensional crystal structure that, despite its atomic thickness, mimics the electronic and mechanical properties of bulk diamond. Among diamane's most attractive electronic features is its tunable bandgap, which varies significantly depending on the functionalization method and surface chemistry. For instance, fluorinated diamane may exhibit a bandgap around 0.85 eV, while hydrogenated forms can exceed 5 eV [25]. This flexibility allows diamane to be tailored for use as either an electron-selective or hole-selective contact, depending on device architecture.

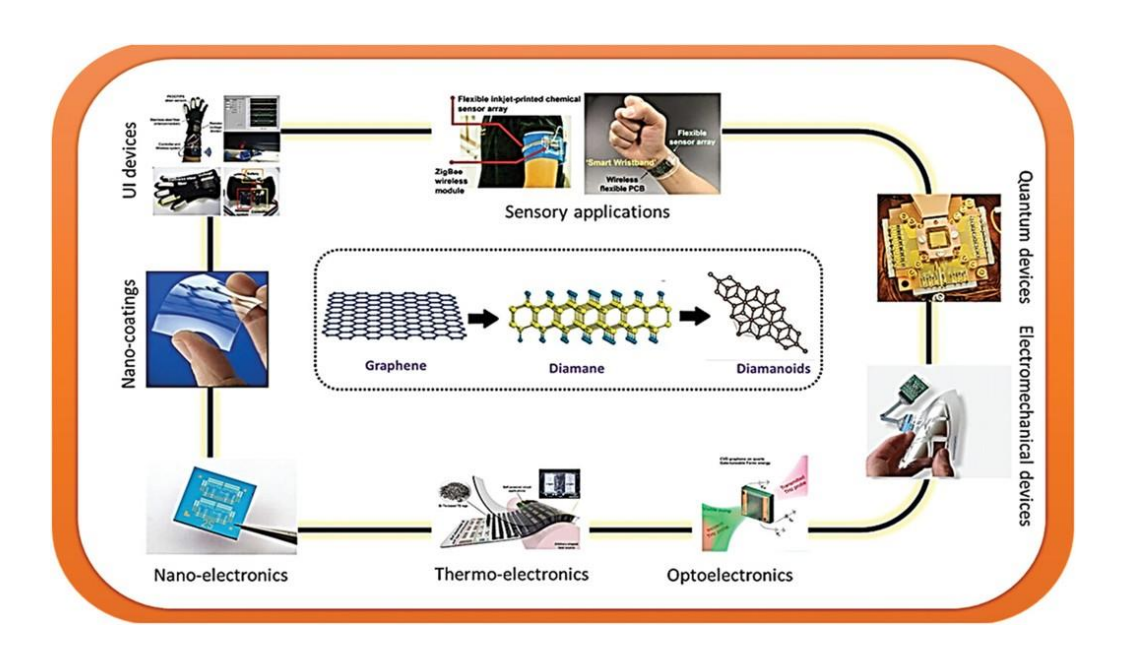


Fig. 2.1 Various applications of diamane in optoelectronic devices [36].

In terms of work function, diamane covers a broad range from approximately 3.5 to 6.5 eV [25, 30], which enables excellent alignment with both the conduction and valence band edges of c-Si. Moreover, theoretical studies suggest high carrier mobilities, with values up to ~2732 cm²/V·s for electrons and ~1565 cm²/V·s for holes with high thermal conductivity [40,41]. These performance indicators are on par with or even exceed those of conventional oxide-based CSLs, aligning closely with the requirements discussed earlier in Section 2.3.

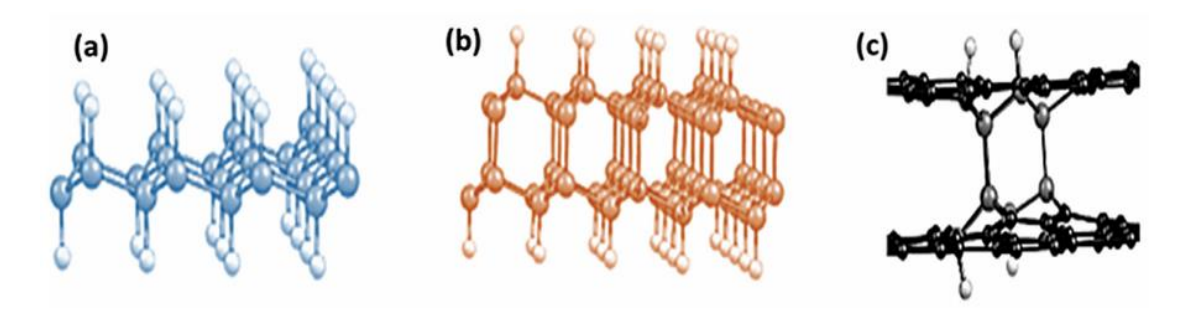


Fig. 2.2 Atomic structures of (a) graphane and (b) diamane, and (c) the mechanism of the diamane nucleus formation on the initial graphene bilayer [37].

#### 2.4.2 Optical and Mechanical Characteristics

In addition to its electronic advantages, diamane also offers excellent optical and mechanical properties. Owing to its atomic thinness, it maintains high optical transparency, especially in monolayer and few-layer configurations, crucial for maximizing light transmission into the silicon absorber and thereby enhancing J<sub>SC</sub> [25]. Mechanically, diamane benefits from its diamond-like stiffness, with a Young's modulus approaching 493.19 Nm<sup>-1</sup>, higher than graphene [42]. This makes it highly resistant to mechanical deformation, a feature that can be particularly valuable in flexible electronic applications [25]. Furthermore, its thermal conductivity remains impressive, though somewhat lower than pristine graphene, at values between 1000 and 1540 W/m·K, supporting effective heat dissipation in high-irradiance environments [25, 35].

#### 2.4.3 Fabrication Challenges and Research Directions

Despite its promising attributes, significant challenges remain in realizing diamane-based devices. One of the foremost issues is scalable synthesis. Techniques such as plasma-assisted hydrogenation and fluorination are effective for small-scale samples but currently lack the uniformity and scalability required for industrial applications. Material stability is another concern. While hydrogenated diamane is more chemically robust than pristine graphene, its long-term stability under ambient, thermal, and UV exposure conditions needs thorough investigation. Moreover, precise doping and

functionalization, essential for tuning work function, are still difficult to control reproducibly across large areas. Fig.2.3 shows the block diagram summarizing the key methods used for the fabrication of diamanes [43].

Finally, integration with crystalline silicon remains a complex task. Achieving low-resistance, defect-free interfaces without disrupting energy band alignment is a key technical hurdle that requires advances in both deposition techniques and surface engineering. Nevertheless, ongoing research in CVD, transfer methods, and in-situ functionalization continues to push the boundaries of what's possible with diamane. As synthesis and integration techniques mature, diamane holds strong promise as a next-generation carrier-selective material for high-efficiency and potentially flexible SHJ solar cells.

#### 2.5 Scope of the Present Work

In the pursuit of enhancing the efficiency and material stability of SHJ solar cells, this work focused on exploring the application of 2D carbon materials, specifically diamane, as carrier-selective contacts. Among the 2D carbon allotropes, diamane emerges as a highly promising candidate. Its sp<sup>3</sup>-hybridized structure endows it with a tunable wide bandgap, high mechanical and thermal stability, and excellent charge carrier mobility. Unlike zero-bandgap graphene, diamane's semiconducting properties make it intrinsically suitable for use as a carrier-selective contact. Moreover, its work function can be modulated over a wide range through doping or functionalization, enabling both n-type and p-type applications in SHJ architectures. While 2D materials like graphene, carbon nanotubes, and graphdiyne have been previously studied in photovoltaic devices, the use of diamane in SHJ or HIT architectures is relatively novel and underexplored. To address this, the present work investigated the electronic and optoelectronic properties of diamane and its integration as an n-type emitter and p-type BSF layer in SHJ solar cells. Theoretical modelling and device simulations were carried out using AFORS-HET, where diamane layers with tunable bandgap and adjustable work function were systematically incorporated into SHJ and HIT structures. Through simulated studies, energy band diagrams, carrier transport behaviour, and recombination characteristics at the diamane/Si interface were analyzed.

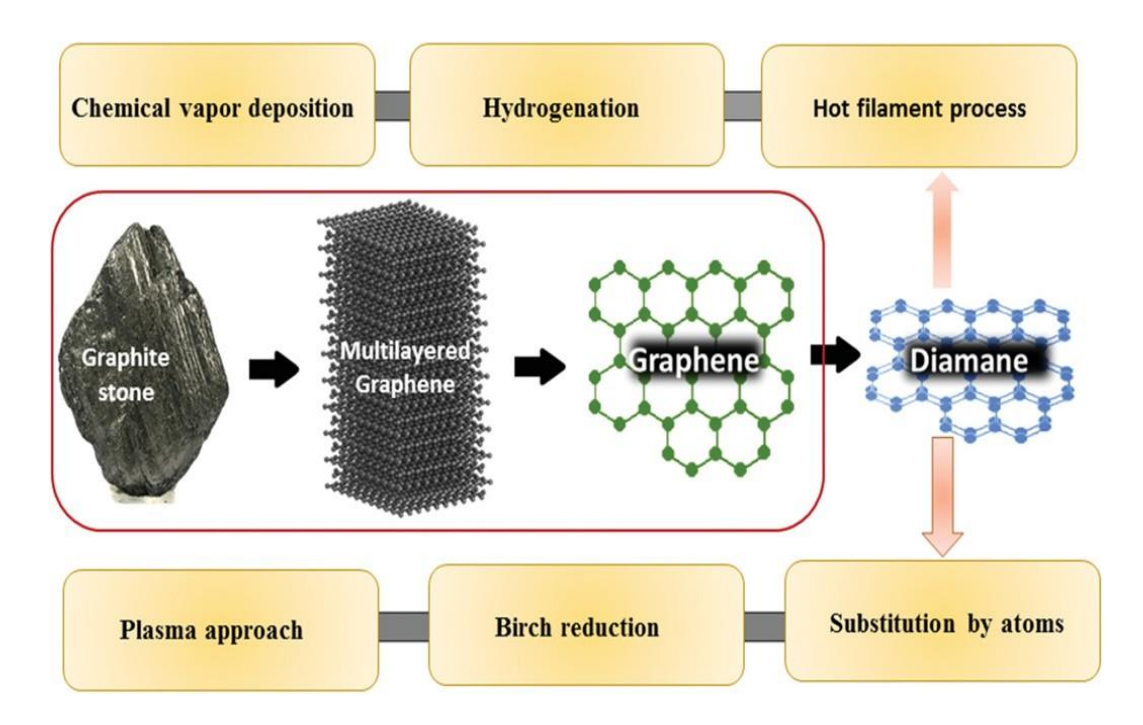


Fig. 2.3 The block diagram summarizing the key methods used for the fabrication of diamanes [37].

The simulation data were validated through variation in material properties such as bandgap (0.8–5.7 eV), doping levels, and thickness, which demonstrated substantial influence on the PCE, Jsc, Voc, and FF of the devices. An optimum configuration of ptype diamane as BSF and n-type diamane as emitter layer led to maximum simulated efficiency exceeding 29.3% under AM1.5G illumination, with minimal recombination and superior charge selectivity. In the most recent contribution, diamane was integrated into a passivated emitter BSFHJ design alongside SiO<sub>2</sub>/Si<sub>2</sub>N<sub>4</sub> dielectric layers, which significantly enhanced passivation and anti-reflection, resulting in a record simulated efficiency of 30.59%, and further extended to 30.69% for a fully passivated BSFHIT cell. Across all studies, material properties such as bandgap, carrier mobility, doping concentration, and layer thickness were optimized using AFORS-HET, revealing how diamane's tunable band structure and high carrier mobility make it a transformative material in photovoltaic applications. This integrated research establishes diamane not only as a viable alternative to doped amorphous silicon but also as a high-efficiency, stable, and scalable solution for next-generation silicon solar technologies.

#### REFERENCES

- [1] Di Sabatino, M., Hendawi, R., and Garcia, A. S. (2024). Silicon Solar Cells: Trends, Manufacturing Challenges, and AI Perspectives. *Crystals*, 14, 2, pp.167.
- [2] Lin, H., Yang, M., Ru, X., Wang, G., Yin, S., Peng, F., Hong, C., Qu, M., Lu, Junxiong., Fang, L., Han, C., Procel, P., Isabella, O., Xu, X., Gao, P., and Li, Z., 2023. Silicon heterojunction solar cells with up to 26.81% efficiency achieved by electrically optimized nanocrystalline-silicon hole contact layers. *Nature Energy*, 8, 8, pp.789–799.
- [3] De Wolf, S., Descoeudres, A., Holman, Z. C., and Ballif, C., 2012. High-efficiency Silicon Heterojunction Solar Cells: A Review. *Green*, 2, 1, pp.7-24.
- [4] Holman, Z. C., Descoeudres, A., Barraud, L., Fernandez, F. Z., Seif, J. P., De Wolf, S., and Ballif, C., 2012. *IEEE Journal of Photovoltaics*, 2, 1, pp.7-15.
- [5] Fehr, M., Simon, P., Sontheimer, T., Leendertz, C., Gorka, B., Schnegg, A., Rech, B., and Lips, K., 2012. Influence of deep defects on device performance of thin-film polycrystalline silicon solar cells. *Applied Physics Letters*, 101, 12, pp.123904.
- [6] Battaglia, C., Yin, X., Zheng, M., Sharp, I.D., Chen, T., McDonnell, S., Azcatl, A., Carraro, C., Ma, B., Maboudian, R. and Wallace, R.M., 2014. Hole selective MoO x contact for silicon solar cells. *Nano letters*, 14, 2, pp.967-971.
- [7] Bivour, M., Temmler, J., Steinkemper, H. and Hermle, M., 2015. Molybdenum and tungsten oxide: High work function wide band gap contact materials for hole selective contacts of silicon solar cells. *Solar Energy Materials and Solar Cells*, 142, pp.34-41.
- [8] Sanyal, S., Dutta, S., Ju, M., Mallem, K., Panchanan, S., Cho, E.C., Cho, Y.H. and Yi, J., 2019. Hole Selective Contacts: A Brief Overview. *Current Photovoltaic Research*, 7, 1, pp.9-14.
- [9] Almora, O., Gerling, L.G., Voz, C., Alcubilla, R., Puigdollers, J. and Garcia-Belmonte, G., 2017. Superior performance of V<sub>2</sub>O<sub>5</sub> as hole selective contact over other transition metal oxides in silicon heterojunction solar cells. Solar Energy Materials and Solar Cells, 168, pp.221-226.
- [10] Sacchetto, D., Jeangros, Q., Christmann, G., Barraud, L., Descoeudres, A., Geissbühler, J., Despeisse, M., Hessler-Wyser, A., Nicolay, S. and Ballif, C., 2017. ITO/MoOx/a-Si: H (i) hole-selective contacts for silicon heterojunction solar cells: degradation mechanisms and cell integration. *IEEE Journal of Photovoltaics*, 7, 6, pp.1584-1590.
- [11] Geissbühler, J., Werner, J., Martin de Nicolas, S., Barraud, L., Hessler-Wyser, A., Despeisse, M., Nicolay, S., Tomasi, A., Niesen, B., De Wolf, S. and Ballif, C., 2015. 22.5% efficient silicon heterojunction solar cell with molybdenum oxide hole collector. *Applied Physics Letters*, 107, 8, pp.081601.
- [12] Azri, F., Meftah, A., Sengouga, N. and Meftah, A., 2019. Electron and hole transport layers optimization by numerical simulation of a perovskite solar cell. *Solar energy*, 181, pp.372-378.
- [13] Lin, H., Yang, M., Ru, X., Wang, G., Yin, S., Peng, F., Hong, C., Qu, M., Lu, J., Fang, L. and Han, C., 2023. Silicon heterojunction solar cells with up to 26.81% efficiency achieved by electrically optimized nanocrystalline-silicon hole contact layers. *Nature Energy*, 8, 8, pp.789-799.
- [14] Donercark, E., Sedani, S.H., Kabaçelik, I., Salimi, A. and Turan, R., 2022. Interface and material properties of wide band gap a-SiCx: H thin films for solar cell applications. *Renewable Energy*, 183, pp.781-790.
- [15] Liang, B., Chen, X., Yuan, H., Wang, X., Hou, G., Zhao, Y. and Zhang, X., 2024. Enhancing Optical and Electrical Performances via Nanocrystalline Si-Based Thin Films for Si Heterojunction Solar Cells. *ACS omega*, 9, 50, pp.49935-49944.
- [16] Cho, J., Radhakrishnan, H.S., Sharma, R., Payo, M.R., Debucquoy, M., van der Heide,

- A., Gordon, I., Szlufcik, J. and Poortmans, J., 2020. Thermal stability improvement of metal oxide-based contacts for silicon heterojunction solar cells. *Solar Energy Materials and Solar Cells*, 206, pp.110324.
- [17] Cho, J., Melskens, J., Payo, M.R., Debucquoy, M., Radhakrishnan, H.S., Gordon, I., Szlufcik, J., Kessels, W.M.M. and Poortmans, J., 2019. Performance and thermal stability of an a-Si: H/tio x/yb stack as an electron-selective contact in silicon heterojunction solar cells. *ACS Applied Energy Materials*, 2, 2, pp.1393-1404.
- [18] Wang, G., Su, Q., Tang, H., Wu, H., Lin, H., Han, C., Wang, T., Xue, C., Lu, J., Fang, L. and Li, Z., 2024. 27.09%-efficiency silicon heterojunction back contact solar cell and going beyond. *Nature Communications*, 15, 1, pp.8931.
- [19] Pasanen, T., 2017. Surface passivation of black silicon phosphorus emitters. (Master's thesis). Aalto University, School of Electrical Engineering.
- [20] Ek, A., 2019. Silicon surface passivation via ultra-thin SiO<sub>2</sub>, TiO<sub>2</sub>, and Al<sub>2</sub>O<sub>3</sub> layers. (Master's thesis, Luleå University of Technology–Department of Engineering Sciences and Mathematics).
- [21] Bullock, J., Hettick, M., Geissbühler, J., Ong, A.J., Allen, T., Sutter-Fella, C.M., Chen, T., Ota, H., Schaler, E.W., De Wolf, S. and Ballif, C., 2016. Efficient silicon solar cells with dopant-free asymmetric heterocontacts. *Nature Energy*, 1, 3, pp.1-7.
- [22] Bullock, J., Cuevas, A., Allen, T. and Battaglia, C., 2014. Molybdenum oxide MoOx: A versatile hole contact for silicon solar cells. *Applied Physics Letters*, 105, 23, pp. 232109.
- [23] Wan, Y., Samundsett, C., Yan, D., Allen, T., Peng, J., Cui, J., Zhang, X., Bullock, J. and Cuevas, A., 2016. A magnesium/amorphous silicon passivating contact for n-type crystalline silicon solar cells. *Applied physics letters*, 109, 11, pp. 113901.
- [24] Nayak, M., Singh, K., Mudgal, S., Mandal, S., Singh, S. and Komarala, V.K., 2019. Carrier-selective contact based silicon solar cells processed at room temperature using industrially feasible Cz wafers. *physica status solidi (a)*, 216, 16, pp.1900208.
- [25] Tiwari, S.K. and Nayak, A.K., 2024. *Diamane: Fabrication, properties and new advances in 2D diamond*. IOP Publishing.
- [26] Odkhuu, D., Shin, D., Ruoff, R.S. and Park, N., 2013. Conversion of multilayer graphene into continuous ultrathin sp3-bonded carbon films on metal surfaces. *Scientific Reports*, 3, 1, pp.3276.
- [27] Barboza, A.P., Guimaraes, M.H., Massote, D.V., Campos, L.C., Barbosa Neto, N.M., Cancado, L.G., Lacerda, R.G., Chacham, H., Mazzoni, M.S. and Neves, B.R., 2011. Room-temperature compression-induced diamondization of few-layer graphene. *Advanced Materials*, 23, 27, pp.3014-3017.
- [28] Chernozatonskii, L.A., Sorokin, P.B., Kvashnin, A.G. and Kvashnin, D.G.E., 2009. Diamond-like C<sub>2</sub>H nanolayer, diamane: Simulation of the structure and properties. *Jetp Letters*, 90, 2, pp.134-138.
- [29] Kvashnin, A.G., Chernozatonskii, L.A., Yakobson, B.I. and Sorokin, P.B., 2014. Phase diagram of quasi-two-dimensional carbon, from graphene to diamond. *Nano Letters*, 14, 2, pp.676-681.
- [30] Bakharev, P.V., Huang, M., Saxena, M., Lee, S.W., Joo, S.H., Park, S.O., Dong, J., Camacho-Mojica, D.C., Jin, S., Kwon, Y. and Biswal, M., 2020. Chemically induced transformation of chemical vapour deposition grown bilayer graphene into fluorinated single-layer diamond. *Nature nanotechnology*, 15, 1, pp.59-66.
- [31] Cellini, F., Lavini, F., Cao, T., de Heer, W., Berger, C., Bongiorno, A. and Riedo, E., 2018. Epitaxial two-layer graphene under pressure: Diamene stiffer than Diamond. *FlatChem*, 10, pp.8-13.
- [32] Niu, C., Cheng, Y., Yang, K., Zhang, J., Zhang, H., Zeng, Z. and Wang, X., 2020. Boron-dopant enhanced stability of diamane with tunable band gap. *Journal of Physics: Condensed Matter*, 32, 13, pp.135503.

- [33] Niu, C., Zhang, J., Zhang, H., Zhao, J., Xia, W., Zeng, Z. and Wang, X., 2022. Configuration stability and electronic properties of diamane with boron and nitrogen dopants. *Physical Review B*, 105, 17, pp.174106.
- [34] Paul, S. and Momeni, K., 2019. Mechanochemistry of stable diamane and atomically thin diamond films synthesis from bi-and multilayer graphene: a computational study. *The Journal of Physical Chemistry C*, 123, 25, pp.15751-15760.
- [35] Raeisi, M., Mortazavi, B., Podryabinkin, E.V., Shojaei, F., Zhuang, X. and Shapeev, A.V., 2020. High thermal conductivity in semiconducting Janus and non-Janus diamanes. *Carbon*, 167, pp.51-61.
- [36] Tiwari, S.K., Pandey, R., Wang, N., Kumar, V., Sunday, O.J., Bystrzejewski, M., Zhu, Y. and Mishra, Y.K., 2022. Progress in diamanes and diamanoids nanosystems for emerging technologies. *Advanced Science*, 9,11, pp.2105770.
- [37] Chernozatonskii, L.A., Demin, V.A. and Kvashnin, D.G., 2021. Fully hydrogenated and fluorinated bigraphenes—diamanes: theoretical and experimental studies. *C*, 7, 1, pp.17.
- [38] Piazza, F., Cruz, K., Monthioux, M., Puech, P. and Gerber, I., 2020. Raman evidence for the successful synthesis of diamane. *Carbon*, 169, pp.129-133.
- [39] Bakharev, P.V., Huang, M., Saxena, M., Lee, S.W., Joo, S.H., Park, S.O., Dong, J., Camacho-Mojica, D.C., Jin, S., Kwon, Y. and Biswal, M., 2020. Chemically induced transformation of chemical vapour deposition grown bilayer graphene into fluorinated single-layer diamond. *Nature nanotechnology*, 15, 1, pp.59-66.
- [40] Cheng, T., Liu, Z. and Liu, Z., 2020. High elastic moduli, controllable bandgap and extraordinary carrier mobility in single-layer diamond. *Journal of Materials Chemistry C*, 8, 39, pp.13819-13826.
- [41] Zhu, L., Li, W. and Ding, F., 2019. Giant thermal conductivity in diamane and the influence of horizontal reflection symmetry on phonon scattering. *Nanoscale*, 11, 10, pp.4248-4257.
- [42] Vu, T.V., Phuc, H.V., Ahmad, S., Nha, V.Q., Van Lanh, C., Rai, D.P., Kartamyshev, A.I., Pham, K.D., Nhan, L.C. and Hieu, N.N., 2021. Outstanding elastic, electronic, transport and optical properties of a novel layered material C<sub>4</sub>F<sub>2</sub>: first-principles study. *RSC advances*, 11, 38, pp.23280-23287.
- [43] Tiwari, S.K., Pandey, R., Wang, N., Kumar, V., Sunday, O.J., Bystrzejewski, M., Zhu, Y. and Mishra, Y.K., 2022. Progress in diamanes and diamanoids nanosystems for emerging technologies. *Advanced Science*, 9, 11, pp.2105770.

### CHAPTER 3

# APPLICATION OF N-TYPE DIAMANE AS AN EFFECTIVE EMITTER LAYER IN CRYSTALLINE SILICON HETEROJUNCTION SOLAR CELLS

This chapter investigates the application of n-type diamane as a novel emitter layer in silicon-based heterojunction solar cells, modelled as: ITO/n-diamane/p-type c-Si/Ag, simulated under AM 1.5 G illumination using AFORS-HET v2.5. We have used n-type diamane as an emitter layer, and the nature of diamane has been considered 3D in spite of 2D, as well as the electronic nature of diamane is considered isotropic. Optimization of emitter and absorber parameters yielded a maximum efficiency of 16.84% at 300 K using a single-layer diamane on a 100 µm c-Si wafer. Using commercial silicon parameters, the structure achieved 10.41% efficiency. Increasing the number of diamane layers slightly reduced performance, with 15.3% efficiency for multilayer diamane, highlighting the advantage of thinner layers. Results highlight n-type diamane's potential as a high-mobility, widebandgap emitter and a promising alternative to doped amorphous silicon. It has been demonstrated that n-type diamane might be used as an effective emitter layer in a crystalline Si heterojunction solar cell.

The results reported in this chapter have been published in Naima et. al. Carbon Trends 9 (2022) 100209.

#### 3.1 Introduction

Recently, a new allotrope of carbon named "Diamane" (Dn) possessing sp<sup>3</sup> carbon bonding has been synthesized and reported to be 2D, being a physical analogue to "graphenegraphane" [1-4]. Recently, Bakharev et al. [5] confirmed that diamane exhibited 2D electronic system. It was confirmed by estimating the optical band gap of diamane, adopting the approach described in previous studies [6, 7] for 2D electronic systems. They found that the experimental optical gap value of 3.3-3.4 eV is consistent with the calculated optical gap of 2.87 eV obtained for F-diamane. Furthermore, Raman spectroscopy was used to confirm the successful synthesis of 2D diamane, and the characterization of its electronic structure has also been reported [8, 9]. It has a thermal conductivity of 1960 W/mK, as high as its bulk counterpart diamond (1000 W/mK), due to which it is considered a promising material for high-temperature electronic applications [1, 10]. Furthermore, density functional theory (DFT) calculations reveal that 2D diamane has a smaller effective mass (0.55m<sub>o</sub>) of conduction electrons in comparison to its bulk counterpart, i.e., diamond (0.57m<sub>o</sub>), which is also very promising to use 2D diamane in various electronic applications such as solar cells [1]. 2D materials are best used in electronic applications as they have large tunability in their bandgaps and they are flexible, strong and extremely thin. It was first predicted by Chernozatonskii et al. in 2009 [11], although its experimental synthesis was reported recently. The detailed verification of its bonding and electronic structure has also been probed by using various characterization techniques like: XPS, UV photo-electron, Raman, UV-Vis and electron energy loss spectroscopies, TEM and XRD [5]. Formerly, the instability of diamane was marked as a big hurdle for its above-mentioned potential applications. Recently, the stability of diamane has been improved by the substitution of N atoms on its surface. The N atom has one more electron than the C atom, which forms a lone pair of electrons and behaves as a passivation, which stabilizes the structure and extends the band gap [2]. The first principal method has investigated the configuration stability and electronic properties of N-doped diamane [2]. This novel 2D material has direct band gaps which can be controlled in the range from 0.86 to 5.68 eV [4]. Furthermore, due to its large bandgap, the intrinsic carrier concentration stays low even at high temperatures. Furthermore, the substitution of N atoms makes these films highly n-type, and it is found that N-substituted diamanes are harder than fully hydrogenated diamanes [2]. Atomistic simulation demonstrated that diamane carries

giant in-plane stiffness (715 N/m) as compared to graphene (238 N/m) and graphane (449 N/m) [1, 11]. It is noteworthy to mention that diamane possesses high carrier mobility, for electrons (2732 cm<sup>2</sup>/Vs) and holes (1565 cm<sup>2</sup>/Vs) in the case of fluorinated and hydrogenated diamane, which is superior to those of III-IV semiconductor compounds [12] and reported in 2D materials. The calculated band gap for fluorinated diamane (C<sub>4</sub>F) (2.93 eV) confirms its high transparency [13]. It has to be noticed that the work function of 2D diamane can also be turned in the range of 7.24 eV to 0.62 eV after vacuum annealing at 700 °C, and the work function of as-grown bilayer graphene was reported to be 4.4 eV [14, 5], which also opens up its use in various electronic applications. The above-mentioned unique properties of ultrathin 2D diamane film motivate us to explore the potential application of n-type diamane as an effective emitter layer in Si-based heterojunction photovoltaic cells. The role of the emitter layer in the crystalline silicon heterojunction solar cell is not only to allow the maximum photons to pass across the interface but also to develop a built-in potential at the diamane/silicon interface, which requires to discrete of the photogenerated charge carriers. In recent times, diamane is expected to be used in various areas such as nano-optics, nanoelectronics, nano-electromechanical systems, mechanical resonators, and electronic devices at high temperature [5]. In spite of that, the application of diamane in the solar cell has not been much investigated yet. This also inspired us to use n-type diamane as an emitter layer in the silicon heterojunction solar cell. As the diamane layer number increases from one to five, there is a small decrement in the efficiency from 8 to 7.53%. Since this small efficiency was not worth obtaining an efficient solar cell, it became more necessary to optimize the values of parameters of p-cSi as well, so that an affordable solar cell with less manufacturing cost can be achieved with better efficiency. Thus, in the present chapter, the solar cell modelled as ITO (front contact)/n-Dn/p-cSi/Ag was optimized under the illumination of monochromatic light with a power density of 100 W/cm<sup>2</sup> and spectral width of 10 nm by using the latest version 2.5 of the software AFORS-HET. This software generally solves the 1-D semiconductor equations, such as the continuity equation, transport, and Poisson's equation for both holes and electrons, by using finite differences under different conditions. In this simulated cell, the n-diamane has been chosen as an emitter layer or conducting electrode, while the p-cSi has been chosen as an absorbing layer. The variables of both ndiamane and p-cSi layers were optimized to achieve notable efficiency for n-diamane/p-cSi solar cell. The simulation was performed by considering the isotropic elastic nature of the

diamane layer. Since diamane is isotropic therefore the efficiency will remain the same for both armchair and zig-zag directions in diamane layer. The purpose of this simulation is to analyse the impact of the isotropic nature of diamane and silicon wafer on the functioning of the solar cell and to enlighten the cell response.

#### 3.2 Device structure and simulation details

The proposed structure of the solar cell is shown in Fig.3.1. To design this structure, we have used the current version 2.5 of AFORS-HET software, which uses Shockley-Read-Hall recombination statistics for different layers of the solar cell [15]. In the proposed structure of solar cell, ITO(TCO)/n-diamane/p-crystalline Silicon/Ag (back contact) is displayed in Fig. 3.1.

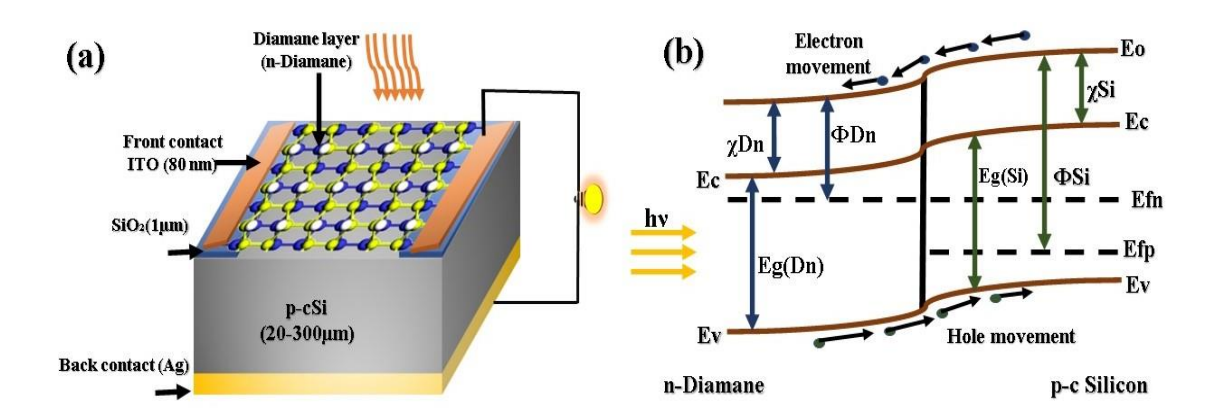


**Fig. 3.1** (a) Schematic diagram of the simulated structure, (b) Schematic diagram under forward biasing just after the formation of heterojunction showing the transportation of electrons and holes.  $\Phi_{Dn}$ ,  $\Phi_{Si}$  and  $\chi_{Dn}$ ,  $\chi_{Si}$  are the diamane and Si work function and the diamane and silicon affinity, respectively.

The ITO was taken as a TCO as well as an anti-reflector to ensure that the maximum number of photons gets transmitted. So, as the light incident on the cell photons get absorbed in the absorber layer, as photon absorption increases in the active layer, more electron and hole pairs will be generated. In this way, to achieve the maximum electron-hole pairs generation in the absorber layer, we intend to use the material of highest transmission efficiency, and to fulfil this purpose, we used ITO as TCO. ITO can be

directly deposited on diamane with the help of an electron beam and the PLD technique transferred on SiO<sub>2</sub>/Si pattern substrate [16–19]. Microstructure, surface morphology, electrical and optical properties of ITO film can be characterized and analysed by using various techniques like XRD, SEM, AFM, and high-resolution transmission electron microscopy. The standard transmission line model (TLM) method was used to evaluate sheet resistance ITO/n-Si contacts in HJ silicon solar cells [20]. This deposition technique might not harm the diamane as well as the SiO<sub>2</sub>/Si substrate. Ag was chosen as the back contact as shown in Fig. 3.1. The [n, k] file for front contact as well as back contact was taken as default, which are in-built in the software. All the details about the parameters of front and back contacts are tabulated in Table 3.1.

**Table 3.1:** Information of the parameters used as front and back contact in the designed solar cell.

Contact variables	Front contact	Back contact
Material	ITO	Ag
Width (m)	$8 \times 10^{-8}$	$1 \times 10^{-4}$
File	ITO.nk	Ag. nk
Metal work function	Yes (flat band)	Yes (flat band)
Absorption loss	ITO. Abs	0
External reflection constant	0	0.05
Surface condition	Plane	Plane
Internal reflection constant	0	0

The proposed structure was illuminated under Air Mass 1.5 G, spectral width 10 nm, with the power density of 100 mW/cm² as a light source. Simultaneously, the temperature of the cell was maintained at 300 K. Since we prefer to take the reflection coefficient of the front contact as smaller and the reflection coefficient of the back contact as higher to get higher efficiency. The front contact should be transparent ideally, so that maximum light can pass through the surface and get collected at the absorbing layer. Therefore, in this simulation, we have taken the reflection coefficient of the front contact as nearly zero, whereas the reflection coefficient of the back contact was taken as 0.05. The generation of electron-hole pairs was described by the Lambert-Beer model, which is in-built in the software, and the reflection from the diamane/Si interface is not considered [15]. Shockley-Read-Hall recombination and/or dangling-bond recombination were

considered as a recombination model within the software, including some defect states within the bandgap. ITO/n-Dn interface is considered as MS-Schottky front interface, and the back interface i.e., p-cSi/Ag is also considered as MS-Schottky. To interpret the transportation of charge carriers in diamane layer, the drift and diffusion model was applied in the software, where the differential transport equation for both holes and electrons was taken as 2-D in nature with carrier densities in A/cm<sup>2</sup> [15]. At diamane/Si interface, two two-dimensional equations are coupled with three-dimensional equations (as we know, diamane is 2D and c-Si is 3D in nature) to act as the transport and boundary conditions at the interface. In this simulation, we have not assumed any mismatching of lattices between the layers, and the movement of minority charge carriers has been considered through the c-axis. Ideally, diamane is 2-dimensional, only if this fulfils the condition  $< t > \le \lambda_F$ , where < t > is average thickness of diamane,  $\lambda_F$  is the Fermi wavelength given as  $\sqrt{\frac{2\Pi}{n_{2D}}}$ , and  $n_{2D}$  is the carrier density in cm<sup>-2</sup> [21]. As diamane is synthesized by chemical exposure of bilayer graphene to H or F atoms, which results in their attachment to the graphene surface, we have taken the value of carrier density reported in graphene. By following the condition reported by Sarma et al. [22], even  $n\sim10^5$  cm<sup>-3</sup> in graphene cannot satisfy the above-mentioned condition. additionally, it has also been reported that doping in 2D materials increases the interlayer spacing [21, 23]. Therefore, we have considered both graphene as well as diamane as quasi-3D. The quantum confinement can be obtained by lowering the thickness. The thickness of a single layer diamane is taken as 0.334 nm, and the [n, k] file has been calculated by using the data provided in the previous literature [24]. The value of refractive index (n) and extinction coefficient (k) are estimated to be 1.5 and 2.7, respectively [24]. Because of the isotropic nature of diamane, properties like mobility and effective mass of charge carriers are the same in both armchair and zigzag directions. For optimizing the cell parameters and to simulate the cell, the bulk and interfacial defect distribution, as well as the recombination rate (G), were taken constant in the software. Moreover, the model chosen for ITO/n-diamane and p-crystalline Si/Ag interface was the MS-Schottky model, and the model chosen for n-diamane/p/cSi interface is drift-diffusion, respectively. The parameters which have to be optimized are: N<sub>D</sub> (donor concentration), N<sub>C</sub>/N<sub>V</sub> (effective conduction and valence band density), energy bandgap ( $E_g$ ),  $\chi$  (affinity),  $\varepsilon_r$  (dielectric

constant), layer thickness, electron and hole mobilities ( $\mu_n$ ,  $\mu_h$ ). The optimization of the above-mentioned parameters for diamane was carried out by taking the set values of parameters of the p-cSi layer in the range of reported values in the literature and has been tabulated in Table 3.2.

Table 3.2 Ranges of other parameters chosen for the simulation.

Input parameters	Diamane	p-cSi
Thickness (cm)	$0.3 \times 10^{-7} - 1.5 \times 10^{-7}$	0.002-0.03
Dielectric constant $(\varepsilon_r)$	4-11	11.9
Electron affinity $\chi$ (eV)	3.3-5.2	3.6-4.5
Band gap, $E_g$ (eV)	0.8-5.6	1.12
Optical band gap, E <sub>g</sub> (eV)	2.8	1.124
Conduction band density, N <sub>C</sub> (cm <sup>-3</sup> )	$1 \times 10^{19} \text{-} 1 \times 10^{21}$	$3 \times 10^{19}$ -1 × $10^{21}$
Valence band density, N <sub>V</sub> (cm <sup>-3</sup> )	$1 \times 10^{19} \text{-} 1 \times 10^{21}$	$3 \times 10^{19} \text{-} 1 \times 10^{21}$
Electron mobility, $\mu_n$ (cm <sup>2</sup> /Vs)	2732	1500
Hole mobility, $\mu_h$ (cm <sup>2</sup> /Vs)	743-1565	500
Acceptor concentration N <sub>A</sub> (cm <sup>-3</sup> )	0	$1 \times 10^{16} - 7 \times 10^{18}$
Donor concentration $N_D$ (cm <sup>-3</sup> )	$3 \times 10^{14} - 1 \times 10^{18}$	0
Electron thermal velocity, V <sub>e</sub> (cms <sup>-1</sup> )	$3 \times 10^{7}$	$1 \times 10^{7}$
Hole thermal velocity, V <sub>h</sub> (cms <sup>-1</sup> )	$3 \times 10^{7}$	$1 \times 10^{7}$
Layer density, (gcm <sup>-1</sup> )	2.328	2.328
Auger electron recombination	0	0
coefficient, (cm <sup>6</sup> s <sup>-1</sup> )		
Auger hole recombination	0	0
coefficient, (cm <sup>6</sup> s <sup>-1</sup> )		
Band-to-band recombination	0	0
coefficient, (cm <sup>3</sup> s <sup>-1</sup> )		
Defect properties	Single acceptor	Single acceptor
Total trap density (cm <sup>-3</sup> )	$1 \times 10^{14}$	$1 \times 10^{14}$
Characteristic energy (eV)	0.56	0.56

 $N_{\text{C}}/N_{\text{V}}$  of diamane have been calculated by using the equation as follows:

$$N_{C/V} = 2\left(\frac{2\pi k_B T m_{e/h}^*}{h^2}\right)^{\frac{3}{2}}$$
 (3.1)

Where  $k_B$  is the Boltzmann constant, T is the temperature in Kelvin,  $m_h^*$  is the hole's effective mass,  $m_e^*$  is the electron's effective mass and h is the Planck's constant [25, 26]. Whereas, the thermal velocity  $(V_{th})$  of charge carriers has been calculated by using the relation  $V_{th} = \sqrt{\frac{3k_BT}{m_{e/h}^*}}$ . After getting the best optimized results of diamane's parameters,

we have further optimized the various parameters of p-type c-Si wafer, such as: NA (acceptor concentration), N<sub>C</sub>/N<sub>V</sub>, χ, and wafer thickness by keeping the parameters of n-Dn at their best optimized values. The range of parameters of n-diamane has been taken from the available literature [4, 12, 14, 16, 21, 26], and the range of parameters of p-cSi, which we have considered here, are for (100) oriented single crystalline Si [26-29] tabulated in Table 3.2. The schematic of the energy band diagram for the proposed structure ITO (TCO)/n-Dn/p-cSi/A Ag has been depicted in Fig. 3.1 (b). Since, driftdiffusion effect is considered at the interface, therefore, the majority of charge carriers, i.e., electrons from the n-diamane and holes from the p-cSi, are diffused towards each other until thermal equilibrium is developed. This happens because of a concentration gradient at the interface; this phenomenon is called the diffusion process. An electric field exists in the depletion region, which spreads up to some width called the depletion width W, in both p and n regions. Both electrons and holes in this depletion region are carried away by this electric field. As a result, a drift current develops, which balances the diffusion current and appears due to the difference in electron and hole densities at the junction. As a result, thermal equilibrium is established, and the energy bands start bending near the Fermi level. The built-in potential (eV<sub>bi</sub>) is the reason for charge segregation across the junction in the solar cell as discussed above. This eV<sub>bi</sub> in both pcSi and n-diamane can be framed in the form of work-functions according to the equations as follows:

e. 
$$V_{bi} = \Phi_{BI} = \Phi_{Si-P-type} - \Phi_{Dn,N-type}$$
  
=  $-\chi_{Dn} - kT \ln \left(\frac{N_C}{N_D}\right) + \chi_{Si} + kT \ln \left(\frac{N_A}{N_V}\right)$  (3.2)

Where  $\Phi_{Dn}$  and  $\Phi_{Si}$  are the work functions of diamane and silicon, respectively. Whereas,  $\chi_{Dn}$  and  $\chi_{Si}$  are the affinities of diamane and Si, respectively. Moreover,  $N_D$  is the donor concentration and  $N_C$  is the effective conduction band density for diamane, while  $N_A$  is the acceptor concentration and  $N_V$  is the effective valence band density for p-cSi [26, 30]. As n-diamane/p-crystalline Si junction is illuminated, it gives rise to electron-hole pairs, which get separated because of the built-in potential. The minority charge carriers flow towards the n-diamane and p-cSi, respectively depicted in Fig. 3.1 (b). When an open circuit condition is applied, the photo-generated charge carriers intensify the carrier density in their corresponding fields, and because of this intensification of charge carriers,

the quasi-Fermi level approaches the conduction band in n-diamane and the valence band in p-cSi; as a result,  $V_{OC}$  develops. In the same manner, under short-circuit conditions, these photo-generated charge carriers do not intensify because of the collection of charge carriers at their respective electrodes, which results in  $J_{SC}$  that flows in the outer circuit.

#### 3.3 Results

#### 3.3.1 Optimization of n-type diamane layer parameters

To simulate the above designed cell, first we have optimized the doping concentration  $(N_D)$  of n-type diamane layer ranging from  $3 \times 10^{14}$  cm<sup>-3</sup> to  $1 \times 10^{18}$  cm<sup>-3</sup> while keeping other parameters of diamane and p-type c-Silicon at some reasonable values reported in the literatures [4, 12, 14, 16, 21, 26-29] and the results obtained from this optimization have been plotted in Fig. 3.2 (a and b). Fig. 3.2 shows that, as N<sub>D</sub> increased from  $3 \times 10^{14}$  cm<sup>-3</sup> to  $1 \times 10^{18}$  cm<sup>-3</sup>,  $V_{OC}$  was found to be constant at 521.1 mV. It might be happened because as we increase the doping concentration above  $3 \times 10^{14}$  cm<sup>-3</sup>, mobility decreases due to enhance collisions of charge carriers with ionized doping atoms which results in decrease of carrier's lifetime according to the relatio:  $\mu_i = \frac{e}{m^*} \tau_i$ here, e is the electronic charge and m\* is the effective mass of electron. Since, mobility and diffusion constant relate by Einstein's relation given by  $\frac{D_i}{u_i} = \frac{k_B}{e}T$  [25, 26] and indicates that as mobility decreases diffusion constant also decreases as it is directly proportional to the mobility of charge carriers and therefore, diffusion length (Li =  $\sqrt{D_i \tau_i}$ ) reduces. Diffusion length is the average distance an electron can move and recombine; it depends on the recombination time as well as the diffusion constant. In this manner,  $J_{SC}$  will also decrease and  $J_0$  increases following the relations given below:

$$J_{SC} = qG(L_n + L_p) \tag{3.3}$$

Where  $L_n$  and  $L_p$  are the diffusion lengths of electron and hole, respectively. q is the electric charge, and G is the electron and hole pair generation rate [26, 31].

$$J_0 = eA\left(\frac{D_p P_n}{L_n} + \frac{D_n n_p}{L_p}\right)$$
(3.4)

Where A is the area of the junction [25, 26]. This increment in  $J_0$  and a decrement in  $J_{SC}$  results in a reduction of  $V_{OC}$ , followed by the relation:

$$V_{OC} = \frac{nqT}{k} ln \left( \frac{lsc}{J_0} + 1 \right)$$
 (3.5)

here, J<sub>0</sub> is the reverse saturation current. But at the same time, V<sub>bi</sub> increases according to Eqn. (3.2), resulting in higher V<sub>OC</sub>. These two processes contradict each other and maintain the balance to keep V<sub>OC</sub> at a constant value of 521.1 mV. Another possibility for V<sub>OC</sub> being constant at 521.1 mV is that V<sub>OC</sub> is independent of N<sub>D</sub> if it satisfies the condition:  $\Delta$  n<sub>o</sub> >> N<sub>D</sub>, where  $\Delta$  n<sub>o</sub> is the additional electron and hole pairs [26, 32]. Further, as we increase N<sub>D</sub> from  $3\times10^{14}$  cm<sup>-3</sup> to  $5\times10^{15}$  cm<sup>-3</sup>, the conductivity of the diamane layer was found to increase, and consequently, J<sub>SC</sub> increased very slightly from 20.87 to 20.99 mA/cm<sup>2</sup>. On further increasing  $N_D$  from  $5\times10^{15}$  cm<sup>-3</sup> to  $1\times10^{18}$  cm<sup>-3</sup>,  $J_{SC}$ starts decreasing from 20.99 to 20.67 mA/cm<sup>2</sup>. This happens because at higher N<sub>D</sub>, diffusion length decreases, and as a result, J<sub>SC</sub> decreases. Another reason behind this decrement in the value of  $J_{SC}$  from 20.99 to 20.67 mA/cm<sup>2</sup> after  $N_D$ ,  $5\times10^{15}$  cm<sup>-3</sup> is that on increasing the doping concentration, the work function will reduce, due to this reduction in work function, J<sub>SC</sub> falls off. From Fig. 3.2 (a), it is observed that there is a sudden increase in the value of FF and  $\eta$  after  $N_D = 3 \times 10^{14}$  cm<sup>-3</sup>. This might have happened because of the decrease in the sheet resistance, which occurred on increasing the doping concentration. After  $N_D$  =  $1\times10^{16}$  cm  $^{\!-3},\,FF$  and  $\eta$  decrease very slightly and then again start to increases as N<sub>D</sub> increases. Maximum efficiency, 7.74 % was achieved at  $N_D$  =  $10^{18}$  cm<sup>-3</sup>. Therefore, the best optimized value of  $N_D$  for n-type diamane layer is found to be  $1 \times 10^{18}$  cm<sup>-3</sup>.

After optimizing  $N_D$  at  $10^{18}$  cm<sup>-3</sup>, the next parameter  $N_C/N_V$  is optimized by varying in the range of  $1\times10^{19}$  cm<sup>-3</sup> to  $6\times10^{21}$  cm<sup>-3</sup> for ultra-single diamane wafer. On increasing  $N_C/N_V$ , the densities of minority charge carriers get reduced. This reduction in minority carriers is possibly because of the smaller period of photo-generated carriers and trapping of the free charge carriers. Due to this,  $V_{OC}$  will remain constant at 521.1 mV as we varied  $N_C/N_V$  from  $1\times10^{19}$  cm<sup>-3</sup> to  $6\times10^{21}$  cm<sup>-3</sup>. From Fig. 3.2 (c-d), we notice that  $J_{SC}$  increases linearly with increasing  $N_C/N_V$  of the diamane layer. This increment in  $J_{SC}$  is due to the high value of  $N_C$ , which leads to higher absorption of photons. It is

also observed that the FF reduces linearly from 71.88 % to 65.12 % on varying the  $N_C/N_V$  from  $1\times10^{19}$  cm<sup>-3</sup> to  $6\times10^{21}$  cm<sup>-3</sup>. Since FF is reducing consequently,  $\eta$  will be reduced from 7.74 % to 7.04 %. Maximum efficiency 7.74% was achieved at  $N_C/N_V =$  $1 \times 10^{19}$  cm<sup>-3</sup>. Hence,  $1 \times 10^{19}$  cm<sup>-3</sup> is the best optimized value of  $N_C/N_V$  for single-layer n-diamane. After optimizing  $N_D$  and  $N_C/N_V$ , the next parameter,  $E_{\mathbf{g}}$  is optimized in the range of 0.86 to 5.6 eV. Here, we have chosen a higher range of bandgap for the simulation by keeping in mind that if the UV light present in solar light could contribute to the higher bandgap. We have taken this range of bandgap in order to see the effect of bandgap on the solar cell's efficiency for all derivatives of diamane, as it has various derivatives of it which possess a range of bandgap depending on the functional group they contain, and many other factors too. But we did not notice any change in the efficiency of the solar cell after the bandgap of 1.3 eV. It is reported that the dielectric constant is inversely proportional to the bandgap energy; therefore, on changing the bandgap value dielectric constant also changes. For higher bandgap dielectric constant becomes smaller, which consequently increases the recombination losses due to the improvement in the exciton binding energy. Therefore, on further increasing the bandgap, there will be no improvement in the value of efficiency of the solar cell, and it becomes constant at 7.74% after the bandgap of 1.3 eV. In this specific section of the manuscript, we discussed only the effect of varying the bandgap because we exclusively want to see the effect of varying the bandgap on the performance of the solar cell. Therefore, we did not discuss the variation in the dielectric constant here. We have discussed the effect of varying the dielectric constant on the performance of the solar cell in another section of the manuscript. As we increased Eg, Voc was found to be increased and attained a constant value of 521.1 mV at 1.3 eV. Whereas, J<sub>SC</sub> remains constant at 20.67 mA/cm<sup>2</sup> as depicted in Fig. 3.2 (f). In Fig. 3.2 (e), it has been shown that FF and  $\eta$  increase from 63.96% to 72.09% and 2.79% to 7.74% respectively, for the bandgap ranging from 0.86 to 1.25 eV and then attain a constant value of 71.88 % for the FF and 7.743 % for efficiency at the bandgap 1.3 eV. Therefore, the bandgap of 1.3 eV is the best optimized bandgap for a single layer n-diamane. The optimized results of the electron affinity in the range from 3.3 eV to 5.2 eV are shown in Fig. 3.2 (g and h). As  $\chi$  increased, a very slight increment in the value of  $\eta$  from 7.92 % to 8 % was

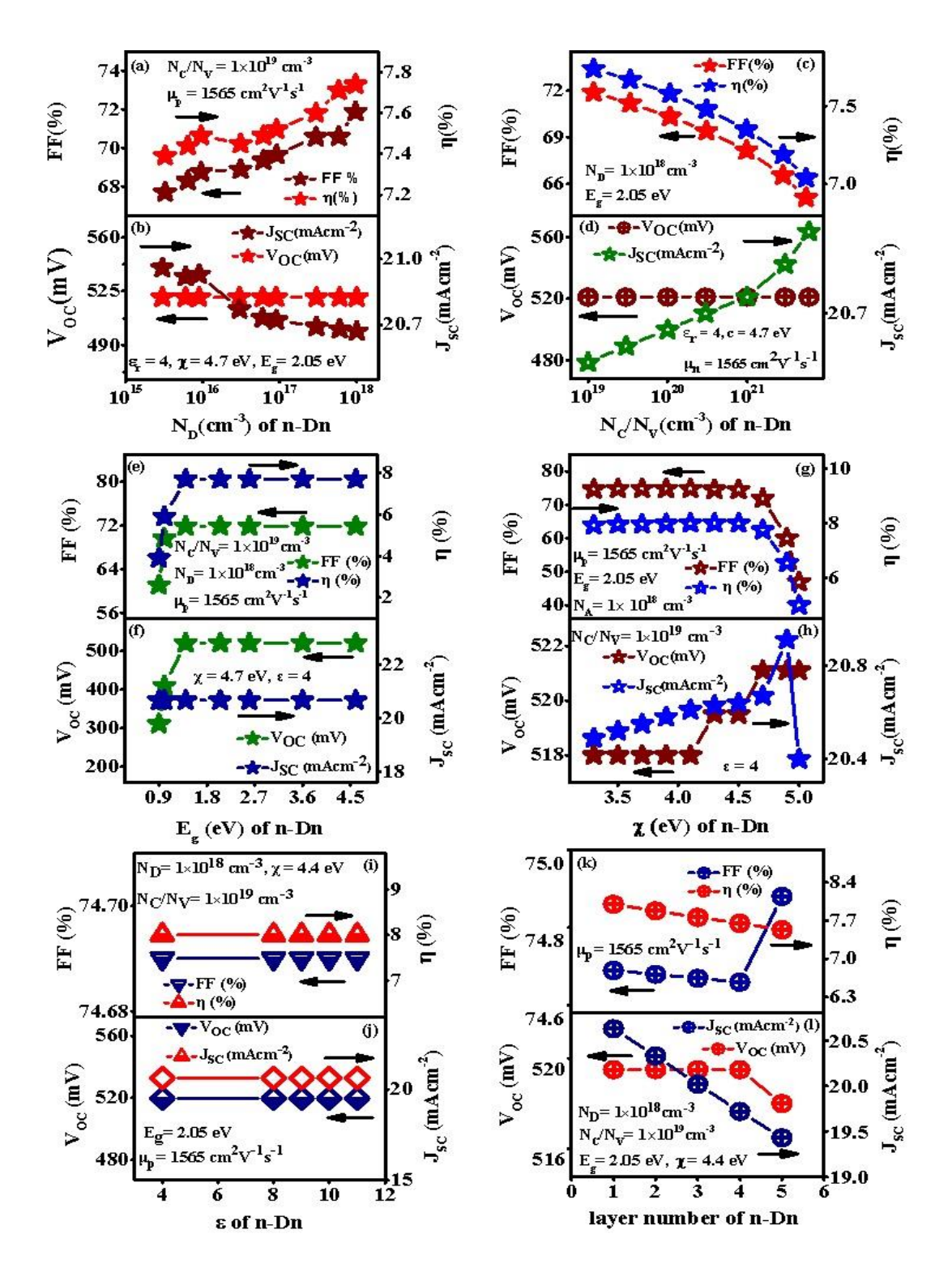


**Fig. 3.2** Graphic representation of the performance of designed cell after optimization of different variables of n-diamane, (a, b)  $N_D$  (cm<sup>-3</sup>) donor concentration, (c, d)  $N_C$  / $N_V$  (cm<sup>-3</sup>) effective conduction/valence band density, (e, f) bandgap  $E_g$  (eV), (g, h)  $\chi$  (eV) electron affinity, (i, j) dielectric constant  $\epsilon_r$ , and (k, l) layer numbers. After fixing the variables of p-cSi at some constant values such as:  $N_A = 1 \times 10^{16}$  cm<sup>-3</sup>,  $N_C/N_V = 3 \times 10^{19}$  cm<sup>-3</sup>,  $\chi = 4.05$  eV, and layer thickness = 100 μm. Remaining variables of both p-cSi and n-Dn are mentioned in Table 3.2.

observed up to the electron affinity 4.4 eV, and then a dramatic reduction in the value of efficiency was noticed, as shown in Fig. 3.2 (g). The reason behind this small linear increment in the efficiency is that as we increase the electron affinity of single-layer diamane above 3.3 eV, the barrier height decreases, which results in the fast movement of minority charge carriers; as a result, J<sub>SC</sub> increases. Thus, η was observed to increase linearly up to 4.4 eV. After 4.4 eV, as we increase affinity, the conduction band lowers down and starts making rapid transportation of charge carriers across the interface, as a result, there would not be any free charge carriers. Consequently, J<sub>SC</sub> and FF will be decreased, which causes the final  $\eta$  to decrease. Here, we found that on increasing  $\chi$ ,  $V_{OC}$  was improved and attained a maximum value of 524.2 mV at  $\chi = 5.2$  eV and maximum  $\eta$  8% was observed for  $\chi = 4.4 \text{eV}$ . Thus, 4.4 eV is the best optimized value of electron affinity for single layer n-type diamane. After this, we have optimized the value of relative permittivity  $(\varepsilon_r)$  or dielectric constant. The value of  $\varepsilon_r$  for a bilayer graphene was found to be in the range from 4 to 9 in different experiments [33]. Here we varied the value of  $\varepsilon_r$  in the range from 4 to 11, and the performance of the proposed solar cell is depicted in Fig. 3.2 (i and j). From Fig. 3.2 (i and j), it is noticed that as the dielectric constant increased from 4 to 5, then may be due to the reduction in the excitation binding energy the recombination losses decreased, and therefore the efficiency increased by a small value from 8.006 % to 8.007 %. But on further increasing the value of the dielectric constant, the efficiency falls off from 8.007 % to 8.006 % rather than increasing, as we know higher dielectric constant reduces the exciton binding energy, which consequently results in decreased recombination losses. This may be have happened because it is reported that  $V_{bi} \propto \frac{1}{\epsilon_r}$  [25-26, 34]. Therefore, an increment in the value of dielectric constant deteriorates V<sub>bi</sub> which consequently decreases the efficiency [26]. In this manner, these two effects balance each other, and no further change in the values of  $V_{OC}$ ,  $J_{SC}$ , FF, and  $\eta$  has been observed. In this way, the maximum efficiency of 8.007 % was achieved at a value of 5 dielectric constant. After optimizing the relative permittivity, we have further optimized the hole mobility of n-Dn layer, ranging from 743-1565 cm<sup>2</sup>V<sup>-1</sup>s<sup>-1</sup>, and we noticed that there is no effect of hole mobility on the performance of the photovoltaic cell, because of the ultra-thin layer of diamane.

To understand the role of layers number of n-diamane in the production of charge carriers due to absorption of photons from sunlight by the solar cell with all parameters those we have optimized above at single layer diamane, the above simulated cell was further optimized up to 5 layers of diamane while keeping the parameters of c-Si at the previous constant values that we have taken for previous simulation. It is reported that as the layer number increases, both sheet resistance as well as transmittance decrease, which results in lowering the electron-hole pair generation rate at the interface that depends on the transmittance of diamane. We found that, as the layer numbers of ndiamane increased, Voc decreased very slightly from 519.5 mV to 518 mV, and a variation in the value of J<sub>SC</sub> was found from 20.63 mA/cm<sup>2</sup> to 19.14 mA/cm<sup>2</sup>. This happened because of a smaller electron-hole pair generation rate. The FF was also found to decrease slightly from 74.69% to 74.66% and then decrease infinitesimally on further increasing the number of layers. Because of the lower value of V<sub>OC</sub>, J<sub>SC</sub>, and FF,  $\eta$  also decreased from 7.88% to 7.53%. The best optimized efficiency 8% was achieved for a single layer n-diamane. Since we found deterioration in the values of V<sub>OC</sub>, J<sub>SC</sub>, FF, and η on increasing the layer numbers of n-diamane, we can say that the thickness of ndiamane does not play an important role in improving the efficiency of the solar cell and the generation of photo carriers. We also know that on increasing the thickness, the bandgap decreases, which increases the dielectric constant, which consequently decreases the recombination losses due to a decrease in exciton binding energy. Therefore, according to this concept, efficiency should increase with increasing the thickness of n-diamane, but this is not seen from the results shown in Fig. 3.2 (k and l). This may have happened because of the reduction in transmittance on increasing the layer number, which compensates for the effect of reduced bandgap on increasing the dimensionality of carbon material (diamane). From Fig. 3.2 (k and l), it is noticed that on increasing the layer number of diamane from 1 to 5, the efficiency changed slightly from 8% to 7.53%. Therefore, we can say that an increased number of layers of diamane does not play a significant role in enhancing the efficiency of a solar cell. It only provides the required Schottky junction at the interface for the current movement and acts as an effective emitter layer in a c-Si heterojunction solar cell.

#### 3.3.2 Optimization and simulation of p-crystalline Silicon wafer parameters

We further optimized the variables of p-crystalline Si wafer while setting the parameters of n-Dn at the best optimized values. To carry out this simulation, first, we optimized the acceptor concentration of the p-cSi wafer. This will intensify the efficiency of the ITO (TCO)/n-Dn/p-cSi/Ag structured solar cell, the value of N<sub>A</sub> for p-cSi wafer was increased from  $1\times 10^{16}$  cm<sup>-3</sup> to  $7\times 10^{18}$  cm<sup>-3</sup>, and the desired outputs are shown in Fig. 3.3 (a and b). As we increase N<sub>A</sub>, the Fermi Level in the Si layer moves towards the valence band edge and increasing the work function of p-type Si ( $\Phi_{p-Si}$ ), and barrier height according to Eqn. (3.2), which will increase both V<sub>bi</sub> and V<sub>OC</sub> according to the equations:

$$V_{OC} = \frac{V_{bi}}{q} - \frac{nkT}{q} \ln \left( \frac{qN_V S_{it}}{J_{SC}} \right)$$
 (3.6)

$$V_{bi} = \frac{kT}{q} \ln \left( \frac{N_A N_D}{n_i^2} \right) \tag{3.7}$$

Where S<sub>it</sub> is the interface recombination velocity [35-37]. Therefore, as N<sub>A</sub> increases V<sub>bi</sub> also increases, which helps the generated charge carriers in approaching their respective electrodes, due to which the values of both V<sub>OC</sub> and J<sub>SC</sub> is enhanced from 519.5 mV to 697.7 mV and 20.63 mAcm<sup>-2</sup> to 28.71 mAcm<sup>-2</sup> respectively, as depicted in Fig. 3.3 (b). FF and  $\eta$  were also noticed to increase with N<sub>A</sub> from 74.69 % to 83.58 % and from 8 % to 16.74 % respectively, as shown in Fig. 3.3 (a). The increment in FF might be related to the decrement in the resistivity of the p-cSi layer [26, 38]. The maximum efficiency 16.74 % was achieved at  $N_A = 7 \times 10^{18}$  cm<sup>-3</sup>. Therefore,  $7 \times 10^{18}$  cm<sup>-3</sup>  $^{3}$  is the best optimized value of  $N_{A}$  for p-cSi layer. After getting best optimized value of  $N_A$ , we carried out the simulation further by optimizing  $N_C/N_V$  of p-cSi ranging from  $3 \times 10^{19}$  cm<sup>-3</sup> to  $1 \times 10^{21}$  cm<sup>-3</sup> and the outputs are plotted in Fig. 3.3 (c-d). Here we found that the  $V_{OC}$  is decreased from 697.7 mV to 516.4 mV as  $N_C/N_V$  increased. As  $N_C/N_V$ increases, V<sub>bi</sub> increases by following Eqn. 3.2. Therefore, the trapping speed of charge carriers inside the Si layer is reduced. On increasing the value of N<sub>C</sub>/N<sub>V</sub>, the mobility and L<sub>i</sub> of charge carriers decrease by following the Eqns. (1, 3 and 4). By taking the Eqn. (5) in consideration ,we can say that  $J_0$  also increases with increasing  $N_C/N_V$ . This increment in the value of J<sub>O</sub> as well as V<sub>bi</sub> result in the decrement of V<sub>OC</sub>. The value of J<sub>SC</sub> was found to increased very slightly from 28.71 mAcm<sup>-2</sup> to 28.74 mAcm<sup>-2</sup> as we increased  $N_C/N_V$  of p-cSi from  $3 \times 10^{19}$  cm<sup>-3</sup> to  $5 \times 10^{20}$  cm<sup>-3</sup>, and then becomes constant.

This may have happened because the bandgap and photons absorption are highly influenced by  $N_C/N_V$  [26, 39]. Therefore, at  $N_C/N_V = 3 \times 10^{19}$  cm<sup>-3</sup>, active silicon layer absorbed more photons which increased the generation rate (G) of EHP and then according to Eqn. (3.3), the higher value of G may balance the lower value of L<sub>i</sub> which results in a constant value of J<sub>SC</sub> 28.74 mAcm<sup>-2</sup>. The FF was first found to increase slightly from 83.58 to 83.63% and then decrease to 75.58% on further increasing the value of N<sub>C</sub>/N<sub>V</sub> after 8×10<sup>19</sup>. The efficiency was found to be decreased linearly from 16.74% to 11.22% on increasing  $N_C/N_V$  from  $3 \times 10^{19}$  cm<sup>-3</sup> to  $1 \times 10^{21}$  cm<sup>-3</sup> as depicted in Fig. 3.3 (c). The initial increment in FF may be because of an increment in J<sub>SC</sub>. At higher values of N<sub>V</sub>, FF decreases abruptly because it depends on V<sub>OC</sub>. Similarly, a direct decrement in the value of  $\eta$  was observed because of its direct dependency on FF. The maximum value of efficiency, 16.74 % was found at  $N_C/N_V = 3 \times 10^{19}$  cm<sup>-3</sup>. So,  $3\times10^{19}~\text{cm}^{-3}$  is the best optimized value of  $N_C/N_V$  for p-cSi layer. After optimizing  $N_A$ and N<sub>C</sub>/N<sub>V</sub> to their best optimized values we further optimized the electron affinity of the p-cSi layer in the range from 3.6 to 4.5 eV. For this affinity, V<sub>OC</sub> was found to slightly increase from 699.2 mV to 697.7 mV on increasing affinity from 3.6 eV to 3.8 eV, and then it stayed constant at the value 697.7 mV on further increase in affinity after 3.8 eV. Whereas, the value of J<sub>SC</sub> was noticed to decrease straight from 28.95 mA/cm<sup>2</sup> to 28.55 mA/cm<sup>2</sup> as depicted in Fig. 3.3 (e-f). The value of FF first increased from 83.19 % to 83.58 % on increasing the electron affinity from 3.6 eV to 4.1 eV, but on further crossing of the value of electron affinity, the FF starts decreasing from 83.58 % and reaches 83.21 % at affinity of 4.5 eV. This reduction in FF on increasing the affinity from 4.2 eV to 4.5 eV can be understood by the concept of changing the work function of p-cSi at the interface by the relation:  $\Phi_B = \Phi_{p-cSi} - \chi$ , where  $\Phi_B$  is the barrier height for p-type semiconductor,  $\Phi_{p-cSi}$  is the work function of p-cSi and  $\chi$  is the affinity of Si, due to which the carrier transportation rate in the p-cSi layer would reduce. This reduction will increase the series resistance of both p-cSi wafer and the cell. Therefore, the FF reduces after  $\chi > 4.1$  eV. The efficiency of the optimized cell was found to decrease linearly from 16.84 % to 16.58 % as we increase the affinity in the range 3.6 to 4.5 eV. In this way, the best optimized cell was obtained at an affinity of 3.6 eV. To further analyze the possibility of a cost-effective cell, the next variable we optimized is the thickness of p-cSi layer.

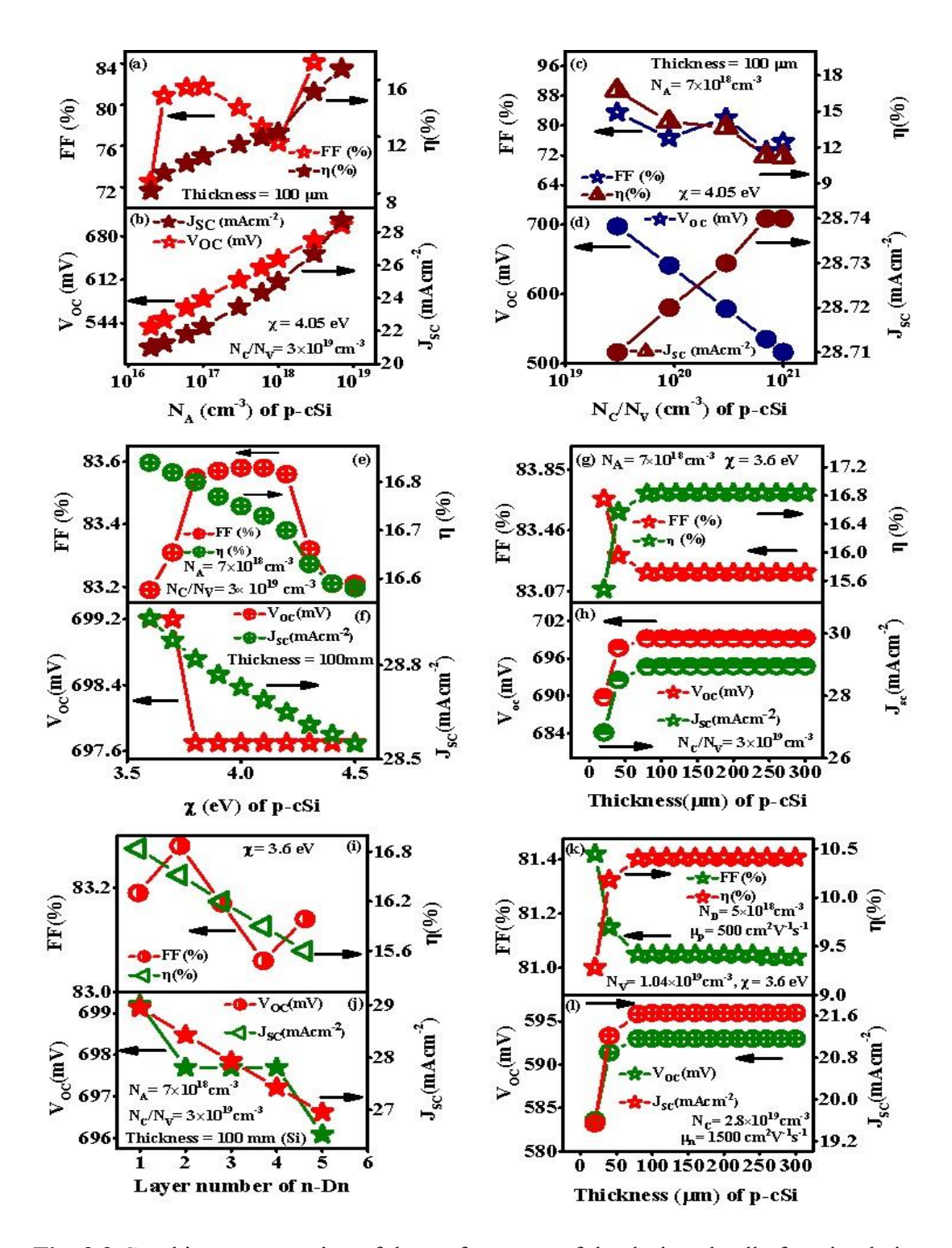


Fig. 3.3 Graphic representation of the performance of the designed cell after simulation of different variables of p-crystalline Si wafer, (a, b)  $N_A$  (cm<sup>-3</sup>), (c, d)  $N_C/N_V$  (cm<sup>-3</sup>), (e-f)  $\chi$  (eV), (g, h) wafer thickness ( $\mu$ m), (i, j) layer number of n-Dn at best optimized values of p-cSi wafer and (k, l) thickness of Si layer at commercially available values of parameters p-cSi wafer, whereas the values of parameters of n-Dn are kept at their best optimized values i.e.,  $N_D=1\times 10^{18}$  cm<sup>-3</sup>,  $N_C/N_V=1\times 10^{19}$  cm<sup>-3</sup>,  $E_g=2.05$  eV,  $\chi=4.4$  eV,  $\mu_n=2732$  cm<sup>2</sup>V<sup>-1</sup>s<sup>-1</sup> and  $\mu_p=1565$  cm<sup>2</sup>V<sup>-1</sup>s<sup>-1</sup>.

We have optimized the thickness of p-cSi wafer ranging from 20-300 µm. From Fig. 3.3 (g-h), it is visible that for a 20 µm thick p-cSi layer, the efficiency is 15.48 %. Higher efficiency, 16.84 % was obtained for a 100 µm thick silicon layer. This is because as the thickness increases number of charge carriers increases; consequently, J<sub>SC</sub> increases. For a thicker layer of p-cSi, the lifespan of minority charge carriers gets reduced because of its shorter drift length. Additionally, the excess photogenerated charge carriers and their recombination rate have been found in proportion in the thicker silicon wafer, which overall results in a constant value of Voc 699.2 mV and J<sub>SC</sub> 28.95 mAcm<sup>-</sup> <sup>2</sup> after a thickness of 100 μm. The FF and efficiency were also constant after getting a value of 83.19 % and 16.84 % respectively, beyond the thickness of 100 μm. Thus, we did not notice any change in the value of V<sub>OC</sub>, J<sub>SC</sub>, FF and η on further increasing the thickness of p-cSi layer after 100 µm and we can say that, these saturated values of V<sub>OC</sub>, J<sub>SC</sub> and FF have produced a maximum efficiency of 16.84 %, even on increasing the thickness of p-cSi wafer up to 300 µm. Another reason for not improving the efficiency further on increasing the thickness of p-cSi wafer beyond 100 µm is that in a thick layer of p-cSi more dangling bonds are found which become the recombination centers for the photogenerated charge carriers due to the increased number of defects on the surface of the thick silicon layer. That is why the decreased bandgap on increasing the thickness of the layer does not contribute in improving the conversion efficiency of the solar cell. Therefore, a large thickness of p-cSi does not appear to play an important role in improving the efficiency of the cell. From Fig. 3.3 (g and h) it is shown that during the optimization of the thickness of p-cSi layer the efficiency increases from 15.48 % to 16.84 % only which is not much recommendable.

After optimization of the silicon wafer's parameters, the cell was further simulated to study the effect of the layer numbers of diamane, and the results are plotted in Fig. 3.3 (i and j), where we found  $\eta$  to decrease from 16.84 % to 15.6 %. For the best commercial appreciation of the simulated cell, we have further optimized the thickness of p-cSi wafer by considering the commercially available parameters of Si layer. For this, we have taken the values of acceptor concentration =  $5 \times 10^{16}$  cm<sup>-3</sup>, effective conduction band density =  $2.8 \times 10^{19}$  cm<sup>-3</sup>, effective valence band density =  $1.04 \times 10^{19}$  cm<sup>-3</sup>, affinity = 3.6 eV, electron mobility = 1500 cm<sup>2</sup>/Vs and hole mobility = 500 cm<sup>2</sup>/Vs from the previously reported data [26, 40-41]. We optimized the thickness of silicon layer in the

range from 20 to 300 µm, and the highest efficiency 10.41% was found for a thickness of 100 µm, as shown in Fig. 3.3 (k and l). Since front and back contacts play an important role in the solar cell as the front contact is required to be highly transparent so that maximum photons can reach the active layer and enhance the conversion efficiency. Therefore, we preferred the front contact with a low reflection coefficient or nearly 0. Hence, we have given more preference to ITO, as TCO in designing our solar cell to intensify the effective illuminating area, because ITO increases the optical absorption instead of reflection that occurs in other metal contacts, and it possesses low sheet resistance, high mobility, and is optically transparent too. Furthermore, in order to check the effect of back contact on the solar cell we have changed the back contacts by Au (where n is taken as 0.27049 and k is taken as 2.7789) and Tin (where n is taken as 1.96 and k is equal to 3.06), these files are present already in the AFORS-HET software and we found that maximum efficiency is achieved in case of Au and Ag because of their larger work function. This indicates that both the reflection coefficient and work function of the front as well as the back constant play a significant role in the solar cells. Here, we have given more preference to ITO, as TCO in the design of our solar cell to intensify the effective illuminating area, because TCO increases the optical absorption instead of reflection that occurs in other metal contacts.

#### 3.3.3 Spectral response, quantum efficiency and temperature dependency

Generally, spectral response is conceptually similar to the QE of the solar cell. The QE is defined as the ratio of the number of electrons collected by the cell as output to the number of photons incident on its surface, whereas spectral response is defined as the ratio of current generated by the cell to the optical power incident on its surface [26]. Quantum efficiency and spectral response are both used in cell analysis; one uses the photon flux and the other uses the power of light at each wavelength, respectively. QE can be converted into SR by using the formula:  $SR = \frac{q\lambda}{hc}$  QE. To analysis the SR, external quantum efficiencies (EQE) and internal quantum efficiency (IQE) of the optimized cell at efficiencies 8 %, 10.41 % and 16.84 % we performed the simulation in the wavelength range 300 nm-1200 nm and the results are shown in Fig. 3.4. We observed that, at shorter wavelengths i.e., below 600 nm the diamane layer was found to absorb most of the light, this results in less photons passing to p-cSi layer subsequently small

amount of current would generate in the shorter wavelengths and the cell response was found to be very low. In the wavelength range from 600 nm to 1000 nm, most of the photons reach silicon layer where the energy they constitute found equal to the bandgap energy of silicon layer, and this energy is then converted into electrical energy inside the silicon layer. Therefore, the optimized cell achieved its ideal response at intermediate wavelengths. Since silicon is an indirect bandgap semiconductor, there will not be any sharp cutoff at the wavelength corresponding to its bandgap ( $E_g$ = 1.12 eV). So, the spectral response falls back to zero at longer wavelengths. From Fig. 3.4, it is visible that for a greater than 100 µm thick silicon layer, the spectral response maintained its uniformity. This is because the effective conversion rate remains constant as we increase the thickness beyond 100 µm. The IQE and EQE of the optimized cell at efficiencies 8 %, 10.41 % and 16.84 % has been observed and the results are being shown in Fig. 3.4. IQE do not consider the reflection and transmission of photon outside the solar cell while, EQE considers the outcomes of optical losses i.e., reflection and transmission. Fig. 3.4 (b and c) reveals that, at an initial wavelength 300 nm EQE and IQE is having smaller value this is because of the optical losses at the shorter wavelengths. The IQE and EQE are maximum at the wavelength 400 nm and above 400 nm both efficiencies start falling off and reaches to zero at 1200 nm. Since, parameter's optimization of silicon as well as diamane was unable to nullify the optical losses on the surface of the solar cell. Hence, maximum EQE and IQE was noticed for the wavelength 400 nm. The higher value of EQE at the wavelength 400 nm suggests that as we optimized doping concentration and effective band density then there would be an increment in the electron-hole pair generation rate and subsequently, collection of surplus charge carriers, due to which the highest efficiency has been achieved at 400 nm. We found that, IQE and EQE responses of the cell with efficiencies 8 %, 10.41 % and 16.84 % are almost the same, which indicates an equal amount of charge carriers gathered for this range of wavelengths parallel to the photons absorbed by the solar cell. At higher wavelength regions, the recombination rate of the generated charge carriers is better; therefore both internal and external efficiencies become negligible at 1200 nm wavelength.

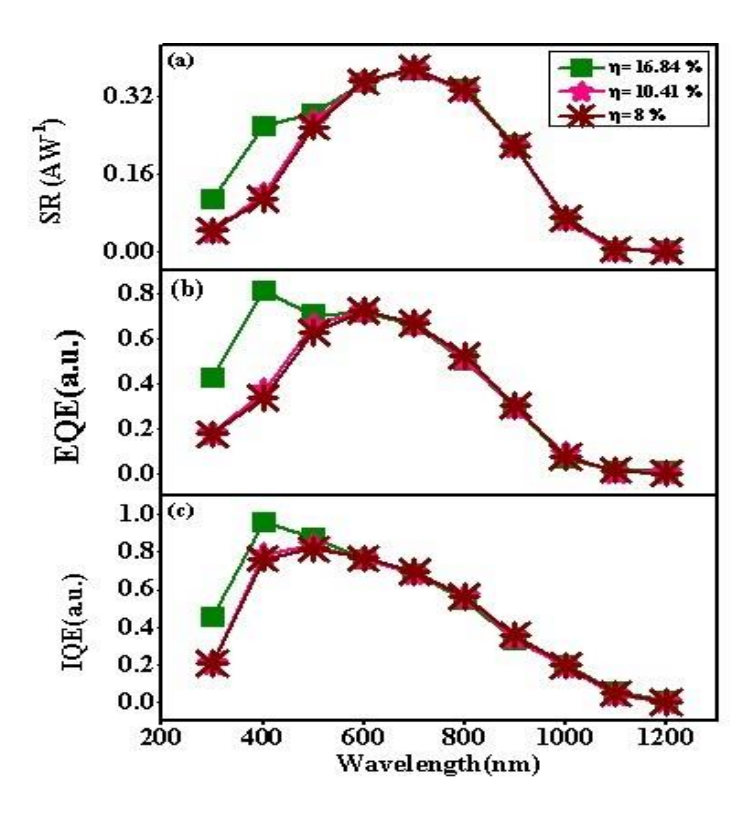


Fig. 3.4 Wavelength dependency of (a) SR, (b) EQE and (c) IQE of the best simulated solar cell at single layer n-Dn/p-cSi (  $\eta=8\%,\,\eta=16.84\%$  with  $N_A=7\times10^{18}$  cm $^{-3},\,N_C/N_V=1\times10^{19}$  cm $^{-3}$  for  $100~\mu m$  p-cSi and efficiency = 10.41% with  $N_A=5\times10^{16}$  cm $^{-3},\,N_V=1.04\times10^{19}$  cm $^{-3}$  and  $N_C=2.8\times10^{19}$  cm $^{-3}$  at  $100~\mu m$  p-cSi).

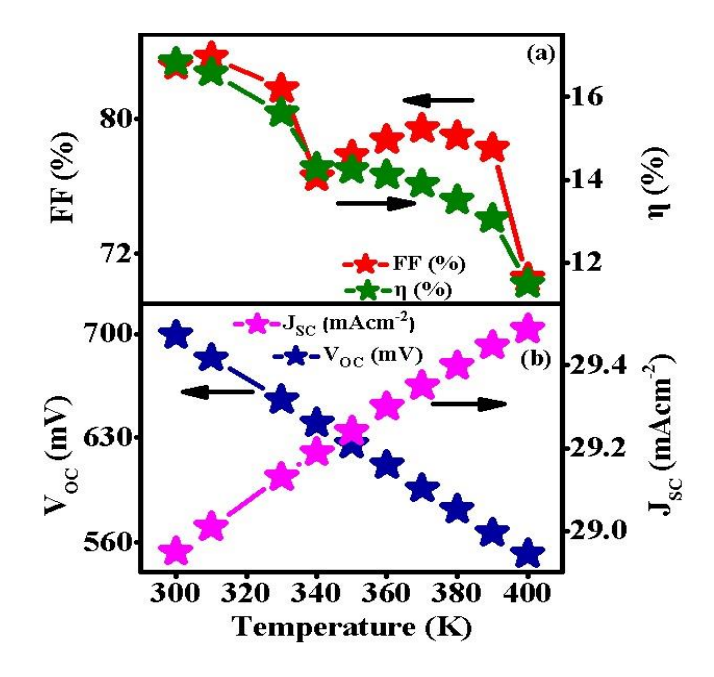


Fig. 3.5 Dependency of the optimized cell response with temperature variation at  $\eta = 16.84\%$ . (a) efficiency and fill factor, (b)  $V_{OC}$  and  $J_{SC}$ .

In order to realize the effect of varying temperature on the operation of a solar cell we have further simulated the best optimized cell comprises an efficiency 16.84 % in the environment of 300 to 400 K temperature, and the outputs are depicted in Fig. 3.5 (a-b). We observed that  $V_{OC}$  decreased from 699.2 mV to 552.3 mV while  $J_{SC}$  increased moderately from 28.95 mA/cm² - 29.49 mA/cm² as we increased the temperature. Following to Energy-Temperature relation written as:  $E_g$  (T) =  $E_g$  (0) –  $\left(\frac{\alpha T^2}{\alpha + \beta}\right)$ , where  $E_g$  (T) is the bandgap of semiconductor at any given temperature T,  $E_g$  (0) is the bandgap at zero temperature and  $(\alpha, \beta)$  are the material constant [26, 31]. As temperature elevates band gap declines smoothly. We also know that, as temperature increases  $J_0$  increases, which results in a decrease of  $V_{OC}$  [26, 31]. Furthermore, at smaller values of  $E_g$  large number of absorbed photons have sufficient energy to create e-h pairs, which results in an increment in the value of  $J_{SC}$ . Since  $V_{OC}$  decreases, the Fill Factor and efficiency also decrease and the maximum efficiency  $\eta$  = 16.84 % found at a temperature of 300K. The optimized results of the designed solar cell are shown in Table 3.3.

**Table 3.3** Overview of the variables of the finest simulated solar cell.

Cell variables	n-diamane layer optimized cell	n-Diamane layer and p-cSi layer optimized cell	p-cSi layer optimized cell for practically available Si parameters
$V_{OC}$ (mV)	519.5	699.2	593
J <sub>SC</sub> (mAcm <sup>-</sup> <sup>2</sup> )	20.63	28.95	21.66
FF (%)	74.69	83.19	81.05
η (%)	8 (@ p-crystalline Si wafer at $N_A = 1 \times 10^{16}$ (cm <sup>-3</sup> ), $N_C/N_V = 3 \times 10^{19}$ (cm <sup>-3</sup> ), $\chi = 4.05$ (eV), and thickness = 100 $\mu$ m	16.84 (@ p-crystalline Si wafer at $N_A = 7 \times 10^{18}$ (cm <sup>-3</sup> ), $N_C/N_V = 3 \times 10^{19}$ (cm <sup>-3</sup> ), $\chi = 3.6$ (eV), and thickness = 100 micrometer	10.41 [@ p-cSi wafer at $N_A = 5 \times 10^{16}$ (cm <sup>-3</sup> ), $N_C = 2.8 \times 10^{19}$ (cm <sup>-3</sup> ), $N_V = 1.04 \times 10^{19}$ (cm <sup>-3</sup> ), $\chi = 3.6$ (eV), and thickness = 100 micrometer]

### 3.4 Summary

In this article, we have proposed the structure (TCO) ITO/n-Dn/p-cSi/ (back contact) Ag. The independent consequences of optimizing seven parameters of n-type diamane wafer on the operation of solar cell were investigated and only single parameter: hole mobility  $(\mu_p)$  was noticed not to influence its working whereas other parameters were directly affecting the behavior of the proposed cell. After optimizing the parameters of diamane as well as silicon, the maximum efficiency of 16.84 % was achieved, and the formation of Schottky junction at n-Dn/p-cSi interface was found to play a major role in the processing of the cell as it helps in carrying current across the junction. This junction is responsible for the current movement across n-Dn/p-cSi interface. As the work function of diamane can be varied in the range 7.24 eV to 0.62 eV and the work function of p-type silicon layer is found in the range 4.9-5.1 eV. Here, we have taken the work function of diamane as 4.4 eV smaller than the work-function of p-type silicon which supports the formation of Schottky junction at the interface. We also compared the optimized values with the reported experimental values and found satisfactory results. Higher thickness of both diamane as well as silicon was not found to contribute to improving the efficiency of the solar cell on a large scale. It has been found that the thickness of front and back contacts does not play an important role in the performance of the modelled heterojunction cell. The results of the modelled cell have also not changed much on changing the metal contacts at the front and back sides of the cell. Finally, it has been concluded that if we could reduce the sheet resistance of diamane and increase its work-function by any technique like chemical doping, then few layers n-diamane can work more efficiently as an emitter layer in Si heterojunction solar cell.

#### REFERENCES

- [1] Zheng, Z., Zhan, H., Nie, Y., Xu, X., Qi, D. and Gu, Y., 2020. Single layer diamond A new ultrathin 2D carbon nanostructure for mechanical resonator. *Carbon*, 161, pp.809–815.
- [2] Pakornchote, T., Ektarawong, A., Pinsook, U. and Bovornratanaraks, T., 2021. Modifying Electronic and Elastic Properties of 2-Dimensional [110] Diamond by Nitrogen Substitution. *Journal of Carbon Research C*, 7, 1, pp.8.
- [3] Pakornchote, T., Ektarawong, A., Busayaporn, W., Pinsook, U. and Bovornratanaraks, T., 2020. Roles of nitrogen substitution and surface reconstruction in stabilizing non-passivated single-layer diamond. *Physical Review B*, 102, 7, pp.075418.
- [4] Raeisi, M., Mortazavi, B., Podryabinkin, E.V., Shojaei, F., Zhuang, X. and Shapeev, A.V., 2020. High thermal conductivity in semiconducting Janus and non-Janus diamanes. *Carbon*, 167, pp.51–61.

- [5] Bakharev, P.V., Huang, M., Saxena, M., Lee, S., Joo, S.H., Park, S.O., Dong, J., Camacho-Mojica, D.C., Jeong, H.Y., Kwak, S.K., Prasai, D., Gunlycke, D., Kim, M.J., Rümmeli, M.H., Shin, H.S. and Ruoff, R.S., 2020. Chemically induced transformation of chemical vapour deposition grown bilayer graphene into fluorinated single-layer diamond. *Nature Nanotechnology*, 15, 1, pp.59–66.
- [6] Nair, R.R., Ren, W., Jalil, R., Riaz, I., Kravets, V.G., Britnell, L., Blake, P., Schedin, F., Mayorov, A.S., Yuan, S., Katsnelson, M.I., Cheng, H.M., Strupinski, W., Bulusheva, L.G., Okotrub, A.V., Grigorieva, I.V., Grigorenko, A.N., Novoselov, K.S. and Geim, A.K., 2010. Fluorographene: A two-dimensional counterpart of teflon. *Small*, 6, 24, pp.2877–2884.
- [7] Kravets, V.G., Grigorenko, A.N., Nair, R.R., Blake, P., Anissimova, S., Novoselov, K.S., Geim, A.K. and Ferrari, A.C., 2010. Spectroscopic ellipsometry of graphene and an exciton-shifted van Hove peak in absorption. *Physical Review B*, 81, 15, pp.155413.
- [8] Piazza, F. and Cruz, K., 2020. Raman evidence for the successful synthesis of diamane. *Carbon*, 169, pp.129–133.
- [9] Ke, F., Zhou, Z., Wang, Y., Liu, Y., Huang, H., Sun, X., Hu, W., Liu, Z., Wu, H., Liu, Y., Zhang, Q., Zhang, X., Shi, J., Zhang, H. and Chen, X., 2019. Synthesis and electronic structure characterization of diamane. *Condensed Matter Materials Science*, 10, 48, pp.48550.
- [10] Zhu, L., Li, W. and Ding, F., 2019. Giant thermal conductivity in diamane and the influence of horizontal reflection symmetry on phonon scattering. *Nanoscale*, 11, pp.4248–4257.
- [11] hernozatonskii, L.A., Sorokin, P.B., Kvashnin, A.G. and Kvashnin, D.G., 2009. Diamond-like C2H nanolayer, diamane: simulation of the structure and properties. *Condensed Matter*, 90, 3, pp.134–138.
- [12] Cheng, T., Liu, Z. and Liu, Z., 2020. High elastic moduli, controllable bandgap and extraordinary carrier mobility in single-layer diamond. *Journal of Materials Chemistry C*, 39, pp.13819–13826.
- [13] Robinson, J.T., Burgess, J.S., Junkermeier, C.E., Badescu, S.C., Reinecke, T.L., Perkins, F.K., Zalalutdniov, M.K., Baldwin, J.W., Culbertson, J.C., Sheehan, P.E. and Snow, E.S., 2010. Properties of Fluorinated Graphene Films. *Nano Letters*, 10, 8, pp.3001–3005.
- [14] Rietwyk, K.J., Koeck, F.A.M., Nemanich, R.J., Nebel, C.E. and Williams, O.A., 2013. Work function and electron affinity of the fluorine-terminated (100) diamond surface. *Applied Physics Letters*, 102, 9, pp.091604.
- [15] Stangl, R., Leendertz, C. & Haschke, J., 2010. Numerical Simulation of Solar Cells and Solar Cell Characterization Methods: the Open-Source on Demand Program AFORS-HET. In *Solar Energy*. InTech, ch.14.
- [16] Patel, K. and Tyagi, P.K., 2015. Multilayer graphene as a transparent conducting electrode in silicon heterojunction solar cells. *AIP Advances*, 5, 7, pp.077165.
- [17] Abd El-Raheem, M.M., El-Kadry, N.A., El-Sadek, M.S. and Hussein, M.A., 2010. Improvement of the optical properties of ITO/SiO<sub>2</sub>/Glass films for photovoltaic applications. *Journal of Non-oxide Glasses*, 2, 2, pp.67–76.
- [18] Ohshima, T., Ogawa, H., Okazaki, S., Endo, S., Yamada, T., Ueda, K., Itoh, H. and Okushi, H., 2010. Preparation of ITO Thin Films by Pulsed Laser Deposition for Use as Transparent Electrodes in Electrochromic Display Devices. *Transactions of the Materials Research Society of Japan*, 35, 3, pp.583–587.
- [19] Zare, S., Izadkhah, H. and Vittoria, C., 2016. Deposition of magnetoelectric hexaferrite thin films on substrates of silicon. *Journal of Magnetism and Magnetic Materials*, 420, pp.245–248.
- [20] Lien, S.Y., 2010. Characterization and optimization of ITO thin films for application in heterojunction silicon solar cells. *Thin Solid Films*, 518, S1, pp.S10–S13.

- [21] Borah, C.K., Tyagi, P.K. and Kumar, S., 2020. The prospective application of a graphene/MoS<sub>2</sub> heterostructure in Si-HIT solar cells for higher efficiency. *Nanoscale Advances*, 2, 8, pp.3231–3243.
- [22] Das Sarma, S., Adam, S., Hwang, E.H. and Rossi, E., 2011. Electronic transport in two-dimensional graphene. *Reviews of Modern Physics*, 83, 2, pp.407–470.
- [23] Lin, Z., Carvalho, B.R., Kahn, E., Lv, R., Rao, R., Terrones, H., Pimenta, M.A. and Terrones, M., 2016. Defect engineering of two-dimensional transition metal dichalcogenides. *2D Materials*, 3, 2, pp.022002.
- [24] Bouzidi, S., Barhoumi, M. and Said, M., 2021. Optical properties of Janus and non-Janus diamanes monolayers using ab-initio calculations. *Optik*, 235, pp.166642.
- [25] Singh, J., 2004. *Semiconductor Devices: Basic Principles*. 2nd ed. New Delhi: Wiley India Pvt Ltd.
- [26] Borah, C.K., Tyagi, P.K. and Kumar, S., 2018. Few-layer p-type phosphorene sheet: An efficient transparent conducting electrode in silicon heterojunction solar cell. *Computational Materials Science*, 151, pp.65–72.
- [27] Wang, Q., Hou, G., Wang, L., Zhao, X. and Hu, H., 2008. Crystal silicon heterojunction solar cells by hot-wire CVD. *Conference Record of the IEEE Photovoltaic Specialists Conference*, pp.1-4.
- [28] Gangopadhyay, U., Chatterjee, A., Pal, P. and Bandyopadhyay, S., 2012. Comparative simulation study between n-type and p-type Silicon Solar Cells and the variation of efficiency of n-type Solar Cell by the application of passivation layer with different thickness using AFORS HET and PC1D. *IOSR Journal of Engineering*, 8, 1, pp.41–48.
- [29] Xu, S., Li, M., Yu, H., Zhao, Y. and Wang, Z., 2017. Simulation and Optimization Characteristic of Novel MoS<sub>2</sub>/c-Si HIT Solar Cell. *Journal of Minerals and Materials Characterization and Engineering*, 5, 5, pp.323–338.
- [30] Lundstrom, M., 1995. Heterostructure fundamentals (electronegatividad de electrones). PDF, pp.43.
- [31] Nair, K.K., Jose, J. and Ravindran, A., 2016. Analysis of temperature dependent parameters on solar cell efficiency using MATLAB. *International Journal of Engineering Development and Research*, 3, 3, pp.536–541.
- [32] Sachenko, A.V., Kostylyov, V.P., Grym, J., Husakou, A.A., Korchak, S.O. and Scherbatyuk, M.V., 2016. Analysis of the silicon solar cells efficiency. Type of doping and level optimization. *Semiconductor Physics, Quantum Electronics and Optoelectronics*, 19, 1, pp.67–74.
- [33] Bessler, R., Duerig, U. and Koren, E., 2019. The dielectric constant of a bilayer graphene interface. *Nanoscale Advances*, 1, 5, pp.1702–1706.
- [34] Zhao, Y., Di, C., Hu, Y. and Yu, G., 2014. Effect of doping on the short-circuit current and open-circuit voltage of polymer solar cells. *AIP*, 116, 15, pp.154506.
- [35] Hamdani, D., Yusoff, M., Ibrahim, Z., Karimov, K.S. and Hashim, A., 2022. The Effects of Dopant Concentration on the Performances of the a-SiOx:H(p)/a-Si:H(i1)/a-Si:H(i2)/µc-Si:H(n) Heterojunction Solar Cell. *International Journal of Renewable Energy Development*, 11, 1, pp.173–181.
- [36] Belfar, A., 2015. The role of p+-layer dopant concentration, p+-layer band gap and p+-layer thickness in the performances of a-Si:H n-i-p-p+ solar cells with double layer window nanocrystalline silicon. *Optik*, 126, 23, pp.5688–5693.
- [37] Jensen, N., Vetterl, O., Hüpkes, J., Rech, B. and Schock, H.W., 2002. Optimization and characterization of amorphous/crystalline silicon heterojunction solar cells. *Progress in Photovoltaics: Research and Applications*, 10, 1, pp.1–13.
- [38] Belarbi, M., Beghdad, M. and Mekemeche, A., 2016. Simulation and optimization of n-type interdigitated back contact silicon heterojunction (IBC-SiHJ) solar cell structure using Silvaco TCAD Atlas. *Solar Energy*, 127, pp.206–215.

- [39] Zhou, Y. and Long, G., 2017. Low Density of Conduction and Valence Band States Contribute to the High Open-Circuit Voltage in Perovskite Solar Cells. *Journal of Physical Chemistry C*, 121, 3, pp.1455–1462.
- [40] Miao, X., Tongay, S., Petterson, M.K., Berke, K., Rinzler, A.G., Appleton, B.R. and Hebard, A.F., 2012. High Efficiency Graphene Solar Cells by Chemical Doping. *Nano Letters*, 12, 6, pp.2745–2750.
- [41] Sze, S.M., 1981. *Physics of Semiconductor Devices*. 2nd ed. Singapore: Wiley Interscience.

## CHAPTER 4

# SIGNIFICANCE OF NOVEL GRAPHENE/DIAMANE INTERFACE IN SILICON HETEROJUNCTION WITH INTRINSIC THIN LAYER (HIT) SOLAR CELL

This chapter presents a simulation-based study of a novel HIT solar cell incorporating a graphene/n-diamane interface, modeled as: graphene (TCO)/n-diamane/a-Si:H(i)/p-cSi/Ag, using AFORS-HET v2.5. Here, n-type diamane functions as the emitter, and graphene serves as the transparent conductive electrode. The a-Si:H(i) layer ensures interface passivation and built-in potential. After optimizing key parameters, the structure achieves a peak efficiency of 31.2%. In comparison, replacing graphene with ITO lowers efficiency to 27.15%, while using commercial c-Si parameters yields 24.15%. The optimal performance occurs with a 3 nm a-Si:H(i) layer and a 1.6 eV bandgap. These findings highlight the promise of 2D carbon materials as multifunctional components in next-generation solar cells.

The results reported in this chapter have been published in Naima et. al. Computational Materials Science 226 (2023) 112252.

#### 4.1 Introduction

The holy grail hurdle in the profitable expansion of photovoltaic solar cells is to make them cost-effective as well as exhibit high efficiency. For this motive, many solar cells have been explored and fabricated with different materials to increase their efficiency [1,2]. Recently, a new 2D material called diamane (Dn) has been used as an emitter layer by Naima *et. al.* [3] and elaborated the significance of using diamane in silicon heterojunction solar cells for enhancing its efficiency to a good extent. To further explore the possibility of achieving higher efficiency, we have explored a HIT (heterojunction solar cell with intrinsic thin layer) module where 2D carbon material (diamane) is used as an emitter layer. It is reported that 26.6 % and more than 30 % efficiency can be achieved for different HIT modules [4,5].

Furthermore, to ease the movement of photons from the emitter layer to the external circuit, a TCO is needed, which must be highly transparent as well as have low sheet resistance and high carrier mobility. In this search, graphene is found to be a potential candidate which possesses 97.4 % optical transparency with sheet resistance of approximately 125 Ωsq<sup>-1</sup> [6] for monolayer graphene and its work function can be manipulated in the range 3.10 eV to 5.57 eV [7,8]. It is reported that the HIT module with graphene/ $MoS_2$  interface is commendable for achieving a higher efficiency 25.61 % [9]. Similarly, another HIT cell has also been simulated previously, in which up to 20.23 % efficiency has been reached for a 156 mm active layer [2]. Therefore, it is plausible to use graphene/diamane interface in HIT solar cells to improve efficiency. Previously, numerous studies have been done on the excellent optoelectronic properties of various 2D materials and their heterojunctions [10-12]. In 2009, 2-D ultra-thin layer of diamond called diamane was predicted and studied [13,14]. The effective mass of conduction electrons in diamane is very small (0.55 m<sub>0</sub>), and it has a wide bandgap, which is diverse ranging from 3.1 eV to 4.5 eV [14,15]. In addition, the carrier's mobility in diamane is also very high as 2732 cm<sup>2</sup>/Vs for electrons and 1565 cm<sup>2</sup>/Vs for holes for its different forms [15]. Its work function can also be tuned in the range 6.78 eV to 7.24 eV by vacuum annealing at 350 °C [16]. Doping of diamane with nitrogen makes it an n-type and highly stable material which can be used in different electronic applications. Also, diamane is a sp<sup>3</sup> hybridized C<sub>2</sub>H based layered structure on the bilayer graphene, which is also sp<sup>3</sup>

hybridized and the neighbouring carbon atoms of both materials are covalently bonded with the hydrogen atoms located out there. In this way, we can state that the graphene/diamane interface would be stable [13], and this heterostructure can find applications in electronic devices.

Since, to the best of our knowledge, this material has not been tested in a solar cell's structure yet, we have selected this material as the emitter layer in HIT solar cell and studied the patentability of novel graphene/diamane interface. The nature of diamane layer is considered isotropic during the entire simulation [15]. The motive of this simulation is to attain the maximum possible efficiency of HIT solar cell by optimizing various parameters of both doped and one intrinsic layer, as well as front and back contacts a minimum possible thin substrate. The main objective of this chapter is to examine the effect of graphene layer as TCE and diamane layer as an emitter layer in HIT solar cells for higher efficiency and to achieve the highest conversion efficiency of HIT solar cells by using the thinnest possible silicon substrate or wafer.

#### 4. 2. Simulation and structural details and junction formation

#### 4.2.1. Simulation and structural details

For all simulation work, a software called AFORS-HET version 2.5 is used in this chapter, which automatize the simulation for heterostructures. This software is a one-dimensional numerical computer program which modelled multi-layer hetero as well as homojunction solar cells and also do modelling for some common solar cell characterization methods [17]. This software usually solves one-dimensional semiconductor equations for both carriers' electrons and holes by using finite difference at different conditions [17]. Within each semiconductor layer, the Poisson equation and the transport and continuity equations for electrons and holes have been solved in one-dimension, given by:

Poisson's equation,

$$\frac{\varepsilon_{0}\varepsilon_{r}}{q}\frac{\partial^{2}\varphi\left(x,t\right)}{\partial x^{2}}=p\left(x,t\right)-n\left(x,t\right)+N_{D}\left(x\right)-N_{A}\left(x\right)+\sum_{trap}\rho_{trap}\left(x,t\right)\tag{4.1}$$

where p (x, t) and n (x, t) are the local particle densities in the system, q is the electronic charge, and  $\varepsilon_0$  and  $\varepsilon_r$  are the absolute and relative permittivity, respectively.

Continuity and transport equations for electrons and holes to be solved in one dimension:

$$-\frac{1}{q}\frac{\partial j_{n}(x,t)}{\partial x} = G_{n}(x,t) - R_{n}(x,t) - \frac{\partial}{\partial t}n(x,t) + \frac{1}{q}\frac{\partial j_{p}(x,t)}{\partial x}$$

$$= G_{p}(x,t) - R_{p}(x,t) - \frac{\partial}{\partial t}p(x,t)$$
(4.2)

Where,  $G_n(x, t)$  and  $G_p(x, t)$  are the electron and hole super-bandgap generation rates and  $R_n(x, t)$  and  $R_p(x, t)$  are their corresponding recombination rates [17].

In the presented report, the electronic nature of both diamane as well as graphene has been considered as 3D instead of 2D. To make sure that a Schottky junction will form at the interface, we have intentionally made the electric contacts along the c-axis so that the maximum number of charge carriers can collect. The intrinsic amorphous silicon can be deposited on a  $SiO_2$  patterned silicon substrate by using PECVD method or hot wire CVD method [2] at a low temperature to prevent thermal damage to the silicon layer. After deposition of the amorphous silicon on the patterned substrate, few layer graphene can be directly transferred by chemical methods used by Sukang Bae *et.al* [6], and these transferred few graphene can be converted to a diamane layer by using a chemical fluorination route [14, 16]. Furthermore, another layer of graphene can also be directly transferred onto diamane [6]. Finally, the back electrode (Ag) at the back surface may be screen printed or deposited to extract the light-generated current [2]. In this way, we have a structure Gr/n-Dn/a-Si: H(i)/p-cSi/Ag shown in Fig. 4.1 (a).

Furthermore, we have explored the HIT solar cell by optimizing the values of some parameters in their possible ranges and by taking some parameters to their default values as well. We have used both electrical and optical simulation. The HIT structure of solar cell modelled here is: Graphene (TCE) / n-Dn / a-Si: H(i) / p-cSi / Ag, shown in Fig. 4.1 (a). The front and back contacts are selected taking the account their optical transparency as well as conductivity. The ranges of parameters for these two contacts have been taken from the literature available [18-22]. The details of front and back contacts are given in Table 4.1, and details about the interfaces are given in Table 4.2. The parameters of different layers used in the simulation are given in Table 4.3. MS-Schottky interface is considered for Graphene / n-Dn and p-cSi / Ag interfaces similarly drift-diffusion interface is chosen for n-Dn / a-Si: H(i) and a-Si: H(i) / p-cSi the interfaces, respectively. The drift-diffusion model drives the interface current. No defects are considered for the interface regions except drift-diffusion interface to avoid additional recombination centres. The electron and hole recombination velocities are taken as  $4 \times 10^7$  cm/sec at

the MS- Schottky interface and tunnelling is kept activated (new feature added in AFORS-HET software version 2.5) during the simulation. The simulation is carried out by taking 20 steps to get better accuracy.

**Table 4.1** List of parameters used as front and back contacts [18-22].

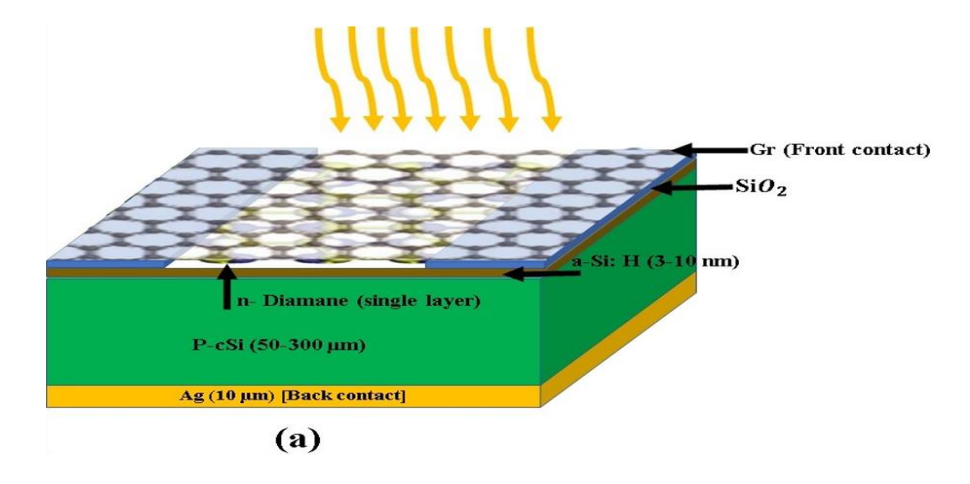
Parameters	Front contact			Back
	Before simulation	After simulation		– contact
Material	Graphene	ITO	Al	Ag
Thickness	1L-5L (1L=0.334 nm)	80 nm	80 nm	10 μm
Optical properties	n = 2.7, k = 1.45	ITO nk (default)	n=1.19 k=7.05	Ag nk (default)
Work function (eV)	4.3 - 4.9	4.4 – 4.5	4.06-4.26	4.64 – 4.74
Absorption loss	0.023	ITO abs (default)	0.056	0
External	1L = 0	ITO Ref (default)	0.868	0
reflection	2L = 0.023			
	3L = 0.046			
	4L = 0.070			
	5L = 0.092			
Surface condition	Plane	Plane	Plane	Plane
Internal reflection	0	0	0	0

The front contact of the cell is taken at positive terminal , whereas the negative terminal is assigned for the back contact of the solar cell. The simulation is carried for the boundary voltage of  $0.7~\rm V$  at a temperature  $300~\rm K$ . The front contact of the cell is illuminated with

monochromatic light of photon flux  $1\times 10^{16}$  cm<sup>-2</sup>s<sup>-1</sup>, spectral width of 10 nm with power density 100 mW/cm<sup>2</sup> under the AM 1.5.

**Table 4.2** List of range of values of parameters used [32-35].

Parameter	n-Dn	a-Si: H (i)	p-cSi
Thickness	1L - 5L (1L = 0.34)	3-10 nm	50-500 μm
	nm)		•
Dielectric constant $(\varepsilon_r)$	8 - 11	11.9	11.9
Electron affinity $\chi$ (eV)	3.6 - 4.1	3.9	4.05-4.5
Band gap $E_g$ (eV)	0.3 - 1.4	1.6-1.7	1.12
$N_C (cm^{-3})$	$9 \times 10^{17} \text{ to } 1 \times 10^{21}$	0	$3 \times 10^{19}$ to $3 \times 10^{21}$
$N_V (cm^{-3})$	$9 \times 10^{17} \text{ to } 1 \times 10^{21}$	0	$3 \times 10^{19}$ to $3 \times 10^{21}$
$\mu_n \ (cm^2V^{-1}s^{-1})$	2732	20	1104
$\mu_p \ (cm^2 V^{-1} s^{-1})$	1565	5	420
$N_A$ $(cm^{-3})$	0	0	$1 \times 10^{16}$ to $1 \times 10^{19}$
$N_D (cm^{-3})$	$2 \times 10^{12}$ to $8 \times 10^{17}$	0	0
$V_e (cm s^{-1})$	$1 \times 10^7$	$1 \times 10^7$	$1 \times 10^{7}$
$V_h (cm s^{-1})$	$1 \times 10^7$	$1 \times 10^7$	$1 \times 10^7$
Layer density $(g cm^{-1})$	2.328	2.328	2.328
Auger electron	0	0	$2.20 \times 10^{-31}$
recombination			
coefficient $(cm^6s^{-1})$			
Auger hole	0	0	$9.90 \times 10^{-31}$
recombination			
coefficient $(cm^6s^{-1})$			
Band- to- band	0	0	$9.50 \times 10^{-15}$
recombination			
coefficient $(cm^3s^{-1})$			
Defect type	Conduction tail	Single	Valence tail
Defect charge	Donor	Acceptor	Acceptor
Total defect density $(cm^{-3})$	$1 \times 10^{14}$	$2.75 \times 10^{16}$	$1 \times 10^{10}$
Specific defect density $(cm^{-3} eV^{-1})$	$6.67 \times 10^{14}$	$2.75 \times 10^{16}$	$1.43 \times 10^{11}$
Defect level energy	0.15 (Urbach)	0.6	0.07 (Urbach)
(eV)	0.13 (010acii)	0.0	0.07 (0100011)
Electron and hole	$1 \times 10^{-14}$	$7\times10^{-19}$	$1 \times 10^{-14}$
capture cross section $(cm^{-2})$			
Optical properties	n = 1.4, k = 0.75	a-Si nk	c-Si nk (default)
Option properties	п 1.7, к 0.75	(default)	o of fix (default)



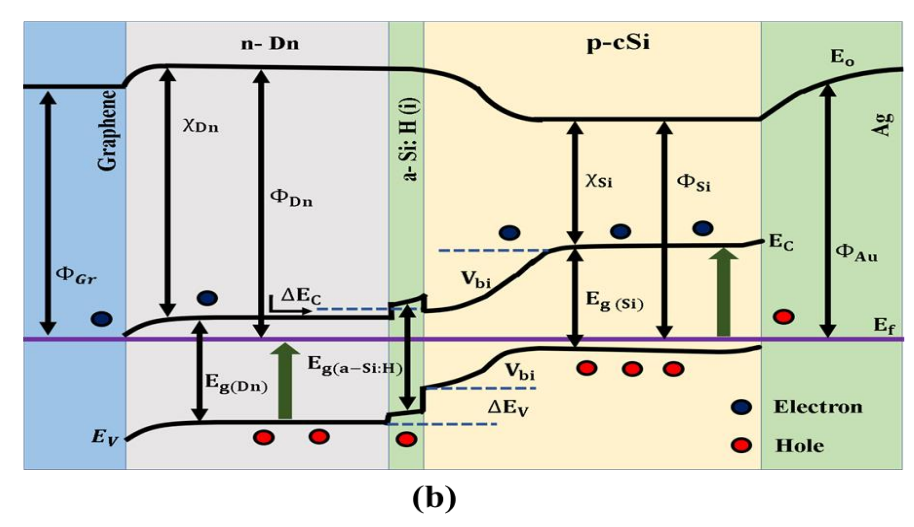


**Fig. 4.1** (a) Schematic of the designed HIT module. (b) Energy band diagram for the designed HIT structure showing separation of charges at the interfaces.

When the cell is operated under these conditions an amount of light or photon flux is get absorbed by the upper-bandgap of the semiconductor layer which creates electron-hole pairs and to calculate this upper-bandgap generation rate  $G_n = G_p\left(\frac{hc}{\lambda} \geq E_g\right)$  Lambert-Beer absorption optical model has been chosen [17] which specifies the reflectivity of the semiconductor and calculates the resulting absorption within the semiconductor layer by using only the specified values of extinction coefficient  $k(\lambda)$ . In this model, the generation rate  $G_n$  is calculated from the resulting absorption, integrating over the entire incident wavelength range. There are some models to describe the recombination in semiconductors, in a diamane layer, the recombination is described by Shockley-Read-Hall recombination model [Sze & Kwok, 2007]. In p-cSi semiconductor, dangling bond recombination model is used to describe the recombination [Sah & Shockley, 1958]. The

structure designed as Graphene (TCE) / n-Dn / a-Si: H(i) / p-cSi / Ag is displayed in Fig. 4.1 (a). Amorphous and crystalline silicon solar cell technologies are used to design it [23]. Single-layer graphene is chosen as the front contact or transparent conducting electrode, which allows maximum photon flux to pass through it, and no internal and external reflection is chosen for this layer to avoid efficiency loss at the front contact of the cell. The front surface is textured by anisotropic etching to reduce reflection [5]. Additionally, no mismatching between the layers of the cell is considered. An ideal 2D semiconductor follows to, condition  $< t > \le \lambda_F$ , where  $\lambda_F$  is the Fermi wavelength given by  $\sqrt{\frac{2\pi}{n_{2D}}}$  nm here  $n_{2D}$  is the carrier density in cm<sup>-2</sup> [24]. It is reported that graphene does not satisfy this condition [25] and the interlayer space increases due to doping [26]. Therefore, both diamane and graphene are considered quasi 3D in nature despite being considered 2D. To improve J<sub>SC</sub>, the quantum confinement is accomplished by controlling the number of layers of diamane and the carrier transport is taken along the c-axis. To avoid the efficiency losses due to defects present on the surface of p-cSi layer, an intrinsic hydrogenated amorphous silicon layer is inserted on the p-cSi layer, which develops a pn heterojunction. This intrinsic silicon passivates the defects of crystalline silicon, which reduces the chances of tunnelling through the localised states present on the doped crystalline silicon due to defects, which makes Voc decrease. In this manner, the passivation of intrinsic amorphous silicon just improved Voc and consequently the efficiency of the HIT solar cell and gives an excellent temperature coefficient. The intrinsic amorphous silicon also reduced dangling bonds and recombination rate, which also became the reason for improved V<sub>OC</sub> [27]. No thermal losses are considered as the deposition is done by CVD under low temperature [28]. An insulating SiO<sub>2</sub> layer is used to avoid surface recombination between the front contact and silicon layer, as shown in Fig. 4.1(a). For diamane layer donor concentration, effective conduction and valence band density, band gap, electron affinity, dielectric constant and layer numbers are being optimized by keeping the parameters of remaining layers to some specified values. For the intrinsic hydrogenated amorphous silicon layer, the parameters which have been optimized are; N<sub>C</sub>/N<sub>V</sub>, E<sub>g</sub> and thickness of the thin intrinsic layer. Further, the optimized parameters in the case of p-cSi are: N<sub>A</sub>, N<sub>C</sub>/N<sub>V</sub>, χ, thickness of the p-cSi wafer. Layer number as well as work function of graphene layer is also being optimized as well as the

material and work function of front and back contact have also been optimized. The details of front and back contacts as well as the details of all three optimized layers are tabulated in Tables 4.1 and 4.2.

**Table 4.3** List of parameters used at interfaces.

Interface	Model applied
Graphene/n-Dn	MS-Schottky contact
n-Dn/a-Si:H (i)	Drift diffusion model
a-Si:H (i)/p-cSi	Drift diffusion model
p-cSi/Ag	MS-Schottky contact

#### 4.2.2 Junction formation

In n-Dn /p-cSi heterojunction, the diamane and crystalline silicon interface plays main role in the conversion of energy. When n-diamane and p-cSi comes in contact, which has a work-function difference, then the electrons in the silicon layer get depleted and the energy band gets bent close to the Fermi level to form a built-in electric field. The energy band diagram is shown in Fig. 4.1(b). The built-in potential further separates the excess electrons and holes generated by the light incident and then converts light energy into electrical energy in the form of current flows in the external circuit. The built-in potential  $(eV_{bi})$  is given by;

$$(eV_{bi}) = E_{g(Dn)} + \Delta E_V + kT \ln \left( \frac{N_A N_D}{N_{V(Si)} N_{C(Dn)}} \right)$$

$$= E_{g(Si)} - \Delta E_C + kT \ln \left( \frac{N_A N_D}{N_{V(Si)} N_{C(Dn)}} \right)$$
(4.3)

Where, e is the electric charge,  $E_g$ ,  $\Delta E_V$  and  $\Delta E_C$  are the bandgap, valence band offset and conduction band offset, respectively and k, T are Boltzmann constant, temperature [K].  $N_A$  and  $N_D$  are the acceptor and donor concentration, and  $N_C$  and  $N_V$  are the conduction and valence band density, respectively [9].

At the graphene/diamane interface there Schottky junction is formed and a barrier for the transportation of hole is built corresponding to the potential energy of eV<sub>bi</sub> given by;

$$eV_{bi} = e(\phi_{Dn} - \phi_{Gr}) \tag{4.4}$$

where  $\varphi_{Dn}$  and  $\varphi_{Gr}$  are the work-function of diamane and graphene, respectively [29]. Since the work-function of the graphene layer can be modulated between 4.5 eV and 4.9

eV [7, 30], then with a large work-function, the built-in potential gets amplified at the junction, which consequently, increases the capacity of collecting the photo-generated charge carriers of the heterojunction. The shift in the Fermi level of graphene at heterojunction graphene/diamane performs better in conduction [31]. Since the dangling bonds over the p-cSi layer degrade the V<sub>OC</sub> and also the efficiency of the solar cell, therefore a perfect passivation is required to improve the overall efficiency. For this type of passivation, an intrinsic hydrogenated amorphous silicon wafer is pressed between the heterojunction n-Dn / p-cSi which successfully prevents the tunnelling through localised states present in p-cSi layer because of the presence of many defects and decreases the recombination rate and hence improves the efficiency of the HIT solar cell.

#### 4.3 Results and discussion

#### 4.3.1 Optimization of diamane layer

In this section, the influence of various parameters of n-type diamane on the performance of the HIT solar cell has been examined. To do so, the very first parameter we optimized here is the N<sub>D</sub> of the n-type diamane layer while keeping the remaining parameters at some viable values, and the results are shown in Fig. 4.2 (a and b). The values of parameters used for diamane are taken from the previous literature [32-35]. The a-Si: H (i) layer (3nm thick) and c-Si layer (500µm thick) are kept constant at values given in Table 4.4. The range in which  $N_D$  is being varied is  $2 \times 10^{12}$  cm<sup>-3</sup> -  $8 \times 10^{17}$  cm<sup>-3</sup>, and it is noticed from Fig. 4.2 (a and b) that V<sub>OC</sub>, J<sub>SC</sub>, FF and η remained almost constant during the optimization. There is a very slight change observed in the case of FF only. The FF is infinitesimally increased from 83.95 % to 83.96 % as the value of N<sub>D</sub> increased from  $6\times10^{17}~\text{cm}^{-3}$  -  $8\times10^{17}~\text{cm}^{-3}$ . Therefore, the optimum donor concentration for n-Dn is  $8\times10^{17}$  cm<sup>-3</sup>. The reason behind the constant value of  $V_{OC}$  (698 mV) is that it does not depend on N<sub>D</sub> until and unless it does not follow the condition  $\Delta n_0 \gg N_D$ , where  $\Delta n_0$ denotes the excess electron-hole pairs [36]. J<sub>SC</sub> remained constant during the optimization at 53.04 mA/cm<sup>2</sup>, this is because, as we increase the donor concentration mobility of photo-generated charge carriers does not change and therefore there is not slight change observed in the value of J<sub>SC</sub> as shown in Fig. 4.2 (b). Since there is observed no variation in the values of  $V_{OC},\,J_{SC}$  and FF on increasing  $N_D$  within the range  $2\times10^{12}$  cm  $^{\!-3}$  -  $8\times10^{17}$ 

cm<sup>-3</sup> therefore, the value of efficiency will also remain the same at 31.08 % as shown in Fig. 4.2 (a). The best optimized value of  $N_D$  we have noticed here is  $8\times10^{17}$  cm<sup>-3</sup>, which we will keep constant throughout the further optimization of the HIT cell.

**Table 4.4** List of initially taken values of parameters.

Parameter	a-Si: H (i)	p-cSi
Thickness	3 (nm)	500 μm
Dielectric constant $(\varepsilon_r)$	11.9	11.9
Electron affinity $\chi$ (eV)	3.9	4.05
Band gap $E_g$ (eV)	1.6	1.12
$N_C (cm^{-3})$	$2 \times 10^{21}$	$3 \times 10^{19}$
$N_V (cm^{-3})$	$2 \times 10^{21}$	$3 \times 10^{19}$
$N_A (cm^{-3})$	0	$1 \times 10^{19}$
$N_D (cm^{-3})$	0	0

After getting the best optimized value of N<sub>D</sub> for the designed HIT solar cell, we will now further optimize the parameter conduction and valence band density (N<sub>C</sub>/N<sub>V</sub>) in the range from  $9\times10^{17}$  cm<sup>-3</sup> to  $1\times10^{21}$  cm<sup>-3</sup> and the result obtained is shown in Fig. 4.2 (c and d). From the Figure, it is observed that, as the value of N<sub>C</sub>/N<sub>V</sub> is increased in the chosen limit there is a continuous decrement in the value of  $V_{OC}$  from 699.7mV to 580.6 mV, this is because of the reduction in barrier height, which offers fewer charge carriers near the junction. As a result, a small built-in potential is formed near the junction, resulting in lower  $V_{OC}$ . The value of  $J_{SC}$  is found to be constant at 53.04 mA/cm<sup>2</sup> as  $N_C/N_V$  goes from 9×10<sup>17</sup> cm<sup>-3</sup> to 3×10<sup>19</sup> cm<sup>-3</sup> and then starts decreasing and reaches 52.97 mA/cm<sup>2</sup> at  $1\times10^{21}$  cm<sup>-3</sup>. The reason behind the J<sub>SC</sub> being constant may be the decrease in the minority carrier density which probably declines due to the short life-time of photogenerated charge carriers and trapping of free charge carriers across the interface. Another reason behind the constant value of J<sub>SC</sub> can be the recombination of photogenerated charge carriers across the interface due to which these new photogenerated charge carriers do not play an active role in the process. On further increasing the value of  $N_C/N_V$ , the barrier height decrease according to Eqn. (4.3) and therefore J<sub>SC</sub> decreased after N<sub>C</sub>/N<sub>V</sub> reached  $3\times10^{19}$  cm<sup>-3</sup>. These reductions in the values of  $V_{OC}$  and  $J_{SC}$  could be the reason for the reduction in the values of FF and  $\eta$  from 84.06 % to 79.71 % and 31.2 % to 24.51 %,

respectively. In this way  $9\times10^{17}$  cm<sup>-3</sup> is the optimum value of  $N_C/N_V$  where we got maximum efficiency 31.2 %.

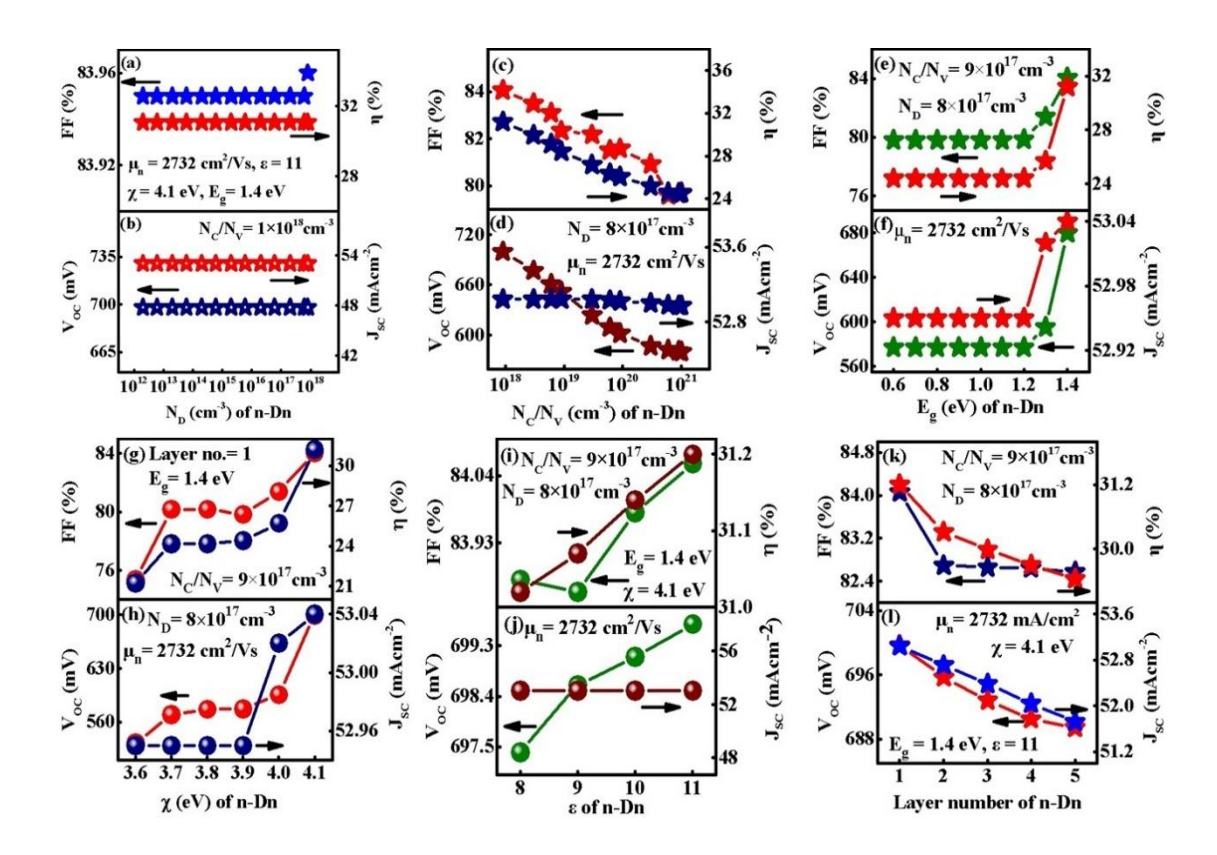


**Fig. 4.2** Simulation of diamane layer by keeping the parameters of remaining layers at values given in Table 4.4. (a and b) optimization of  $N_D$  (cm<sup>-3</sup>), (c and d) optimization of  $N_C$  (cm<sup>-3</sup>), (e and f) optimization of  $E_g$  (eV), (g and h) optimization of  $\chi$  (eV), (i and j) optimization of  $\varepsilon_r$ , (k and l) optimization of layer numbers of diamane by keeping its other parameters at optimum set of values.

After optimizing the parameters  $N_D$  and  $N_C/N_V$ , the next parameter we have optimized here is the bandgap of the n-type diamane layer within the range 0.3 eV to 1.4 eV and the results obtained are displayed in Fig. 4.2 (e and f). It is observed from the figure that, as the bandgap increased from 0.3 eV to 1.1 eV, no variation is found in the values of  $V_{OC}$ ,  $J_{SC}$ , FF, and  $\eta$ , they remained constant at 577.1 mV, 52.95 mA/cm<sup>2</sup>, 79.8 % and 24.38 %, respectively. On further increasing the range of bandgap from 1.2 eV to 1.4 eV, the values of all these parameters get increase because of the increment in the barrier height according to Eqn. (4.1) as increased  $V_{bi}$  separates the photogenerated charge carriers very

effectively across the interface and hence increases the value of  $J_{SC}$ . In this way, the best efficiency, 31.2 % was found at the bandgap 1.4 eV.

The next parameter after  $N_D$ ,  $N_C/N_V$  and bandgap, we have simulated the electron affinity of the diamane layer within 3.6 eV- 4.1 eV and the results are shown in Fig. 4.2 (g and h). On increasing electron affinity, barrier height increases resulting in increment in the value of  $V_{OC}$  from 532.8 mV to 699.7 mV, higher barrier height increases the minority charge carriers which consequently increase the current density from 52.95 mA/cm<sup>2</sup> to 53.04 mA/cm<sup>2</sup>, and therefore the FF and the efficiency also get increased from 75.35 % to 84.06 % and 21.25 % to 31.2 %, respectively as shown in Fig. 4.2 (g and h).

The optimization of the parameter, dielectric constant ( $\epsilon_r$ ) of the diamane layer is shown in Fig. 4.2 (i and j). We have optimized the value of dielectric constant within the values 8 to 11. It is observed from the figure that, as the dielectric constant increases from 8 to 11,  $V_{OC}$  and efficiency get increase from 697.4 mV to 699.7 mV and from 31.02 % to 31.2 % respectively, as efficiency was found largely dependent on  $V_{OC}$ . The reason behind the increment of  $V_{OC}$  is the more electron-hole pair generation in the diamane layer on increasing dielectric constant according to the Coulomb's law;  $F \propto \frac{1}{\epsilon_r}$ , where F is the electrostatic force between the electrons and holes [29]. From the Figure it is found that  $J_{SC}$  is constant at 53.04 mA/cm² throughout the variation of relative permittivity and FF is slightly increased from 83.87 % to 84.06 %. Therefore, the maximum efficiency of 31.2 % we obtained at dielectric constant ( $\epsilon_r$ ) value of 11.

After optimizing various parameters as mentioned above, the number of diamane layers was optimized to see its effect on the working of the HIT solar cell. The layers were varied up to 5 and the result obtained is shown in Fig. 4.2 (k and l). As the layers number increased, the transmittance decreased [9], which raise difficulty for photons in reaching the junction, and therefore the electron-hole pair generation rate decreased which resulting in poor efficiency. Therefore, Voc decreased from 699.7 mV to 689.4 mV, Jsc decreased from 53.04 mA/cm² to 51.72 mA/cm² and efficiency decreased from 31.2 % to 29.44 % as the number of layers increased from 1 to 5. Since the sheet resistance decreases on increasing the number of layers. Therefore, the value of FF also gets reduced from 84.06 % to 82.57 % as shown in Fig. 4.2 (k). In this way, maximum efficiency of 31.2 % was achieved at a single layer diamane.

#### 4.3.2 Optimization of a-Si: H(i) layer

Since an extremely high-quality thin a-Si: H(i) layer plays the main role in proving HIT solar module better than a general heterojunction solar cell module, because it passivates the defects present in the silicon layer, which causes the poor conversion efficiency of heterojunction solar cells. The placing of a thin a-Si: H(i) layer enhances V<sub>OC</sub> because it decreases the interface recombination velocity [23,27]. This thin layer also contributes in the depletion region, drift current and electric field strength as well [37]. Therefore, it became essential to inspect the effect of optimizing the parameters of this thin layer on the working of HIT solar cell. To do this simulation, the optimized parameters of diamane layer are used, and the parameters of p-cSi and the remaining parameters of a-Si: H (i) are kept at their initial taken values. To do so, we first have optimized the effective conduction and valence band density  $(N_C/N_V)$  of a-Si: H(i). We have optimized  $N_C/N_V$  in the range  $1.5 \times 10^{21}$  cm<sup>-3</sup> -  $3 \times 10^{21}$  cm<sup>-3</sup> by keeping the thickness of a-Si: H(i) at 3 nm and bandgap at 1.6 eV. The obtained results are depicted in Fig. 4.3 (a and b). It is noticed from the figure that on increasing the value of N<sub>C</sub>/N<sub>V</sub>, V<sub>OC</sub> and J<sub>SC</sub> remain constant at 699.7 mV and 53.04 mA/cm<sup>2</sup>. The value of FF gets slightly increased from 84.04 to 84.06 and therefore there was certainly tiny increment observed in the value of efficiency also, it increased from 31.19 % to 31.20 % which is a really tiny increment. Therefore, the optimization of the parameter N<sub>C</sub>/N<sub>V</sub> of a-Si: H(i) does not seem to have any major effect on the efficiency of the HIT solar module and the maximum efficiency of 31.2 % was obtained in the range  $1.5 \times 10^{21}$  cm<sup>-3</sup> -  $3 \times 10^{21}$  cm<sup>-3</sup>.

By assigning a value  $2\times10^{21}$  cm<sup>-3</sup> to the N<sub>C</sub>/N<sub>V</sub> we further have optimized the bandgap of a-Si: H(i) at two values, 1.6 eV and 1.7 eV, and the results are shown in Fig. 4.3 (c and d). From Fig. it is noticed that on increasing the bandgap from 1.6 eV to 1.7 eV, V<sub>OC</sub> get decreased from 699.7 mV to 696.3 mV. The values of J<sub>SC</sub>, FF and efficiency were also decreased from 53.04 mA/cm<sup>2</sup> to 53.02 mA/cm<sup>2</sup>, 84.06 % to 82.43 % and 31.2 % to 30.43 %, respectively. The deterioration in the value of J<sub>SC</sub> is because the number of photons which get absorbed only when their energy is less than the bandgap of intrinsic hydrogenated amorphous layer, decreases. This decrement in the absorbed photon numbers leads to a decrease in the number of electron-hole pairs, which consequently decreases J<sub>SC</sub>. For the better performance of the HIT solar cell, 1.6 eV is the best optimized bandgap for a-Si: H(i) at which efficiency is maximum 31.2 % as shown in Fig

4.3 (c). This may be because of the absorbed photons by the diamane layer corresponding to the bandgap value of a-Si: H(i) layer [9].

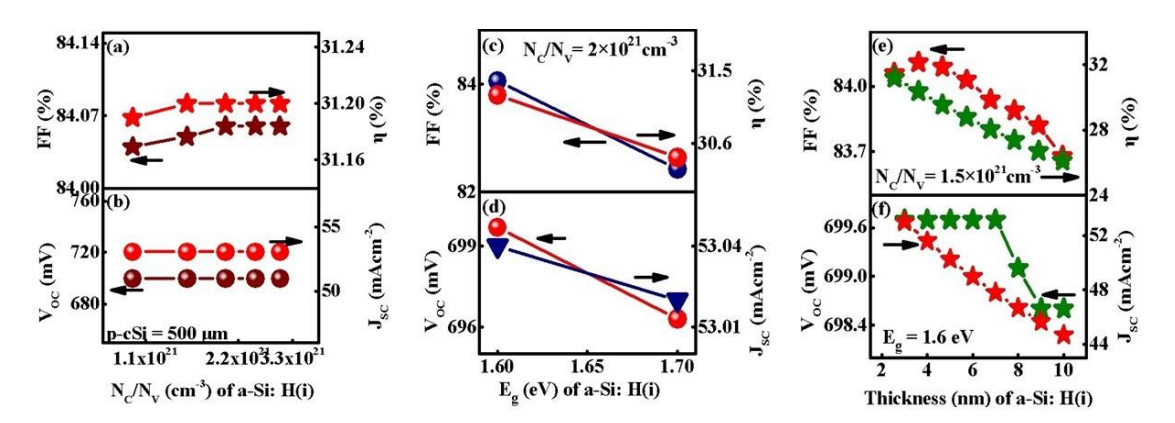


**Fig. 4.3** Simulation of a-Si: H (i) at optimized diamane and other layers at the previous set of values (Table 4.4). (a and b) optimization of  $N_C/N_V$  (cm<sup>-3</sup>), (c and d) optimization of  $E_g$  (eV), (e and f) optimization of thickness (nm).

After getting our best optimized values of N<sub>C</sub>/N<sub>V</sub> and bandgap for a-Si: H(i), next we have optimized the thickness of a-Si: H(i) which majorly effects the performance of HIT solar cell module. The thickness of a-Si: H(i) is optimized between 3 nm to 10 nm and the obtained results are shown in Fig. 4.3 (e and f). As the thickness increases from 3 nm to 7 nm V<sub>OC</sub> remains constant at 699.7 mV, but as the thickness increases further it decrease from 699.7 mV to 698.6 mV as shown in Fig. 4.3 (f). This happens because as the thickness of amorphous layer increases more dangling bonds will affect the efficiency of the solar cell, as more photogenerated charge carriers get trapped by these dangling bonds which causes the deterioration of V<sub>OC</sub> [27]. The J<sub>SC</sub> was also found to decreases from 53.04 mA/cm<sup>2</sup> to 44.67 mA/cm<sup>2</sup> as shown in Fig. 4.3 (f). This decrement in the value of J<sub>SC</sub> is because of the increased sheet resistance in thicker intrinsic layer [9]. The FF decrease from 84.06 % to 83.68 % which consequently leads to the decrease in the conversion efficiency from 31.2 % to 26.11 % on increasing the thickness from 3 nm to 10 nm, results are shown in Fig. 4.3 (e). Therefore, on increasing the thickness of the a-Si: H (i) layer the power conversion efficiency of the HIT solar cell decreases. In this way, the best optimized efficiency is achieved at the thickness 3 nm shown in Fig. 4.3 (e). The passivation is done by using the high quality thinnest possible intrinsic hydrogenated amorphous silicon layer in HIT structured solar cells.

#### 4.3.3 Optimization of p-cSi layer

Since, an intrinsic amorphous silicon layer is introduced in between two doped layers of diamane and crystalline silicon like; Graphene (TCE) / n-Dn / a-Si: H(i) / p-cSi / Ag displayed in Fig. 4.1 (a) therefore, the processing of c-Si layer of achieving good efficiency get improved as the effective lifetime of the cell becomes lower which improves efficiency with higher Voc. The inserted intrinsic layer basically passivates crystalline silicon layer, which drastically changes the working principle of c-Si wafer or active layer, which affects the power conversion efficiency of the HIT structured solar cell in a positive way. This passivation improves the efficiency of cell in a such a way that the active layer effectively separates the generated charge carriers which reduce the recombination velocity at the interface and improve Voc. This improved Voc then improved the efficiency and temperature coefficient of the HIT solar cell [38]. If the recombination velocity is low as in the case of HIT solar cells, then it becomes easy for a thinner silicon wafer to maintain excess carrier density and that is how  $V_{\text{OC}}$  improves [28] and more cost-effective solar cell is achieved. In this section, we have discussed the effect of optimization of the parameters of the p-cSi wafer on the power conversion efficiency of HIT structured solar cell. While doing the simulation up on the p-cSi wafer the parameters of n-Dn layer and a-Si: H(i) layer was fixed to their best optimal values. For doing so, initially we have simulated the acceptor concentration N<sub>A</sub> of p-cSi wafer in the rage  $1\times10^{16}$  cm<sup>-3</sup> to  $1\times10^{19}$  cm<sup>-3</sup> and the results are depicted in Fig. 4.4 (a and b).  $V_{OC}$ , J<sub>SC</sub>, FF and η was found to increase from 622.6 mV to 699.7 mV, 39.88 mA/cm<sup>2</sup> to 53.04 mA/cm<sup>2</sup>, 83.06 % to 84.06 % and 20.62 % to 31.2 %, respectively. The improvement in the value of V<sub>OC</sub> is because of the increment of barrier height on increasing the acceptor concentration according to Eqn. (4.3). Since the higher eV<sub>bi</sub> deteriorates the recombination rate due to which photo-generated charge carriers move rapidly from the depletion region to the contact region and no trapped effect is experienced by the carriers in the neutral region [9,39]. Therefore, J<sub>SC</sub> get increased which reduces the sheet resistance; consequently, FF increases. The increment in these parameters leads to an increased efficiency. In this way, the maximum efficiency of 31.2 % was obtained at N<sub>A</sub>  $1 \times 10^{19} \text{ cm}^{-3}$ .

After obtaining the best optimized value of  $N_A$ , we have optimized the value of  $N_C/N_V$  of p-cSi layer from  $3\times10^{19}$  cm<sup>-3</sup> to  $3\times10^{21}$  cm<sup>-3</sup> and the results are shown in Fig. 4.4 (c and

d). From Figure it is shown that, as  $N_C/N_V$  increases  $V_{OC}$  decreases linearly from 699.7 mV to 485.6 mV. It is because according to Eqn. (4.1), barrier height decreases as  $N_V$  of p-cSi increases which makes  $V_{OC}$  to decrease. The value of  $J_{SC}$  was found to remained constant at 53.04 mA/cm<sup>2</sup> as we go from  $3\times10^{19}$  cm<sup>-3</sup> to  $3\times10^{21}$  cm<sup>-3</sup> this might be because of the recombination and trapping of carriers across the interface. The FF on increasing the  $N_C/N_V$  gets decrease from 84.06 mA/cm<sup>2</sup> to 79.15 mA/cm<sup>2</sup> which leads to decrease the efficiency from 31.2 % to 20.39 %. Therefore, the optimum value of  $N_C/N_V$  for p-cSi wafer is  $3\times10^{19}$  cm<sup>-3</sup>.

The next parameter to get optimized in this report after optimizing  $N_A$  and  $N_C/N_V$  of p-cSi layer is the electron affinity of p-cSi layer. The electron affinity we have optimized in the range from 4.05 eV to 4.5 eV and the desired results are depicted in Fig. 4.4 (e and f). The figure shows that on increasing the  $\chi$ ,  $V_{OC}$  decreased from 699.7 mV to 604.7 mV and FF decreased from 84.06 % to 49.52 % and therefore the efficiency also dropped from 31.2 % to 15.89 %. The reason behind this deterioration is may be the variation in the work-function of p-cSi layer which consequently reduces the transportation of the charge carriers across the p-cSi layer. This reduction in the transportation rate of charge carriers through the p-cSi layer increase the series resistance in the p-cSi layer due to which FF and  $\eta$  decreased. A tiny increment was observed in the value of  $J_{SC}$  from 53.04 mA/cm<sup>2</sup> to 53.05 mA/cm<sup>2</sup> as shown in Fig. 4.4 (f).

Since, in this report we have simulated the result keeping in mind to reduce the production cost of solar cell therefore the next parameter we have optimized here is the thickness of p-cSi wafer because the thickness of p-cSi wafer enhanced the manufacturing cost of solar cell. So, we have simulated the keeping the thickness of p-cSi wafer within the range of 50  $\mu$ m to 300  $\mu$ m and the result is shown in Fig. 4.4 (g and h). As we increase the thickness, the V<sub>OC</sub> does not change at all and it remains uniform throughout, maintaining the value 699.7 mV as shown in Fig. 4.4 (h). As the thickness increases, photogenerated charge carriers increase but at the same time, the recombination and trapping of these charge carriers also increase due to the defects present in the p-cSi layer, which restricts the V<sub>OC</sub> either to get increased or decreased therefore it remains constant as the thickness increases. Further, J<sub>SC</sub> was found to slightly increase from 52.89 mA/cm<sup>2</sup> to 53.04 mA/cm<sup>2</sup> as the thickness increased. This is because of the increased photogenerated charge carriers on increasing the thickness of layer. The FF and  $\eta$  also get slightly

increased from 84.04 % to 84.06 % and 31.1 % to 31.2 %, respectively, as shown in Fig. 4.4 (g). The reduction in series resistance of the p-cSi layer may be the reason behind this small improvement in the value of FF [9]. Since HIT structure solar cell has a tendency of getting good efficiency even for thin silicon wafer therefore, the best efficiency of the solar cell is achieved at the thickness 90 µm which makes it comparatively less costly. After achieving the best optimized parameters of n-Dn, a-Si: H (i) and p-cSi layers, the cell then again simulated by optimizing the layer numbers of diamane and thickness of intrinsic amorphous silicon to see the effect of changing the layer number of n-Dn and the thickness of a-Si: H (i) wafer on the best simulated solar cell and the results are shown in Fig. 4.4 (i and j) and (k and l) respectively. From Fig. 4.4 (i and j) it is shown that, all the parameters such as  $V_{OC}$ ,  $J_{SC}$ , FF and  $\eta$  decreased as the number of diamane layers increased from 1 to 5. Voc decreased from 699.7 mV to 689.4 mV, J<sub>SC</sub> decreased from 53.04 mA/cm<sup>2</sup> to 51.71 mA/cm<sup>2</sup>, FF varied from 84.06 % to 82.57 % and efficiency decreased from 31.2 % to 29.44 %. This deterioration in the values of these parameters is because of the reduction of absorbed photons as the transmittance increases on increasing the layers.

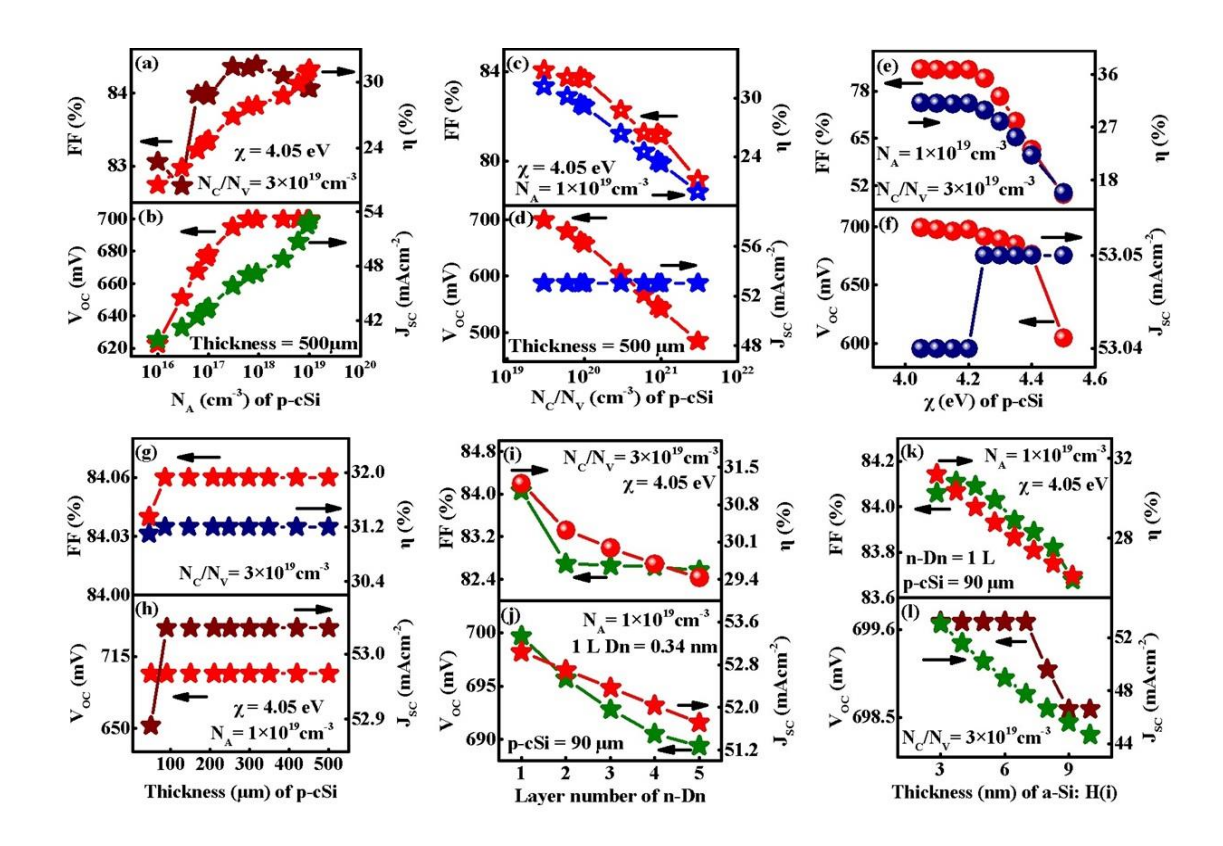


**Fig. 4.4** Simulation of p-csi layer at optimized diamane as well as a-si: H (i) layer. (a and b) optimization of  $N_A$  (cm<sup>-3</sup>), (c and d) optimization of  $N_V$  (cm<sup>-3</sup>), (e and f) optimization of  $\chi$  (eV), (g and h) optimization of thickness ( $\mu$ m), (i and j) optimization of layer numbers of diamane at fully optimized cell, (k and l) optimization of thickness (nm) of a-Si: H (i) again at fully optimized cell.

From figure it is shown that as the thickness of a-Si: H (i) wafer increases from 3 nm to 10 nm the values of  $V_{OC}$ ,  $J_{SC}$ , FF and  $\eta$  decreases from 699.7 mV to 698.6 mV, 53.04 mA/cm<sup>2</sup> to 44.67 mA/cm<sup>2</sup>, 84.06 % to 83.68 % and 31.2 % to 26.11 % respectively. This happened probably because of addition of more dangling bonds and less excitations of charge carriers on increasing the thickness of intrinsic layer [40]. Minimum efficiency 26.11 % was seen at the thickness 10 nm and therefore the maximum efficiency of 31.2 % was achieved for 3 nm thick a-Si: H (i) layer.

#### 4.3.4. Optimization of the TCE (graphene) parameters

In this section, we have optimized the work-function as well as the layer numbers of graphene, which is used as a transparent conducting electrode in the present article. It is now well established that graphene can be transferred on another substrate by using a chemical route [41]. To study the influence of the work function and layer numbers of graphene layer (TCO) on the efficiency of solar cell we have varied the layer from 1 to 5 and the work function in the range from 4.3 eV to 4.9 eV and the results are shown in Fig. 4.5 (a and b) and (c and d) respectively. From Fig. 4.5 (a and b) it is shown that, as the layer numbers increases from 1 to 5 where the thickness of single layer graphene is 0.334 nm and the external reflection, we have considered zero for single layer graphene, the value of  $V_{OC}$  decreased from 699.7 mV to 111.4 mV and  $J_{SC}$  decreased from 53.04 mA/cm<sup>2</sup> to 48.02 mA/cm<sup>2</sup>. The FF and the efficiency also decreased from 84.06 % to 49.97 % and from 31.2 % to 2.672 % as shown in Fig. 4.5 (a and b). The reason behind this decrement in the value of efficiency is that as the layer number increases the reflection coefficient of the graphene layer increases which opposes the photons from entering into the cell and therefore the efficiency gets decline. Fig. 4.5 (c and d) shows that, on increasing the work function of the graphene layer at single layer diamane and graphene at 90 µm thickness of c-Si layer, the V<sub>OC</sub> decreases from 699.7 mV to 114.3 mV on increasing the work function of graphene from 4.30 eV to 4.90 eV. J<sub>SC</sub> decreases very slightly from 53.04 mA/cm<sup>2</sup> to 53.01 mA/cm<sup>2</sup>. Furthermore, a noticeable decrement in

the value of fill factor is also noticed from 84.06 % to 50 % while increasing the value of work function from 4.30 eV to 4.90 eV. As a result, the overall efficiency of the HIT cell decreased from 31.2 % to 3.028 % as work function decreased the considered range of values. The deterioration in the value of V<sub>OC</sub> on increasing the work function of the graphene layer is maybe due to the reduction of the potential barrier energy eVbi of graphene/n-Dn following Eqn. (4.4). It is also reported that if the work function of TCO in the case of Si HIT cells, is low then the direction of eV<sub>bi</sub> of TCO/n-type emitter and ntype emitter/p-type Si will be in the same direction [9]. Conversely, if the work function of TCO is high then eV<sub>bi</sub> of TCO/n-type emitter will be in the opposite direction that of n-type emitter/p-type Si [9]. Furthermore, the increment in the work function of the TCO in case of Si HIT cells causes the depletion in the emitter regions to gets wider which in results the overlapping of TCO/n- diamane emitter region and n-type emitter/p-cSi region coincide if the emitter layer is also not sufficiently thick [42]. Therefore, an increment in the work function of the graphene layer may increase the chances of overlapping between the graphene/n-type emitter depleted region and n-type emitter/p-cSi depleted region and subsequently an overall deterioration in the value of  $V_{OC}$  can be seen [9] from Fig. 4.5 (d). The reason for  $J_{\text{SC}}$  being decreased can be understood by the fact that on increasing the work function of graphene layer, since the depletion region of graphene/n-type emitter and n-type emitter/p-cSi gets overlap which causes the eV<sub>bi</sub> of n-Dn/p-cSi layer to get influenced or decreased which in turn reduces the built-in electric field and this poor electric field gets unable to push the photogenerated charge carrier to its respective electrode under short circuit condition. Therefore, the J<sub>SC</sub> gets declined as shown in Fig. 4.5 (d). Since, there is a decrement in the values of  $V_{\text{OC}}$  and  $J_{\text{SC}}$  is found therefore the overall efficiency and FF will also suffer and gets declines on increasing work function from 4.30 eV to 4.90 eV as shown in Fig. 4.5 (c). In this manner, the highest efficiency 31.2 % was achieved at the lowest value 4.30 eV of work function for pristine graphene. The optimization is further carried out to optimized value of work function and thickness of graphene layer for commercially available parameters of crystalline silicon layer and the results are shown in Fig. 4.5 (e and f) and (g and h), respectively. This optimization is carried at the single layer graphene and single layer diamane. During this optimization of graphene's work function the thickness of p-cSi is taken as 90 µm and for optimizing

the thickness of silicon layer, the best optimized work function 4.31 eV is considered as revealed from Fig. 4.5 (e and f) and (g and h), respectively.

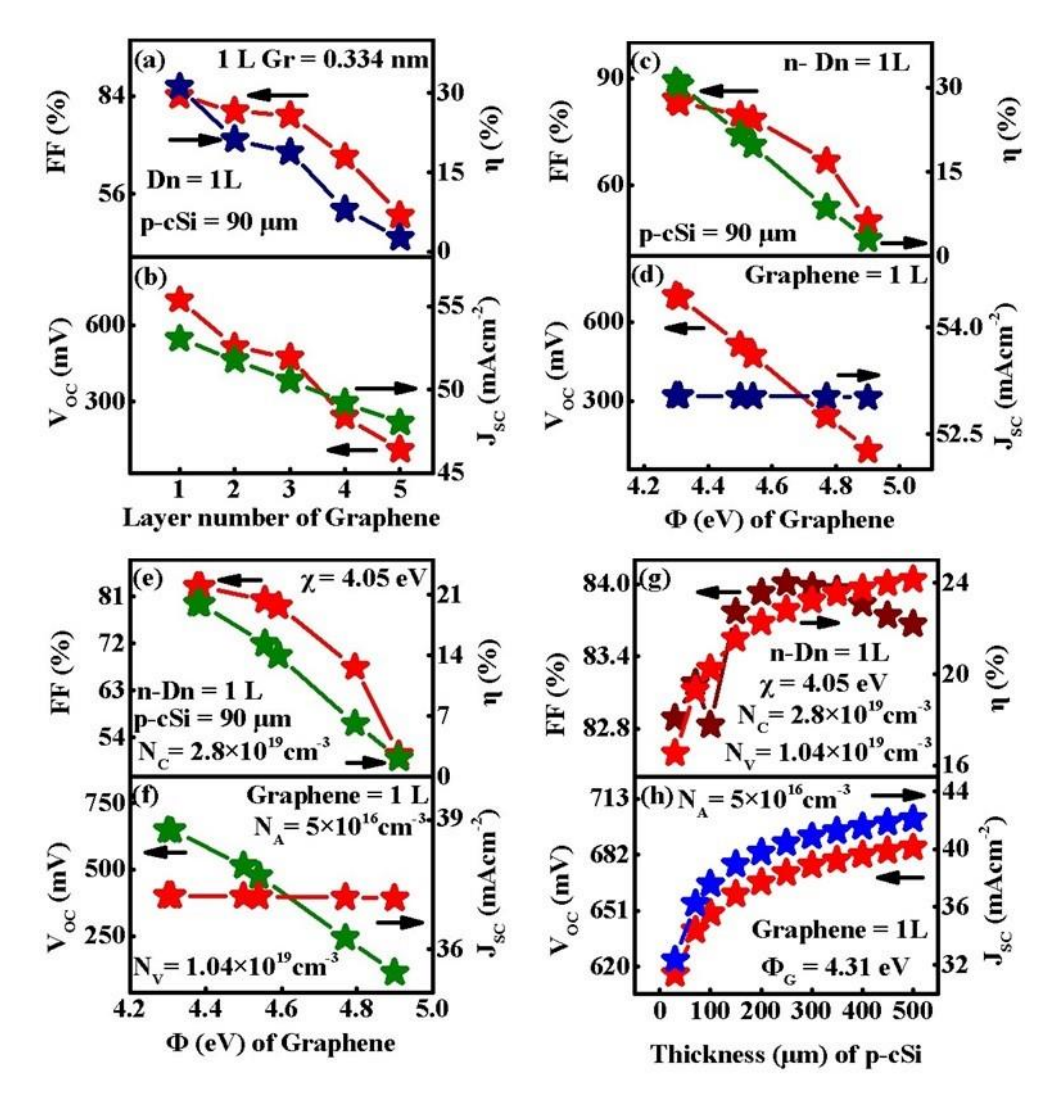


**Fig. 4.5** Simulation of graphene (TCE) at optimized cell. (a and b) optimization of layer numbers, (c and d) optimization of  $\varphi$  (ev) at single layer graphene, (e and f) optimization of  $\varphi$  (ev) of graphene layer by taking commercially available values of p-csi layer. (g and h) thickness of p-csi layer at single layer graphene with  $\varphi$  = 4.31 eV (other parameters of p-cSi layer are at a practically available set of values).

We have extended this work to validate the best simulated results and to make a comparison at all best optimized parameters of diamane and a-Si: H (i) and the commercially available data of p-cSi layer is picked from the available literature [43]. From Fig. 4.5 (e and f) it is shown that, the maximum efficiency of 19.98 % is achieved at the smaller value of work-function 4.30 eV as we increase it from 4.30 eV to 4.9 eV.

This indicates that as the work function of graphene layer increased the efficiency decreased in the same manner as happened for our best optimized results, shown in Fig. 4.5 (c and d) and the best optimized value of work function 4.30 eV in Fig. 4.5 (e and f) is also so close to the best optimized results, Fig. 4.5 (c and d). In the same manner, it is found from Fig. 4.5 (g and h) that the maximum efficiency 24.15 % is obtained for 500 µm thickness of p-cSi layer which is also valid for the best optimized cell as shown in Fig. 4.4 (g and h).

#### 4.3.5. Optimization and simulation of front and back contact material

To investigate the effect of the material selected as the front contact and the back contact on the performance or efficiency of the photovoltaic cell, we have further done the simulation by varying the material used as the front and back contact and its parameters. The simulation is done at the fully optimized cell with single layer diamane and 90  $\mu$ m thick p-cSi layer and the results are shown in Fig. 4.6.

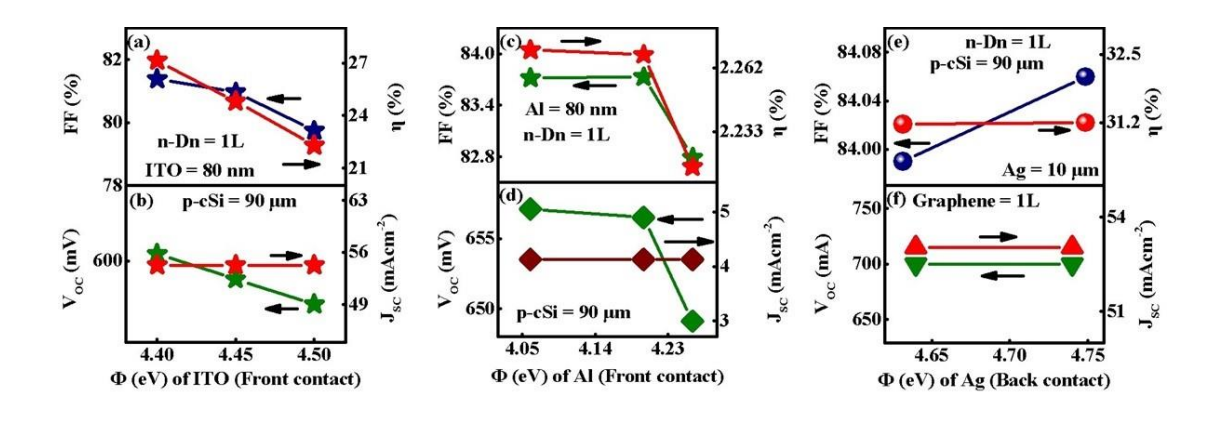


**Fig. 4.6** Simulation of front as well as back contact surfaces for final optimized cell. (a and b) optimization of the work function (eV) of ITO at thickness 80 nm, (c and d) optimization of work function (eV) of Al (front contact) at thickness 80 nm, (e and f) optimization of work function (eV) of Ag (back contact) at thickness 10  $\mu$ m.

A comparison has been made between the front contact materials: graphene, ITO and aluminium by varying their work function to find the optimum material with its optimum work function. The work function of graphene is already optimized in the above section of the report and we have found that the maximum efficiency 31.2 % is gained at work function 4.3 eV whereas, the maximum efficiency attained by ITO is 27.15 % at the work function 4.4 eV and in case of Al the maximum attainable efficiency is found to be 2.27

% at 4.06 eV of work function as shown in Fig. 4.6 (a and b) and (c and d), respectively. The thickness of ITO was taken 80 nm and its work function is varied in the range 4.40 eV-4.50 eV [44] whereas, the work function of aluminium is varied within the range 4.06 eV-4.26 eV. These results clearly show that the optimum material for to use as the front contact is graphene with its work function of 4.3 eV. After deciding the optimum front contact material, the next optimization is carried out around the work function of the back contact Ag. The work function of Ag is varied from 4.64 eV and 4.74 eV and the thickness is considered as  $10 \, \mu m$ . The results are shown in Fig. 4.6 (e and f). It is seen from the Figure that, the  $V_{OC}$  and  $J_{SC}$  is constant at values  $699.7 \, \text{mV}$  and  $53.04 \, \text{mAcm}^{-2}$  as the work function is increased from the value 4.64 eV to 4.74 eV whereas, the value of FF

**Table 4.5** Crystalline silicon-based solar cells.

Study type	Structure Type	Area/Wafer Thickness	V <sub>oc</sub>	$J_{SC}$	FF	η	Ref.
Experim ental	ITO/Gr/ MoS <sub>2</sub> /n-	3 mm × 3 mm	590 mV	36.8 mA/cm <sup>2</sup>	73 %	15. 8	46
Experim ental	cSi/Ag TCO/p- aSi/(i) aSi:H/n- cSi/(i) aSi;H/n-	100.5 cm <sup>2</sup>	725 mV	39.09 mA/cm <sup>2</sup>	79.1 0 %	% 22. 30 %	47
Experim ental	aSi/TCO ITO/p- MoO <sub>x</sub> /(i) aSi:H/n- cSi/(i) aSi:H/n-	3.93 cm <sup>2</sup>	725.4 mV	38.60 mA/cm <sup>2</sup>	80.3 6 %	22. 50 %	48
Theoreti cal	aSi/ITO/Ag Ag/TCO/p- aSi/(i) aSi:H/n- cSi/(i) aSi:H/n- aSi/TCO/A	161 μm	747.1 mV	39.56 mA/cm <sup>2</sup>	84.9 8 %	25. 11 %	49
Theoreti cal	g Gr/n- MoS <sub>2</sub> /a- Si:H/p- cSi/Au	500 μm	697 mV	44.25 mA/cm <sup>2</sup>	82.9 5 %	25. 61 %	11

Experim ental	TCO/(i)aSi: H/n-cSi/(i) aSi;H/(n/p) aSi/Electrod	165 μm	744 mV	42.30 mA/cm <sup>2</sup>	83.8 0 %	26. 30 %	50
Experim ental	e TCO/(i)aSi: H/n-cSi/(i) aSi;H/(n/p) aSi/Electrod	180 cm <sup>2</sup>	740 mV	42.50 mA/cm <sup>2</sup>	84.6 0 %	26. 60 %	51
Theoreti cal	e Gr/n-Dn/a- Si:H(i)/p- cSi/Ag	90 μm	699.7 mV	53.04 mA/cm <sup>2</sup>	84.0 6 %	31. 20 %	Our Work

and efficiency are increased from 83.99 % to 84.06 % and 31.17 % to 31.2 %, respectively. Therefore, the maximum efficiency 31.2 % is achieved at the work function 4.74 eV. In this way, Ag is chosen as the back contact with optimum work function 4.74 eV.

Finally, to validate the method applied in our work, we have also simulated previously reported model as  $Gr/MoS_2/c$ -Si in [45] and we have attained an efficiency of 15.68 % with  $V_{OC} = 468$  mV,  $J_{SC} = 42.93$  mA/cm² and FF = 78.08 %. These results are found to be much convincing with the reported values of the conversion efficiency 15.8 %,  $V_{OC} = 590$  mV,  $J_{SC} = 36.80$  mA/cm² and FF = 73 %. Similarly, another evidence regarding this method has already been provided by our research group in their report [25] in which they have attained an efficiency of 9.81 % which was in close approximation of experimentally obtained results ( $\eta = 9.27$  %) [46]. Furthermore, to show the novelty of the presented work a comparison between our work and previously reported similar work on Si-based solar cells, along with their sizes and parameters, has been tabulated in Table 4.5. Additionally, to our knowledge to date, no one has used the graphene/diamane interface in silicon-based solar cells except for our work.

# 4.4 Summary

In this work, we have examined the potential of the graphene/diamane interface in Si-HIT solar cells. we have also made a comparison between ITO and graphene to be used as TCO and diamane as emitter layer, which has not ever done so far. Also, various parameters of the hydrogenated intrinsic thin amorphous silicon layer have also been optimized, except its bandgap. Due to which the efficiency of the considered HIT cell is influenced and found to increase from 25.61% to 31.2% from the previous report. Furthermore, a comparison has been made between the theoretical and commercially possible cell to validate the obtained results, which are found to be in accordance. The maximum efficiency for the commercially possible cell is reported to be 24.15 % at graphene (TCO) work function 4.3 eV, single layer diamane and 500 µm thick silicon wafer, which is matched with the theoretical results. The independent effect of different parameters of n-diamane and p-cSi layer has also been studied. The variation in layer numbers of graphene has also been carried out, and it is found that the maximum efficiency of 31.2 % can only be achieved for single-layer graphene. The obtained results suggest that graphene and diamane can be used as a good transparent conducting electrode and emitter layer.

## **REFERENCES**

- [1] Bera, S.R. and Saha, S., 2016. Fabrication of CdTe/Si heterojunction solar cell. *Applied Nanoscience*, 6, 6, pp.1037–1042.
- [2] Yang, X., Bian, J., Liu, Z., Li, S., Chen, C. and He, S., 2018. HIT solar cells with n-type low-cost metallurgical Si. *Advances in Optoelectronic*, 2018, 1, pp.7368175.
- [3] Naima, Tyagi, P.K. and Singh, V., 2022. N-type diamane: An effective emitter layer in crystalline silicon heterojunction solar cell. *Carbon Trends*, 9, 1, pp.100209.
- [4] Alla, M., Manjunath, V., Chawki, N., Singh, D., Yadav, S.C., Rouchdi, M. and Boubker, F., 2022. Optimized CH<sub>3</sub>NH<sub>3</sub>PbI<sub>3</sub>-XClX based perovskite solar cell with theoretical efficiency exceeding 30%. *Optical Materials*, 124, 1, pp.112044.
- [5] Yoshikawa, K., Kawasaki, H., Yoshida, W., Irie, T., Konishi, K., Nakano, K., Uto, T., Adachi, D., Kanematsu, M., Uzu, H. and Yamamoto, K., 2017. Exceeding conversion efficiency of 26% by heterojunction interdigitated back contact solar cell with thin film Si technology. *Solar Energy Materials and Solar Cells*, 173, 1, pp.37–42.
- [6] Bae, S., Kim, H., Lee, Y., Xu, X., Park, J.-S., Zheng, Y., Balakrishnan, J., Lei, T., Kim, H.R., Song, Y.I., Kim, Y.-J., Kim, K.S., Özyilmaz, B., Ahn, J.-H., Hong, B.H. & Iijima, S., 2010. Roll-to-roll production of 30-inch graphene films for transparent electrodes. *Nature Nanotechnology*, 5, 8, pp.574–578.
- [7] Kim, J.-H., Lee, H.J., Noh, J.H., Lee, J.Y., Cho, S., Kang, S.J. & Lee, S.Y., 2013. Work function engineering of single layer graphene by irradiation-induced defects. *Applied Physics Letters*, 103, 17, pp.171604.
- [8] Lazar, P., Zbořil, R., Pumera, M. and Otyepka, M., 2014. Chemical nature of boron and nitrogen dopant atoms in graphene strongly influences its electronic properties. *Physical Chemistry Chemical Physics*, 16, 29, pp.14231–14235.
- [9] Borah, C.K., Tyagi, P.K. and Kumar, S., 2020. The prospective application of a graphene/MoS2 heterostructure in Si-HIT solar cells for higher efficiency. *Nanoscale Advances*, 2, 8, pp.3231–3243.

- [10] Abdulameer, M.J., Al-Abbas, S.S.A. and Jappor, H.R., 2021. Tuning optical and electronic properties of 2D ZnI2/CdS heterostructure by biaxial strains. *Journal of Applied Physics*, 129, 22, pp.225104.
- [11] Bafekry, A., Faraji, M. and Fadlallah, M.M., 2021. Two-dimensional porous graphitic carbon nitride C6N7 monolayer: First-principles calculations. *Applied Physics Letters*, 119, 14, pp.142102.
- [12] Bafekry, A., Faraji, M., Hoat, D.M., Ghergherehchi, M., Pham, T.T., Feghhi, S.A.H., Shojaei, F., Fadlallah, M.M., Ghosh, B., Gülseren, O. and Cuong, D.D., 2022. Biphenylene monolayer as a two-dimensional nonbenzenoid carbon allotrope: a first-principles study. *Journal of Physics: Condensed Matter*, 34, 1, pp.015001.
- [13] Chernozatonskii, L.A., Sorokin, P.B., Kvashnin, A.G., Kvashnin, D.G. and Yakobson, B.I., 2009. Diamond-like C2H nanolayer, diamane: Simulation of the structure and properties. *JETP Letters*, 90, 3, pp.134–138.
- [14] Chernozatonskii, L.A., Demin, V.A. and Kvashnin, D.G., 2021. Fully hydrogenated and fluorinated bigraphenes–diamanes: Theoretical and experimental studies. *C*, 7, 1.
- [15] Cheng, T., Liu, Z. and Liu, Z., 2020. High elastic moduli, controllable bandgap and extraordinary carrier mobility in single-layer diamond. *Journal of Materials Chemistry C*, 8, 41, pp.13819–13826.
- [16] Rietwyk, K.J., Uhl, C., Hansen, J. and Ley, L., 2013. Work function and electron affinity of the fluorine-terminated (100) diamond surface. *Applied Physics Letters*, 102, 9, pp.091604.
- [17] Stangl, R., 2010. Numerical simulation of solar cells and solar cell characterization methods: The open-source on demand program AFORS-HET. In: Leendertz, C. (Ed.), *IntechOpen*, Ch.14.
- [18] Schlaf, R., Murata, H. and Kafafi, Z.H., 2001. Work function measurements on indium tin oxide films. *Journal of Electron Spectroscopy and Related Phenomena*, 120, 1-3, pp.149–154.
- [19] Uda, M., Kanai, K., Kawai, J., Yoshihara, A., Ishii, H. and Ouchi, Y., 1998. Work function of polycrystalline Ag, Au and Al. *Journal of Electron Spectroscopy and Related Phenomena*, 88–91, 1-3, pp.643–648.
- [20] Nunes de Carvalho, C., Teixeira, V., Gaspar, J. and Conde, O., 2002. Effect of thickness on the properties of ITO thin films. *Surface and Coatings Technology*, 151–152, 1-3, pp.252–256.
- [21] Hess, P., 2020. Thickness of elemental and binary single atomic monolayers. *Nanoscale Horizons*, 5, 3, pp.385.
- [22] Shin, Y. and Kim, J., 2019. Influences of the Ag and the ITO thicknesses on multilayer films. *Journal of the Korean Physical Society*, 74, 8, pp.871–875.
- [23] Tsunomura, Y., Yoshimine, Y., Taguchi, M., Baba, T., Kinoshita, T., Maruyama, E., Ichihashi, N., Inoue, T., Fujita, H. and Okamoto, S., 2009. Twenty-two percent efficiency HIT solar cell. *Solar Energy Materials and Solar Cells*, 93, 4, pp.670–673.
- [24] Das Sarma, S., Adam, S., Hwang, E.H. and Rossi, E., 2011. Electronic transport in two-dimensional graphene. *Reviews of Modern Physics*, 83, 2, pp.407–470.
- [25] Patel, K. and Tyagi, P.K., 2017. P-type multilayer graphene as a highly efficient transparent conducting electrode. *Carbon*, 116, 1, pp.744–752.
- [26] Lin, Z., Carvalho, B.R., Kahn, E., Lv, R., Rao, R., Terrones, H., Pimenta, M.A. and Terrones, M., 2016. Defect engineering of two-dimensional transition metal dichalcogenides. *2D Materials*, 3, 2, pp.022002.
- [27] Patel, K., Chauhan, M., Tyagi, P.K., Singh, V.N. and Kumar, S., 2012. Simulation studies on heterojunction and HIT solar cells. In: *Proc. SPIE*, 8549, 1, pp.85490E.
- [28] Tohoda, S., Taguchi, M., Baba, T., Kinoshita, T., Maruyama, E., Tanaka, M. and Okamoto, S., 2012. Future directions for higher-efficiency HIT solar cells. *Journal of Non-Crystalline Solids*, 358, 17, pp.2219–2222.

- [29] Singh, J., 2007. Semiconductor Devices: Basic Principles. Wiley India Pvt. Ltd.
- [30] Shi, Y., Hamsen, C., Jia, X., Kim, K.K., Reina, A., Hofmann, M., Hsu, A.L., Zhang, K., Li, H., Juang, Z.-Y., Dresselhaus, M.S., Li, L.-J. and Kong, J., 2010. Work function engineering of graphene electrode via chemical doping. *ACS Nano*, 4, 5, pp.2689–2694.
- [31] Dao, V.A. et al., 2013. High-efficiency heterojunction with intrinsic thin-layer solar cells: A review. *Current Photovoltaic Research*, 2, pp.73–81.
- [32] Dao, V.A., Jeong, J.Y., Oh, J.Y., Lee, D.H., Lee, S. and Kim, D.H., 2006. High thermal conductivity in semiconducting Janus and non-Janus diamanes. *arXiv* preprint condmat.mtrl-sci, 2006, 3, 1, pp.04091.
- [33] Bouzidi, S., Barhoumi, M. and Said, M., 2021. Optical properties of Janus and non-Janus diamanes monolayers. *Optik*, 235, 1, pp.166642.
- [34] Bakharev, P.V., Huang, M., Saxena, M., Lee, S., Joo, S.H., Park, S.O., Dong, J., Camacho-Mojica, D.C., Jeong, H.Y., Kwak, S.K., Prasai, D., Gunlycke, D., Kim, M.J., Rümmeli, M.H., Shin, H.S. and Ruoff, R.S., 2019. Chemically induced transformation of bilayer graphene into fluorinated single-layer diamond. *Nature Nanotechnology*, 14, 6, pp.585–591.
- [35] Shen, W., Liang, T., Wang, Y., Sun, W. and Peng, J., 2019. Electron affinity of boron-terminated diamond (001) surface. *Journal of Materials Chemistry C*, 7, 32, pp.9756–9765.
- [36] Sachenko, A.V., Kostylyov, V.T., Scherbak, L.I., Konakova, R.V., Lashkarev, G.V., Nychyporuk, T.Y., Tovstyuk, K.D. and Lysenko, V.S., 2015. Silicon solar cells efficiency analysis, 2015, 1. arXiv preprint cond-mat.mtrl-sci.
- [37] Lisheng, W., Fengxiang, C. and Yu, A., 2011. Simulation of high efficiency heterojunction solar cells with AFORS-HET. *Journal of Physics: Conference Series*, 276, 1, pp.012177.
- [38] Korte, L., Schulze, T., Conrad, E., Stangl, R. and Rech, B., 2009. Advances in a-Si:H/c-Si heterojunction solar cell fabrication and characterization. *Solar Energy Materials and Solar Cells*, 93, 6-7, pp.905–910.
- [39] Zhao, Y., Zhou, W., Tan, H.S., Fu, R., Yu, S., Liu, X., Sum, T.C., Gao, F. and Wong, L.M., 2015. Anomalously large interface charge in perovskite devices. *Energy and Environmental Science*, 8, 4, pp.1256–1260.
- [40] Sakata, H., Taguchi, M., Baba, T., Maruyama, E., Ichihashi, N., Tsuda, S., Kinoshita, T. and Okamoto, S., 2000. 20.7% highest efficiency large area HIT<sup>TM</sup> cell. In: *28th IEEE Photovoltaic Specialists Conference*, pp.7–12.
- [41] Gorantla, S., Pandey, T., Passi, V., Aggarwal, N., Bhattacharyya, R., Kumar, R., Tyagi, P.K. and Jariwala, D., 2013. A universal transfer route for graphene. *Nanoscale*, 5(20), pp.10452–10458.
- [42] Zhao, L., Wang, Y., Yang, J., Chen, J. and Yan, B., 2008. Design optimization of bifacial HIT solar cells. *Solar Energy Materials and Solar Cells*, 92, 6, pp.673–681.
- [43] Zhao, L., Wang, Y., Yang, J., Chen, J. and Yan, B., 2009. Optimized resistivity of ptype Si substrate for HIT solar cell. *Solar Energy*, 83, 6, pp.812–816.
- [44] Park, Y., Lee, C., Kim, Y. and Lee, C.,1996. Work function of indium tin oxide transparent conductor. *Applied Physics Letters*, 68, 19, pp.2699–2701.
- [45] Li, X., Zhu, H., Wang, K., Cao, A., Wei, J., Li, C., Jia, Y., Li, Z., Li, X. and Wu, D., 2013. Ion doping of graphene for high-efficiency heterojunction solar cells. *Nanoscale*, 5, 5, pp.1945–1948.
- [46] Ma, J., Deng, D., Liu, Y., Hu, W. and Chen, X., 2018. High efficiency graphene/MoS2/Si Schottky barrier solar cells. *Solar Energy*, 160, 1, pp.76–84.
- [47] Tsunomura, Y., Yoshimine, Y., Taguchi, M., Baba, T., Kinoshita, T., Maruyama, E., Ichihashi, N., Inoue, T., Fujita, H. and Okamoto, S., 2009. Twenty-two percent efficiency HIT solar cell. *Solar Energy Materials and Solar Cells*, 93, 4, pp.670–673.

- [48] Geissbühler, J., Werner, J., Martin de Nicolas, S., Barraud, L., Hessler-Wyser, A., Tomasi, A., Despeisse, M., Boccard, M., Nicolay, S., Niesen, B., Ballif, C. and De Wolf, S., 2015. 22.5% efficient silicon heterojunction solar cell with molybdenum oxide. *Applied Physics Letters*, 107, 8, pp.081601.
- [49] Long, W., He, Y., Li, H., Shen, W., Lu, Y., Huang, H. and He, H., 2021. On the limiting efficiency for silicon heterojunction solar cells. *Solar Energy Materials and Solar Cells*, 231, 1, pp.111291.
- [50] Yoshikawa, K., Kawasaki, H., Yoshida, W., Irie, T., Konishi, K., Nakano, K., Uto, T., Adachi, D., Kanematsu, M., Uzu, H. and Yamamoto, K., 2017. Silicon heterojunction solar cell with interdigitated back contacts. *Nature Energy*, 2, 5, pp.17032.

# CHAPTER 5

# DOPED DIAMANE: AN EFFICIENT ELECTRON/HOLE COLLECTION LAYER IN SILICON SOLAR CELLS

This chapter presents the optimization of electron/hole collection layers, buffer, and absorber layers in a HIT solar cell using AFORS-HET simulation. The study introduces doped diamane as both n-type and p-type carrier-selective contacts, replacing conventional doped a-Si:H layers to enhance carrier selectivity and reduce parasitic losses. The optimized structure achieves 27.88% efficiency, with a  $V_{OC}$  of 691.1 mV,  $J_{SC}$  of 49.3 mA/cm², and FF of 81.83%. Simulations highlight the impact of front contact absorption and texturing on performance, demonstrating the potential of doped diamane for high-efficiency HIT solar cells.

The results reported in this chapter have been published in Naima et. al. Materials Science & Engineering B 310 (2024) 117754.

#### 5.1 Introduction

Photovoltaic solar cell is the only eco-friendly and constant energy source that has the capability of meeting the world's rising energy demand [1]. In this context, numerous research have been done to improve the efficiency of solar cells by using crystalline silicon as the active layer. It has been found that HIT solar cells with BSF may provide higher conversion efficiency with a comparably thin layer of c-Si [1-6]. Previous research has demonstrated that crystalline silicon-based HIT solar cells can offer more than 25 % conversion efficiency [7]. An efficiency of 25.6 % has reportedly been attained on a cell area of 143.7 cm<sup>-2</sup> with 1 solar illumination. This might happen because of the passivation of the c-Si layer, which has lowered recombination losses at the interface. This passivation is carried out by inserting an extremely thin intrinsic hydrogenated amorphous silicon layer over the crystalline silicon layer [7]. Also, an efficiency of 31.07 % was reported for 15 µm thick crystalline silicon layer by optimizing the doping concentration as well as by passivating the rear surface on the optimized geometry of interdigitated back contacts (IBC) [8]. In conventional silicon heterojunction solar cells, the conversion efficiency was strongly manipulated by the electron/hole collection layers, where these layers were made of inversely doped amorphous silicon layers [9,10]. Due to the lower bandgap (approximately 1.7 eV) and high defect density of these layers, the parasitic light absorption occurs throughout the solar spectrum's ultraviolet and visible range [11]. This absorption deteriorates the efficiency of the cell. Therefore, alternative materials having a wider bandgap and lower defect density are needed. These wider band gap layers will be beneficial for the electron/hole collection under illumination. Because the high Schottky barrier in the voltage range (>0.7 V) resulted in the formation of a significant space charge region or inversion layer between the hole selective layer (MoOx) and c-Si interface. This barrier influenced how well photo-generated carriers were captured, resulting in good transverse trans portation which enhanced the V<sub>OC</sub> and FF [12]. We believe that the development of HIT solar cells is not yet complete, and cells' overall efficiency might still be increased. But the parasitic light absorption losses that occur at interfaces are the main impediment to enhance the conversion efficiency of HIT solar cells. It was reported that the electron/hole collection layers of doped amorphous silicon can be

replaced by wide-bandgap transition metal oxide to reduce the parasitic light absorption loss in HIT solar cells [13]. In this direction, it has been suggested that titanium dioxide (TiO<sub>2</sub>) and zinc oxide (ZnO) can be employed as hole transporting layer materials, and copper (I) thiocyanate (CuSCN) as an electron transporting layer material and an efficiency of 25.02 % has been attained [14]. Furthermore, TMDs are reported to possess adequate work function with high optical transparency which is required for gathering charge carriers, so adding of TMDs layer between the p-type amorphous silicon and the TCO electrode as window layer maylead to better optical gains [15,16]. A coating of molybdenum oxide also applied to replace p type amorphous silicon in SHJ cell in the liter ature [13] and act as a proof of concept, and an efficiency of 22.5 % with a fill factor of more than 80 % was achieved [13]. This novel MoO/c-Si interface based heterojunction solar cells have an inherent potential of high efficiency [12]. The annealing process was conducted at temperatures exceeding 130 °C while printing the metal contacts [13]. This heating significantly increases the thickness of the molybdenum oxide/hydrogenated indium oxide (MoOx/InO:H) interface and possibly be the cause of the hole-blocking behaviour. This also affected how charge carriers were transported in MoOx layer. So, to make sure that the holes flowed smoothly in the heterojunction solar cell, the hole carrier layer which should not react with TCO, has to be added. It is noteworthy to mention that electron-hole pairs are generated only in the active layer of silicon, and the electron/hole collection layers play a vital role in the separation and transportation of these charge carriers. Therefore, to enhance the performance of the HIT solar cell, it is necessary to carefully select a suitable material for the electron/hole collection layer. According to reports, the material used for the electron/hole collection layer should possess the following characteristics: high reflectivity of minority carriers at the interface, high electrical conductivity, minimal series resistance, tunable band gap, low recombination velocity, and thermal, chemical, and mechanical stability [12,14–16]. Recently, Bakharev et al. [17] reported that they have synthesized a new 2D carbon material called diamane. Diamane, also commonly referred to as ultrathin diamond film, is a promising quasi-2D material with strong chemical stability, exceptional wear resistance, and high stiffness, significantly higher than that of most other 2D materials [18]. It was found to possess high carrier mobility for both electrons (2732 cm<sup>2</sup>/V.s) and holes (1565 cm<sup>2</sup>/V.s), superior than the carrier

mobility of III-IV semiconductor compounds [19], whether they are fluorinated or hydrogenated. Fluorinated diamane (C<sub>4</sub>F) possesses a band gap of 2.93 eV, resulting in 12 % optical transparency in the visible and NIR regions, comparable to that of diamond [20]. The work function of 2D diamane can also be varied in the range of 6.5eV to 3.5 eV, following from monolayer up to six layers, supports its application in electronic devices [21]. The bandgap of diamane (0–3.52eV) can be modulated by doping with boron and nitrogen dopants [22]. Additionally, diamane has abroad adjustable band gap ranging from 0.86 to 5.68 eV [23], allowing it to encompass the entire spectrum. Moreover, the thermal conductivity of 1960 W/mK [24,25] makes this material highly promising for high temperature electrical applications. Our research group also found that diamane can be used as the TCE in heterojunction solar cells and as the emitter layer in HIT solar cells, respectively, and that this can improve the efficiency of the solar cells [26–28]. Taking account of these exceptional properties, diamane has the potential to serve as a promising material for electron/hole collection layers. Being motivated, we have designed the HIT structure using n-type diamane as the emitter layer and p-type diamane as the BSF layer.

# 5.2 Structural model and junction formation

The modelled structure is: Graphene/n-type Diamane/a Si:H (i)/p-type crystalline Si/p-Diamane/Au, shown in Fig. 5.1. This HIT cell is then simulated by using the AFORS-HET software under AM 1.5G spectrum of monochromatic light with photon flux 1×10<sup>16</sup> cm²s⁻¹ and 10 nm spectral width in the range 300 nm 1200 nm at power density 100 mW/cm² and temperature 300K. AFORS-HET is a 1D numerical computer programme that models multi-layer homo as well as heterojunction solar cells and characterisation methods. This solves one-dimensional semiconductor equations (Poisson's equation, transport and continuity equations for electrons and holes) with finite differences under different conditions. The programme enables arbitrary tuning of parameters and multi-dimensional parameter comparing to match simulated and real measurements [29]. Six layers have been stacked to ensure that the maximum number of photons can effectively reach the active layer when uniformly illuminated under AM1.5G. During simulation, we did not take into account the carriers' ability to tunnel

at interfaces or the formation of defects between the absorber and the electron and hole collection layers in order to avoid further recombination. For electron and hole transportation drift—diffusion model is selected, and Shockley-Read-Hall recombination is chosen to describe the recombination in different semiconductor layers. The details are mentioned in Table 5.1.

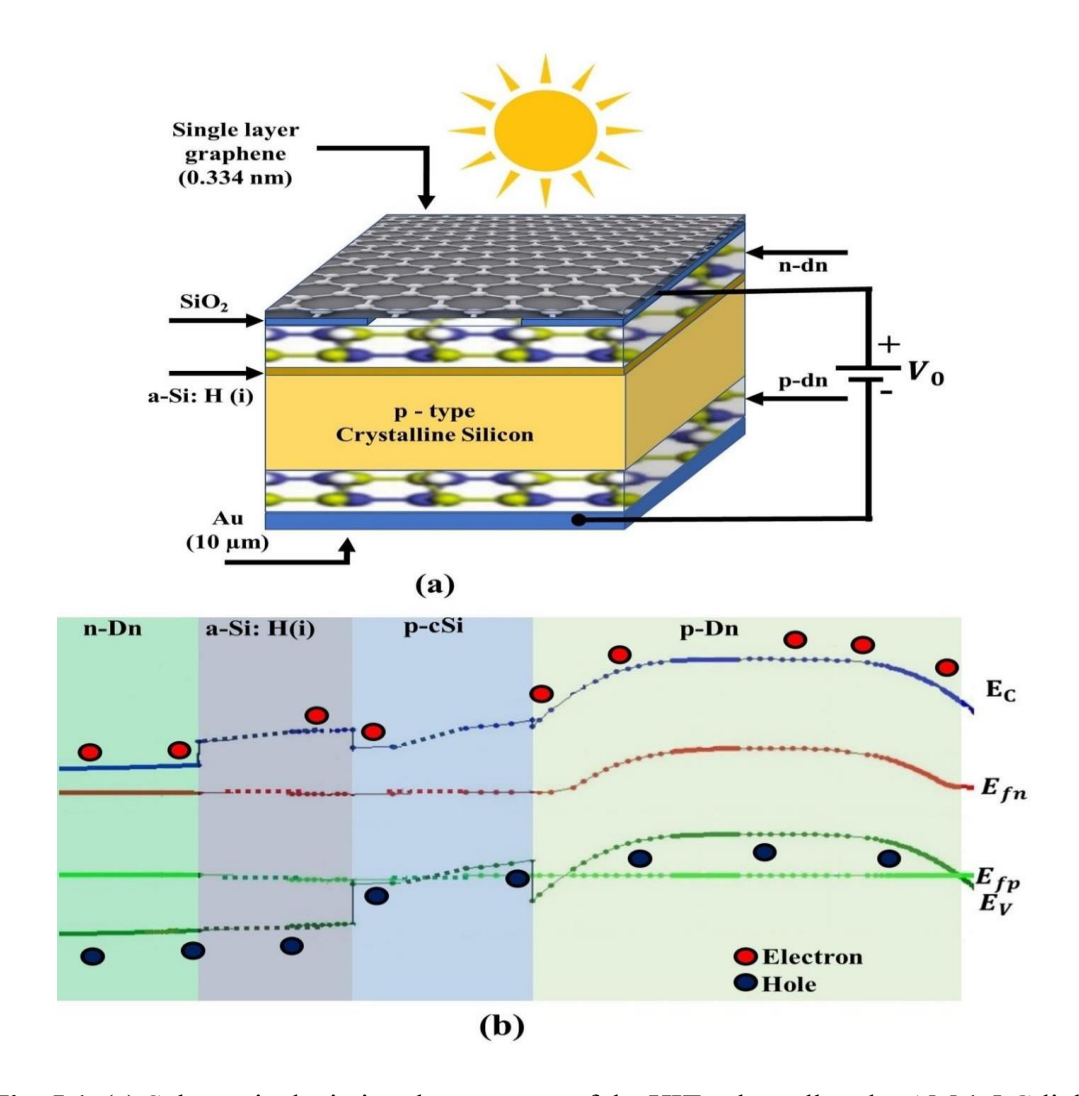


**Fig. 5.1** (a) Schematic depicting the structure of the HIT solar cell under AM 1.5 G light that was simulated. (b) Simulated energy band diagram of the proposed HIT structure as generated by the software.

The optical absorption was calculated by adopting the optical model Lambert-Beer absorption model because we have taken the textured surfaces. The user defined angle has been set to 90° for the textured crystalline silicon layer.

**Table 5.1** List of models applied at different interfaces between the layers used in the structure of the designed solar cell investigated in this report.

Interface	Model applied			
Graphene/n-Dn	MS-Schottky contact			
n-Dn/a-Si:H (i)	Drift diffusion model			
a-Si:H (i)/p-cSi	Drift diffusion model			
p-cSi/p-Dn	Drift diffusion model			
p-Dn/Au	MS-Schottky contact			

The absorption of photons at position x in the stack is determined by using the absorption coefficient  $\alpha x(\lambda) = 4\pi k(\lambda)/\lambda$  of the semiconductor layer, which can be calculated from the layer's extinction coefficient (λ) [29]. Additionally, we have thoroughly investigated the interfaces diamane/Si and diamane/Au in order to understand the formation of junctions at these different interfaces. The schematic of the energy band alignment diagram is constructed and presented in Fig. 5.1 (b). Since diamane is an ultra thin layer of diamond, the diamane/silicon interface can be understood as an alogous of diamond/silicon interface. It is reported that the interface bonding between diamond-Si is covalent and more stable. Charge depletion was found to occur in the region near the Si atoms and charge accumulation at the interface near the C atoms. This resulted charge gradient that leads to a significant number of electrons transfer from the Si to the C atoms. This might happen due to the difference in charge density at the interface [30] and suggests that diamane-Si interface has potential application in HIT solar cell. Similarly, the diamane/Au interface can also be understood by the interface between diamond and Au as reported in Ref. [31]. The interface between diamond and Au has Schottky nature [31]. As it is reported that due to the higher work function of gold than that of diamond electrons will transfer from diamond to gold and develop positive space charge region close to the diamond surface. We have used a SiO<sub>2</sub> layer as an insulator to ensure that charge carrier transport takes place only in a radial direction, i.e., through the planer diamane layer, and no carrier transport occurs in the transverse direction i.e., between TCO and the p-c-Si layer [32].

In addition, a metallic contact (Au) is employed as the back contact to facilitate the flow of the output current in the external circuit. To do so flatband metal/semiconductor contact boundary model has been chosen for both front/back boundaries, specifying work-function 4.3 eV (front boundary) and 5.4 eV (back boundary). The details for the front and back surfaces are given in Table 5.2.

**Table 5.2** Values of parameters of front and back contacts used in the designed solar cell investigated in this work [18–20,55-56,63].

Parameter	Front contact	Back contact	
Material	Graphene	Au	
Thickness	0.334 nm	10 μm	
Absorption loss	0	0	
Work function (eV)	4.3 eV	5.4 eV	
Refractive index	2.7	0.1	
Extinction coefficient	1.45	3	
Internal reflection	0	0	
External reflection	0	0	
Surface condition	Textured	Textured	
Angle of incidence ( $\delta$ )	90°	90°	

The initial set of values for different layer's parameters has been tabulated in Table 5.3, which are then varied in the viable ranges while performing the simulation. These values have been taken from the available literature [21,26,33–44]. The parameters of the emitter layer and BSF layer optimized during simulation are  $N_D/N_A$ ,  $E_g$ ,  $N_C/N_V$ ,  $\chi$ ,  $\epsilon_r$ , and thickness. The optimized parameters of p–type c-Si layer and a-Si: H(i) are:  $N_A$ ,  $N_C/N_V$ , and thickness, as well as  $E_g$ ,  $N_C/N_V$ , and thickness, respectively. After optimizing the emitter layer and BSF layer, the optimum conversion efficiency achieved was 35.57% which is then increased up to 35.58% after optimizing hydrogenated amorphous intrinsic silicon layer. At last, after optimizing the active layer (p-cSi) the efficiency reached up to 36.95%. While performing the simulation on the emitter layer, the parameters of the remaining layers were kept constant at their initial values from Table 5.3. On the other hand, while moving on to the simulation of the next layer the parameters of the previously optimized layer were kept at their best optimum values.

**Table 5.3** List of initial set of values of parameters used for different layers before optimization [21, 29, 36-47].

Parameter	n-Diamane	a-Si: H (i)	p-cSi	p-Diamane	
Thickness	0.34 nm	3 nm	500 μm	0.34 nm	
Dielectric constant	11	11.9	11.9	11	
Electron affinity (eV)	4.1	3.9	4.05	4.1	
Band gap (eV)	1.4	1.6	1.12	1.4	
$N_C (cm^{-3})$	$1 \times 10^{18}$	$3 \times 10^{21}$	$3 \times 10^{19}$	$1 \times 10^{18}$	
$N_V (cm^{-3})$	$1 \times 10^{18}$	$3 \times 10^{21}$	$3 \times 10^{19}$	$1 \times 10^{18}$	
$\mu_n \ (cm^2V^{-1}s^{-1})$	2732	20	1104	2732	
$\mu_p \ (cm^2V^{-1}s^{-1})$	1565	5	420	1565	
$N_A (cm^{-3})$	0	0	$1 \times 10^{19}$	$9 \times 10^{17}$	
$N_D (cm^{-3})$	$9 \times 10^{17}$	0	0	0	
$V_e$ (cm s <sup>-1</sup> )	$1 \times 10^{7}$	$1 \times 10^{7}$	$1 \times 10^{7}$	$1 \times 10^{7}$	
$V_h$ (cm s <sup>-1</sup> )	$1 \times 10^{7}$	$1 \times 10^{7}$	$1 \times 10^{7}$	$1 \times 10^{7}$	
Layer density	2.328	2.328	2.328	2.328	
$(g cm^{-1})$					
Auger electron	0	0	2.20	0	
recombination			$\times 10^{-31}$		
coefficient $(cm^6s^{-1})$					
Auger hole	0	0	9.90	0	
recombination			$\times 10^{-32}$		
coefficient $(cm^6s^{-1})$					
Band- to- band	0	0	9.50	0	
recombination			$\times 10^{-15}$		
coefficient $(cm^3s^{-1})$					
Refractive index (n)	1.75	(default)	(default)	1.4	
Extinction coefficient	0.8	(default)	(default)	0.7	
(k)			. ,		

## 5.3 Results and discussion

## 5.3.1 Evaluation of approach

It is vital to validate the reported work with previously reported experimental results because we have only simulated the HIT solar cell. So, we have simulated the previously designed solar cell's structure to corroborate our findings. To do this, we simulated the structure using the AFORS-HET software in this section. In this order, first we have simulated the cell Ag/ITO/n-type a-Si:H/intrinsic a-Si:H/n-type textured c-Si/intrinsic a-Si:H/MoOx/Ag fabricated by Li *et al.* [12]. The simulated results under the same condition AM 1.5, and at the same values of parameters reported by Li *et al.* [12] are  $V_{OC}$ 

= 699.1 mV,  $J_{SC}$  = 66.22 mA/cm<sup>2</sup>, FF = 51.7% and  $\eta$  = 23.93 %. The simulated results are found in correlation with the results obtained by Li *et al.* (i.e.,  $V_{OC}$  = 713 mV,  $J_{SC}$  = 37.50 mA/cm<sup>2</sup>, FF = 78.92 % and  $\eta$  = 21.10 %) [12]. The notable difference in the values of  $J_{SC}$  and FF may be due to the variation in values of parameters that are not reported in this work. We have taken an estimated value from the literature. Therefore, this difference may be overlooked. Furthermore, our research group has previously presented more proof of this approach in their articles [26]. These results proved the validation of software used and justified our approach of simulation.

#### 5. 3.2. Fabrication details

Fig. 5.1 depicts the structure of the HIT solar cell that can be fabricated by using the ptype textured wafer of crystalline silicon. An intrinsic thin layer of hydrogenated amorphous silicon a-Si: H(i) can be deposited on the front side of the crystalline silicon substrate by using any of the techniques such as CVD, glow discharge, laser decomposition and sputtering [45]. Subsequently, on the both sides of the substrate CVD grown bilayer graphene is transferred by using the chemical methods discussed in ref. [46]. The transferred layers of bilayer graphene are then converted into diamane by exposing to H radicals produced by the hot-filament process [47] which are then doped with nitrogen and boron in order to get stable n and p-type diamane [25, 48]. After that single layer graphene is transferred on the front side of the stack formed which is working as TCE or antireflecting layer by using chemical methods [46]. In this study, we employed single-layer graphene as TCE in place of the commonly used ITO. We chose graphene for its high transparency of about 97.4%, low sheet resistance of around 125  $\Omega/\Box$ , and superior quantum efficiency in the ultraviolet spectrum [46, 49]. An extremely thin SiO<sub>2</sub> layer is introduced between graphene and n-type diamane to avoid direct transportation of charge carriers between the graphene layer (TCE) and the active layer in order to avoid recombination losses and parasitic absorption losses. Finally, Au deposited or screen printed on the back side of the cell formed called the back surface or the metal electrode, which is responsible for the execution of current across the external circuit [50].

#### 5.3.3 Optimization of emitter layer

This study is being carried out in order to attain the maximum conversion efficiency by using a designed multi-layered solar cell. For this purpose, first we designed the cell's

structure and then simulated its different layers parameters. The emitter layer, which is n-type diamane, is the first simulated layer.  $N_D$ ,  $E_g$ ,  $N_C/N_V$ ,  $\chi$ ,  $\varepsilon_r$  and the layer thickness are the parameters that were optimised; the results are plotted in Fig. 5.2. Initially, the efficiency was found to be 34.48 % at some random set of values given in Table 5.3. The simulation results of  $N_D$  of n-Dn are shown in Fig. 5.2 (a and b) and found to be in the range  $1 \times 10^{16}$  cm<sup>-3</sup> -  $2 \times 10^{20}$  cm<sup>-3</sup>. It is observed that as  $N_D$  increases, the efficiency increases linearly and it reaches to 35.06 %. This can be understood like that as the photons enter the structure, the electron and hole pairs are first formed in the active layer of c-Si and then get separated in a formed depletion region. Since the graphene and semiconductor interface ideally forms a Schottky barrier, a built-in voltage ( $V_{bi}$ ) develops in the depletion region. This  $V_{bi}$  was the consequence of different interfaces' work functions. In this order, the electron and hole majority barrier height at the interface is related as follows:

$$\Phi_{\text{Bn}}^{\text{Schottky}} = q \left\{ \Phi^{front/back} - \chi^{front/back} \right\}$$
 (5.1)

$$\Phi_{\rm Bp}^{\rm Schottky} = q \left\{ E_g - \Phi^{front/back} + \chi^{front/back} \right\}$$
 (5.2)

Where,  $E_g$  is the bandgap,  $\Phi^{front/back}$  is the work function of front/back contact and  $\chi^{front/back}$  is the electron affinity of the front/back contact [29]. This built-in voltage at the interface separates the photogenerated charge carriers formed in the depletion region as well as from those carriers formed around a diffusion length distance from the space charge region, which is then subsidised to the solar cell current [51]. From Fig. 5.2 (b), it is noticed that for the initial range of values of  $N_D$ , i.e., from  $1 \times 10^{16}$  cm<sup>-3</sup> to  $3 \times 10^{18}$  cm<sup>-3</sup>  $V_{OC}$  is constant at 677.8 mV. This is because for smaller values of  $N_D$ ,  $V_{OC}$  does not depend on it until and unless it does not satisfy the condition  $\Delta n_o >> N_D$ , where  $\Delta n_o$  is the concentration of excess electron and hole pairs which contribute to the open-circuit voltage [52]. Beyond  $N_D = 3 \times 10^{18}$  cm<sup>-3</sup>, the value of  $V_{OC}$  was found to increase because as the doping concentration increases, the built-in potential (e $V_{bi}$ ) increases in accordance with the equation written below [53]:

$$eV_{bi} = e\left(\Phi_{n-Dn} - \Phi_{Gr}\right) \tag{5.3}$$

where,  $eV_{bi}$  is given by,

$$eV_{bi} = E_{g(n-Dn)} + \Delta E_V + kT \ln \left( \frac{N_A N_D}{N_{V(p-cSi)} N_{D(n-Dn)}} \right)$$

$$= E_{g(p-cSi)} - \Delta E_C + kT \ln \left( \frac{N_A N_D}{N_{V(p-cSi)} N_{D(n-Dn)}} \right)$$
(5.4)

Where k and T is the Boltzmann constant and the temperature in Kelvin, respectively, and e is the electronic charge,  $E_g$  is the bandgap,  $\Delta E_V$  &  $\Delta E_C$  are the conduction band offset and valence band offset, respectively. While  $N_A & N_D$  represent the concentration of the acceptor and donor, respectively, and  $N_C$  &  $N_V$  stand for the density of the conduction band and the valence band, respectively [54]. The short circuit current density  $I_{SC}$  is noticed to remain almost constant at 62.41 mA/cm<sup>2</sup> as  $N_D$  increased. It might have happened because the photogenerated carriers' mobility is constant even as the doping concentration increases [55]. According to Ref [55], only N<sub>C</sub> and N<sub>V</sub> had an impact on mobility. With increasing doping concentration, it was found that the FF and efficiency increased from 81,49% to 81.78% and from 34.47% to 35.06%, respectively. This may have happened because as  $N_D$  increases work function  $(\Phi_{n-Dn})$  increases, which results in an increase of barrier height and reduction in sheet resistance [56]. The simulation is further proceeded to the effective conduction and valence band density  $(N_C/N_V)$  from 6 ×  $10^{17}$  cm<sup>-3</sup> to  $7 \times 10^{21}$  cm<sup>-3</sup> while taking  $N_D$  at its optimum value and the results are shown in Fig. 5.2 (c and d). As  $N_C/N_V$  increased,  $V_{OC}$  was found to be abruptly decreased from 698 mV to 473.5 mV as shown in Fig. 5.2 (c). This might be due to a reduction in barrier height. This change is a consequence of a decrease in the density of free charge carriers near the interface, which caused the built-in voltage to drop, resulting in a smaller  $V_{OC}$ . On the other hand,  $J_{SC}$  was found to be decreased very slightly as  $N_C/N_V$  goes up from 7  $\times$  10<sup>20</sup> cm<sup>-3</sup> to 7  $\times$  10<sup>21</sup> cm<sup>-3</sup>. This is because of the deterioration in the minority carrier density, which may have happened because of the shorter lifetime of photogenerated carriers and the entrapping of free charge carriers [56]. The FF as well as the conversion efficiency were found to be decreased on the large scale from 81.65 % to 73.07 % and 35.57 % to 21.57 %, respectively, as  $N_C/N_V$  increases as shown in Fig. 5.2 (c). This decrement can be understood as by the sharp decrement in the barrier height that occurs when  $N_C/N_V$  increases. As a result, the optimum efficiency 35.57% was obtained at the smallest value of  $N_C/N_V$  i.e.,  $6 \times 10^{17}$  cm<sup>-3</sup>. Further optimization is carried out by varying the bandgap of emitter layer (n-Dn) in the range of 0.3 eV - 1.4 eV [25] and the result showing the possible outcomes is plotted in Fig. 5.2 (e & f).

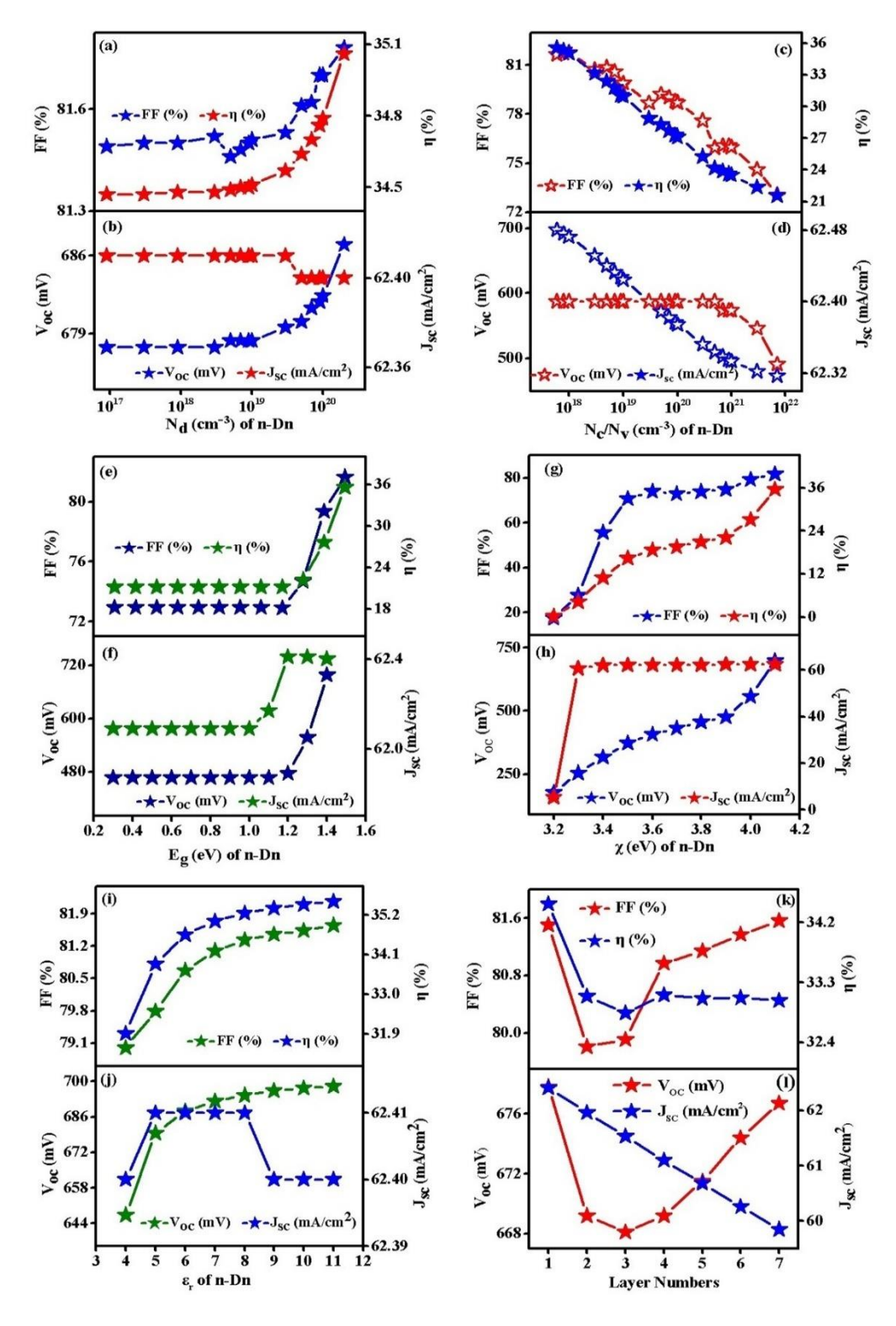


**Fig. 5.2** Results obtained for optimising the emitter layer (n-Dn) (a & b) optimization of  $N_D$  within the range  $1 \times 10^{16}$  cm<sup>-3</sup> -  $2 \times 10^{20}$  cm<sup>-3</sup>, (c & d) optimization of  $N_C/N_V$  within

the range  $6 \times 10^{17}~cm^{-3} - 7 \times 10^{21}~cm^{-3}$ , (e & f) optimization of  $E_g$  within 3.2 eV - 4.1 eV, (g & h) optimization of  $\chi$  in the range 3.2 eV - 4.1 eV, (i & j) optimization of  $\varepsilon_r$  in the range 4 – 11. (k & l) Optimization of the number of layers of n-Dn from 1 – 7.

It is noticed that as  $E_g$  elevates, the value of all parameters increases. This may have happened because, as the bandgap increases, the electric field in the depletion region of c-Si layer increases[57]. Thus, as the bandgap of the emitter layer is increased, the effective interface recombination reduces, which results in higher parameter values. In this manner, the emitter layer's optimum bandgap value of 1.4 eV, which corresponds to an optimal efficiency of 35.57%, is found. After getting the best optimized bandgap for emitter layer, the optimization is carried out by adjusting the values of electron affinity in the range 3.2 eV to 4.1 [28] eV and the possible achieved outcomes are plotted in Fig. 5.2 (g and h). From Fig. 5.2 (g and h), it is noticed that as the affinity increases  $V_{OC}$  and  $J_{SC}$  increase linearly. Similarly, the FF as well as efficiency were found to increase with affinity. The improvement in all these values can be understood from the fact that as affinity increased, the barrier height will also increase, which probably elevated the transference of minority carriers, consequently raised *Isc* [56]. Also, a little improvement in the  $\Delta E_C$  was seen with the increment in  $\chi$  [55], resulting in an increased  $V_{OC}$  and  $J_{SC}$  at  $\chi = 4.1$  eV. In this way, the optimized electron affinity for n-type diamane is found to be 4.1eV, attaining an efficiency of 35.57%. After determining the best optimized value for  $\chi$ , the next parameter we optimised was the dielectric constant or relative permittivity  $\varepsilon_r$ , which was optimized from 4 to 11 and the corresponding results are given in Fig. 5.2 (i and j). From Fig. 5.2 (i and j), it can be seen that as  $\varepsilon$ r increases from 4 to 11, the value of  $V_{0C}$ , FF, and  $\eta$  increase linearly, while the value of  $J_{SC}$  remains almost constant. The growth of the electron-hole pair in the diamane layer increases with a rise in  $\varepsilon r$ , according to Coulomb's law as  $F \propto 1/\varepsilon_r$ , where F represents the electrostatic force between the electrons and holes; however, the increase in  $\varepsilon_r$  simultaneously decreases eV<sub>bi</sub>. Consequently, we achieved a stable J<sub>SC</sub>. The optimum value of dielectric constant is found to be 11 having efficiency of 35.57%. To investigate the impact of the thickness of the emitter layer on the cell's performance, the cell was further simulated up to seven layers of n-Dn. The results obtained are shown in Fig. 5.2 (k and l). The results showed that as the layer number increased, J<sub>SC</sub> reduced significantly from 62.41 mA/cm<sup>2</sup> to 59.85 mA/cm<sup>2</sup> whereas, V<sub>OC</sub> decreased

slightly from 677.8 mV to 676.7 mV. This may have happened due to a decrease in transmittance with an increase in layer numbers, which in turn caused a reduction in the rate at which electron-hole pairs are formed. Additionally, it was found that FF decreased from 81.5% to 79.81%. Consequently, the conversion efficiency was also observed to decrease from 34.48% to 33.03%. Thus, at a single layer n-Dn maximum efficiency is observed. Niu et al. [15] reported that in diamane, N atom occupies substitutional site rather than the interstitial site, and this configuration is the most stable when the N atom is positioned at the external substitutional site without hydrogen saturation. They also found that B and N atoms co-doped in diamane exhibited a preference for forming a covalent bond, where N being saturated by H. The stability of a lone pair of electrons in nitrogen is diminished by the boron dopant. These co-dopants B and N may adjust the bandgap within the range of 0–3.52 eV. This band gap tuning opens the possibility of controlling  $N_D$ ,  $N_C/N_V$ ,  $\chi$ ,  $\varepsilon_r$ . Here it is worthy to mentioned that, these parameters can also be controlled for a-Si: H(i) layer but in case of p-cSi only doping concentration can be controlled.  $N_C/N_V$  depends on effective mass of charge carriers and temperature by relation:

$$N_{C/V} = \left(\frac{2\Pi k_{\rm B} m^*_{\rm e/h}}{h^2}\right)^{\frac{3}{2}} \tag{5.5}$$

Here,  $k_B$  is the Boltzman's constant and  $m_{e/h}$  is the effective mass of the electron/hole.

## 5.3.4 Optimization of BSF layer

Furthermore, to investigate the effect of BSF layer on the efficiency of the designed solar cell, the cell is further investigated by optimizing various parameters of p-type diamane. The  $N_A$  is the first parameter that has been optimized. During the simulation the optimum values of n-Dn have been taken into account, and the remaining parameters has been set to the values tabulated in Table 5.3. The values of parameters of the emitter layer (n-Dn) are set at their optimized values.  $N_A$  of p-Dn is varied within  $1 \times 10^{16}$  cm<sup>-3</sup> -  $1 \times 10^{21}$  cm<sup>-3</sup> and the corresponding results are plotted in Fig. 5.3 (a and b). As demonstrated in Fig. 5.3 (a and b), the acceptor concentration of p-Dn has no effect on the cell performance. This demonstrates that the excess number of holes has no effect on the process of generating current in the solar cell and the output of the simulated cell is not significantly affected by extra collections of holes in the BSF.

In the next step, the parameter  $N_C/N_V$  is being optimized in the range of values from  $1 \times 10^{12} \ cm^{-3}$  -  $9 \times 10^{21} \ cm^{-3}$  and the results are shown in Fig. 5.3 (c and d). The results show that the maximum value of efficiency is achieved at  $N_C/N_V$  3 × 10<sup>15</sup>  $cm^{-3}$ , after that it remained constant on further increasing the value of  $N_C/N_V$ . This may have happened because as the  $N_C/N_V$  increases, the minority carrier density reduces perhaps, as a result of the smaller lifetime of photogenerated charge carriers and entrapping of free charge carriers [56], resulting in constant  $J_{SC}$ . The values of FF and consequently the conversion efficiency increase till  $N_C/N_V$  3 × 10<sup>15</sup>  $cm^{-3}$  and attain their optimum values 81.65 % and 35.57 %, respectively.

After optimizing these two parameters of BSF, the next parameter we have optimized here is the band gap of BSF to see the effect of optimizing its values in the wider range from 0.8 eV to 1.8 eV on the performance parameters of the cell. The outcomes are shown in Fig. 5.3 (e and f) and it has been observed that the optimum value of bandgap is 1.4 eV. The conversion efficiency was found to first increase with bandgap till 1.4 eV and then start decreasing with further improvement in bandgap. One possible explanation for this decrement is a wider band gap, which obstructs the movement of majority carriers and simultaneously acts as an obstacle for minority carriers. In this way, the best simulated value of  $\eta$  was found to be 35.57 % at a bandgap of 1.4 eV.

After complete observation of the bandgap on the efficiency of the HIT solar cell, further optimization is carried out on the  $\chi$  of the BSF layer. The range we have taken here for  $\chi$  is 3.6 eV - 4.5 eV, and the outcomes are shown in Fig. 5.3 (g and h).  $V_{OC}$  was found constant at 698 mV whereas  $J_{SC}$  was found to increase with  $\chi$ , and the FF as well  $\eta$  were found to first increase with  $\chi$  and then decrease, as shown in Fig. 5.3 (g and h). From the results, we have considered 4.1 eV as the best simulated value of  $\chi$  for p-Dn. Next, we have optimized the  $\varepsilon_r$  of p-Dn in the range 4-11 and the observed results are shown in Fig. 5.3 (i and j). It is perceived from the graph that  $\varepsilon$  of BSF material does not play a responsive role on the output of HIT solar cell. Furthermore, the impact of changing the number of p-Dn layers from 1 to 7 on the HIT cell's performance has been investigated, and the outputs are shown in Fig. 5.3 (k and l). Here, we found that the values of all the parameters stayed constant with thickness. This suggests that the thickness of the BSF material has no appreciable impact on the output of the HIT solar cell.

#### 5.3.5 Optimization of buffer layer

After simulating both the emitter layer as well as BSF, the simulation is further carried out on the intrinsic layer of hydrogenated amorphous silicon, which is being used to passivate the active layer from dangling bonds present on its surface. Till both the emitter layer and BSF have been optimized, an efficiency of 35.57 % was noticed as the highest efficiency. Furthermore, in order to improve the obtained efficiency further, the simulation is first carried out on  $N_C/N_V$  and the desired outcomes are depicted in Fig. 5.4 (a and b). The value of  $N_C/N_V$  is varied in the range from  $1 \times 10^{21}$  cm<sup>-3</sup> -  $3 \times 10^{21}$  cm<sup>-3</sup>, and the results can be observed from Fig. 5.4 (a and b). The findings indicate that a lower value of  $N_C/N_V$  corresponds to increased efficiency. The optimal value of  $N_C/N_V$  for a-Si: H(i) is found to be constant in the range from  $1.5 \times 10^{21}$  cm<sup>-3</sup> to  $2.5 \times 10^{21}$  cm<sup>-3</sup>, resulting in a maximum efficiency of 35.58%. After simulating the value of  $N_C/N_V$  for a-Si: H (i) the subsequent parameter that we have optimized is the bandgap of the intrinsic layer in the range 1.6 eV - 1.7 eV [55] and the results are shown in Fig. 5.4 (c and d) which shows that the value of  $V_{OC}$  and  $J_{SC}$  are decreasing with bandgap although, the variation in the value of  $I_{SC}$  was minimal. Furthermore, FF as well as  $\eta$  were found to decrease drastically with bandgap. It has been observed that, at the optimum bandgap of 1.6 eV, the efficiency holds its highest value i.e., 35.58 % as shown in Fig. 5.4 (c and d). This could be because the emitter layer only absorbs photons that match this value of bandgap of the a-Si: H (i) layer i.e., 1.6 eV [55]. The final parameter optimised for a-Si: H (i) is its thickness, which has been adjusted between 3 and 10 nm. Fig. 5.4 (e and f) presents the results, which clearly show that as the thickness of a-Si: H (i) layer is increased, the efficiency of the designed HIT cell decreases and the optimum value of thickness is found at its minimum value taken initially as 3 nm. At the smallest thickness of a-Si: H (i) the conversion efficiency was found to be 35.58 % which is the optimum value. All the parameters of HIT module were found to decrease with increased thickness of a-Si: H (i) as shown in Fig. 5.4 (e and f). This deterioration in the value of performance parameters of the cell can be understood by the reported fact that as the intrinsic layer becomes thicker, the series resistance of the cell increases [58]. Therefore, the J<sub>SC</sub> decreases, which consequently results in decreased FF and  $\eta$  [58].

#### 5.3.6 Optimization of active layer

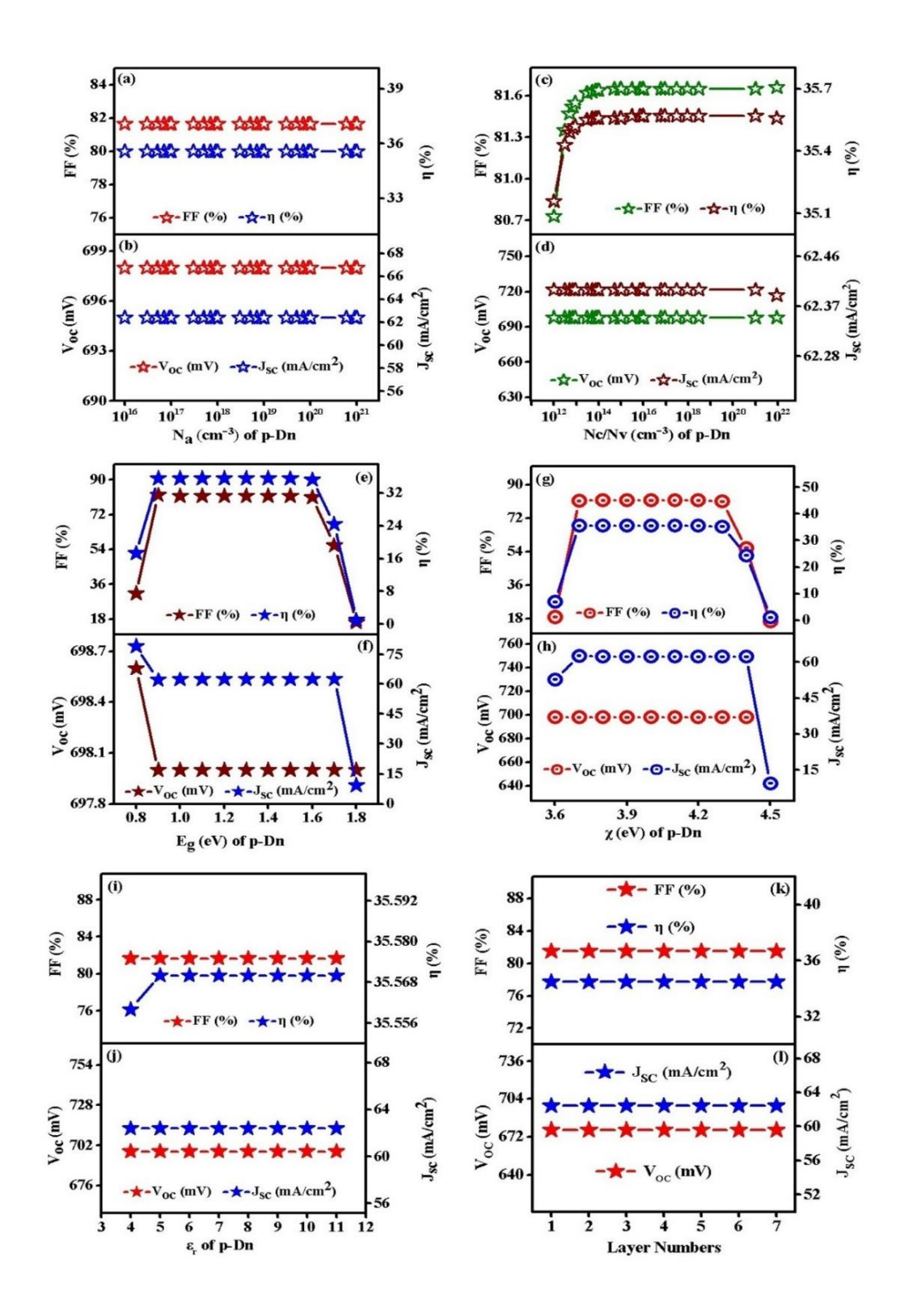


**Fig. 5.3** Results obtained for the optimization of BSF (p-Dn) (a & b) optimization of  $N_A$  within the range  $1 \times 10^{16}$  cm<sup>-3</sup> -  $1 \times 10^{21}$  cm<sup>-3</sup>, (c & d) optimization of  $N_C/N_V$  within the range  $1 \times 10^{12}$  cm<sup>-3</sup> -  $9 \times 10^{21}$  cm<sup>-3</sup>, (e & f) optimization of  $E_g$  within 0.8 eV - 1.8 eV, (g & h) optimization of  $\chi$  in the range 3.6 eV - 4.5 eV, (i & j) optimization of  $\varepsilon_r$  in the range 4 - 11. (k & l) Optimization of the number of layers of p-Dn from 1 - 7.

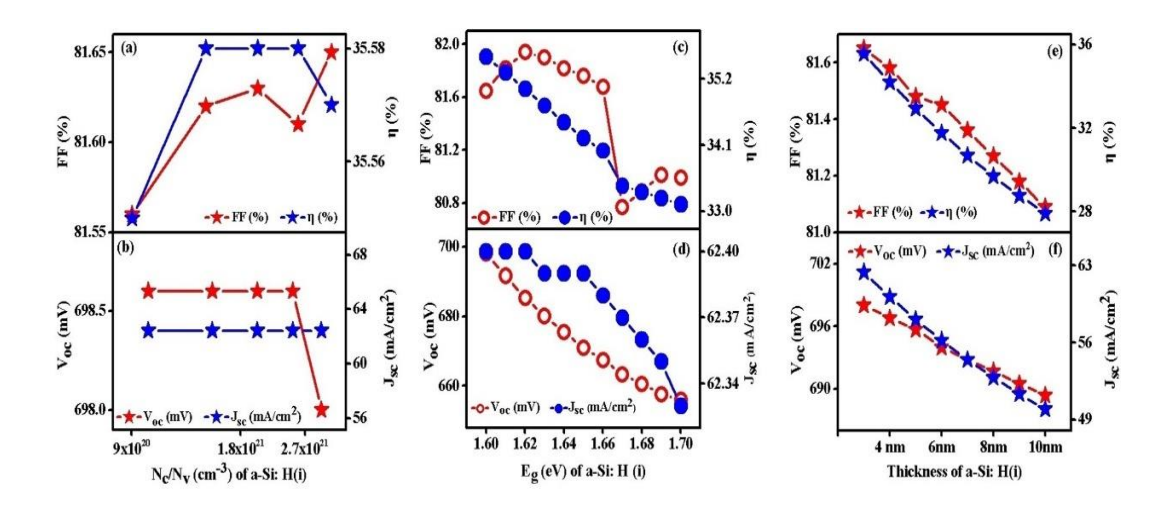


**Fig. 5.4** Results obtained for the optimization of buffer layer a-Si: H(i) (a&b) optimization of Nc/N<sub>V</sub> within  $1\times10^{21}$  cm<sup>3</sup> -  $3\times10^{21}$  cm<sup>3</sup>, (c & d) optimization of E<sub>g</sub> within the range 1.6 eV – 1.7 eV, (e & f) optimization of thickness of a-Si: H(i) within the range 3 nm – 10 nm.

The c-Si layer was also optimised following the optimisation of all the previously described layers' parameters. In this layer, all photogenerated charge carriers split and flow as output current in an external circuit. The maximum efficiency attained prior to optimising the active layer's parameters was 35.58%. So, at this point, additional simulation is further initiated by maintaining the values of all other parameters of different layers at their optimal values. The first parameter we optimized for the c-Si layer was  $N_A$  in the range of  $2 \times 10^{16}$  cm<sup>-3</sup> –  $1.5 \times 10^{19}$  cm<sup>-3</sup>.

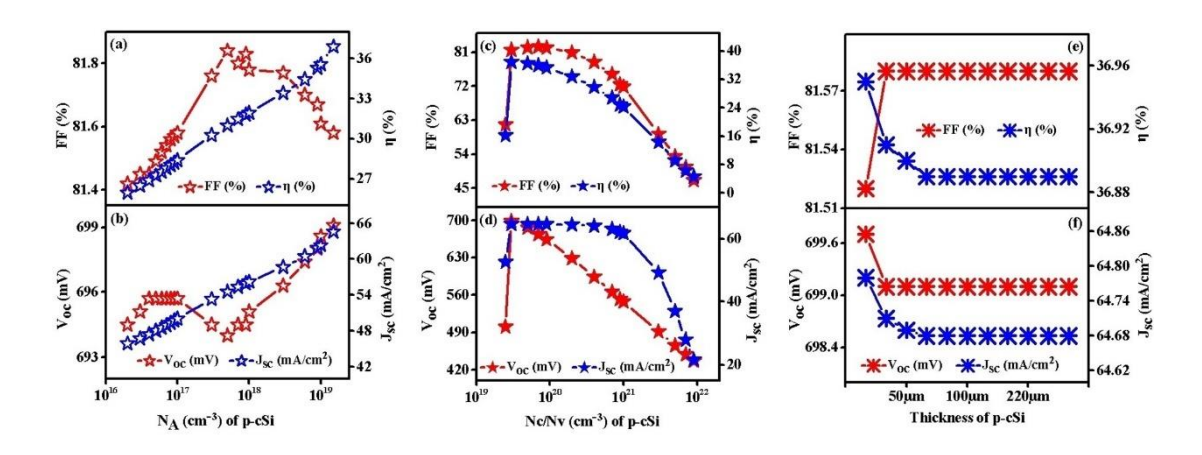


**Fig. 5.5** Results obtained for the optimization of active layer p-cSi (a & b) optimization of  $N_A$  within  $2 \times 10^{16}$  cm<sup>-3</sup> –  $1.5 \times 10^{19}$  cm<sup>-3</sup>, (c & d) optimization of  $N_C/N_V$  within the range  $2.5 \times 10^{19}$  cm<sup>-3</sup> –  $9 \times 10^{21}$  cm<sup>-3</sup>, (e & f) optimization of thickness of p-cSi layer within the range 30  $\mu$ m to 300  $\mu$ m.

The plotted data in Fig. 5.5 (a and b) depict that  $V_{OC}$  as well as  $J_{SC}$  increase linearly with  $N_A$ . The linear enhancement in both values of  $V_{OC}$  and  $J_{SC}$  led to an improvement in the value of FF and η. The increase in FF may be ascribed to the decrease in sheet resistance, which also leads to an increase in J<sub>SC</sub> [55]. Thus, the maximum efficiency of 36.89 % is attained at value of  $N_A$  1.5 × 10<sup>19</sup> cm<sup>-3</sup>. In order to further improve the efficiency, the simulation is carried out on  $N_C/N_V$ . The optimized range of values of  $N_C/N_V$  is  $2.5 \times 10^{19}$  $cm^{-3}$  - 9 × 10<sup>21</sup>  $cm^{-3}$ , results are plotted in Fig. 5.5 (c and d). It was observed that as  $N_C/N_V$  increase, the parameters  $V_{OC}$ ,  $J_{SC}$ , FF and  $\eta$  are first increased and attain their optimum value at  $3 \times 10^{19}$  cm<sup>-3</sup> and then decrease linearly. Therefore, the optimal value of  $N_C/N_V$  for p-cSi is found to be  $3 \times 10^{19}$  cm<sup>-3</sup>. This outcome can be elucidated by Eqn. (5.4), where an increase in the N<sub>V</sub> of the p-cSi layer results in a decrease in eV<sub>bi</sub>, which subsequently leads to a corresponding reduction in V<sub>OC</sub> [54-55]. Furthermore, we have optimised the p-cSi layer's thickness, varying it between 30 and 300 µm. The outcomes are displayed in Fig. 5.5 (e and f). The Fig. 5.5 (e and f), reveals that the efficiency is decreasing from 36.95 % to 36.89 % as the thickness rises from 30 to 300 µm. Subsequently, the values of  $V_{OC}$  as well as  $J_{SC}$  were also found to decrease with thickness from 699.7 mV to 699.1 mV and from 64.78 mA/ $cm^2$  to 64.68 mA/ $cm^2$ , respectively. Therefore, the optimum value of the thickness of the active layer was found to be 30 µm. The variation in results might come from variations in the recombination of the carriers generated by photons under open circuit conditions.

After conducting simulations and optimizing the emitter, buffer, active, and BSF layers, we achieved a maximum efficiency of 36.95%. Furthermore, to ensure commercially viable conversion efficiency, we performed another round of simulation. During the simulation, we used reported values from literature [59-60] to set the parameters for the crystalline silicon layer. The values of the parameters are as follows:  $N_A = 9 \times 10^{16} \ cm^{-3}$ ,  $N_C = 2.8 \times 10^{19} \ cm^{-3}$ ,  $N_V = 1.12 \ eV$  at thickness = 30 µm. While conducting this simulation, the parameters of the remaining layers such as emitter layer (n-type Diamane), active layer, buffer layer, and BSF layer (p-type diamane) were kept at their optimum values. Following our analysis, the values for  $V_{OC}$ ,  $J_{SC}$ , FF, and  $\eta$  were found to be 699.7 mV, 44.21 mA/ $cm^2$ , 81.11%, and 25.09%, respectively.

The designed structure's maximum efficiency of 36.95% with open circuit voltage of 699.7 mV, current density of 64.78 mA/cm<sup>2</sup>, and fill factor of 81.52 % is surprisingly exceeding the modern Shockley–Queisser limit ~33% [61]. If we ignore absorption loss at the front contact, which in practice appears to be impossible, we obtain these high values. It should be noted that we used a silicon surface with a 90° texturing angle is a further factor contributing to the current density and efficiency values exceeding expectations. In order to understand how the texturing angle affects the performance of the designed cell, we have also simulated the cell and optimised the texturing angle for monolayer graphene throughout the range of 0 to 90° at an absorption loss of 2.3%. The results are shown in Fig. 5.6 (a and b). The optimised texturing angle is determined to be 90°. It appears that the closed packing density on the textured surface increases internal multiple reflection of light and increases absorption loss, both of which contribute to collecting extra charge carriers. This leads to the finding that the cell's conversion efficiency increases linearly with texturing angle [62]. After that, we optimized the monolayer graphene's absorption loss from 0 to 0.239, and the results are shown in Fig. 5.6 (c and d).

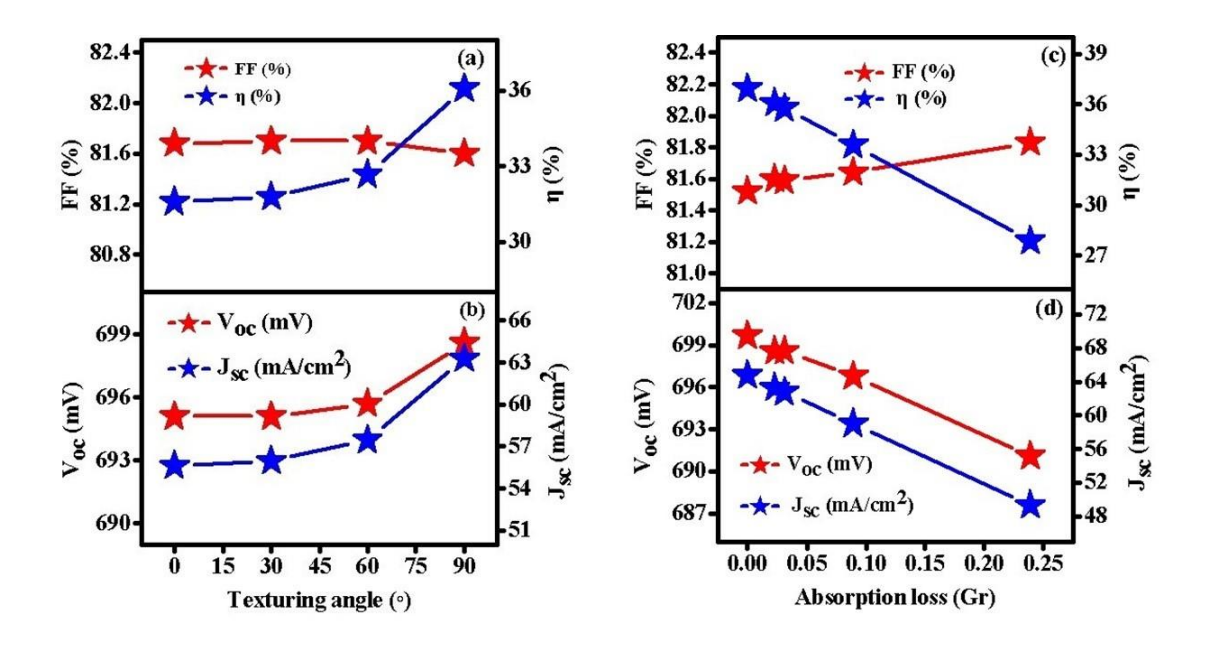


**Fig. 5.6** (a & b) Results obtained for the optimization of the angle at which texturing is done (texturing angle). (c & d) Results obtained for the optimization of absorption loss at the front contact (single layer graphene) while taking the texturing angle at 90°.

Fig. 5.6 (c and d) demonstrates that the value of both current density and conversion efficiency drops as a larger absorption loss occurs at the solar cell's front contact. This might have happened as a result of the front layer's absorption loss, which prevents more photons from entering the active layer and generating fewer photogenerated carriers therein [63-64]. It finds out that the designed solar cell at 90° texturing angle has a maximum physically achievable conversion efficiency of 27.88% with a current density of 49.3 mA/cm². It indicates that the conversion efficiency and current density values decline and approach the modern SQ efficiency limit when the absorption loss in the single-layer graphene is taken into account, which also supports our findings.

# **5.4 Summary**

To improve the efficiency of the HIT cell, we have simulated various parameters of the materials used in the cell. These materials include c-Si, a-Si: H(i), n-diamane, p-diamane, and graphene. We achieved the highest theoretical conversion efficiency of 27.88 %, accounting for absorption losses at the front contact, by using a 30 µmthick textured c-Si wafer under 1.5 G illumination. we have investigated the crucial role of texturing angle and absorption loss found at front contact, on the performance of the solar cell. If there are no losses at the front contact and with an optimized texturing angle of up to 90°, the efficiency can be increased beyond the current SQ limit of approximately 33 %. In this study, we have explored the patentability of oppositely doped diamane layers to be used as the electron/hole collection layers. We found that diamane can effectively replace amorphous silicon and other TMD materials used for electron/hole collecting layers, due to its tunable band gap. This study is expected to contribute to further advancements in the field of HIT cells.

#### REFERENCES

- [1] Wolf, S.D., Descoeudres, A., Holman, Z.C. and Ballif, C., 2012. High-efficiency silicon heterojunction solar cells: a review. *Green*, 2, 1, pp.7–24.
- [2] Lu, M., Bowden, S., Das, U. and Birkmire, R., 2007. Interdigitated back contact silicon heterojunction solar cell and the effect of front surface passivation. *Applied Physics Letters*, 91, 6, pp.67–70.

- [3] Ferdiansjah, Faridah and Mularso, K.T., 2011. Analysis of back surface field (BSF) performance in p-type and n-type monocrystalline silicon wafer. *E3S Web of Conferences*, 43, pp.01006.
- [4] Mingirulli, N., Haschke, J., Gogolin, R., Ferré, R., Schulze, T.F., Düsterhöft, J., Harder, N.P., Korte, L., Brendel, R. and Rech, B., 2011. Efficient interdigitated back-contacted silicon heterojunction solar cells. *Physica Status Solidi Rapid Research Letters*, 5, 5-6, pp.159–161.
- [5] Tomasi, A., Paviet-Salomon, B., Lachenal, D., De Nicolas, S.M., Ledinsky, M., Descoeudres, A., Nicolay, S., De Wolf, S. and Ballif, C., 2014. Photolithography-free interdigitated back-contacted silicon heterojunction solar cells with efficiency >21%. *Proceedings of the 2014 IEEE 40th Photovoltaic Specialists Conference (PVSC)*, pp.3644–3648.
- [6] Lee, S.Y., Choi, H., Li, H., Ji, K., Nam, S., Choi, J., Ahn, S.W., Lee, H.M. and Park, B., 2014. Analysis of a-Si:H/TCO contact resistance for the Si heterojunction back-contact solar cell. *Solar Energy Materials and Solar Cells*, 120, pp.412–416.
- [7] Masuko, K., Shigematsu, M., Hashiguchi, T., Fujishima, D., Kai, M., Yoshimura, N., Yamaguchi, T., Ichihashi, Y., Mishima, T., Matsubara, N., Yamanishi, T., Takahama, T., Taguchi, M., Maruyama, E. and Okamoto, S., 2014. Achievement of more than 25% conversion in a silicon heterojunction solar cell. *IEEE Journal of Photovoltaics*, 4, 6, pp.1433–1435.
- [8] Bhattacharya, S. and John, S., 2019. Beyond 30% conversion efficiency in silicon solar cells: a numerical demonstration. *Scientific Reports*, 9, pp.1–15.
- [9] Descoeudres, A., Holman, Z.C., Barraud, L., Morel, S., De Wolf, S. and Ballif, C., 2013. >21% efficient silicon heterojunction solar cells on n- and p-type wafers compared. *IEEE Journal of Photovoltaics*, 3, 1, pp. 53–58.
- [10] Seif, J.P., Descoeudres, A., Filipič, M., Smole, F., Topič, M., Holman, Z.C., De Wolf, S. and Ballif, C., 2014. Amorphous silicon oxide window layers for high-efficiency silicon heterojunction solar cells. *Journal of Applied Physics*, 115, 2, pp.024502.
- [11] Holman, Z.C., Descoeudres, A., Barraud, L., Fernandez, F.Z., Seif, J.P., De Wolf, S. and Ballif, C., 2012. Current losses at the front of silicon heterojunction solar cells. *IEEE Journal of Photovoltaics*, 2, 1, pp.7–15.
- [12] Li, F., Zhou, Y., Yang, Y., Dong, G., Zhou, Y., Liu, F. and Yu, D., 2020. Silicon heterojunction solar cells with MoOx hole-selective layer by hot wire oxidation-sublimation deposition. *Solar RRL*, 4, 9, pp.2000243.
- [13] Geissbühler, J., Werner, J., De Nicolas, S.M., Barraud, L., Hessler-Wyser, A., Despeisse, M., Nicolay, S., Tomasi, A., Niesen, B., De Wolf, S. and Ballif, C., 2015. 22.5% efficient silicon heterojunction solar cell with molybdenum oxide hole collector. *Applied Physics Letters*, 107, 8, pp.081601.
- [14] Azri, F., Meftah, A., Sengouga, N. and Meftah, A., 2019. Electron and hole transport layers optimization by numerical simulation of a perovskite solar cell. *Solar Energy*, 181, pp.372–378.
- [15] Bivour, M., Temmler, J., Steinkemper, H. and Hermle, M., 2015. Molybdenum and tungsten oxide: High work function wide band gap contact materials for hole selective contacts of silicon solar cells. *Solar Energy Materials and Solar Cells*, 142, pp.34–41.
- [16] Battaglia, C., De Nicolas, S.M., De Wolf, S., Yin, X., Zheng, M., Ballif, C. and Javey, A., 2014. Hole selective MoOx contact for silicon heterojunction solar cells. *Proceedings of the 2014 IEEE 40th Photovoltaic Specialists Conference (PVSC)*, pp.968–970.
- [17] Bakharev, P.V., Huang, M., Saxena, M., Lee, S.W., Joo, S.H., Park, S.O., Dong, J., Camacho-Mojica, D.C., Jin, S., Kwon, Y., Biswal, M., Ding, F., Kwak, S.K., Lee, Z. and Ruoff, R.S., 2020. Chemically induced transformation of chemical vapour

- deposition grown bilayer graphene into fluorinated single-layer diamond. *Nature Nanotechnology*, 15, 1, pp.59–66.
- [18] Sorokin, P.B. and Yakobson, B.I., 2021. Two-dimensional diamond—Diamane: Current state and further prospects. *Nano Letters*, 21, 13, pp.5475–5484.
- [19] Cheng, T., Liu, Z. and Liu, Z., 2020. High elastic moduli, controllable bandgap and extraordinary carrier mobility in single-layer diamond. *Journal of Materials Chemistry C*, 8, 39, pp.13819–13826.
- [20] Robinson, J.T., Burgess, J.S., Junkermeier, C.E., Badescu, S.C., Reinecke, T.L., Perkins, F.K., Zalalutdniov, M.K., Baldwin, J.W., Culbertson, J.C., Sheehan, P.E. and Snow, E.S., 2010. Properties of fluorinated graphene films. *Nano Letters*, 10, 8, pp.3001–3005.
- [21] Tantardini, C., Kvashnin, A.G., Azizi, M., Gonze, X., Gatti, C., Altalhi, T. & Yakobson, B.I., 2023. Electronic Properties of Functionalized Diamanes for Field-Emission Displays. *Applied Materials & Interfaces*, 15, 13, pp.16317–16326.
- [22] Niu, C., Zhang, J., Zhang, H., Zhao, J., Xia, W., Zeng, Z. & Wang, X., 2022. Configuration stability and electronic properties of diamane with boron and nitrogen dopants. *Physical Review B*, 105, 7, pp.1–10.
- [23] Raeisi, M., Mortazavi, B., Podryabinkin, E.V., Shojaei, F., Zhuang, X. & Shapeev, A.V., 2020. High thermal conductivity in semiconducting Janus and non-Janus diamanes. *Carbon*, 167, pp.51–61.
- [24] Zheng, Z., Zhan, H., Nie, Y., Xu, X., Qi, D. & Gu, Y., 2020. Single layer diamond–A new ultrathin 2D carbon nanostructure for mechanical resonator. *Carbon*, 161, pp.809–815.
- [25] Zhu, L., Li, W. & Ding, F., 2019. Giant thermal conductivity in diamane and the influence of horizontal reflection symmetry on phonon scattering. *Nanoscale*, 11, 9, pp.4248–4257.
- [26] Naima, Tyagi, P.K. & Singh, V., 2023. Potential application of novel graphene/diamane interface in silicon-based heterojunction with intrinsic thin layer solar cell. *Computational Materials Science*, 226, pp.112252.
- [27] Naima, Tyagi, P.K. & Singh, V., 2023. Affinity Optimization of Commercially Available Crystalline-Silicon Heterojunction Solar Cell by Using AFORS-HET Software. In: *Recent Advances in Nanotechnology ICNOC 2022*, Springer Proceedings in Materials 28, pp.111–115.
- [28] Naima, Tyagi, P.K. & Singh, V., 2022. N-type diamane: An effective emitter layer in crystalline silicon heterojunction solar cell. *Carbon Trends*, 9, pp.100204.
- [29] Stangl, R., 2010. Numerical Simulation of Solar Cells and Solar Cell Characterization Methods: the Open-Source on Demand Program AFORS-HET. In: Leendertz, C. (ed.), *IntechOpen*, Ch. 14, Rijeka.
- [30] Wang, J., Huang, X., Zhang, H., Wang, L., Huang, W., Kuang, S. & Huang, F., 2021. Diamond (001)—Si(001) and Si(001)—Ti(0001) interfaces: A density functional theory study. *Journal of Physics and Chemistry of Solids*, 150, pp.109865.
- [31] Liu, K., Zhang, S., Liu, B., Sun, M., Zhao, J. et al., 2019. Impact of positive space charge depletion layer on negatively charged and neutral centers in gold–diamond Schottky junction. *Carbon*, 152, pp.218–225.
- [32] Lin, Y., Li, X., Xie, D., Feng, T., Chen, Y. et al., 2013. Graphene/semiconductor heterojunction solar cells with modulated antireflection and graphene work function. *Energy & Environmental Science*, 6, 4, pp.108–115.
- [33] Sai, H., Hsu, H.J., Chen, P.W., Chen, P.L. & Matsui, T., 2021. Intrinsic Amorphous Silicon Bilayers for Effective Surface Passivation in Silicon Heterojunction Solar Cells: A Comparative Study of Interfacial Layers. *Physica Status Solidi A*, 218, 19, pp.1–9.

- [34] Qin, G., Wu, L. & Gou, H., 2021. Diamane: design, synthesis, properties, and challenges. *Functional Diamond*, 1, 2, pp.83–92.
- [35] Ge, L., Liu, H., Wang, J., Huang, H., Cui, Z. et al., 2021. Properties of diamane anchored with different groups. *Physical Chemistry Chemical Physics*, 23, 24, pp.14195–14204.
- [36] Rietwyk, K.J., Wong, S.L., Cao, L., O'Donnell, K.M., Ley, L. et al., 2013. Work function and electron affinity of the fluorine-terminated (100) diamond surface. *Applied Physics Letters*, 102, 9, pp.91604.
- [37] Bessler, R., Duerig, U. & Koren, E., 2019. The dielectric constant of a bilayer graphene interface. *Nanoscale Advances*, 1, 5, pp.1702–1706.
- [38] Chernozatonskii, L.A., Demin, V.A. & Kvashnin, D.G., 2021. Fully Hydrogenated and Fluorinated Bigraphenes–Diamanes: Theoretical and Experimental Studies. *C*, 7, 1, pp.1-12.
- [39] Chernozatonskii, L.A., Sorokin, P.B., Kvashnin, A.G. & Kvashnin, D.G., 2009. Diamond-like C2H nanolayer, diamane: Simulation of the structure and properties. *JETP Letters*, 90, 3, pp.134–138.
- [40] Shen, W., Pan, Y., Shen, S., Li, H., Zhang, Y. & Zhang, G., 2019. Electron affinity of boron terminated diamond (001) surfaces: A density functional theory study. *Journal of Materials Chemistry C*, 7, 31, pp.9756–9765.
- [41] Bouzidi, S., Barhoumi, M. & Said, M., 2021. Optical properties of Janus and non-Janus diamanes monolayers using ab-initio calculations. *Optik*, 235, pp.166642.
- [42] Fang, J., Vandenberghe, W.G. & Fischetti, M.V., 2016. Microscopic dielectric permittivities of graphene nanoribbons and graphene. *Physical Review B*, 94, 24, pp.245429.
- [43] Benda, V., 2018. A Comprehensive Guide to Solar Energy Systems: Crystalline Silicon Solar Cell and Module Technology.
- [44] Futako, W., Kamiya, T., Fortmann, C.M. & Shimizu, I., 2000. The structure of 1.5-2.0 eV band gap amorphous silicon films prepared by chemical annealing. *Journal of Non-Crystalline Solids*, 266–269 A, pp.630–634.
- [45] Cramarossa, F. & Pio, C., 1983. Deposition techniques and applications of amorphous silicon films. *Materials Chemistry and Physics*, 9, 3-4, pp.213–233.
- [46] Bae, S., Kim, H., Lee, Y., Xu, X., Park, J.-S. et al., 2010. Roll-to-roll production of 30-inch graphene films for transparent electrodes. *Nature Nanotechnology*, 5, 8, pp.574–578.
- [47] Piazza, F., Cruz, K., Monthioux, M., Puech, P. & Gerber, I., 2020. Raman evidence for the successful synthesis of diamane. *Carbon*, 169, pp.1–5.
- [48] Niu, C., Cheng, Y., Yang, K., Zhang, J., Zhang, H. et al., 2020. Boron-dopant enhanced stability of diamane with tunable band gap. *Journal of Physics: Condensed Matter*, 32, 13, pp.135503.
- [49] Revollo, H., Ferrada, P., Martin, P., Marzo, A. & del Campo, V., 2023. HIT Solar Cell Modeling Using Graphene as a Transparent Conductive Layer Considering the Atacama Desert Solar Spectrum. *Applied Sciences*, 13, 13, pp.9323.
- [50] Yang, X., Bian, J., Liu, Z., Li, S., Chen, C. & He, S., 2018. HIT Solar Cells with N-Type Low-Cost Metallurgical Si. *Advances in Optoelectronics*, 2018.
- [51] Padmanabhan, B., Ashok, A., Vasileska, D. & Zhang, Y.H., 2009. Drift diffusion modeling of solar cells. *AIP Conference Proceedings*, 1199, 1, pp.501–502.
- [52] Sachenko, A., Kostylyov, V., Gerasymenko, M., Korkishko, R. et al., 2015. Silicon solar cells efficiency analysis, Doping Type and Level Optimization. *arXiv preprint*.
- [53] Singh, J., 2007. Semiconductor Devices: Basic Principles, Wiley India Pvt. Limited.
- [54] Rana, F., 2011. Chapter 2: Semiconductor Heterostructures. *Semiconductor Optoelectronics*, pp.1–29.

- [55] Borah, C.K., Tyagi, P.K. & Kumar, S., 2020. The prospective application of a graphene/MoS<sub>2</sub> heterostructure in Si-HIT solar cells for higher efficiency. *Nanoscale Advances*, 2, 8, pp.3231–3243.
- [56] Patel, K. & Tyagi, P.K., 2017. P-type multilayer graphene as a highly efficient transparent conducting electrode in silicon heterojunction solar cells. *Carbon*, 116, pp.744–752.
- [57] Zhong, C.L., Luo, L.E., Tan, H.S. & Geng, K.W., 2014. Band gap optimization of the window layer in silicon heterojunction solar cells. *Solar Energy*, 108, pp.570–575.
- [58] Lisheng, W., Fengxiang, C. & Yu, A., 2011. Simulation of High Efficiency Heterojunction Solar Cells with AFORS-HET. *Journal of Physics: Conference Series*, 276, pp.012177.
- [59] Elyukhin, V.A., 2016. Chapter 1 Semiconductor Materials & Physics. *Statistical Thermodynamics of Semiconductor Alloys*, pp.1–23.
- [60] Hu, C.C., 2010. *Modern Semiconductor Devices for Integrated Circuits*. Ch. 1, Prentice Hall, United States.
- [61] Zanatta, A.R., 2022. The Shockley–Queisser limit and the conversion efficiency of silicon based solar cells. *Results in Optics*, 9, pp.100320.
- [62] Yadav, C. & Kumar, S., 2022. Numerical Simulation for Optimization of Ultra-thin n-type AZO and TiO<sub>2</sub> Based Textured p-type c-Si Heterojunction Solar Cells. *SILICON*, 14, 9, pp.4291–4299.
- [63] Gee, J.M., 1988. The effect of parasitic absorption losses on light trapping in thin silicon solar cells. *IEEE Photovoltaic Specialists Conference*, 1, pp.549–554.
- [64] Tiwari, P., Patel, K., Krishnia, L., Kumari, R. & Tyagi, P.K., 2017. Potential application of multilayer n-type tungsten diselenide (WSe<sub>2</sub>) sheet as transparent conducting electrode in silicon heterojunction solar cell. *Computational Materials Science*, 136, pp.102–108.

## CHAPTER 6

# SIGNIFICANCE OF PASSIVATING C-SI LAYER IN SILICON HETEROJUNCTION SOLAR CELLS

This study examines the impact of layer thickness and bandgap variation on the performance of single-junction HJ and HIT solar cells using AFORS-HET simulations. Both designs use c-Si as the absorber with a BSF layer for improved carrier reflection and passivation. The optimized HJ cell achieved 26.86% efficiency, while the HIT solar cell showed further improvement, reaching an efficiency of 29.38% through comprehensive parameter optimization. The ideal emitter bandgap was found to be  $\sim$ 1.4 eV, ensuring efficient carrier selectivity and minimal recombination. Key parameters include  $V_{OC}$  of 631.2 mV,  $J_{SC}$  of 51.16 mA/cm², and FF of 83.16% for the HJ cell; and  $V_{OC}$  of 683 mV,  $J_{SC}$  of 52.74 mA/cm², and FF of 81.55% for the HIT cell. Additional analyses such as J–V characteristics, spectral response, and quantum efficiency, were also carried out to validate and understand the performance behavior of both cell types.

The results reported in this chapter have been published in Naima et. al. Semicond. Sci. Technol. 39 (2024) 125021.

#### 6.1 Introduction

The greatest challenge in the world at present is to find a green energy source that can meet the world's growing energy needs and decrease its dependence on traditional energy sources, which are harmful to both human beings and the environment, especially fossil fuels [1]. To meet climate goals by the end of this century, we must move promptly to a green economy. This means transitioning the world economy from being dominated by the fossil-fuelled (brown) sector to being dominated by the low-emission (green) sector. By utilising PV technology, the sun, which is a prominent energy source across the globe, may be effectively utilised to generate electricity. This technology has the ability to fulfil the growing need for power. As we know that primary renewable energy sources with zero operating carbon emissions are PV solar cells [2, 3]. Consequently, photovoltaic solar cell is acknowledged as an indispensable energy source, and their viability is essentially evaluated by their power conversion efficiency, commonly referred to as PCE. Wafer-based c-Si solar cell is the dominant technology in the global photovoltaic market due to their cost-effectiveness, robust stability, and high PCE [2]. The c-Si wafer accounts for around 20% of the overall production cost of the PV module [4]. Thus, the production cost of PV modules can be reduced by systematically decreasing the thickness of wafers and, consequently, the amount of crystalline material used will be lowered [4, 5]. Recently, there has been a major emphasis on to design and manufacture of extremely efficient solar cells by utilising innovative materials and topologies. Various materials have been explored and utilised [6-10] to enhance efficiency and reduce the overall cost of solar cells. In a recent study published by our group, Naima et al [9, 10] utilised a new 2D material called diamane in solar cells. They examined and studied the potentiality of Dn as TCE and emitter layer in HJ as well as HIT solar cells, respectively, to significantly enhance the PCE. However, [9, 10] did not take into account Auger electron and hole recombination as well as band-to-band recombination. Furthermore, it has been reported that in HIT architectures, the thickness of the active wafer can be reduced despite having excellent efficiency. In the HIT structure, the primary reason for contributing to enhanced efficiency is the utilisation of an extremely thin layer of a-Si: H (i) that mitigates defects on the surface of the crystalline silicon wafer. By depositing a-Si: H (i) layers onto the c-Si wafers, we may achieve efficient passivation of the hetero-interface, consequent a remarkably low density of interface defects [1, 11-12]. However, it is essential to precisely calibrate the thickness of the passivating layer in order to have a strong passivation, while avoiding any adverse effect on the potential drop across the layer. In addition, researchers have also improved the efficiency of the cell by around 27% through simulation studies by optimizing the basic parameters [1]. Still, there remains ample potential to improve the efficiency of solar cells by methodically improving their fundamental components. As we know that the optimal performance of a photovoltaic system typically relies on three factors: the quantity of incident light that enters the absorber layer, the passivation of surface imperfections, and the efficient accumulation of photo-generated charge carriers. In the present study, we have replaced the standard ITO in solar cells with single-layer graphene to enhance light absorption towards the absorber [13, 14]. Recently, it has been demonstrated that graphene can be used as an efficient TCE material in both hybrid inorganic-organic tandem (HIT) and simple heterojunction solar cells [15, 16]. This is due to its remarkable transparency, which reaches approximately 97.4% [17]. According to reports, the transmittance of monolayer CVD graphene is approximately 97.4%. However, this value declines as the layer numbers increase. Therefore, in this study, we exclusively utilised singlelayer graphene with an atomic thickness. Furthermore, crystalline silicon surfaces were also passivated employing thin layers of a-Si: H (i) on both the front and rear surfaces. The primary reason for passivating the front and rear layers of c-Si is the significant conduction band bending and mere reduction of interface sites [18]. An additional layer known as the BSF layer was employed on the back side of p-type c-Si to further enhance the progress in PCE of HJ & HIT cells [12]. The HJ and HIT solar cell with BSF layer deposited on the back side of the Si wafer is named as HJBSF and HITBSF. This BSF layer decreases recombination losses, which effectively blocks minority charge carriers from making contact with the a-Si: H/c-Si interface on the rear side [12]. A HJBSF cell is designed by introducing an extra p-doped a-Si: H (i) layer to the backside of the p-doped c-Si wafer in a HJ solar cell. Another cell, which is HITBSF made by adding a p-doped a-Si: H (i) BSF layer to the backside of a p-doped c-Si wafer in a standard HIT solar cell [1]. The HJBSF cell achieved its highest efficiency of 25.56% when the c-Si thickness was 98 µm. It is worth mentioning that the HITBSF cell achieves the highest efficiency, 24.85% with a 58 µm thick layer of c-Si [1]. Thus, bifacial cells taking c-Si are highly significant and advantageous since they effectively reduce the thickness of the silicon layer as well as the making cost of solar cells. Recently, Brendel et al claimed a world record efficiency of 29% for bifacial solar cells [19].

Furthermore, cell efficiency is reduced when parasitic photon absorption occurs in doped hydrogenated amorphous silicon, since the active layer's ability to generate photo carriers is greatly reduced [20, 21]. Therefore, alternative materials for doped a-Si: H layers need to be investigated. It was recently demonstrated by Bivour et al that doped a-Si: H might be replaced in HIT solar cells by WO<sub>x</sub> and MoO<sub>x</sub>, which have a wide bandgap and a high work function [7]. Furthermore, diamane possesses a tunable bandgap (0–3.52 eV), high electron (2732 cm<sup>2</sup>/Vs) and hole (1565 cm<sup>2</sup>/Vs) mobility, larger work function (3.5–6.5 eV), and stable doping with nitrogen and boron atoms [22-25]. Because diamane has these extraordinary properties, and can be used instead of doped a-Si: H layers in HJ and HIT cells, simulated by using AFORS-het software [26]. It is well known that a heterojunction is formed when two semiconducting materials with different band gaps are joined together, resulting in the creation of band offsets and band discontinuities. The potential of heterojunctions became apparent in the 1950s, when they were initially employed in various technologies such as solar cells, light-emitting diodes, and lasers [12, 27]. Furthermore, HJ solar cell technology integrates the exceptional efficacy of c-Si cell technology combined with the cost-effective a-Si: H cell technology in a single cell configuration. Nevertheless, the efficiency of this technology is hindered by a significant recombination rate at the interface involving a-Si: H and c-Si, leading to a decline in performance. To address this constraint, a layer of intrinsic a-Si: H has been inserted between the doped a-Si: H and c-Si layers. The solar cell with this specific configuration was referred to as the HIT solar cell [1]. Furthermore, it has been reported that silicon HIT solar cells with heterojunction back contact (HBC) can achieve a remarkable efficiency of 27.09% [28], making it suitable for commercial-scale production. Recently, LONGi Green Energy Technology Co. Ltd, a module manufacturer, has announced that silicon HBC technology has achieved 27.30% efficiency [29]. In the presented chapter, the AFORS-HET programme was used as a computer simulation tool for analysing the performance of HJ and HIT cells. Two solar cell configurations were simulated: (i) a HJ solar cell with a p-type diamane as the BSF layer and an n-type diamane as the emitter layer; and (ii) a HIT solar cell with a-Si: H (i) layers used for passivation and p-type and n-type diamane as the BSF and emitter layers, respectively to efficiently suppress the recombination of minority carriers near the contacts. In both configurations, single-layer graphene was used as a TCE, while gold was used as the metal electrode on the back. Utilising the AFORS-HET software [26], we evaluated the performance of both HJBSF and HITBSF solar cells,

optimising critical parameters such as bandgap energy and layer thicknesses in the single-junction HJBSF and HITBSF configurations, which are shown in Fig. 6.1 (a) and (b) as (i) Gr/Dn(n)/c-Si(p)/Dn(p)/Au and (ii) Gr/Dn(n)/a-Si: H(i)/c-Si(p)/a-Si: H(i)/Dn(p)/Au. HJBSF and HITBSF models are studied in this paper, which further reveals how passivation affects solar cell efficiency. Furthermore, in the presented study, Auger electron and hole recombination as well as band-to-band recombination for diamane and a-Si: H (i) layer were not taken into account.

### 6.2 Simulation model and junction formation

AFORS-HET has proved to be a valuable simulator for accurately modelling silicon HJ and HIT solar cells. AFORS-HET software provides methods for simulating as well as evaluating the performance of solar cells [26]. This program addresses the 1-D semiconductor equation, specifically Poisson's equation, transport and continuity equations related to Shockley-Reed Hall statistics. It uses finite differences to calculate solutions under various conditions, including the (a) equilibrium mode, (b) equilibrium state, (c) equilibrium state with slight additional sinusoidal perturbations, (d) simple transitory mode, which permits any change in external quantities. This allows the selection of multiple boundary conditions, including metal/insulator/semiconductor contacts, or flat band or Schottky-like metal/semiconductor contacts. In addition to this, one can also select insulating boundary contacts. The system's interface is designed to be simple to understand and allows customisation of parameter values to analyse the performance of the cell. The simulated HJBSF structure is modelled as Gr/n-Dn/p cSi/p-Dn/Au, while the HITBSF cell structure is modelled as Gr/n-Dn/intrinsic type a-Si: H/p-cSi/intrinsic type a-Si: H/p-Dn/Au, as seen in Fig. 6.1 (a) and 6.1 (b). Solar cell modelling of both HJBSF and HITBSF has been organised into the following subsections: (1) optimisation of the thickness and bandgap of the HJBSF & HITBSF structure, which includes the emitter, absorber, and BSF layers. (2) The thickness and E<sub>g</sub> of the intrinsic a-Si: H passivation layer have been optimised. The plausible values of the parameters reported in the literature have been used in the simulations for both the HJBSF and HITBSF models, tabulated in Tables 6.1 and 6.2 [30-49]. Since minority carrier concentrations in doped semiconductors are much lower than majority carrier concentrations, we did not consider them in this analysis.

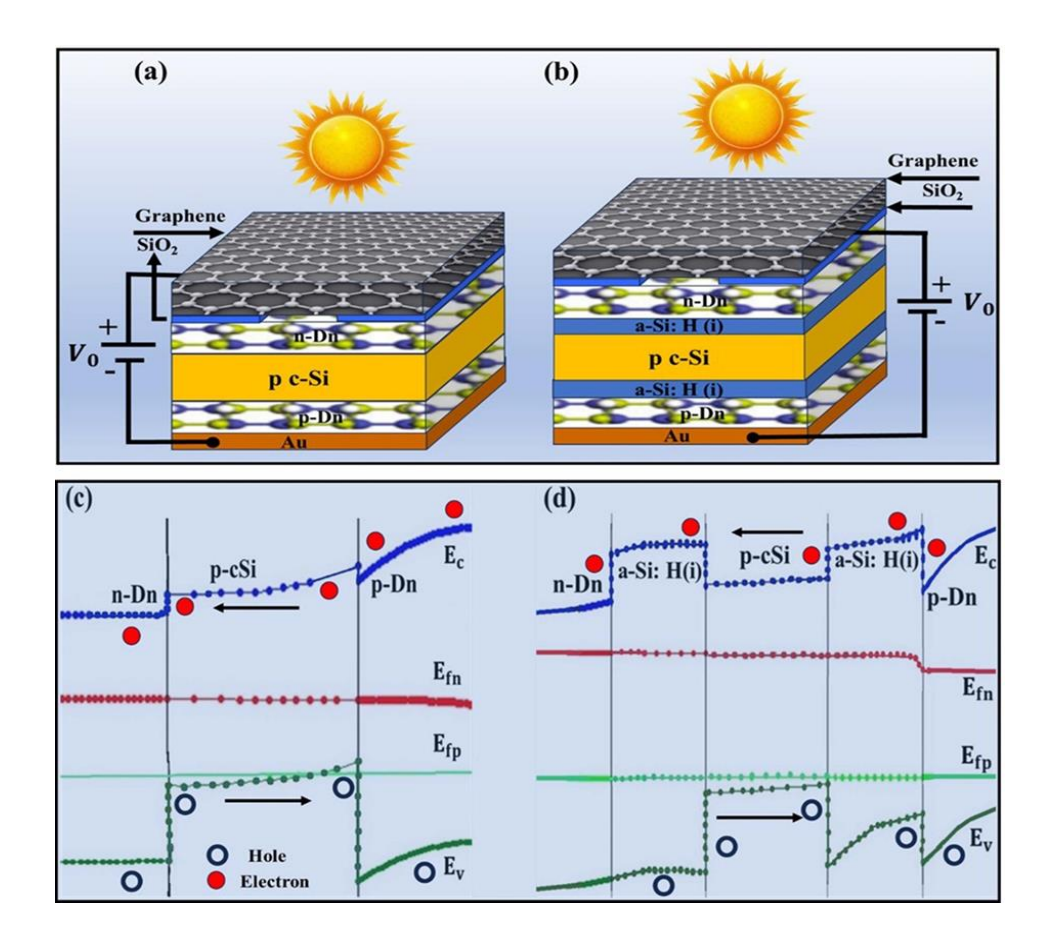


**Fig. 6.1** Schematic of the designed HJBSF (a) and HITBSF (b) cells. The band bending diagram showing the separation of charges at the hetero-interfaces for the HJ (c) and HIT (d) cell.

This is because the dopant concentration in these layers is typically substantially greater than the intrinsic carrier concentration  $(n_i)$  of doped silicon or doped diamane. Since acceptor atoms are not intentionally added to n-Dn, they are considered insignificant, so acceptor density  $(N_A)$  can be taken to zero. The analysis is made simpler by concentrating only on the majority carriers, which are electrons. In the same vein, the donor density  $(N_D)$  in p-Dn is taken to be zero since donor atoms are not intentionally added, so their concentration is negligible. The values of parameters of front and rear contacts have been fixed at values given in Table 6.3, which are kept the same for both HJBSF and HITBSF solar cells [48,50]. To determine the no. of electrons and holes generated by absorption of light at a specific position (x) and time (t), per unit volume and per second, we have used the Lambert-Beer model. This selection was made due to the presence of a textured surface in this particular scenario. In the presented simulation, we considered metal contact flatbands.

**Table 6.1** List of the initial values of all parameters used for performing the simulation in HJBSF cell [30–49].

Parameter	N-type Diamane	P–type c–Si	P–type Diamane
Thickness	0.34 nm	$80~\mu\mathrm{m}$	2.04 nm
Dielectric constant	11	11.9	11
Electron affinity (eV)	4.1	4.05	4.1
Band gap (eV)	1.4	1.12	1.6
$N_{\rm C}~({\rm cm}^{-3})$	$3 \times 10^{18}$	$3 \times 10^{19}$	$1 \times 10^{19}$
$N_{\rm V}~({\rm cm}^{-3})$	$3 \times 10^{18}$	$3 \times 10^{19}$	$1 \times 10^{19}$
$\mu_{\rm n}  ({\rm cm}^2 {\rm V}^{-1} {\rm s}^{-1})$	2732	1104	2732
$\mu_{\rm p}({\rm cm^2V^{-1}s^{-1}})$	1565	420	1565
$N_{\rm A}~({\rm cm}^{-3})$	0	$1 \times 10^{18}$	$5 \times 10^{18}$
$N_{\rm D}$ (cm <sup>-3</sup> )	$1 \times 10^{18}$	0	0
$V_{\rm e}~({\rm cm s^{-1}})$	$1 \times 10^7$	$1 \times 10^7$	$1 \times 10^7$
$V_{\rm h}~({\rm cm s^{-1}})$	$1 \times 10^7$	$1 \times 10^7$	$1 \times 10^7$
Auger electron	0	$2.2 \times 10^{-31}$	0
recombination coefficient (cm <sup>6</sup> s <sup>-1</sup> )			
Auger hole recombination coefficient (cm <sup>6</sup> s <sup>-1</sup> )	0	$9.9\times10^{-32}$	0
Band- to- band recombination coefficient (cm <sup>3</sup> s <sup>-1</sup> )	0	$9.5 \times 10^{-15}$	0

The illumination source employed is solar radiation of AM 1.5 and 100 mWcm<sup>-2</sup> of power density. To achieve optimal ohmic contact at the metal-semiconductor interface, the flat band Schottky front and back interfaces were considered. The Shockley-Read-Hall recombination algorithm is applied to elucidate the process of recombination in various semiconductor layers, also the drift-diffusion model is chosen for electron and hole transportation.

**Table 6.2** List of the initial parameter values of all layers used for performing simulation over HITBSF cell [30–49].

Parameter	n-Dn	Front a- Si: H (i)	p-cSi	Back a- Si: H (i)	p-Dn
Thickness	0.34 nm	3 nm	$30 \mu m$	3 nm	1.7 nm
Dielectric constant	11	11.9	11.9	11.9	5
Electron affinity (eV)	4.1	3.9	4.05	3.9	4.1
Band gap (eV)	1.4	1.6	1.12	1.6	1.4
$N_{\rm C}~({\rm cm}^{-3})$	$1 \times 10^{18}$	$1 \times 10^{21}$	$3 \times 10^{19}$	$3 \times 10^{21}$	$1 \times 10^{19}$
$N_{\rm V}~({\rm cm}^{-3})$	$1 \times 10^{18}$	$1 \times 10^{21}$	$3 \times 10^{19}$	$3 \times 10^{21}$	$1 \times 10^{19}$

$\mu_{\rm n}  ({\rm cm}^2 {\rm V}^{-1} {\rm s}^{-1})$	2732	20	1104	20	2732
$\mu_{\rm p}  ({\rm cm}^2 {\rm V}^{-1} {\rm s}^{-1})$	1565	5	420	5	1565
$N_{\rm A}~({\rm cm s^{-1}})$	0	0	$1 \times 10^{18}$	0	$5 \times 10^{19}$
$N_{\rm D}~({\rm cm s^{-1}})$	$1 \times 10^{20}$	0	0	0	0
$V_{\rm e}~({ m cm s^{-1}})$	$1 \times 10^{7}$	$1 \times 10^{7}$	$1 \times 10^{7}$	$1 \times 10^{6}$	$1 \times 10^{7}$
$V_{\rm h}~{\rm (cms^{-1})}$	$1 \times 10^7$	$1 \times 10^7$	$1 \times 10^{7}$	$1 \times 10^6$	$1 \times 10^7$
Auger electron	0	0	$2.2 \times 10^{-31}$	0	0
recombination coefficient					
$(cm^6s^{-1})$					
Auger hole	0	0	$9.9 \times 10^{-32}$	0	0
recombination coefficient					
$(cm^6s^{-1})$					
Band- to- band	0	0	$9.5 \times 10^{-15}$	0	0
recombination coefficient					
$(cm^3s^{-1})$					

The proposed solar cell configurations exhibit concentration gradients at the n-Dn/p-cSi interface. This gradient results in the dispersion of surplus carriers, while the stationary ions stay in the interface vicinity. A space-charge region is created at the contact due to the presence of stationary ions, which generates an electric field. The presence of this electric field in the space charge region is responsible for the band bending observed at the interfaces, as seen in Fig. 6.1 (c) and (d). The positioning of Fermi levels at the junction is the consequence of the bending of energy levels. The valence and conduction level experience a sudden shift at the junction as a consequence of the space charge effect. This band offset configuration allows for the selective carriage of one type of minority carrier while impeding the movement of the other type of minority carrier. Consequently, the photo-generated carriers are separated by using a carrier-selective layer, which leads to a lower recombination rate of charge carriers [30]. Therefore, HJ and HIT solar cells consist of carrier-selective layers, have been discovered to have a crucial impact in enhancing the conversion efficiency of solar cells. Therefore, differently doped diamane layers are being used as the carrier-selective layers or the emitter and BSF layers.

**Table 6.3** Values of parameters of front and back contacts used in the designed solar cells (both HJBSF & HITBSF) investigated in this work [48, 50].

Parameter	Front contact	Back contact
Material	Graphene	Au

Thickness	0.334 nm	$10 \mu m$
Work function	4.3 eV	5.4 eV
(eV)		
Internal	0	0
reflection		
External	0	0
reflection		
Surface	Textured	Plane
condition		
Texturing angle	89°	$0^{\circ}$
$(\delta)$		
Absorption loss	0.023	0

**Table 6.4** Optimum values of the simulated parameters of layers, n-Dn, p-Dn, p-cSi and front/back passivation layers of HJBSF and HITBSF cell.

		HJBSF cell				HITBSF cell		
Optimized parameter	n-Dn	p-c-Si	p-Dn	n-Dn	Front a-Si: H (i)	p-c-Si	Back a-Si: H (i)	p-Dn
Thickness	1.36 nm	80 μm	2.04 nm	0.34 nm	3 nm	35 μm	7 nm	0.34 nm
E <sub>g</sub> (eV)	1.4 eV	1.12 eV	1.6 eV	1.4 eV	1.6 eV	1.12 eV	1.6 eV	1.4 eV
$N_A (cm^{-3})$	0	$1 \times 10^{18}$	$5 \times 10^{18}$	0	0	$1 \times 10^{18}$	0	$5 \times 10^{19}$
$N_D (cm^{-3})$	$\begin{array}{c} 1\times\\ 10^{18} \end{array}$	0	0	$1 \times 10^{20}$	0	0	0	0
$N_{\text{C}}/_{\text{V}}$	$\begin{array}{c} 3\times \\ 10^{18} \end{array}$	$3 \times 10^{19}$	$1 \times 10^{19}$	$1 \times 10^{18}$	$1\times10^{21}$	$3 \times 10^{19}$	$3 \times 10^{21}$	$1 \times 10^{19}$
χ	4.1	4.05	4.1	4.1	3.9	4.05	3.9	4.1
$\varepsilon_{\rm r}$	11	11.9	11	11	11.9	11.9	11.9	5

#### 6.3 Results and discussion

#### 6.3.1 Fabrication details

This particular design can be developed on an industrial scale by using relatively thin silicon wafers, hence decreasing the overall production cost of solar cells. HJ solar cells may be fabricated by using a p-type textured crystalline silicon wafer. Bilayer graphene

synthesised using CVD [51] can be transferred onto both sides of the p-cSi wafer using the chemical methods described in [48]. Furthermore, hydrogenation of graphene by the chemisorption of H generated from the dissociation of H<sub>2</sub> in a hot filament reactor at low temperature and low pressure results in subsequent structure conversion of bilayer graphene into highly hydrogenated genuine diamane [49]. To create stable n and p-type diamane, these layers are then doped with boron and nitrogen [22, 23]. Subsequent to that, a single layer of graphene is chemically transferred to the front of the stack to serve as the TCE, or antireflecting layer [48]. Finally, the metal electrode of Au that is responsible for conducting current across the external circuit is made by screen printing or deposited on the front and rear surfaces of the cell [52]. In this way, the simple heterojunction with BSF layer has been fabricated as shown in Fig. 6.1 (a). The main distinction between a HJBSF and HITBSF solar cell is the process of passivation of the absorbing layer, to stop recombination losses arising because of dangling bonds present on c-Si. This passivation can be done by using any of the methods, such as CVD, glow discharge, laser decomposition, and sputtering [47]. Two intrinsic thin layers of a-Si: H, are deposited on both the front and rear surfaces of the c-Si substrate, and the BSFHIT structure can be fabricated as shown in Fig. 6.1 (b) [47].

# 6.3.2 Optimisation of the thickness of the n-Dn, p-Dn, and p-cSi layers in HJBSF and HITBSF cell

In this part, we have first optimised the thickness of n-Dn, p-Dn and p-cSi layers of HJBSF and HITBSF cells, and the expected results are shown in Figures 6.2–6.4, respectively. For a heterojunction solar cell, the initially optimized efficiency at the values given in Table 6.1 was 26.86% at a single layer n-Dn. To analyse the effect of emitter layer thickness on HJBSF cell's efficiency and have varied the n-type Dn's layer number from one to six. Fig. 6.2 (a) and 6.2 (b) depict the optimization of n-type diamane layer thickness of HJBSF cell concerning  $V_{\rm OC}$ ,  $J_{\rm SC}$ , FF and  $\eta$ . During the optimisation process, the thicknesses of the p-c-Si layer and the p-Dn BSF layer are maintained at 80  $\mu$ m and 2.04 nm, respectively. However, all the remaining parameters are maintained at their initial values given in Table 6.1. It is seen from Fig. 6.2 (a) and 6.2 (b), a noticeable deterioration was found in the conversion efficiency from 26.86% to 25.99% as the emitter layers vary from 1 to 6. The decline in efficiency can be attributed to the simultaneous decrease in FF from 83.14% to

82.5% & J<sub>SC</sub> from 51.17 mA cm<sup>-2</sup> to 48.76 mA/cm<sup>2</sup> as layer's thickness increases. When the emitter layer's thickness increases, a high density of injected carriers may enhance the scattering of the carriers that limits the carrier's conduction. Consequently,  $J_{SC}$  &  $\eta$  were observed to decrease. Conversely, the V<sub>OC</sub> was shown to have increased from 631.2 mV to 646.2 mV as the emitter layer number increased from 1 to 6. Reducing the emitter layer's thickness can increase J<sub>SC</sub> by allowing extra photons to reach the active layer, minimising parasitic absorption, and facilitating effective transfer of the photo-generated charge carrier through the layer due to lower resistance. Therefore, the best optimized thickness of the emitter layer for HJBSF cell was determined to be 0.34 nm. After optimizing the emitter layer's thickness of HJBSF cell, we have also optimized emitter layer's thickness in HITBSF solar cell within the same range, specifically from layer 1 to layer 6 as depicted in Fig. 6.2 (c) and 6.2 (d). Furthermore, it was observed that when the emitter layer's thickness expands, Voc got slightly increase from 682.4 mV to 683 mV and then remain constant whereas, J<sub>SC</sub>, FF and η were noticed to deteriorate from 52.27 mAcm<sup>-2</sup> to 52.01 mAcm<sup>-2</sup>, 81.57% to 80.82% & 29.09% to 28.71%, respectively with an increase in thickness. The behaviour of J<sub>SC</sub>, FF, and η is similar to that observed HJBSF solar cell structure; i.e., their values continuously decline, which might also be related to surface absorption losses [30]. Because of the low resistance, photo-generated charge carriers can more easily move across the thin emitter layers and enhance the efficiency [53]. Furthermore, Voc remained consistent at ~683 mV for all variations in emitter layer thickness, which ranged from layer 2 to layer 6. This uniformity in the V<sub>OC</sub> value can be attributed to the passivation that occurred as a result of the insertion of a thin a-Si: H (i) layer, which decreases the chances of recombination [30]. The optimized value for the emitter layer's thickness was observed as 0.34 nm. Therefore, we have set the thickness of n-Dn to 0.34 nm for both HJ and HIT cells in order to conduct further simulations on both cells. After optimizing the thickness of emitter layer for both HJBSF and HITBSF cell, the second parameter that we have optimized here is the thickness of BSF layer i.e., p-type diamane layer for both cells and the obtained outcomes are shown in Fig. 6.3 (a)-6.3 (d). To examine the impact of thicknesses of BSF layer on the efficiency of the HJ & HIT cell, we have simulated the number of p-Dn layers for both cells. The range of layer numbers tested was from 1 to 6, as depicted in Fig. 6.3 (a) -6.3 (d).

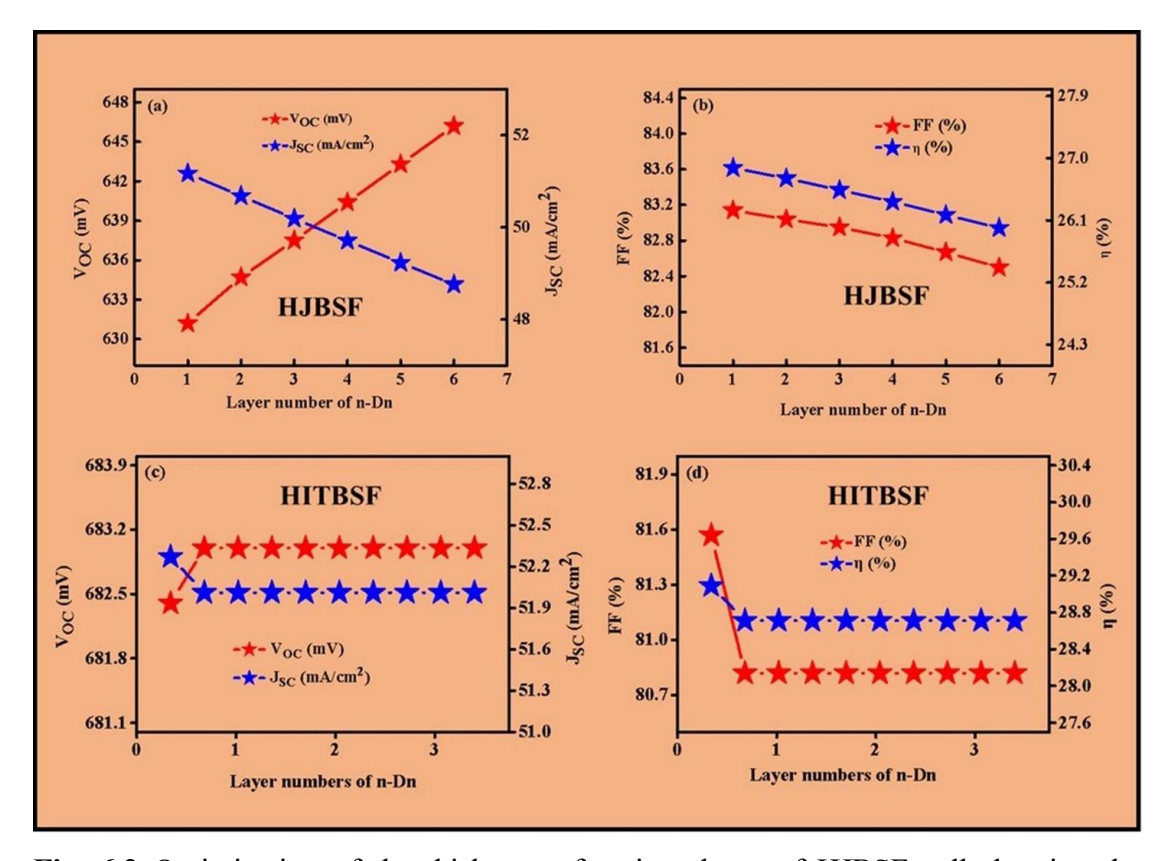


**Fig. 6.2** Optimization of the thickness of emitter layer of HJBSF cell showing the variation of  $V_{OC}$ ,  $J_{SC}$  (a) and FF,  $\eta$  (b), respectively. Optimization of the thickness of the emitter layer of HITBSF cell showing the variation of  $V_{OC}$ ,  $J_{SC}$  (c) and FF,  $\eta$  (d), respectively, with layer numbers of n-type diamane, acting as the emitter layer.

For the HJ cell, it has been observed that as the thickness of the BSF layer increased, all the parameters such as  $J_{SC}$ , FF, and  $\eta$  were also found to increase. Specifically,  $J_{SC}$  increases from 50.86 mAcm<sup>-2</sup> to 51.17 mAcm<sup>-2</sup>, fill factor increases from 83.11% to 83.14%, and  $\eta$  increases from 26.68% to 26.86%. However, the  $V_{OC}$  parameter stays constant at 631.2 mV, as shown in Fig. 6.3 (a) and 6.3(b). Additionally, we have also carried out the simulation to optimize the BSF layer thickness of the HIT cell, while maintaining previously simulated parameters at their optimal values. In order to conduct the simulation, we have systematically changed the number of layers of p-Dn from 1 to 6. The results of this variation may be observed in Fig. 6.3, specifically in figures 6.3(c) and 6.3(d). It has been observed that  $V_{OC}$  remains constant at 683 mV as layer number increases.  $J_{SC}$ , FF, and  $\eta$  exhibit similar behaviour, with their values being constant at 52.74 mAcm<sup>-2</sup>, 81.55%, and 29.38%, respectively, regardless of thickness variation. This can be understood as the electric field at the n-Dn/p-cSi is unaffected by the insertion of BSF layers. However, at p-

cSi/p-Dn junctions, the BSF enhances the field effect passivation, causing the expulsion of minority carriers from the interface between c-Si/Dn at the rear side. This results in a further reduction of recombination losses.

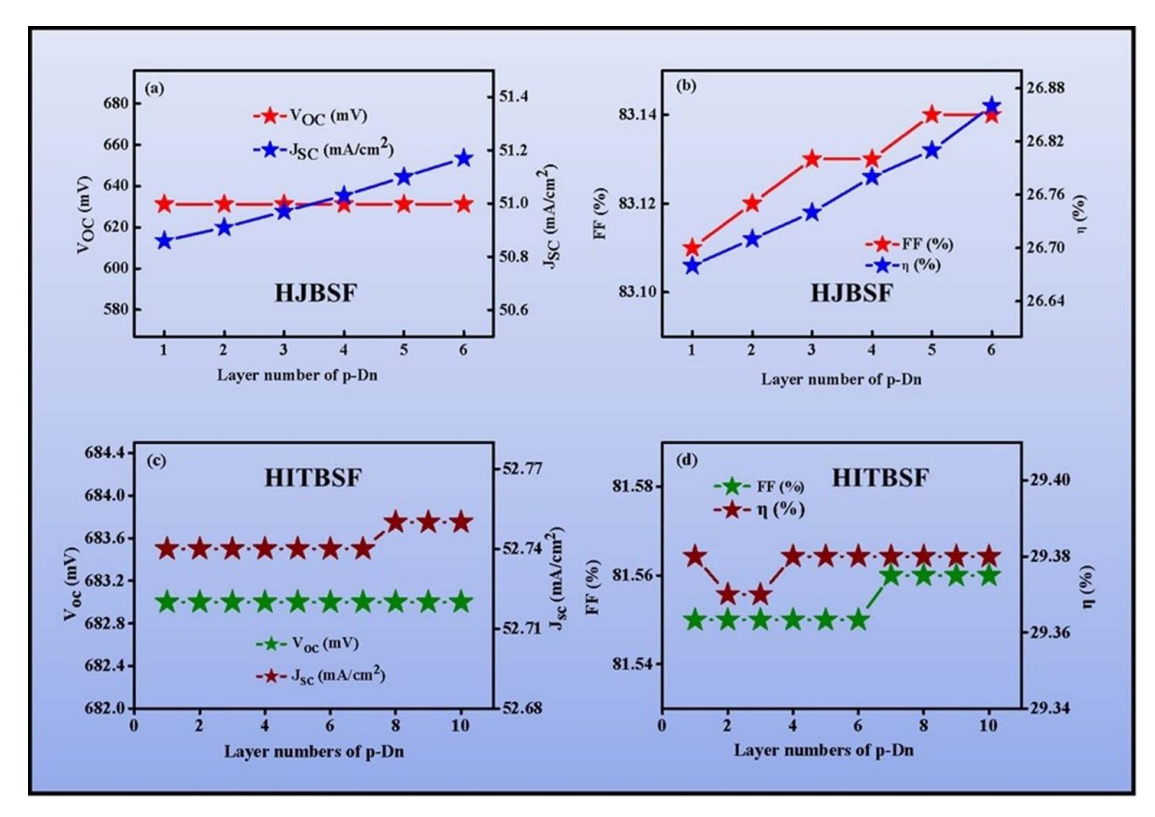


**Fig. 6.3** Optimization of the thickness of BSF layer of HJ cell showing the variation of  $V_{OC}$ ,  $J_{SC}$  (a) and FF,  $\eta$  (b), respectively. Optimization of the thickness of BSF layer of HIT cell showing the variation of  $V_{OC}$ ,  $J_{SC}$  (c) and FF,  $\eta$  (d), respectively with layer numbers of p-type diamane, acting as the BSF layer.

So, it can be stated that the efficiency of both HJBSF as well as HITBSF cells is significantly increased by the insertion p-type BSF layer into a basic HJ and HIT cell. This can be explained as the p-type BSF layer introduces a barrier for the transport of electrons, preventing them from entering the p-region. Therefore, the presence of BSF reduces the probability of recombination. The optimal thickness for the BSF layer was determined to be 2.04 nm for both types of cells. This led to the highest possible efficiency of 26.86% for the HJBSF cell and 29.38% for the HITBSF cell, respectively. After that, we optimised the p-cSi's layer thickness, here it is working as the active and absorbent layer in the HJBSF and HITBSF solar cells, respectively.

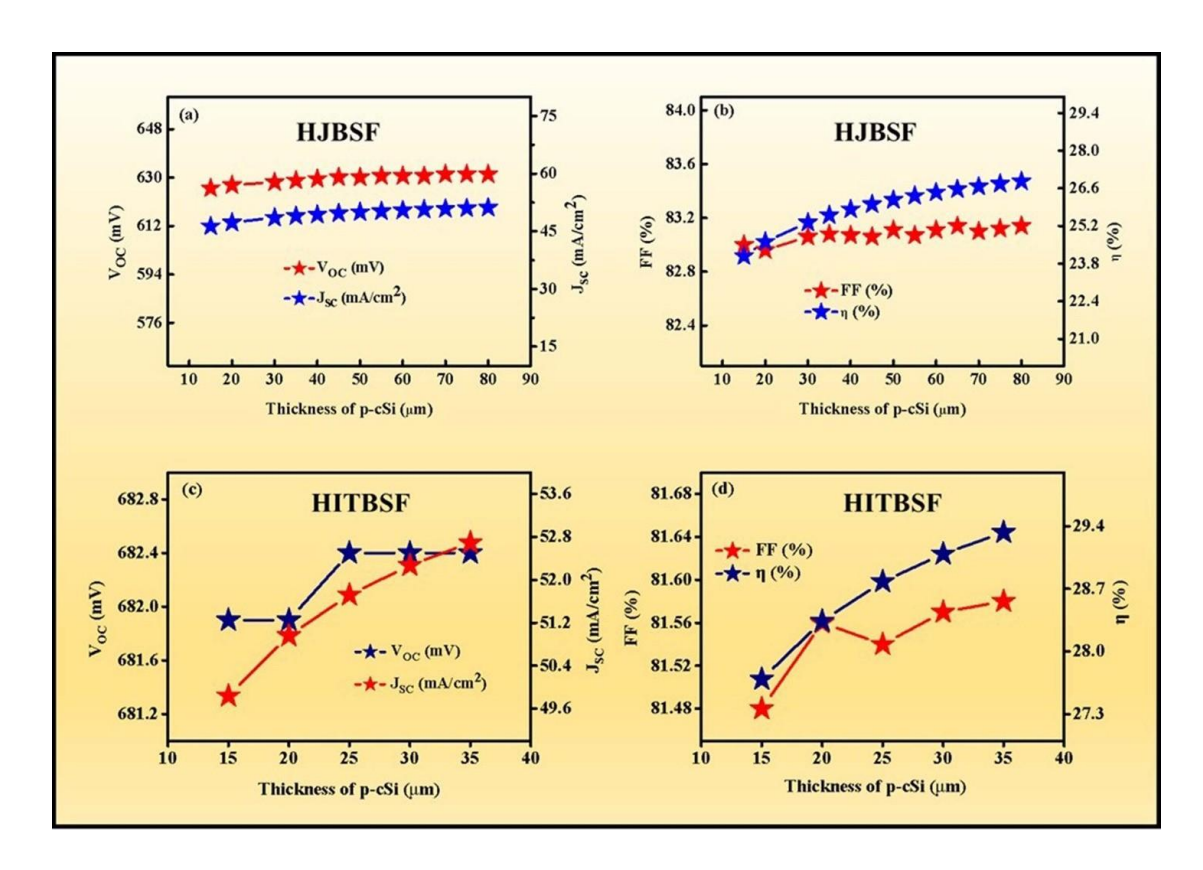


**Fig. 6.4** Optimization of the thickness of active layer (p-cSi) in the range from 15 to 80  $\mu$ m for HJBSF cell showing the variation of V<sub>OC</sub>, J<sub>SC</sub> (a) and FF,  $\eta$  (b), respectively. Optimization of the thickness of active layer (p-cSi) in the range from 15 to 35  $\mu$ m for HITBSF cell showing the variation of V<sub>OC</sub>, J<sub>SC</sub> (c) and FF,  $\eta$  (d), respectively.

The range of thickness varies from 15 to 80  $\mu$ m for HJBSF and from 15 to 35  $\mu$ m for HJTBSF. The resulting outcomes are shown in Figures 6.4(a) and 6.4(b) for HJBSF and Figures 6.4(c) and 6.4(d) for HITBSF. As shown in Figures 6.4(a) and 6.4(b), as the thickness of the p-cSi layer increases, all the performance parameters of the cell also increase. Such as,  $V_{OC}$  increases from 626 mV to 631.2 mV,  $J_{SC}$  increases from 46.34 mAcm<sup>-2</sup> to 51.17 mAcm<sup>-2</sup>, FF increases from 83% to 83.14%, and  $\eta$  increases from 24.08% to 26.86%, respectively. Consequently, a maximum efficiency of 26.86% was attained by optimizing the c-Si thickness to 80  $\mu$ m. As seen in Fig. 6.4(b), there is a fluctuation in the FF values, which first dropped at 55  $\mu$ m of thickness before increasing again at 60  $\mu$ m. In the range of thickness from 55  $\mu$ m to 60  $\mu$ m for p-Si thickness, FF fluctuation can be attributed to the slight change of series resistance (R<sub>S</sub>) from 0.5  $\Omega$ cm<sup>-2</sup> to 0.51  $\Omega$ cm<sup>-2</sup> and shunt resistance (R<sub>sh</sub>) from 8.7 k $\Omega$ cm<sup>-2</sup> to 8.8 k $\Omega$ cm<sup>-2</sup> in the range of thickness from 55  $\mu$ m to 60  $\mu$ m for p-Si thickness. By examining figures 6.4(c) and 6.4(d),

it is evident that the performance parameters of the HITBSF cell increase in a linear fashion as the thickness of the active layer increases. The  $V_{\rm OC}$ ,  $J_{\rm SC}$ , FF and  $\eta$  all experience an improvement from 681.9 mV to 682.4 mV, from 49.84 mAcm<sup>-2</sup> to 52.69 mAcm<sup>-2</sup>, from 81.48% to 81.58% and from 27.69% to 29.33%, respectively. The analysis of the results reveals that the highest efficiency, 29.38%, is attained when the thickness is 35  $\mu$ m. The reason behind an increase in  $J_{\rm SC}$  with larger thickness of the c-Si base appears to be associated to the generation of more electron-hole pairs, which in turn enhance the efficiency [1]. The remaining parameters may get enhanced with c-Si thickness as the number of photo-generated carriers increases. The absorption of incident light increases with c-Si layer thickness. As a consequence, the enhanced generation of charge carriers increases the flow of carriers across the junction, potentially leading to a significant increase in current density. The findings show that the optimal thickness for the active layer in the HJBSF solar cell is 80  $\mu$ m, whereas for the HITBSF solar cell it is 35  $\mu$ m.

# 6.3.3 Optimisation of the band gap of the emitter and BSF layer in HJBSF and HITBSF cells

Here, we performed a simulation to analyse the bandgap of the emitter and BSF layer for both HJ and HIT cells. We have kept the thickness of all layers at their optimal values. The results of the simulation are shown in figures 6.5(a)–6.5(d) and figures 6.5(a)–6.5(d). First, we have optimised the bandgap of the emitter layer in the HJBSF solar cell within the range of 0.8 eV to 1.4 eV by keeping the thickness of the n-Dn, p-Dn, and p-cSi at 0.34 nm, 2.04 nm, and 80 µm, respectively. These values remained constant throughout the entire simulation process. The results of this optimisation are shown in Figures 6.5 (a) and 6.5 (b). As shown in Figures 6.5 (a) and 6.5 (b), V<sub>OC</sub> increased from 250.1 mV to 631.2 mV when  $E_{\rm g}$  varied from 0.8 eV to 1.4 eV. A slight increment in the value of  $J_{\rm SC}$  was observed, increasing from 51.02 mAcm<sup>-2</sup> to 51.17 mAcm<sup>-2</sup>. Fill factor increased from 66.95% to 83.14% as the bandgap varied. As shown in Figures 6.5(c) and 6.5(d), the overall efficiency of the HJBSF cell increases as the bandgap increases, reaching up to 26.86%. This is because the conversion efficiency, which is the product of the current density and open circuit voltage, is positively affected by the increase in bandgap. Therefore, the optimum bandgap value for the n-type diamane layer of the heterojunction solar cell is found to be 1.4 eV. Afterwards, we have modified the bandgap of the HITBSF cell's n-Dn layer within

the range from 0.8 eV to 1.4 eV. The corresponding results may be seen in Figures 6.5(c) and 6.5(d). The efficacy of the HITBSF cell was evaluated using a similar methodology to that of the HJBSF cell. All of the parameters exhibited an increase in correlation with the bandgap, and the optimal value of the bandgap for the emitter layer in the HITBSF cell was found to be the same as that of the HJBSF cell, which is 1.4 eV. The maximum η of 29.38% % was achieved for HITBSF cell at 1.4 eV of bandgap of the emitter layer. Furthermore, we performed a simulation on the BSF layer (p-Dn) for both the HJBSF and HITBSF cells. We varied E<sub>g</sub> of the BSF layer from 1.2 eV to 1.9 eV. The end outcomes are depicted in figures 6.6 (a)–6.6(d). Firstly, the simulation is performed on the HJBSF solar cell, and the results are depicted in Figures 6.6 (a) and 6.6 (b). From the results that were obtained, it is evident that the V<sub>OC</sub> remained constant at 631.2 mV until the bandgap reached 1.6 eV. After that, it decreased to 497.1 mV as the bandgap increased to 1.9 eV. The initial J<sub>SC</sub> increased from 51.02 mAcm<sup>-2</sup> to 53.47 mAcm<sup>-2</sup> until the bandgap reached 1.8 eV. As the bandgap increased further to 1.9 eV, the J<sub>SC</sub> decreased to 2.88 mAcm<sup>-2</sup>. With an increasing bandgap, from 1.5 eV to 1.6 eV, FF as well as  $\eta$  increased from 83.14% to 83.16% and from 26.77% to 26.86%, respectively. Thus, optimized bandgap value for the p-Dn layer of HJBSF is determined to be 1.6 eV. In order to determine the optimised value of the band gap of the BSF layer in the HITBSF cell, we performed further simulations for HITBSF. These simulations varied the  $E_g$  of the p-Dn layer from 1.2 eV to 1.9 eV, and the obtained results are presented in Figures 6.6 (c) and 6.6 (d). The figure shows that  $V_{OC}$  as well as  $J_{SC}$ remained nearly consistent at 683 mV and 52.74 mA/cm<sup>2</sup>, respectively, as E<sub>g</sub> increased from 1.2 eV to 1.7 eV. Yet, the fill factor and efficiency slightly decreased from 81.55% to 81.54% and from 29.38% to 29.37%, respectively, with the increment in bandgap. When the bandgap reaches 1.9 eV, both FF & η decline to 74.02% and 26.64%, respectively. Thus, the optimized bandgap for the p-Dn layer in the HITBSF cell is found to be 1.3 eV. Increasing further the value of the band gap does not have any impact on the working parameters of the HITBSF cell, as illustrated in Figures 6.6 (c) and 6.6 (d).

# 3.2.4 Optimisation of the thickness and band gap of the front and rear/back layers of a-Si: H(i) in HITBSF cell

In this part, we altered the thickness and bandgap of the passivating layers, specifically the a-Si:H(i) layers, which are deposited at the front and rear side of c-Si active layer.

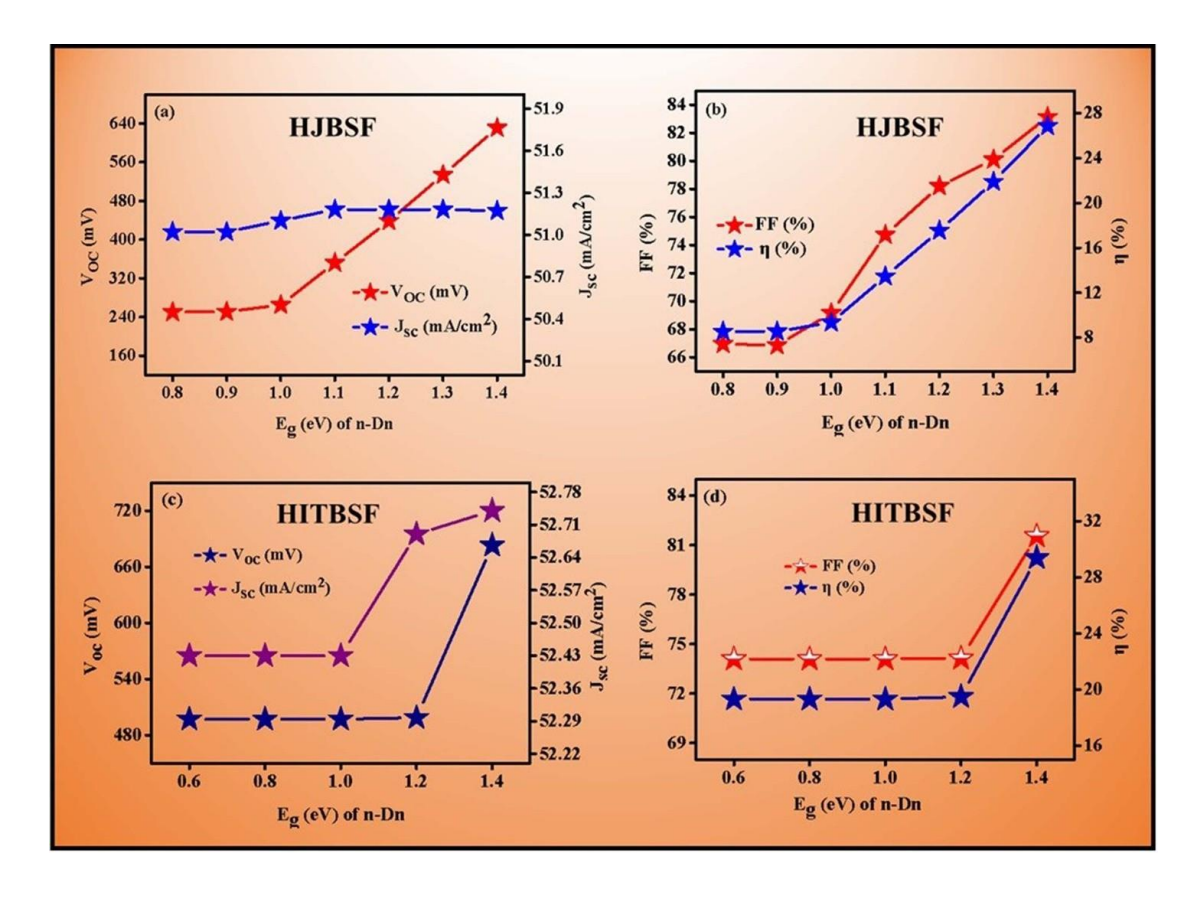


**Fig. 6.5** Optimization of the bandgap of emitter layer (n-Dn) of HJBSF cell showing the variation of  $V_{OC}$ ,  $J_{SC}$  (a) and FF,  $\eta$  (b), respectively in the range from 0.8 eV to 1.4 eV. Optimization of the bandgap of emitter layer of HITBSF cell in the range from 0.8 eV to 1.4 eV, showing the variation of  $V_{OC}$ ,  $J_{SC}$  (c) and FF,  $\eta$  (d), respectively.

The objective was to examine how these modifications impact the performance of the HITBSF cell. The results of this simulation are displayed in Figures 6.7 and 6.8. Initially, we have optimized the thickness of the front intrinsic layer employed for the intention of passivating the front side of the active layer. The optimisation of thickness of the intrinsic a-Si:H has been performed within a range of 3 nm to 10 nm. The results that were obtained can be observed from figures 6.7 (a) and 6.7 (b). Evidently, both the V<sub>OC</sub> and J<sub>SC</sub> decrease significantly from 682.4 mV to 676.7 mV and from 52.27 mAcm<sup>-2</sup> to 47.04 mAcm<sup>-2</sup>, respectively, when the thickness increases from 3 nm to 10 nm. An increase in the thickness of the front intrinsic a-Si: H results in a decrease in both the FF and the conversion efficiency. Specifically, the FF decreases from 81.57% to 81.3%, while the conversion efficiency decreases from 29.09% to 25.88%. The optimal thickness for the front passivating layer a-Si: H(i) is found to be 3 nm. At this thickness, the highest values of the V<sub>OC</sub>, J<sub>SC</sub>, and η are achieved.

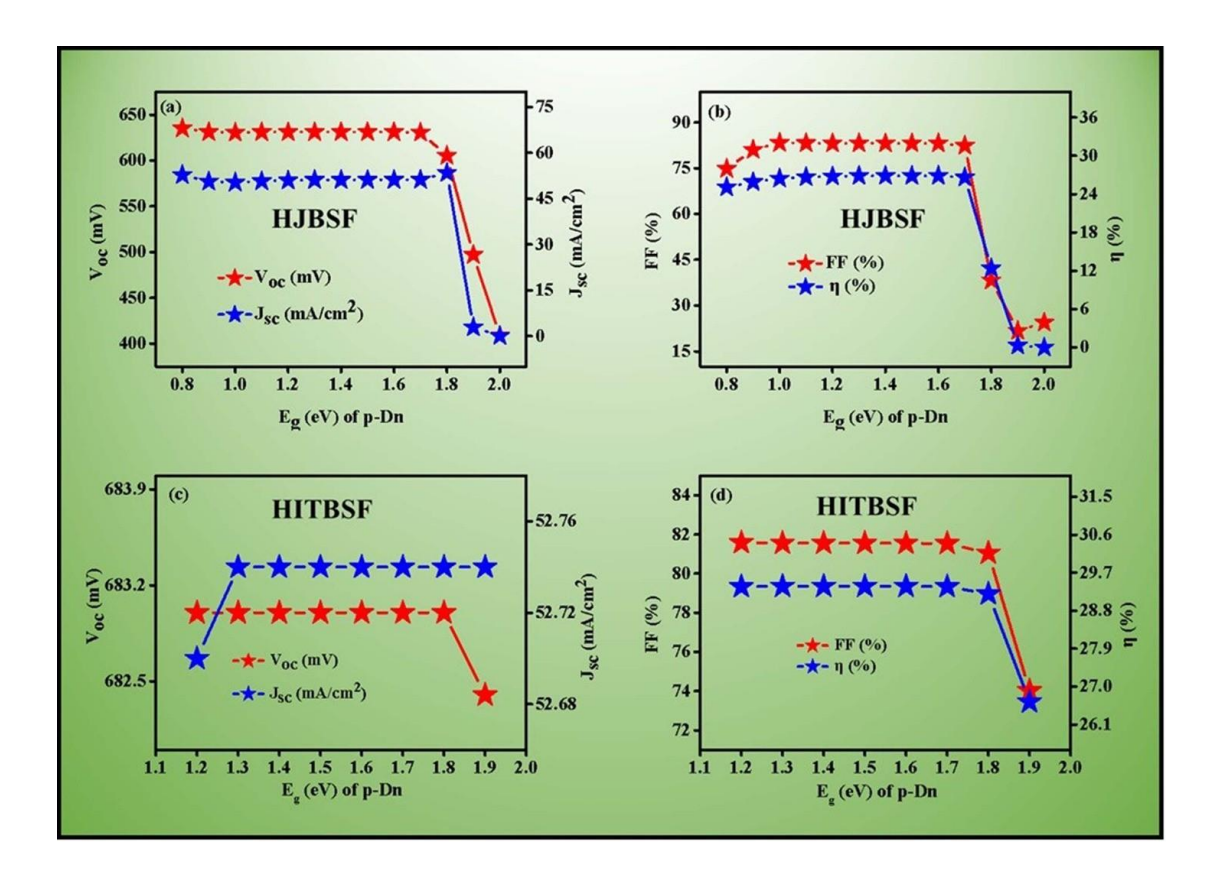


**Fig. 6.6** Optimization of the bandgap of BSF layer (p-Dn) of HJBSF cell showing the variation of  $V_{OC}$ ,  $J_{SC}$  (a) and FF,  $\eta$  (b), respectively, in the range from 1.2 eV to 1.9 eV. Optimization of the bandgap of BSF layer of HITBSF cell in the range from 1.2 eV to 1.9 eV, showing the variation of  $V_{OC}$ ,  $J_{SC}$  (c) and FF,  $\eta$  (d), respectively.

In addition, we carried out further simulations to determine the optimal thickness for the rear passivating layer of the HITBSF cell. We examined the thickness of the back a-Si: H (i) layer in the range of 3 nm to 10 nm, which is the same range used for the front a-Si: H(i) layer. The results were obtained, are shown in Figures 6.7(c) and 6.7(d). To conduct the simulation, the remaining parameters of other layers, namely the emitter layer and the front a-Si: H(i) layer, have been set to their optimized values. The figure shows there is no change in the  $V_{\rm OC}$  value as the layer thickness changes from (3–10 nm). The  $V_{\rm OC}$  remains consistent at a value of 683 mV, as depicted in Figures 6.7 (c) and 6.7 (d). Furthermore, there is no additional change observed in the value of  $J_{\rm SC}$ . Its value remains constant at 52.74 mAcm<sup>-2</sup> across the whole range of thicknesses. The current density shows a minor rise from 52.69 mAcm<sup>-2</sup> to 52.74 mAcm<sup>-2</sup> when the thickness varies from 3 nm to 6 nm. Similarly, at 4 nm the FF was found to decrease from 81.58% to 81.49%

and then at 5 nm it increased to 81.55%, and then remained constant as the thickness continued to increase up to 10 nm. This may have happened because of the decrease in  $R_{\rm sh}$  (from 4.3 k $\Omega$ cm<sup>-2</sup> to 4.2 k $\Omega$ cm<sup>-2</sup>) at 4 nm [53]. Thus, the overall conversion efficiency exhibited a similar trend, as it is the result of the multiplication of the FF and J<sub>SC</sub>. The efficiency decreased by 29.38% when the thickness of the back intrinsic a-Si: H layer was increased. The increase in the thickness of the rear passivation layer a-Si: H(i) leads to an increase in the  $\eta$  of the HITBSF module, as seen in Figures 6.7 (c) and 6.7 (d). Therefore, the optimal thickness for the rear a-Si: H(i) was found to be 7 nm, which exceeds the optimised thickness of 3 nm for the front a-Si: H(i) layer. Furthermore, we have adjusted the bandgap of the front a-Si: H(i) layer within the range of 1.6 eV-1.72 eV. The results that were obtained are depicted in Figures 6.8 (a) and 6.8 (b). It has been observed that as the bandgap increases from 1.6 eV to 1.72 eV, both V<sub>OC</sub> and J<sub>SC</sub> decrease. Specifically, V<sub>OC</sub> decreases from 683 mV to 645 mV, and J<sub>SC</sub> decreases from 52.74 mAcm<sup>-2</sup> to 52.68 mAcm<sup>-2</sup>, as depicted in Fig. 6.8 (a) and 6.8 (b). Since both V<sub>OC</sub> and J<sub>SC</sub> have decreased, it is expected that FF will also diminish, resulting in a reduction in conversion efficiency. According to the results, there is a clear decrease in the FF and n value.

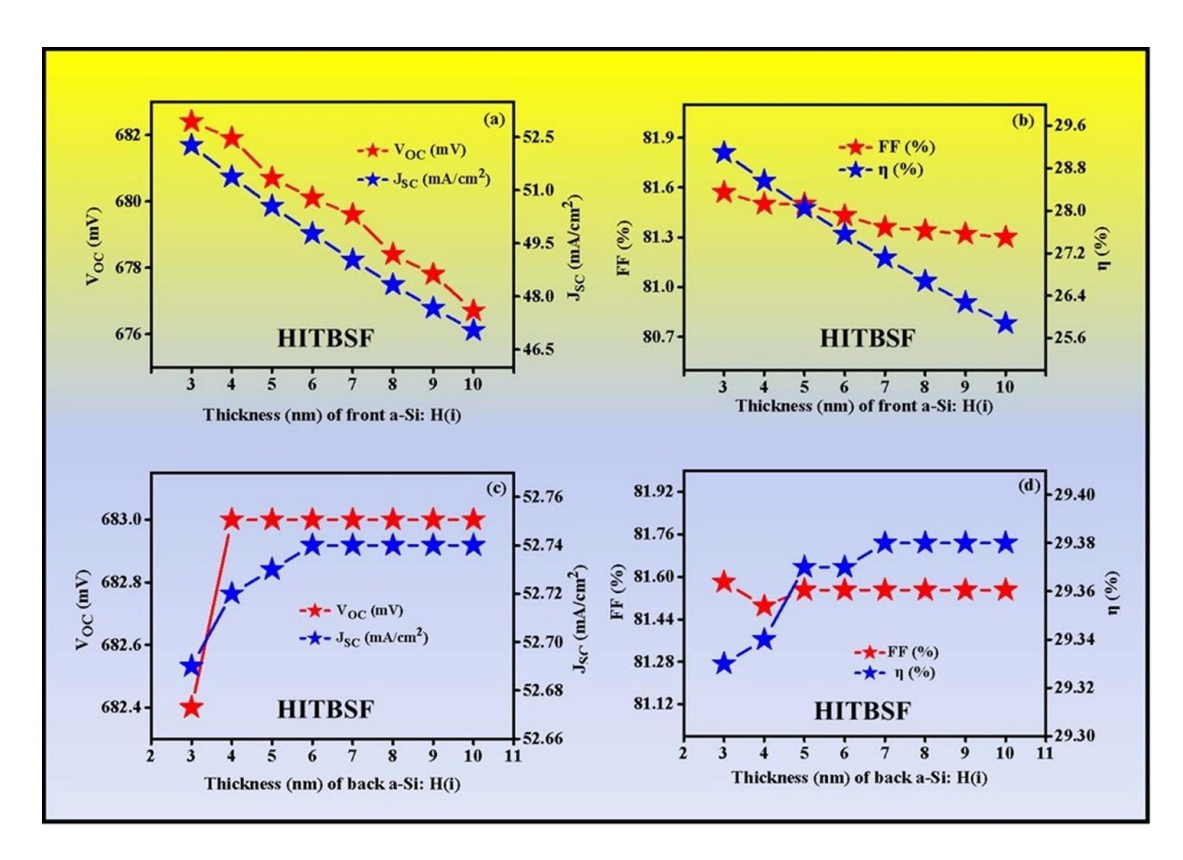


**Fig. 6.7** Optimization of the thickness of front intrinsic a-Si: H layer in the range from 3 nm to 10 nm for HITBSF solar cell showing the variation of  $V_{OC}$ ,  $J_{SC}$  (a) and FF,  $\eta$  (b), respectively. Optimization of the thickness of back intrinsic a-Si: H layer in the range from 3 nm to 10 nm for HITBSF solar cell, showing the variation of  $V_{OC}$ ,  $J_{SC}$  (c) and FF,  $\eta$  (d), respectively.

In particular, the FF value decreases from 81.55% to 79.98%, and the  $\eta$  value decreases from 29.38% to 27.18%. As a consequence, the maximum attainable conversion efficiency has been attained when the bandgap is 1.6 eV. Thus, 1.6 eV is the most optimal value of Eg for the front passivating layer in the HITBSF solar cell. Next, we have optimised the bandgap of the rear or back intrinsic layer of a-Si: H ranging from 1.6 eV to 1.72 eV, as depicted in figures 6.8 (c) and 6.8 (d). The plots in figures 6.8 (c) and 6.8 (d) demonstrate the correlation between E<sub>g</sub> of the rear intrinsic layer of a-Si: H and the variations in V<sub>OC</sub>, J<sub>SC</sub>, FF, and η. The V<sub>OC</sub> & J<sub>SC</sub> remain almost constant at 683 mV and 52.74 mAcm<sup>-2</sup>, respectively as the band gap increased. The FF and η of the HITBSF cell observe a slight decrease, from 81.55% to 81.49% and from 29.38% to 29.36%, respectively, as the Eg increases from 1.6 eV to 1.72 eV. Hence, the optimal bandgap value for the rear side passivating layer is determined to be 1.6 eV. Based on these results, we concluded that the optimal bandgap value for both the front and rear a-Si: H(i) layer is 1.6 eV. Yet, the optimised thickness for the front layer is 3 nm and for the rear layer is 7 nm. The addition of a 3 nm thin passivating layer of intrinsic a-Si:H, led to a boost of cell efficiency from 26.86% to 29.38%. This may have happened because of the increased carrier lifetime and decreased carrier recombination rate of photo-generated carriers, which further lead to improved values of performance parameters of the HITBSF cell [53–56].

In the final analysis, it has been found that the implementation of these optimal cell parameters may contribute to the fabrication and modelling of highly efficient heterojunction and HITBSF cells. Table 6.4 presents the input parameters of the most efficient heterojunction and HITBSF cells.

# 6.3.5 Spectral response, J-V curve and quantum efficiency of HJBSF & HITBSF Cell

In this section, we have studied the J–V curve, SR and the quantum efficiency IQE as well as EQE of heterojunction as well as HIT solar cells. Key parameters like R<sub>s</sub>, R<sub>sh</sub>, and the density of interface traps (D<sub>it</sub>) or surface states (N<sub>ss</sub>) have a direct impact on the efficiency, FF, and current-voltage (I–V) properties of silicon HJ and HIT solar cells. Series resistance mostly influences the FF and power output, but it also affects the solar cell's I–V characteristics. The thermionic emission equation illustrates the impact of R<sub>S</sub>:

$$I = I_o \exp\left(\frac{q (V - IR_S)}{nkT}\right) \left[1 - \exp\left(\frac{-q (V - IR_S)}{kT}\right)\right]$$
(6.1)

where I<sub>o</sub> stands for reverse saturation current, I for output current, V for output voltage, n for ideality factor, k for Boltzmann constant, T for temperature, and q for electron charge, in that order [57, 58]. The output current (I) decreases as R<sub>s</sub> increases, decreasing the FF and overall efficiency. Taking series resistance into account, the fill factor can be approximately calculated as follows:

$$FF \approx FF_{ideal} \times \left(1 - \frac{R_{sh} \times I_{SC}}{V_{oc}}\right)$$
 (6.2)

where,  $FF_{ideal}$  stands for fill factor without resistive losses,  $I_{SC}$  for short-circuit current, and  $V_{oc}$  for open-circuit voltage. A higher  $R_s$  leads to a high decline in FF and efficiency. The effect of  $R_{sh}$  on FF can be expressed as:

$$FF \approx FF_{ideal} \times \left(1 - \frac{v_{oc}}{R_{sh} \times I_{sc}}\right)$$
 (6.3)

where  $R_{sh}$  is the sheet resistance. This indicates that a lower  $R_{sh}$  reduces the fill factor [59]. For HIT solar cells, the intrinsic a-Si layer helps to passivate these traps, lowering  $D_{it}/N_{ss}$  and reducing recombination losses. Lower  $N_{ss}$  values lead to reduced recombination current, higher  $V_{OC}$ , and improved overall efficiency. The reduction in recombination current due to surface passivation can be described by:

$$J_o \alpha \frac{q}{\tau_{eff} N_{SS}}$$
 (6.4)

where  $N_{ss}$  is the surface state density,  $\tau_{eff}$  is the effective carrier lifetime, and  $J_0$  is the reverse saturation current [58].

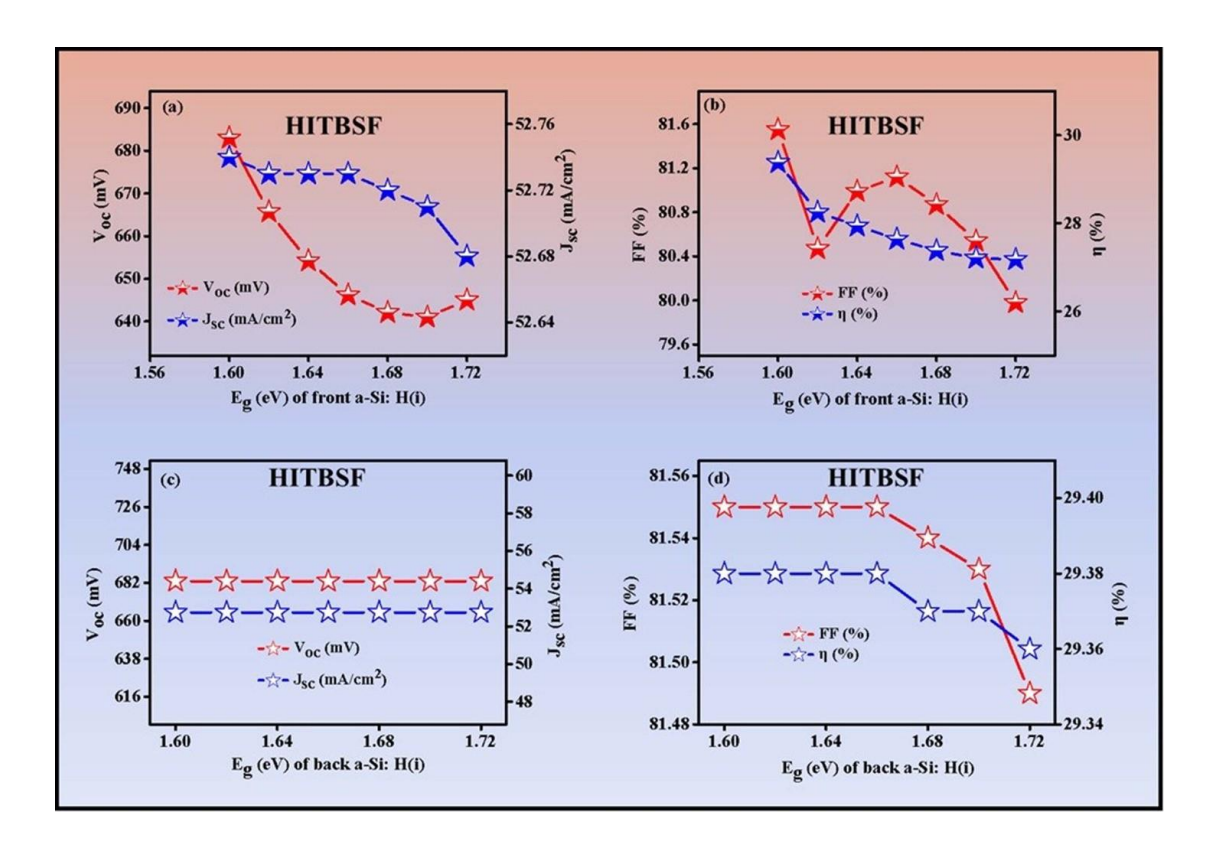


**Fig. 6.8** Optimization of the bandgap of front intrinsic a-Si: H layer in the range from 1.6 eV to 1.72 eV for HITBSF solar cell showing the variation of  $V_{OC}$ ,  $J_{SC}$  (a) and FF,  $\eta$  (b), respectively. Optimization of the bandgap of back intrinsic a-Si: H layer in the range from 1.6 eV to 1.72 eV for the same HITBSF cell, showing the variation of  $V_{OC}$ ,  $J_{SC}$  (c) and FF,  $\eta$  (d), respectively.

Furthermore, factors like  $R_S$ ,  $R_{sh}$ , and  $D_{it}/N_{ss}$  have a direct impact on a solar cell's efficiency. The overall efficiency is defined as the ratio of the electrical power output  $P_{out}$  to the incident power input  $P_{in}$ :

$$\mu = \frac{P_{out}}{P_{in}} = \frac{V_{OC}I_{SC} FF}{P_{in}}$$
 (6.5)

where,  $V_{OC}$  is the open-circuit voltage,  $I_{SC}$  is the short-circuit current, FF is the fill factor, and  $P_{in}$  is the incident light power [60]. As discussed above, efficiency is directly impacted by the  $R_S$ ,  $R_{sh}$ , and  $D_{it}$ . Incorporation of passivation provided by inorganic and polymer-based composite interlayers might lower the  $R_S$ ,  $N_{ss}$  and  $D_{it}$  [57, 61–64]. The simulation is being performed with a monochromatic intensity of  $1 \times 10^{16}$  cm<sup>2</sup>s<sup>-1</sup> and a spectral length of 10 nm. The simulation spans the range of 300–1200 nm, as defined in

the software. Figures 6.9 (a)-6.9(d) and 6.10 (a)-6.10(d) show the J-V curve, SR, IQE, and EQE of the most efficient simulated solar cells. The efficiencies obtained from these solar cells are 26.86% for HJBSF structure and 29.38% for HITBSF structure, respectively. Figures 6.9 (a) and 6.9 (c) show the J-V curve for HJBSF and HITBSF cell, respectively. The results derived from the J-V characteristics or J-V curve of both cells are tabulated in Table 6.5. Subsequently, the SR has been examined, the outcomes are graphed in Figures 6.9 (b) and 6.9 (d), respectively. The spectral response is the ratio of the electric current generated by a cell and the amount of power that incident on the surface of the cell [65]. The measurement is usually expressed as amperes per watt. The fundamental equation of SR can be written as the ratio of cell current  $I_{SC}$  ( $\lambda$ ) to light intensity and can be defined as: SR ( $\lambda$ ) =  $\frac{I_{SC}(\lambda)}{I_{light}(\lambda)}$ . As shown in Fig. 6.9, the SR increased from 0.236 to 0.629 A/W as the wavelength (λ) varied from 300 to 868 nm. The SR decreased at  $\lambda$  of 915 nm and became zero at  $\lambda$  of 1200 nm for both HJ and HIT cell, respectively. Despite an overall decreasing trend, the rear reflector's function is responsible for an increase in SR at about 900 nm in silicon HJBSF & HITBSF solar cells. As the silicon collects photons that have not been absorbed back from these reflectors. By increasing the probability of absorption in the c-Si, boost the SR before it finally drops near the material's bandgap. Beyond 1100 nm (approaching 1200 nm), the energy of incoming photons drops below the c-Si layer's bandgap (~1.12 eV), so they are not absorbed, resulting in the drop in SR [66]. After analysing the studies presented in Fig. 6.9 (b) and 6.9 (d), it is evident that there is a greater photon absorption within the range of  $\lambda$  from 300 nm to 868 nm.

**Table 6.5** Values of performance parameters of the optimal cells; HJBSF cell & HITBSF cell at the optimized values of all the parameters as tabulated in Tables 1, 3 and 4.

Parameter	HJBSF cell	HITBSF cell
$V_{OC}$	631.2 mV	683 mV
$J_{SC}$	$51.16 \text{ mAcm}^{-2}$	$52.74~\mathrm{mAcm}^{-2}$
FF	83.16%	81.55%
η	26.86%	29.38%

The enhanced absorption is closely correlated with the increase in J<sub>SC</sub>, as described by

the equation:  $SR(\lambda) = \frac{I_{SC}(\lambda)}{I_{light}(\lambda)}$ . Spectral response light is an essential parameter that directly influences the efficiency of solar cells and can be evaluated by determining its value at different wavelengths of light. The QE of any solar cell can be determined using these data. QE analyses the consequences happen because of optical losses, like; transmission and reflection, on the efficiency of the cell and directly relies on the wavelength or frequency of the light. As reported earlier, there is a direct correlation between QE of a solar cell and its efficiency. IQE in a solar cell relates to the precise measurement of the efficiency of photons that are neither reflected nor transmitted from the cell. Conversely, EQE, involves the influence of optical losses, for example, reflection & transmission, that happen within the cell.

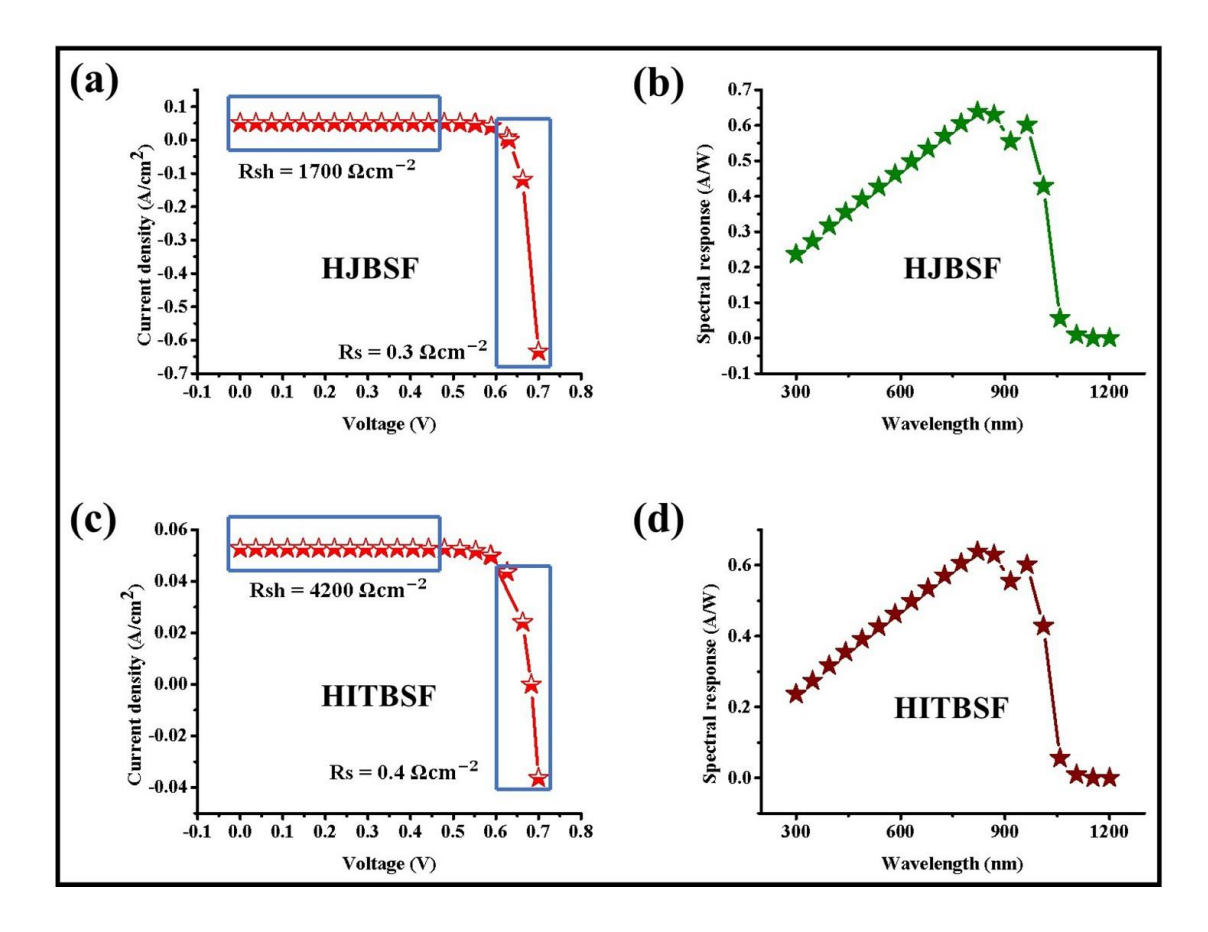


**Fig. 6.9** J-V characteristics of the best optimised HJBSF cell ( $\eta = 26.86\%$ ) (a) and Wavelength dependency of (b) SR in the range (300 nm–1200 nm) at 80  $\mu$ m p-cSi wafer. J-V characteristics of the best optimised HITBSF cell ( $\eta = 29.38\%$ ) (c) and Wavelength dependency of (d) SR in the range (300 nm–1200 nm) at 35  $\mu$ m p-cSi wafer.

The IQE and EQE of both HJBSF and HITBSF show an increase in value from 0.975 to 0.994 as the wavelength increases from 300 to 395 nm, as shown in Figures 6.10 (a)—6.10(d). However, the increasing trend is thereafter reversed and decreased to zero at a wavelength of 1200 nm as the wavelength continues to increase. This indicates that the device will attain optimal efficiency across a broad spectrum of frequencies in the visible region. The J-V curve, SR, IQE, and EQE responses of both cells, which have optimum efficiency of 26.86% (HJBSF) and 29.38% (HITBSF), exhibit nearly identical behaviour. This indicates that the amount of charge carriers generated at these wavelengths is dependent on the number of photons that were absorbed.

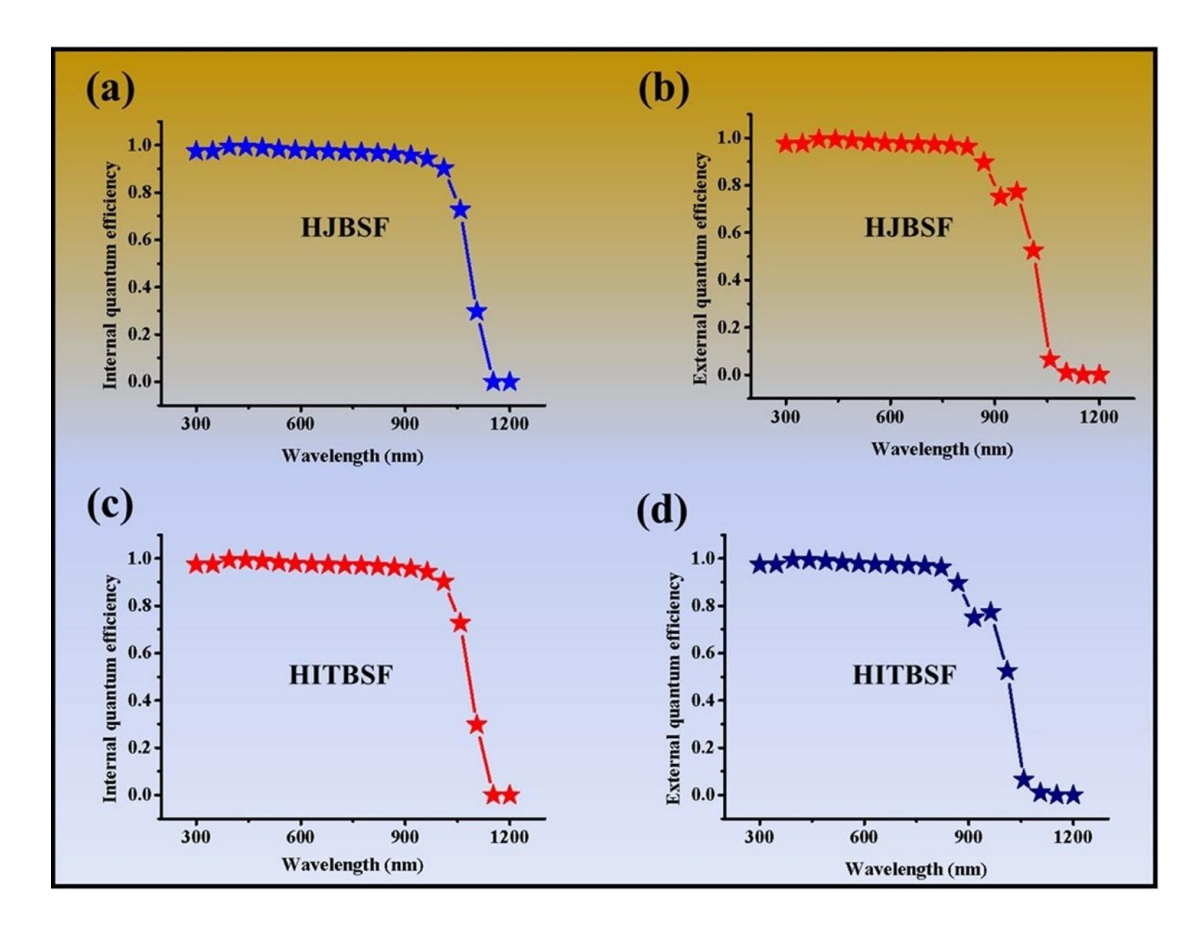


**Fig. 6.10** (a) IQE and (b) EQE of the best simulated HJBSF solar cell ( $\eta = 26.86\%$ ) at 80  $\mu$ m p-cSi wafer in the range of wavelength from 300 nm to 1200 nm. (c) IQE and (d) EQE of the best simulated HIJBSF solar cell (29.38%) at 35  $\mu$ m p-cSi wafer in the same range of wavelength from 300 nm to 1200 nm.

In order to verify the validity of this work, we have conducted a simulation under the experimental study conducted in [67]. We conducted a numerical simulation using the

AFORS-het software on a cell structure: Ag/ITO/n- type a-Si: H/a-Si: H(i)/p-cSi/a-Si: H(i)/MoO<sub>x</sub>/Ag. This structure is similar to the cell's structure: Ag/ITO/n+ a-Si: H/a- Si: H(i)/m-cSi/a-Si: H(i)/MoO<sub>x</sub>/Ag fabricated in [67]. We have obtained an efficiency of 23.93%, which aligns with the experimentally achieved efficiency of 21.10%. Similarly, we also provided evidence for this successful approach in [15], obtaining an efficiency of 9.81% theoretically, which closely matched experimentally obtained results ( $\eta$  = 9.27%) [68]. To further illustrate the originality of the presented work, our research group have further made a comparison between their work and previously published similar work on Si-based solar cells, along with their sizes and properties, listed in Table 6.6 [10, 16, 69–74]. A comparison of the presented study along with the previously reported studies has also been added in Table 6.6 [10, 16, 69–74]. Based on this discussion, we can confidently state that our approach of simulation for the solar cells is genuine and may be expanded to appraise the operational performance of the PV cells.

**Table 6.6** Comparison and details solar cells based on crystalline silicon [10, 16, 69–74].

Research methodology	Structure	Area/Thic kness	V <sub>oc</sub>	$\mathbf{J}_{\mathbf{SC}}$	FF	η	Refs.
Experimental	ITO/Gr/MoS <sub>2</sub> /n -cSi/Ag	$3 \text{ mm} \times 3 \text{ mm}$	590 mV	36.8 mAcm <sup>-2</sup>	73%	15.8 %	[69]
Experimental	TCO/p-a-Si/(i) a-Si:H/n-cSi/(i) a-Si;H/n-a-	100.5 cm <sup>2</sup>	725 mV	39.09 mAcm <sup>-2</sup>	79.10 %	22.3 0%	[70]
Experimental	Si/TCO ITO/p-MoO <sub>x</sub> /(i) a-Si:H/n-c-Si/(i) a-Si:H/n-a-		725.4 mV	38.60 mAcm <sup>-2</sup>	80.36 %	22.5 0%	[71]
Theoretical	a-Si.H/II-a- Si/ITO/Ag Ag/TCO/p-a- Si/(i) a-Si:H/n- c-Si/(i) a-Si:H/n-a-	161 μm	747.1 mV	39.56 mAcm <sup>-2</sup>	84.98 %	25.1 1%	[72]
Theoretical	Si/TCO/Ag Gr/n-MoS <sub>2</sub> /a- Si:H/p-c-Si/Au	500 μm	697 mV	44.25 mAcm <sup>-2</sup>	82.95 %	25.6 1%	[16]
Experimental	TCO/(i)aSi:H/n -cSi/(i) a-Si;H/(n/p)a-	165 μm	744 mV	42.30 mAcm <sup>-2</sup>	83.80 %	26.3 0%	[73]
Experimental	Si/Electrode TCO/(i)a-	180 cm <sup>2</sup>	740 mV	$42.50 \\ \mathrm{mAcm}^{-2}$	84.60 %	26.6 0%	[74]

	Si:H/n-c-Si/(i)						
Theoretical	a-Si;H/(n/p)a- Si/Electrode Gr/n-Dn/a- Si:H(i)/p-c- Si/Ag	90 μm	699.7 mV	53.04 mAcm <sup>-2</sup>	84.06 %	31.2 0%	[10]
Theoretical	Gr/n-Dn/p-c- Si/p-Dn/Au	80 μm	631.2 mV	51.16 mAcm <sup>-2</sup>		26.8 6%	Present work
Theoretical	Gr/n-Dn/a- Si:H(i)/p-c-Si/ a-Si:H(i)/Au	35 μm	683 mV	52.74 mAcm <sup>-2</sup>	81.55		Present work

### **6.4 Summary**

The primary goal of this study is to increase the efficiency of solar cells. This study examines two different cell structures: a basic HJBSF cell (Gr/n-type diamane/p-type c-Si/p-diamane/Au) and a HITBSF cell (Gr/n-type diamane/a-Si: H(i)/p-type c-Si/a-Si: H(i)/p-type diamane/Au). The performed study concluded as follows: first, in order to attain high efficiency, the thickness and bandgap of the n-diamane emitter layer and the p-diamane BSF layer for the HJBSF cell should be 1.36 nm and 1.4 eV, and 2.04 nm and 1.6 nm, respectively. Whereas, for HITBSF, these values are 0.34 nm and 1.6 eV and 0.34 nm and 1.3 eV, respectively. Second, at 80  $\mu$ m of c-Si thickness, the HJBSF cell operates at maximum efficiency. It is interesting to note that the HITBSF cell operates most efficiently at 35 µm for c-Si thickness. The HITBSF cells, which are fabricated on c-Si active layer with a thickness of 35  $\mu$ m, are very significant and feasible due to their substantial decrease in thickness which resulting in cost reduction. However, the handling of such thin wafers may present an additional significant technological challenge. Furthermore, a HITBSF structure has also been optimised to achieve a remarkable efficiency of 29.38%. Finally, it has been concluded that the insertion of passivation layers as well as BSF layers enhanced V<sub>OC</sub> and PCE. We believe that the performed work will advance the development of highly efficient solar cells; yet, aligning theory with experiment remains a substantial challenge.

#### REFERENCES

- [1] Dwivedi, N., Kumar, S., Bisht, A., Patel, K. and Sudhakar, S., 2013. Simulation approach for optimization of device structure and thickness of HIT solar cells to achieve ~27% efficiency. *Solar Energy*, 88, 1, pp.31–41.
- [2] Plakhotnyuk, M., 2018. Nanostructured Heterojunction Crystalline Silicon Solar Cells with Transition Metal Oxide Carrier Selective Contacts. DTU Nanotech.
- [3] Lin, H., Zeng, X., Zhang, S., Zhang, J., Liu, Y., Yang, W., Liu, C., Lu, S., Huang, J., Liu, Y., Yin, X. and Chen, Z., 2023. Silicon heterojunction solar cells with up to 26.81% efficiency achieved by electrically optimized nanocrystalline-silicon hole contact layers. *Nature Energy*, 8, 8, pp.789–799.
- [4] Iftiquar, S.M., Lee, Y., Ju, M., Balaji, N., Dhungel, S.K. and Yi, J., 2012. Fabrication of Crystalline Silicon Solar Cell with Emitter Diffusion, SiNx Surface Passivation and Screen Printing of Electrode. In: *Photodiodes From Fundamentals to Applications*. IntechOpen, pp.106–132.
- [5] Fujishima, D., Taguchi, M., Kiyama, S., Kinoshita, T., Nara, H., Sakata, H. and Maruyama, E., 2010. High-performance HIT solar cells for thinner silicon wafers. In: *35th IEEE Photovoltaic Specialists Conference*, pp.003137–003140.
- [6] Battaglia, C., Cuevas, A., and De Wolf, S., 2014. Hole selective MoOx contact for silicon solar cells. *Nano Letters*, 14, 2, pp.967–971.
- [7] Bivour, M., Temmler, J., Steinkemper, H. and Hermle, M., 2015. Molybdenum and tungsten oxide: high work function wide band gap contact materials for hole selective contacts of silicon solar cells. *Solar Energy Materials and Solar Cells*, 142, pp.34–41.
- [8] Singh, M.K., Shinde, P.V., Singh, P. and Tyagi, P.K., 2021. Two-Dimensional Materials for Advanced Solar Cells. In: *Solar Cells—Theory, Materials and Recent Advances*. IntechOpen, pp.1–27.
- [9] Naima, Tyagi, P.K. and Singh, V., 2022. N-type diamane: an effective emitter layer in crystalline silicon heterojunction solar cell. *Carbon Trends*, 9, p.100209.
- [10] Naima, Tyagi, P.K. and Singh, V., 2023. Potential application of novel graphene/diamane interface in silicon-based heterojunction with intrinsic thin layer solar cell. *Computational Materials Science*, 226, p.112252.
- [11] Tanaka, M., Taguchi, M., Matsuyama, T., Fujita, H., Kamiyama, E., Takeuchi, T., Nakano, S. and Hanafusa, H., 1992. Development of new a-Si/c-Si heterojunction solar cells: ACJ-HIT (artificially constructed junction-heterojunction with intrinsic thin-layer). *Japanese Journal of Applied Physics*, 31, 11R, pp.3518–3522.
- [12] Van Sark, W., 2016. Heterojunction silicon solar cells. In: *Photovoltaic Solar Energy: From Fundamentals to Applications*. Wiley, pp.104–113.
- [13] Zhang, D., Wang, G., Zhang, X., Chen, B., Chen, H. and Zhang, Z., 2011. Influence of ITO deposition and post annealing on HIT solar cell structures. *Energy Procedia*, 8, pp.207–213.
- [14] Lien, S., 2010. Characterization and optimization of ITO thin films for application in heterojunction silicon solar cells. *Thin Solid Films*, 518(Suppl), pp.S10–S13.
- [15] Patel, K. and Tyagi, P.K., 2017. P-type multilayer graphene as a highly efficient transparent conducting electrode in silicon heterojunction solar cells. *Carbon*, 116, pp.744–752.
- [16] Borah, C.K., Tyagi, P.K. and Kumar, S., 2020. The prospective application of a graphene/MoS<sub>2</sub> heterostructure in Si-HIT solar cells for higher efficiency. *Nanoscale Advances*, 2, 8, pp.3231–3240.
- [17] Nair, R.R., Blake, P., Grigorenko, A.N., Novoselov, K.S., Booth, T.J., Stauber, T., Peres, N.M.R. and Geim, A.K., 2008. Fine structure constant defines visual transparency of graphene. *Science*, 320, 5881, pp.1308–1308.

- [18] Lu, M., Bowden, S., Das, U. and Birkmire, R., 2007. Interdigitated back contact silicon heterojunction solar cell and the effect of front surface passivation. *Applied Physics Letters*, 91, 6, pp.063507.
- [19] Brendel, R., Knorr, J., Preu, R., Hermle, M. and Glunz, S.W., 2015. Breakdown of the efficiency gap to 29% based on experimental input data and modelling. *Progress in Photovoltaics: Research and Applications*, 24, 12, pp.1475–1486.
- [20] Street, B.A., 1982. Doping and the fermi energy in amorphous silicon. *Physical Review Letters*, 49, 17, pp.1187–1190.
- [21] Holman, Z.C., Descoeudres, A., Barraud, L., De Wolf, S., Ballif, C. and Battaglia, C., 2012. Current losses at the front of silicon heterojunction solar cells. *IEEE Journal of Photovoltaics*, 2, 1, pp.7–15.
- [22] Niu, C., Wang, J., Zhang, J., Dong, X., Zheng, Y. and Song, L., 2020. Boron-dopant enhanced stability of diamane with tunable band gap. *Journal of Physics: Condensed Matter*, 32, 13, pp.135503.
- [23] Niu, C., Wang, J., Zhang, J., Dong, X., Zheng, Y. and Song, L., 2022. Configuration stability and electronic properties of diamane with boron and nitrogen dopants. *Physical Review B*, 105, 17, pp.174106.
- [24] Qin, G., Wu, L. and Gou, H., 2021. Diamane: design, synthesis, properties, and challenges. *Functional Diamond*, 1, 12, pp.83–92.
- [25] Ge, L., Ma, C., Wang, Y., Zhao, X., Xie, S., Cui, P. and Zhang, W., 2021. Properties of diamane anchored with different groups. *Physical Chemistry Chemical Physics*, 23, 25, pp.14195–14202.
- [26] Stangl, R., Leendertz, C. and Haschke, J., 2010. Numerical Simulation of Solar Cells and Solar Cell Characterization Methods: the Open-Source on Demand Program AFORS-HET. In: R.D. Rugescu, ed. *Solar Energy*. IntechOpen, pp.319–352.
- [27] Kroemer, H., 2001. Quasi-electric fields and band offsets: teaching electrons new tricks (nobel lecture). *ChemPhysChem*, 2, 8-9, pp.490–499.
- [28] Wang, G., Zhao, H., Li, X., Xu, Y., Zhang, Y., Sun, X., Yang, Y., Zhang, C., Lin, H., Li, Y. and Wu, W., 2024. 27.09%-efficiency silicon heterojunction back contact solar cell and going beyond. *Nature Communications*, 15, 1, pp.8931.
- [29] Bellini, E., 2024. Longi announces 27.30% efficiency for heterojunction back contact solar cell. *PV Magazine International*. Available at: www.pv-magazine.com/2024/05/08/longi-announces-27-30-efficiency-for-heterojunction-back-contact-solar-cell/
- [30] Rawat, A., Kumar, S., Dwivedi, N., Tyagi, P.K. and Sudhakar, S., 2014. Numerical simulations for high efficiency HIT solar cells using microcrystalline silicon as emitter and back surface field (BSF) layers. *Solar Energy*, 110, pp.691–703.
- [31] Sorokin, P.B. and Yakobson, B.I., 2021. Two-Dimensional Diamond—diamane: current state and further prospects. *Nano Letters*, 21, 13, pp.5475–5484.
- [32] Cheng, T., Liu, Z. and Liu, Z., 2020. High elastic moduli, controllable bandgap and extraordinary carrier mobility in single-layer diamond. *Journal of Materials Chemistry C*, 8, 37, pp.13819–13826.
- [33] Robinson, J.T., Burgess, J.S., Junkermeier, C.E., Badescu, S.C., Reinecke, T.L., Perkins, F.K., Zalalutdniov, M.K., Baldwin, J.W., Culbertson, J.C., Sheehan, P.E. and Snow, E.S., 2010. Properties of fluorinated graphene films. *Nano letters*, 10, 8, pp.3001-3005.
- [34] Tantardini, C., Kvashnin, A.G., Azizi, M., Gonze, X., Gatti, C., Altalhi, T. and Yakobson, B.I., 2023. Electronic properties of functionalized diamanes for field-emission displays. *Applied Materials & Interfaces*, 15, 14, pp.16317–16326.

- [35] Raeisi, M., Mortazavi, B., Podryabinkin, E.V., Shojaei, F., Zhuang, X. and Shapeev, A.V., 2020. High thermal conductivity in semiconducting Janus and non-Janus diamanes. *Carbon*, 167, pp.51–61.
- [36] Zheng, Z., Zhan, H., Nie, Y., Xu, X., Qi, D. and Gu, Y., 2020. Single layer diamond—a new ultrathin 2D carbon nanostructure for mechanical resonator. *Carbon*, 161, pp.809–815.
- [37] Zhu, L., Li, W. and Ding, F., 2019. Giant thermal conductivity in diamane and the influence of horizontal reflection symmetry on phonon scattering. *Nanoscale*, 11, 10, pp.4248–4257.
- [38] Rietwyk, K.J., Wong, S.L., Cao, L., O'Donnell, K.M., Ley, L., Wee, A.T.S. and Pakes, C.I., 2013. Work function and electron affinity of the fluorine-terminated (100) diamond surface. *Applied Physics Letters*, 102, 9, pp.091604.
- [39] Bessler, R., Duerig, U. and Koren, E., 2019. The dielectric constant of a bilayer graphene interface. *Nanoscale Advances*, 1, 5, pp.1702–1706.
- [40] Chernozatonskii, L.A., Demin, V.A. and Kvashnin, D.G., 2021. Fully hydrogenated and fluorinated bigraphenes–diamanes: theoretical and experimental studies. *C Journal of Carbon Research*, 7, 1, pp.17.
- [41] Chernozatonskii, L.A., Sorokin, P.B., Kvashnin, A.G. and Kvashnin, D.G., 2009. Diamond-like C<sub>2</sub>H nanolayer, diamane: simulation of the structure and properties. *JETP Letters*, 90, 2, pp.134–138.
- [42] Shen, W., Pan, Y., Shen, S., Li, H., Zhang, Y. and Zhang, G., 2019. Electron affinity of boron-terminated diamond (001) surfaces: a density functional theory study. *Journal of Materials Chemistry C*, 7, 31, pp.9756–9765.
- [43] Bouzidi, S., Barhoumi, M. and Said, M., 2021. Optical properties of Janus and non-Janus diamanes monolayers using ab-initio calculations. *Optik*, 235, pp.166642.
- [44] Fang, J., Vandenberghe, W.G. and Fischetti, M.V., 2016. Microscopic dielectric permittivities of graphene nanoribbons and graphene. *Physical Review B*, 94, 4, pp.045318.
- [45] Benda, V., 2018. Crystalline Silicon Solar Cell and Module Technology. In: T.M. Letcher and M. Fthenakis, eds. *A Comprehensive Guide to Solar Energy Systems: With Special Focus on Photovoltaic Systems*. Academic Press, pp.181–213.
- [46] Futako, W., Kamiya, T., Fortmann, C.M. and Shimizu, I., 2000. The structure of 1.5–2.0 eV band gap amorphous silicon films prepared by chemical annealing. *Journal of Non-Crystalline Solids*, 266–269, pp.630–634.
- [47] Cramarossa, F. and Pio, C., 1983. Deposition techniques and applications of amorphous silicon films. *Materials Chemistry and Physics*, 9, 3, pp.213–233.
- [48] Bae, S. et al., 2010. Roll-to-roll production of 30-inch graphene films for transparent electrodes. *Nature Nanotechnology*, 5, 8, pp.574–578.
- [49] Piazza, F., Cruz, K., Monthioux, M., Puech, P. and Gerber, I., 2020. Raman evidence for the successful synthesis of diamane. *Carbon*, 169, pp.129–133.
- [50] Uda, M., Nakamura, A., Yamamoto, T. and Fujimoto, Y., 1998. Work function of polycrystalline Ag, Au and Al. *Journal of Electron Spectroscopy and Related Phenomena*, 88–91, pp.643–648.
- [51] Somani, P.R., Somani, S.P. and Umeno, M., 2006. Planer nano graphenes from camphor by CVD. *Chemical Physics Letters*, 430, 1-3, pp.56–59.
- [52] Yang, X., Bian, J., Liu, Z., Li, S., Chen, C. and He, S., 2018. HIT solar cells with N-type low-cost metallurgical Si. *Advances in OptoElectronics*, 5, pp.7368175.
- [53] Kumar, M. and Kumar, S., 2023. 24.13% efficient TiO<sub>2</sub>/i–a–Si:H/p–c–Si heterojunction solar cell by AFORS-HET numerical simulation. *Optical and Quantum Electronics*, 55, 9, pp.441.

- [54] Hsu, C., Zhang, X., Zhao, M., Lin, H., Zhu, W. and Lien, S., 2019. Silicon heterojunction solar cells with p-type silicon carbon window layer. *Crystals*, 9, 8, pp.402.
- [55] Pham, D.P., Kim, S., Park, J., Cho, J., Kim, H., Le, A.H.T. and Yi, J., 2017. Role of a-Si:H buffer layer at the p/i interface and band gap profiling of the absorption layer on enhancing cell parameters in hydrogenated amorphous silicon germanium solar cells. *Optik*, 136, pp.507–512.
- [56] Rahal, W.L., Rached, D., Mahi, F. and Azzemou, F., 2021. Simulation and optimization of back surface field for efficient HIT solar cells. *Silicon*, 14, 3, pp.1–5.
- [57] Tan, S.O., Uslu Tecimer, H., Cicek, O., Tecimer, H., Orak, I. and Altındal, S., 2016. Electrical characterizations of Au/ZnO/n-GaAs Schottky diodes under distinct illumination intensities. *Journal of Materials Science: Materials in Electronics*, 27, 9, pp.8340–8347.
- [58] Singh, J., 2000. Semiconductor Devices: Basic Principles. Wiley.
- [59] Green, M.A., 2016. Accurate expressions for solar cell fill factors including series and shunt resistances. *Applied Physics Letters*, 108, 8, pp.081111.
- [60] Singh, P. and Ravindra, N.M., 2012. Temperature dependence of solar cell performance—an analysis. *Solar Energy Materials and Solar Cells*, 101, pp.36–45.
- [61] Güçlü, Ç.S., Ulusoy, M. and Şemsettin, S., 2024. A comparison electrical characteristics of the Au/(pure-PVA)/n-Si and Au/(CdTe doped-PVA)/n-Si (MPS) type Schottky structures using I–V and C–V measurements. *Journal of Materials Science: Materials in Electronics*, 35, 2, pp.881.
- [62] Taşçıoğlu, I., Pirgholi-Givi, G., Yeriskin, S.A. and Azizian-Kalandaragh, Y., 2023. Examination on the current conduction mechanisms of Au/n-Si diodes with ZnO–PVP and ZnO/Ag<sub>2</sub>WO<sub>4</sub>–PVP interfacial layers. *Journal of Sol-Gel Science and Technology*, 107, 3, pp.536–547.
- [63] Tanrıkulu, E.E., 2023. Investigation of photon-induced effects on some diode parameters and negative capacitance of the Schottky structure with Zn-doped organic polymer (PVA) interface. *Physica Scripta*, 98, 1, pp.015804.
- [64] Güçlü, Ç.Ş., 2024. On the impact of pure PVC and (PVC:Ti) interlayer on the conduction mechanisms and physical parameters of classic metal-semiconductor (MS) Schottky diodes (SDs). *Physica B: Condensed Matter*, 689, pp.416173.
- [65] Farah Khaleda, M.Z., Vengadaesvaran, B. and Rahim, N.A., 2021. Spectral response and quantum efficiency evaluation of solar cells: a review. In: S.J. Dhoble, N.T. Kalyani, B. Vengadaesvaran and A.K. Arof, eds. *Energy Materials—Fundamentals to Applications*. Elsevier, pp.525–566.
- [66] Sarkar, M.N.I. and Ghosh, H.R., 2021. Performance enhancement of an a-Si:H/μc-Si:H heterojunction p-i-n solar cell by tuning the device parameters. *Dhaka University Journal of Science*, 69, 2, pp.88–95.
- [67] Li, F., Liu, X., Wu, X., Xiao, C., Zeng, X., Wang, Z., Ye, T., Xiang, H., Tang, J., Liu, J., Li, Y. and Liu, Y., 2020. Silicon heterojunction solar cells with MoO<sub>x</sub> hole selective layer by hot wire oxidation-sublimation deposition. *Solar RRL*, 4, 2, pp.1900514.
- [68] Li, X., Zhu, H., Wang, K., Cao, A., Wei, J., Li, C., Jia, Y., Li, Z., Li, X. and Wu, D., 2013. Ion doping of graphene for high-efficiency heterojunction solar cells. *Nanoscale*, 5, 5, pp.1945–1948.
- [69] Ma, J., Bai, H., Zhao, W., Yuan, Y. and Zhang, K., 2018. High efficiency graphene/MoS<sub>2</sub>-Si Schottky barrier solar cells using layer-controlled MoS<sub>2</sub> films. *Solar Energy*, 160, pp.76–84.
- [70] Tsunomura, Y., Yoshimine, T., Taguchi, M., Maruyama, E., Tanaka, M., Uzu, H. and Uchida, M., 2009. Twenty-two percent efficiency HIT solar cell. *Solar Energy Materials and Solar Cells*, 93, 4, pp.670–673.

- [71] Geissbühler, J., Werner, J., Martin de Nicolas, S., Barraud, L., Correa-Baena, J.P., Béland, D., Hessler-Wyser, A., Despeisse, M., Alexander, D.T.L., Nicolay, S., Wolf, S.D. and Ballif, C., 2015. 22.5% efficient silicon heterojunction solar cell with molybdenum oxide hole collector. *Applied Physics Letters*, 107, 8, pp.081601.
- [72] Long, W., Fang, G., Shen, Y., Wei, N., Huang, H., Deng, W., Li, X. and Zhao, X., 2021. On the limiting efficiency for silicon heterojunction solar cells. *Solar Energy Materials and Solar Cells*, 231, pp.111291.
- [73] Yoshikawa, K., Kawasaki, H., Yoshida, W., Irie, T., Konishi, K., Nakano, K., Uto, T., Adachi, D., Kanematsu, M., Uzu, H. and Yamamoto, K., 2017. Silicon heterojunction solar cell with interdigitated back contacts for a photoconversion efficiency over 26%. *Nature Energy*, 2, 5, pp.17032.
- [74] Yoshikawa, K., Kawasaki, H., Yoshida, W., Irie, T., Konishi, K., Nakano, K., Uto, T., Adachi, D., Kanematsu, M., Uzu, H. and Yamamoto, K., 2017. Exceeding conversion efficiency of 26% by heterojunction interdigitated back contact solar cell with thin film Si technology. *Solar Energy Materials and Solar Cells*, 173, pp.37–42.

## CHAPTER 7

## INFLUENCE OF PASSIVATION LAYER (SiO<sub>2</sub>/Si<sub>3</sub>N<sub>4</sub>) EMPLOYING IN COMMERCIALLY AVAILABLE SILICON SOLAR CELL

This chapter presents a simulation of crystalline silicon BSFHJ solar cells with SiO<sub>2</sub>/Si<sub>3</sub>N<sub>4</sub> passivation. It achieves a current density of 54.53 mA/cm<sup>2</sup> and an outstanding power conversion efficiency of 30.59%. Diamane doped with nitrogen and boron is introduced as the emitter and BSF layers in the device structure. Using AFORS-HET simulations, key performance parameters such as carrier lifetime and layer thickness were optimised. On the contrary, the efficiency of a typical PERC cell was only 24.01%. This study emphasises the significance of surface passivation for enhancing optical absorption and reducing recombination losses. The results suggested that the studied structure is an excellent option for next-generation, highly efficient solar systems.

The results reported in this chapter have been communicated in **Carbon**, I.F. = 11.6.

#### 7.1 Introduction

Rising global energy requirements and the pressing challenge of climate change have driven a rapid shift toward renewable energy solutions. Solar PV, as a cornerstone of renewable energy technologies, have witnessed remarkable advancements over the past few decades [1]. In the relentless pursuit of enhancing PV technologies to achieve maximum efficiency, researchers have explored an extensive array of materials, designs, and innovative techniques [2-3]. Among these advancements, Passivated Emitter and Rear Cell (PERC) solar technology emerges as a transformative option, setting new benchmarks in solar energy conversion [4-6]. The PERC is an advanced silicon solar cell architecture designed to enhance light absorption and reduce recombination losses, thereby improving overall conversion efficiency [7]. Unlike conventional cells, PERC integrates a rear surface passivation layer typically made of SiO<sub>2</sub>, Al<sub>2</sub>O<sub>3</sub>, or Si<sub>3</sub>N<sub>4</sub> that acts as both a reflector of unabsorbed photons and a barrier to charge carrier recombination at the rear contact [8-9]. This additional layer improves light absorption within the silicon, thereby boosting generation of charge carriers. Simulations using Silvaco ATLAS have demonstrated that optimized PERC structures can achieve efficiencies exceeding 24%, with improved V<sub>OC</sub>, Jsc, and FF compared to standard silicon cells [5]. As a result, PERC technology has become a cornerstone in the evolution of silicon photovoltaics because of its excellent performance and ease of integration with existing manufacturing techniques. Furthermore, comprehensive studies have emphasized the role of passivation and advanced emitter designs in PERC cells for addressing recombination losses and enhancing light trapping [10,11]. The standard PERC structure comprises an active c-Si layer, a lightly doped emitter, and a substantially doped BSF layer, along with passivation and anti-reflective coatings such as SiO<sub>2</sub> and Si<sub>3</sub>N<sub>4</sub>, respectively. These extra passivation layers significantly minimize surface recombination and enhance light trapping efficiency. Previously, differentially doped amorphous silicon layers were used as an emitter layer and BSF layer, which were referred to as electron and hole collecting layers. Here, the BSF layer facilitates the collection of minority carriers, along with providing extra passivation at the rear side of the cell. This type of cell with an extra BSF layer is also known as BSF solar cells [14]. However, these electron and hole collection layers, which are differentially doped a-Si, have been reported to generate parasitic photon

absorption, diminishing the active layer's ability to generate electron-hole pairs [15]. As a consequence, the PCE has decreased significantly, spurring the search for alternative materials to replace the doped amorphous silicon layers serving as emitter and back surface field in BSF solar cells. In the context of this challenge, Naima et al. [16-17] designed and simulated BSFHJ and BSFHIT solar cells integrating nitrogen and borondoped diamane as emitter layer and a BSF layer, respectively, with a p-type c-Si layer as an active layer, achieving an efficiency of up to 29.38% [17]. They successfully replaced the a-Si layer with a newly reported material called diamane and attained a higher PCE. Diamane is an ultra-thin, diamond-like material that offers a promising pathway for nextgeneration nano-optoelectronic devices [18-20]. Diamane's high thermal conductivity (~2240 W/mK at 300 K), high carrier mobility (2732 cm<sup>2</sup>/Vs for electrons & 1565 cm<sup>2</sup>/Vs for holes), and excellent optical transparency make it a promising candidate for enhancing carrier transport and thermal management in semiconductor devices, with its tuneable bandgap (0-3.52 eV) [21-24]. Previously, diamane was used in solar cells as both an emitter and a BSF layer, taking graphene as a transparent conductive electrode (TCE), resulting in anticipated efficiencies of up to 29.38% [25–27]. However, these studies lacked the integration of passivation approaches and realistic optical modelling. The present study addresses this issue by incorporating SiO<sub>2</sub>/Si<sub>2</sub>N<sub>4</sub> stacks into the diamanebased heterojunction cell.

So, we proposed a novel BSFHJ solar cell structure that incorporates both standard dielectric passivation layers and proficient 2D carbon materials as carrier collecting layers and TCE. The proposed device structure, Graphene/Si<sub>3</sub>N<sub>4</sub>/SiO<sub>2</sub>/n-Diamane/p-c-Si/p-Diamane/Au, includes SiO<sub>2</sub> for chemical passivation and Si<sub>3</sub>N<sub>4</sub> for anti-reflection [10, 28-31], graphene as TCE, doped diamane as both emitter and BSF layers, and p-type c-Si as the active layer. The structure was modelled and optimized using AFORS-HET simulation software, accounting for carrier lifetimes, doping levels, optical absorption, and interface properties. Here, SiO<sub>2</sub> provides chemical passivation by reducing interface trap densities, while Si<sub>3</sub>N<sub>4</sub> offers AR properties. The AR coating that is offered here allows the maximum amount of light to enter the solar cell without being reflected. This synergistic combination of state-of-the-art 2D materials and well-established passivation layers aims to minimize recombination losses, enhance carrier collection, and improve optical absorption, ultimately leading to superior energy conversion efficiency.

Numerical simulations are carried out using AFORS-HET, a robust software tool for modelling heterostructure solar cells [32]. The simulations provide detailed insights into key performance parameters such as V<sub>OC</sub>, J<sub>SC</sub>, FF, and PCE. The influence of diamane layer on band alignment, carrier dynamics, and recombination rate is systematically analysed by optimizing their doping concentrations and thickness, along with a comparative study of the cell's performance with and without the SiO<sub>2</sub>/Si<sub>3</sub>N<sub>4</sub> passivation layers. An optimization on the carrier lifetime of the active layer has also been performed. Furthermore, we have performed a comparison analysis of the PCE on different BSFHJ and BSFHIT structures simulated by our group with and without passivation to understand the crucial role of passivating the emitter layer and to achieve the most efficient solar cell. This detailed simulation and optimization approach underscores the potential of the Graphene/Si<sub>3</sub>N<sub>4</sub>/SiO<sub>2</sub>/n-Diamane/p-cSi/p-Diamane/Au, structure in achieving high-performance solar cells. In the proposed design, unlike traditional PERC cells, we did not use dielectric layers on rear side of the cell. Instead, a p-doped diamane layer was employed as the BSF, which not only reflects unabsorbed photons to the active layer, boosting electron-hole generation and current density, but also enhances back-side passivation, leading to improved overall PCE. The objective is to understand how diamane-based selective contacts, when combined with conventional passivation layers, may exceed theoretical performance limits under idealized and realistic circumstances. We also compared the performance of this innovative structure to that of a standard a-Sibased PERC cell to understand the significance and advantages of the proposed design.

## 7.2 Structure and simulation details

The proposed solar cell structure: Graphene/Si<sub>3</sub>N<sub>4</sub>/SiO<sub>2</sub>/n-Diamane/p-cSi/p-Diamane/Au, is depicted in Fig. 7.1 (a). This structure is designed and simulated using the AFORS-HET software version 2.5, which employs Shockley-Read-Hall recombination statistics for different layers of the solar cell [32]. The AFORS-HET software solves one-dimensional semiconductor equations, including Poisson's equation, and transport and continuity equations for electrons and holes using finite differences under various conditions [32]. It facilitates the arbitrary tuning of parameters to compare simulations with experimental measurements. The simulation

was performed under standard conditions such as Air Mass 1.5 G, using a photon flux of  $1 \times 10^{16}$  cm<sup>-2</sup>s<sup>-1</sup>, a spectral resolution of 10 nm, and a wavelength range of 300–1200 nm, using a power density of 100 mW/cm<sup>2</sup> and temperature 300 K. The designed multilayer configuration facilitates optimal photon absorption in the active region, which is critical for achieving high conversion efficiency. The materials and their parameters used for front and back contacts are listed in Table 7.1 [33-38]. During the simulation, carrier tunnelling at interfaces and defect formation between layers were neglected to minimise recombination effects.

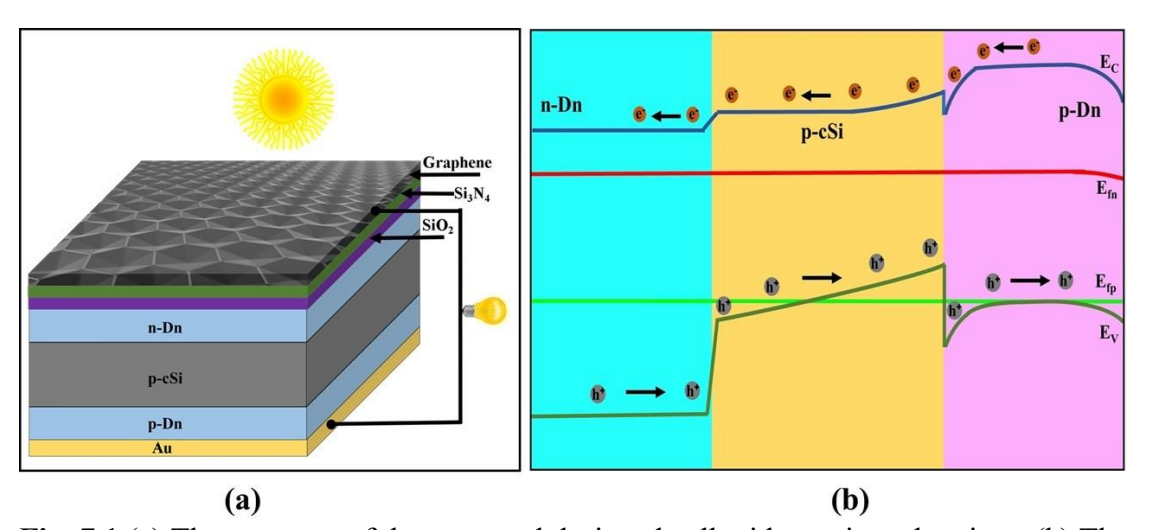


**Fig. 7.1** (a) The structure of the proposed designed cell with passivated emitter. (b) The energy band diagram of the fully simulated cell generated by the software.

# 7.3 Energy Band Diagram and Carrier Dynamics

The schematic of the energy band, as displayed in Fig. 7.1(b), highlights the junction properties. At the n-Diamane/p-c-Si interface, a built-in potential develops, segregating charge carriers due to concentration gradients. The depletion region spreads into both p- and n-type layers, establishing equilibrium through drift and diffusion currents. This results in energy band bending near the Fermi level and determines  $V_{OC}$  and  $J_{SC}$ , that contribute to calculating FF and  $\eta$  of the solar cell. These parameters can be expressed as:  $V_{OC} = kT/q \ln (I_L/I_0 + 1)$ , where  $I_L$  is the photocurrent,  $I_0$  reverse saturation current,  $I_0$  is Boltzmann's constant,  $I_0$  is the temperature (K), and  $I_0$  is the elementary charge [44],  $I_0$  is the elementary charge [44],  $I_0$  is the elementary charge [45]. Efficiency  $I_0$  is the density of charge carriers, and  $I_0$  is the elementary charge [45]. Efficiency  $I_0$  is the elementary  $I_0$  in  $I_0$  is the elementary charge [45].

here  $V_{OC}$  is the open-circuit voltage,  $I_{SC}$  is the short-circuit current, and FF is the fill factor [46]. FF =  $P_{max}/V_{OC}$ .  $J_{SC}$ , here  $P_{max}$  is the maximum power output of the solar cell, and  $J_{SC}$  is the short circuit current density [46]. The p-Diamane/Au interface exhibits Schottky behaviour, where the higher work function of Au results in electron transfer from diamane to Au, creating a positive space charge region near the diamane region. The electron and hole transport were modelled using a drift-diffusion approach, while recombination was handled via Shockley-Read-Hall dynamics. The optical absorption was computed by utilizing the Lambert-Beer absorption model, considering the textured surfaces of the c-Si. A user-defined angle of 89° was applied for light entering the textured silicon layer. The photon absorption at a position (x) in the stack was calculated using the absorption coefficient:  $\alpha_x$  ( $\lambda$ ) =  $4\pi k(\lambda)/\lambda$ , where  $k(\lambda)$  is the extinction coefficient of the semiconductor material [47].

**Table 7.1** The parameters of the front and rear contacts utilised in the solar cell design were examined in this study [33-38].

Parameter	Front contact	Back contact
Material	Si <sub>3</sub> N <sub>4</sub> /SiO <sub>2</sub>	Au
Thickness	1 nm	10 μm
Work function (eV)	4.28 eV	5.4 eV
Refractive index	1.9	0.1
Extinction coefficient	0	3
Internal reflection	0	0
External reflection	0	0
Surface condition	Textured	Plane
Texturing angle ( $\delta$ )	89°	0°
Absorption loss	0	0

## 7.4 Results and Discussion

## 7.4.1 Optimization of carrier lifetime in active layer

This study aims to achieve the highest efficiency by designing a multi-layered solar cell. To accomplish this, we first developed the cell's structural design and then

simulated various parameters for its layers. The first optimized parameter is the minority carrier lifetime (τ) in the active layer of p-type textured c-Si. Bulk, surface, auger, and radiative recombination all have an impact on carrier lifetime [9, 32]. The c-Si active layer's carrier lifetime, which depends on recombination dynamics, has an immediate impact on PERC solar cell performance. Carrier lifetime is a crucial factor to attain high-performance of solar cells, and it is significantly influenced by bulk composition and surface passivation. In this section, we have varied  $\tau$ , in the range from 1  $\mu$ s to 10<sup>3</sup>  $\mu$ s, and the corresponding results have been illustrated in the Fig. 7.2 (a, b). While performing this simulation, the values of the remaining parameters are kept constant at values tabulated in Table 7.2; these values have been taken from the reported data [18, 22-24, 48-51]. Fig. 7.2 (a & b) reveals that at 1 µs of carrier lifetime (electron/hole), the values of V<sub>OC</sub>, J<sub>SC</sub>, FF, and η are 663.4 mV, 51.22 mA/cm<sup>2</sup>, 83.46%, and 28.36%, respectively. The figure shows that increasing the carrier lifetime to 10<sup>3</sup> us improves all performance parameters, including V<sub>OC</sub> (664.6 mV), J<sub>SC</sub> (51.85 mA/cm<sup>2</sup>), FF (83.47%), and η (28.76%). This indicates that a higher carrier lifetime is desirable for higher conversion efficiency. As a result, for the further simulated solar cell, we opted for 1 ms as the optimal carrier lifetime for both electrons and holes. It is reported that an essential factor in achieving higher efficiencies is a long carrier lifetime, which must be about 1 ms or exceed 1 ms to minimize recombination. Furthermore, the thickness of the active layer, as well as the doping concentration, are crucial in light absorption and photogeneration. This layer is made of lightly doped ptype material. If this layer is excessively thin, the likelihood of electron-hole pair formation falls. In contrast, if the layer is excessively thick, then the tendency for charge carriers to recombine increases. As a consequence, on the rear side of the active layer (p-type c-Si), a heavily doped p-type layer named BSF was used. This layer is used to minimize recombination losses at the interface of metal contacts and semiconductor material.

## 7.4.2. Optimization of thickness of p-type c-Si

The active layer is the main area for light absorption and electron-hole generation. So, a thicker active layer improves light absorption, particularly at longer wavelengths, although it also increases bulk recombination, which results in decreased carrier lifetime. A thinner active layer can result in lowered absorption, particularly in the infrared spectrum, but it minimizes recombination losses and increases life-time.

**Table 7.2** Initial parameter values for various layers prior to optimisation [18, 22-24, 48-51].

Parameter	n-Diamane	p-cSi	p-Diamane
Thickness	0.68 nm	80 μm	2.04 nm
Electron affinity (eV)	4.1	4.05	4.1
Dielectric constant	8	11.9	8
Band gap (eV)	1.4	1.12	1.4
$\mu_n (cm^2V^{-1}s^{-1})$	2732	1104	2732
$\mu_p \ (cm^2V^{-1}s^{-1})$	1565	420	1565
$N_C(cm^{-3})$	$3 \times 10^{18}$	$2.8\times10^{19}$	$1 \times 10^{21}$
$N_V(cm^{-3})$	$3 \times 10^{18}$	$1.04 \times 10^{19}$	$1 \times 10^{21}$
$N_A (cm^{-3})$	0	$1 \times 10^{15}$	$9 \times 10^{20}$
$N_D (cm^{-3})$	$2 \times 10^{18}$	0	0
$V_e (cm s^{-1})$	$1 \times 10^{7}$	$1 \times 10^{7}$	$1 \times 10^{7}$
$V_h (cm \ s^{-1})$	$1 \times 10^{7}$	$1 \times 10^{7}$	$1 \times 10^{7}$
Refractive index (n)	1.75	(default)	1.75
Extinction coefficient (k)	0.8	(default)	0.8
Layer density $(g cm^{-1})$	2.328	2.328	2.328
Band- to- band recombination	0	$9.50 \times 10^{-15}$	0
coefficient $(cm^3s^{-1})$			
Auger hole recombination	0	$9.90 \times 10^{-32}$	0
coefficient $(cm^6s^{-1})$			
Auger electron recombination	0	$2.20 \times 10^{-31}$	0
coefficient $(cm^6s^{-1})$			

Therefore, it is always difficult to figure out the optimal thickness of the active layer to attain the optimal performance of PV cell. This section focuses on the optimization of the p-type c-Si layer thickness while keeping the carrier lifetime at 1 ms and the other parameters kept at the values presented in Table 7.2. Fig. 7.3 (a & b) demonstrates that  $V_{OC}$  ascended to 666.3 mV from 661.1 mV,  $J_{SC}$  increased to 53.59 mA/cm<sup>2</sup> from 48.94 mA/cm<sup>2</sup>, FF increased to 83.49% from 83.24%, but  $\eta$  decreased to 29.81% from 26.97%, as the thickness of the p-c-Si increased from 30  $\mu$ m to 180  $\mu$ m. We may conclude that optimal active layer thickness is 80  $\mu$ m [52].

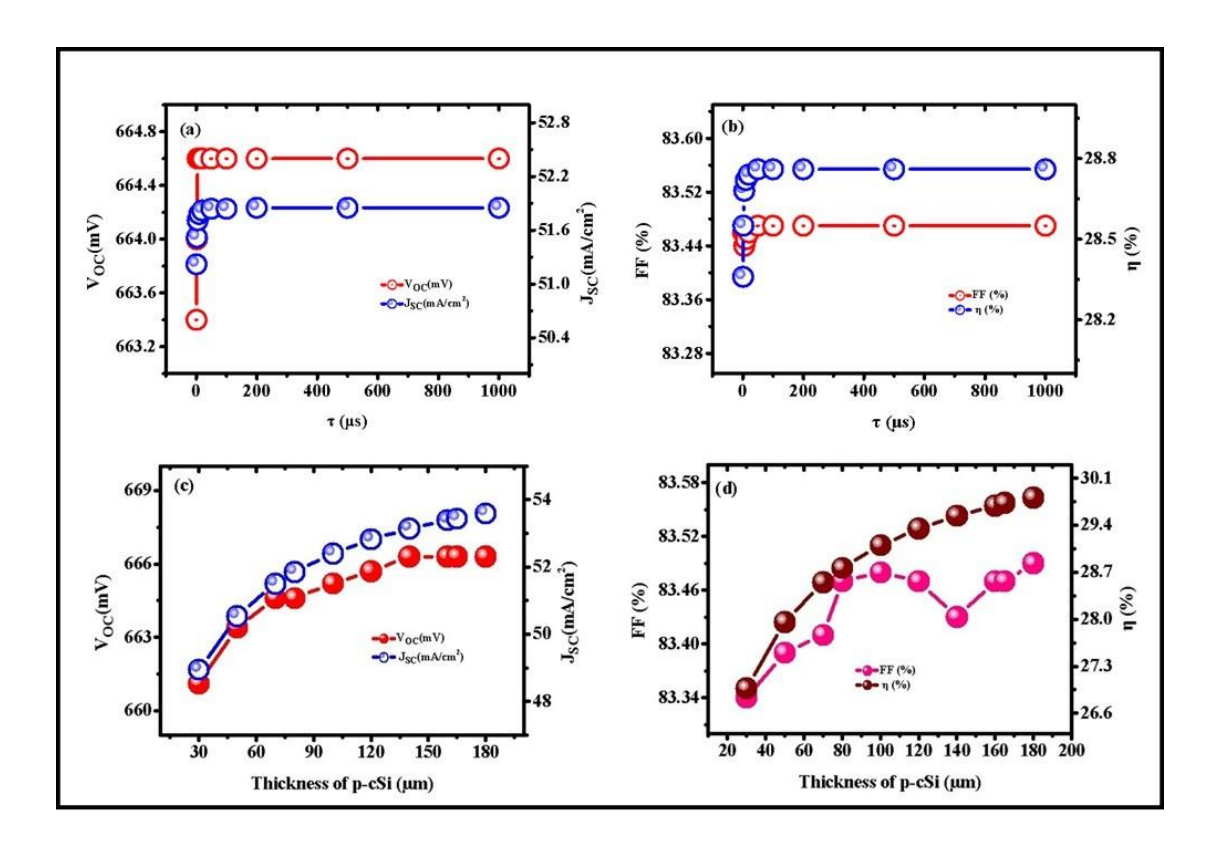


**Fig. 7.2** (a & b) The effect of variation of carrier lifetime ( $\tau$ ) of the p-c-Si layer (active layer) on the performance parameters of the designed cell. (c & d) The effect of thickness ( $\mu$ m) of the active layer (p-c-Si) on the performance parameters of the designed cell.

# 7.4.3. Optimization of the doping concentration of the BSF layer

In this section, we optimized the doping concentration (N<sub>A</sub>) in p-type diamane, which was used as the BSF layer in the proposed solar cell. The BSF layer has a higher carrier concentration than that of the active and emitter layers. The doping concentration of about 1×10<sup>18</sup> cm<sup>-3</sup> and more is to be reported to attain the maximum conversion efficiency [53]. We varied the doping concentration from 1×10<sup>18</sup> cm<sup>-3</sup> to 9×10<sup>20</sup> cm<sup>-3</sup>, and the results are illustrated in Fig. 7.4 (a, b). The BSF layer has made it much easier to separate free electrons and holes in the bulk [53]. As N<sub>A</sub> increases from 1×10<sup>18</sup> cm<sup>-3</sup> to 9×10<sup>20</sup> cm<sup>-3</sup>, the current density and conversion efficiency increase from 53.50 mA/cm<sup>2</sup> to 53.59 mA/cm<sup>2</sup> and 29.76% to 29.81%, respectively, as shown in Fig. 7.4 (a & b). Furthermore, FF exhibited an infinitesimal increase with doping concentration, from 83.48% to 83.49%. The V<sub>OC</sub> remains constant at 666.3 mV. The results presented suggest that a doping BSF layer more than 10<sup>18</sup> cm<sup>-3</sup> does not affect cell performance.

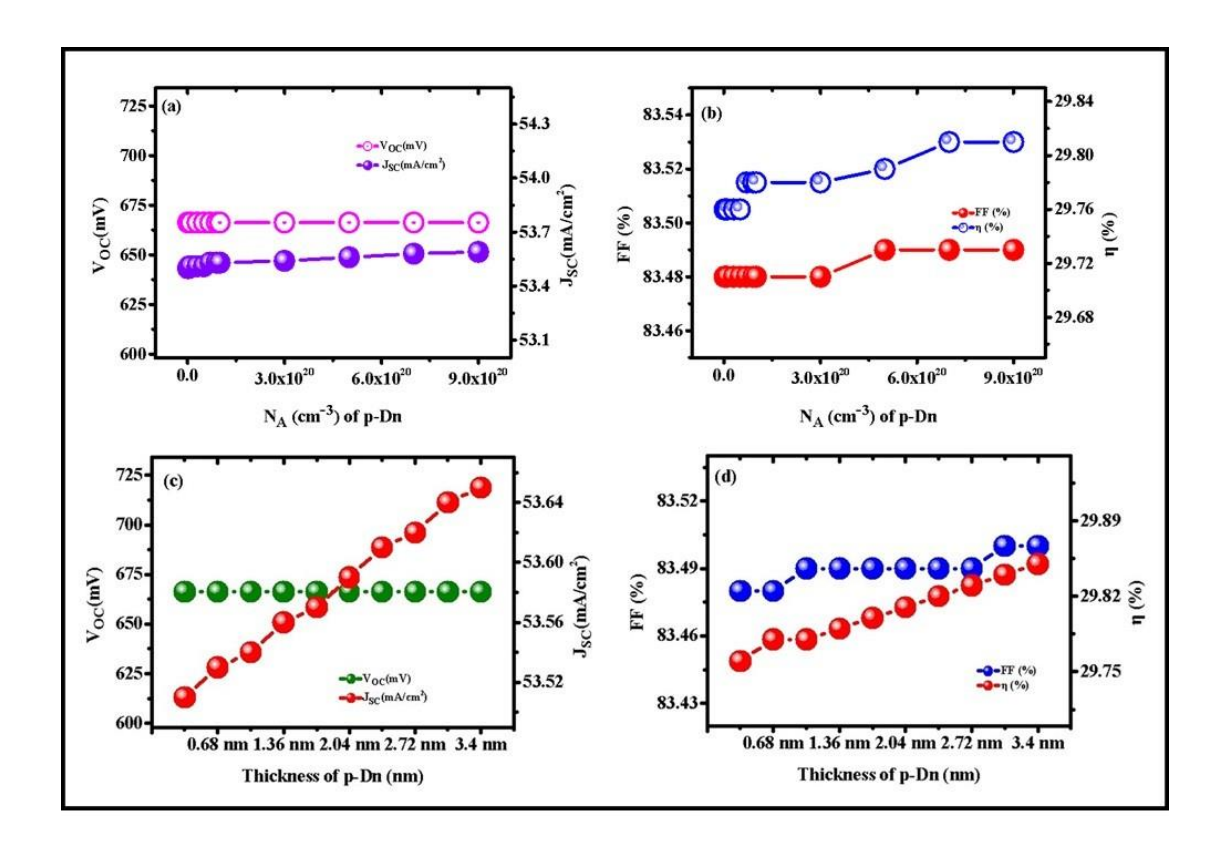


**Fig. 7.3** (a & b) The effect of variation of doping concentration ( $N_A$ ) of the BSF layer (p-Dn) on the performance parameters of the designed cell. (c & d) The effect of variation of thickness (nm) of the BSF layer (p-Dn) on the performance parameters of the designed cell.

# 7.4.4. Optimization of the thickness of the BSF layer

After optimising the doping concentration, we optimised the thickness of the BSF layer. Fig. 7.5 (a, b) shows slight changes in performance parameters as the layer's number increases from 1 to 10. While  $V_{OC}$  remained constant at 666.3 mV but  $J_{SC}$ , FF, and  $\eta$  increased from 53.51 mA/cm<sup>2</sup> to 53.65 mA/cm<sup>2</sup>, 83.48% to 83.5%, and 29.76% to 29.85%, respectively. An optimized BSF layer thickness of 3.4 nm was found to yield the best performance. Based on this trend, we found that as the thickness increases, cell performance improves slightly.

# 7.4.5. Optimization of the thickness of the emitter layer

The emitter layer is typically a thin semiconductor layer that is lightly doped opposite to the active layer, and is designed to collect and channel photogenerated charge carriers, primarily electrons, into the external circuit. The emitter layer is positioned on top of the solar cell, where it interacts with incoming sunlight. When light interacts with the cell, charge carriers are produced in the active region. The emitter layer builds a pn junction with the active layer, separating electron-hole pairs by directing electrons towards the external contacts and holes towards the base layer, resulting in the flow of electric current. In the simulated design, the single-layer n-type diamane thickness is set to 0.34 nm. Passivation is the most important feature in passivated emitter solar cells. To lower surface states and defect density, we incorporated SiO<sub>2</sub>/Si<sub>3</sub>N<sub>4</sub> as a passivation layer on the n-type diamane surface. These measures reduce the surface recombination velocity, allowing more charge carriers to reach the external circuit, thereby improving V<sub>OC</sub>, J<sub>SC</sub>, and overall conversion efficiency. The benefits of using ntype diamane as an emitter, combined with effective passivation, are significant because its ultra-thin nature minimises optical losses, letting more photons to reach the active layer of the cell for photon absorption. Furthermore, the outstanding thermal stability and conductivity of n-type diamane lead to improved FF and efficiency. Fig. 7.6 (a, b) depicts the influence of varying emitter layer thickness on solar cell performance. As the thickness of the emitter layer increases J<sub>SC</sub>, FF, and η consistently decrease. As emitter layer thickness increases from 0.34 nm to 3.4 nm, a reduction in J<sub>SC</sub> from 53.95 mA/cm<sup>2</sup> to 51.63 mA/cm<sup>2</sup>, in FF from 83.68% to 82.57%, and in efficiency from 30.08% to 29.51% was observed. The observed trends show that increasing emitter thickness has a significant impact on efficiency and current density, owing mostly to increased recombination processes within the layers. Interestingly, Voc responds differently, increasing from 666.3 mV to 692.2 mV as the emitter layer thickness increases, as shown in Figure 6 (a & b). Optimum efficiency is attained with a singlelayer n-type diamane emitter. At this thickness, the maximum conversion efficiency is 30.08%. To ensure maximum efficiency, the emitter should have a thin diamane layer. The simulation results suggest a uniform emitter thickness of 0.34 nm for the following simulation.

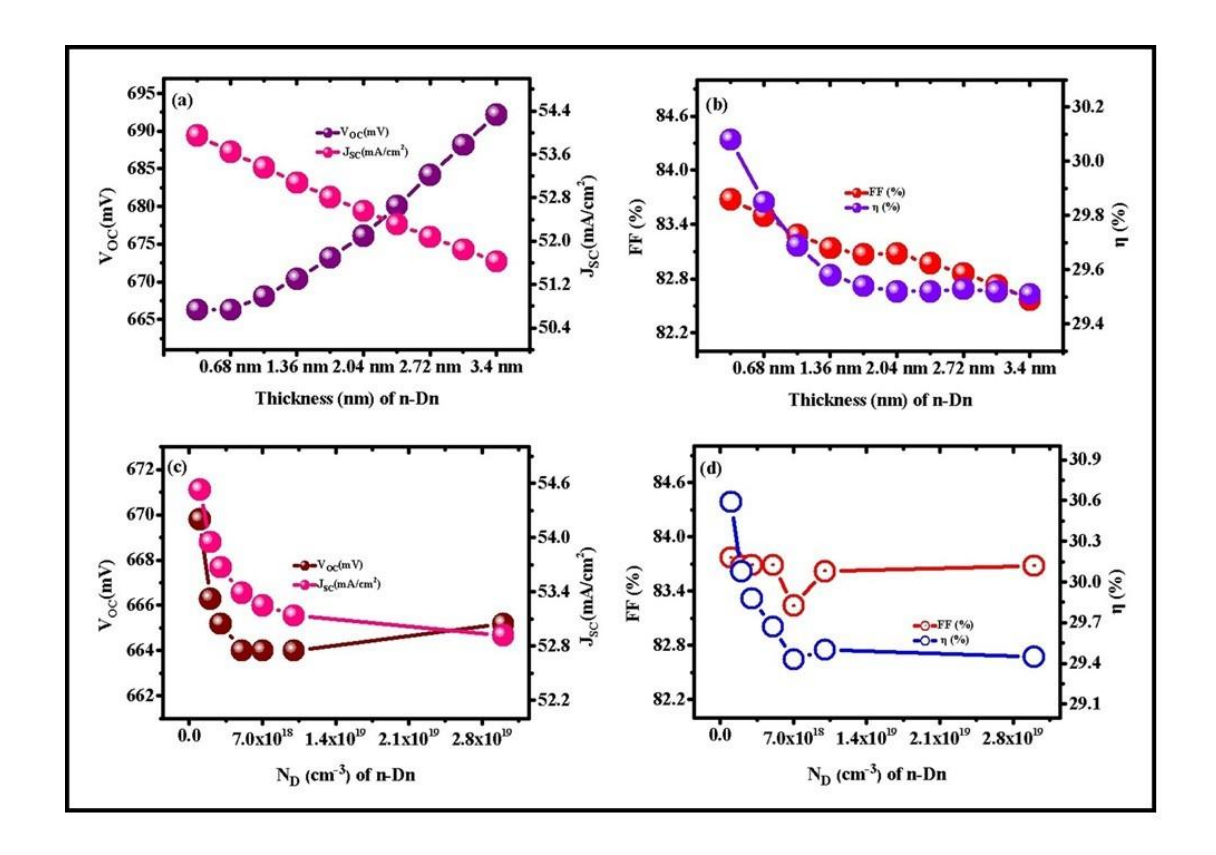


Fig. 7.4 (a & b) The effect of variation of thickness (nm) of the emitter layer (n-Dn) on the performance parameters of the designed cell. (c & d) The effect of variation of doping concentration  $(N_D)$  of the emitter layer (n-Dn) on the performance parameters of the designed cell.

# 7.4.6. Optimization of the doping concentration of the emitter layer

The doping of the emitter layer is also vital for optimising the solar cell's electrical and spectral parameters. Appropriate doping is essential to enhanced efficiency. Inadequate doping leads to insufficient electric field strength, whereas excessive doping increases recombination losses and lowers performance parameters. Since n-type diamane is utilised as an emitter layer, the doping concentration ( $N_D$ ) of n-type diamane must be optimised. We simulated  $N_D$  ranging from  $1\times10^{18}$  to  $3\times10^{19}$  cm<sup>-3</sup>, and the results are illustrated in Fig. 7.7 (a and b). The obtained results depict that as the doping concentration increases; the values of all the performance parameters decrease. For example, as  $N_D$  increased from  $1\times10^{18}$  to  $3\times10^{19}$  cm<sup>-3</sup>,  $V_{OC}$  declined from 669.8 mV to 665.2 mV,  $J_{SC}$  decreased from 54.53 mA/cm<sup>2</sup> to 52.92 mA/cm<sup>2</sup>, FF slightly dropped from 83.77% to 83.68%, and  $\eta$  from 30.59 to 29.45%, respectively. These values attained the maximum value when the simulation was conducted at  $N_D$  of  $1\times10^{18}$ , as

shown in Fig. 7.7. Excessive doping may have caused this, as it promotes Auger recombination, which reduces carrier lifetimes and Voc. Similarly, higher doping reduces the depletion width, limiting the region where carriers are efficiently captured, potentially lowering the value of J<sub>SC</sub>. In the same way, excessive doping increases recombination losses and shunt resistance, lowering FF. As a result, lower V<sub>OC</sub>, J<sub>SC</sub>, and FF lead to a considerable reduction in efficiency. By optimising carriers' lifespan, doping concentration, and layer thickness, we achieved a remarkable efficiency of 30.59% for the proposed passivated emitter solar cell, with J<sub>SC</sub> of 54.53 mA/cm<sup>2</sup>. The design incorporates passivating layers (SiO<sub>2</sub> and Si<sub>3</sub>N<sub>4</sub>) only on the illuminated side of the cell that is; at the emitter layer. It is commonly understood that applying passivation to both the front and rear surfaces, as in a PERC architecture, can boost efficiency even more.

To investigate the potential of the PERC structure and to validate the presented finding, we simulated the experimentally reported PERC solar cell. The simulation was based on a previously reported cell design [9], enabling validation of our results. The referenced structure, composed of Al<sub>2</sub>O<sub>3</sub>/SiN<sub>X</sub>/FSF(n+)/Si(n)/BSF(p+)/Au, achieved a conversion efficiency of 23.82% [9]. Using this reported design as a reference, we developed a modified PERC cell structure with the configuration Al<sub>2</sub>O<sub>3</sub>/Si<sub>3</sub>N<sub>4</sub>/n+ a-Si/p-c-Si/p+ a-Si/Au. Simulations conducted using the AFORS-HET numerical simulator produced an efficiency of 24.01%, closely aligning with the previously reported values. These findings provide strong validation for the methodologies and results presented in this study.

In order to further examine the worthiness of 2D carbon materials in Si-based solar cell heterostructures, an extensive investigation was carried out in other heterostructures. A series of additional simulations were carried out in order to gain more insight into the application of 2D carbon materials such as graphene and diamane with and without surface passivation, and to find the most efficient structure. These simulations focused on a number of HJ and HIT solar cell structures, as tabulated in Table 7.3 [16-17, 25–26]. As shown in Fig. 7.5 (a), a simple HJ design, ITO/n-Dn/p-cSi/Au, with ITO as TCE and n-Dn as the emitter, was simulated, obtaining η of 17.32%, a Voc of 699.7 mV, a J<sub>SC</sub> of 29.42 mA/cm², and FF of 84.13%.

**Table 7.3** The results obtained after analysing previously reported cell with and without passivation along with newly simulated cells with and without passivation [16-17, 25-26].

HJ & BSFHJ Structures	Voc (mV)	Jsc (mA/cm <sup>2</sup> )	FF (%)	η (%)
ITO/n-Dn/p-cSi/Au	699.7	29.42	84.13	17.32
Gr/n-Dn/p-cSi/Au	644.5	46.87	76.3	23.05
Gr/n-Dn/p-cSi/p-Dn/Au	631.2	51.16	83.16	26.86 [17]
Gr/Si <sub>3</sub> N <sub>4</sub> /SiO <sub>2</sub> /n-Dn/p-cSi/p- Dn/Au	669.8	54.53	83.77	30.59
HIT & BSFHIT Structures	Voc (mV)	Jsc (mA/cm <sup>2</sup> )	FF (%)	η (%)
Gr/n-Dn/a-Si: H(i)/p-cSi/Au	686.7	45.6	83.65	26.19
Gr/n-Dn/a-Si: H(i)/p-cSi/ a-Si: H(i)/Au	686.7	45.61	83.64	26.20
Gr/n-Dn/a-Si: H(i)/p-cSi/p-DnAu	660.2	51.79	80.65	27.57
Gr/n-Dn/a-Si: H(i)/p-cSi/ a-Si: H(i)/p-Dn/Au	683	52.74	81.55	29.38 [17]
$Gr/Si_3N_4/SiO_2/n$ -Dn/a-Si: $H(i)/p$ -cSi/Au	694.5	46.37	83.65	26.94
Gr/ Si <sub>3</sub> N <sub>4</sub> /SiO <sub>2</sub> /n-Dn/a-Si: H(i)/p-cSi/ a-Si: H(i)/Au	691.4	48.89	83.28	28.15
$Gr/Si_3N_4/SiO_2/n$ - $Dn/a$ - $Si:H(i)/p$ - $cSi/p$ - $DnAu$	678.9	51.95	81.45	28.73
Gr/ Si <sub>3</sub> N <sub>4</sub> /SiO <sub>2</sub> /n-Dn/a-Si: H(i)/p-cSi/ a-Si: H(i)/p-Dn/Au	683	52.74	81.55	30.69

Since graphene possesses outstanding optical transparency and excellent electrical conductivity. Motivated by this, we examined the structure Gr/n-Dn/p-cSi/Au - Replacing ITO with graphene, shown in Fig. 7.5 (b). Consequently, the PCE gets enhanced to 23.05% with  $V_{OC}$  of 644.5 mV,  $J_{SC}$  of 46.87 mA/cm², and FF of 76.3%. These findings confirm that graphene can be served as a TCE. This structure was further modified to Gr/n-Dn/p-cSi/p-Dn/Au, with the addition of a p-Dn as BSF layer as shown in Fig. 7.5(c). The PCE was enhanced to 26.86% with a  $V_{OC}$  of 631.2 mV,  $J_{SC}$  of 51.16 mA/cm², and FF of 83.16% [26].

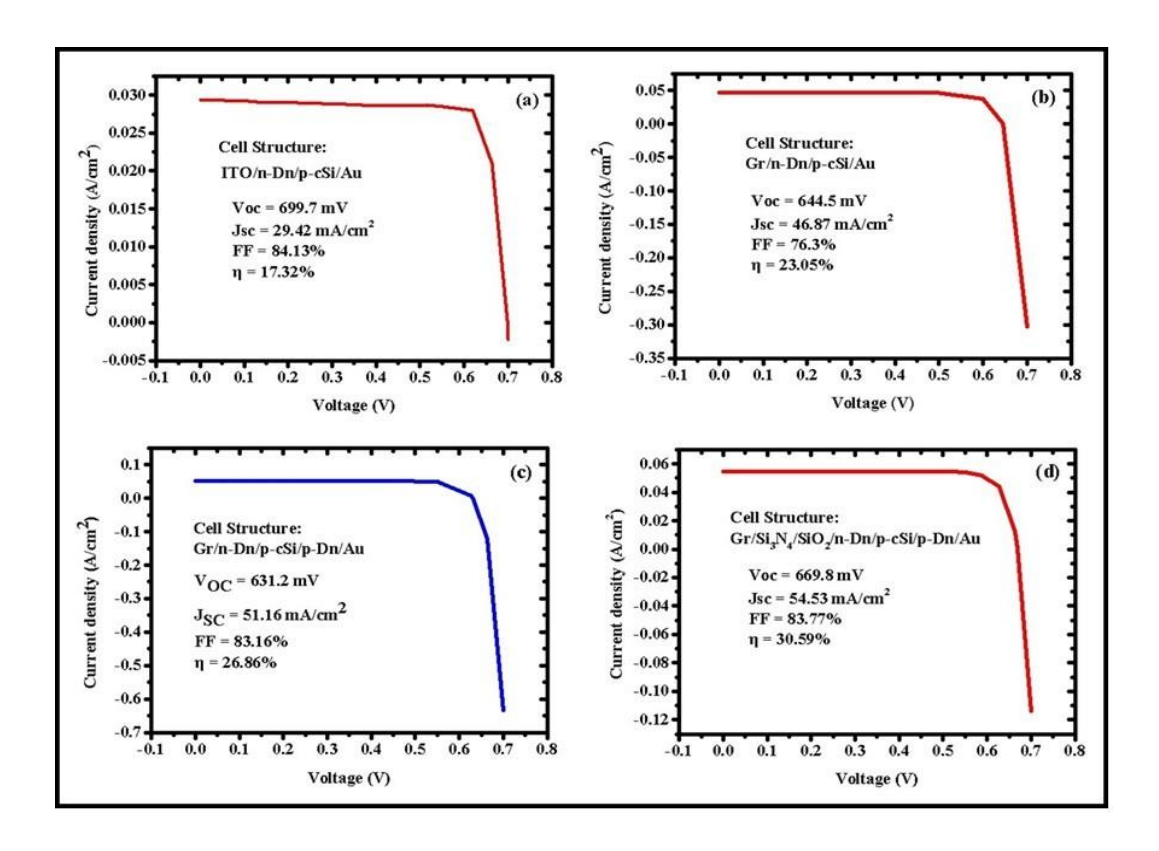


**Fig. 7.5** shows the I-V characteristics of optimized HJ solar cells: **(a)** ITO/n-Dn/p-cSi/Au – A simple HJ design with ITO as TCE and n-Dn as the emitter, achieving 17.17% PCE. **(b)** Gr/n-Dn/p-cSi/Au – Replacing ITO with graphene improves PCE to 23.05%. **(c)** Gr/n-Dn/p-cSi/p-Dn/Au – Adding a p-Dn as BSF, boosts PCE to 26.86% [17]. **(d)** Gr/Si<sub>3</sub>N<sub>4</sub>/SiO<sub>2</sub>/n-Dn/p-cSi/p-Dn/Au – Emitter passivation with Si<sub>3</sub>N<sub>4</sub>/SiO<sub>2</sub> raises PCE to 30.59%.

As discussed above, passivation of the emitter may enhance the PCE. So, the structure  $Gr/Si_3N_4/SiO_2/n$ -Dn/p-cSi/p-Dn/Au - adding a passivation layer of  $Si_3N_4/SiO_2$  is examined, and further enhancement in PCE to 30.59% is noticed with  $V_{OC}$  of 669.8 mV,  $J_{SC}$  of 54.53 mA/cm², and FF of 83.77% as shown in Fig. 7.5 (d). Thus, we can say that 2D carbon material has the potential to enhance PCE even more. If this is rational, similar patterns should be observed in HIT solar cells. Fig. 7.6 (a) showed the I-V curve of the cell structure Gr/n-Dn/a-Si:H(i)/p-cSi/Au - representing a simple HIT design with single-sided passivation, yielding  $\eta$  of 26.19%, along with  $V_{OC}$  of 686.7 mV,  $J_{SC}$  of 45.6 mA/cm², and FF of 83.65%. In the structure Gr/n-Dn/a-Si:H(i)/p-cSi/a-Si:H(i)/Au - Double-sided passivated c-Si layer, PCE advances slightly to 26.20%, with  $V_{OC}$  of 686.7 mV,  $J_{SC}$  of 45.61 mA/cm², and FF of 83.64%, as shown in Fig. 7.6 (b). Then, we have simulated another structure Gr/n-Dn/a-Si:H(i)/p-cSi/p-Dn/Au, adding a p-Dn

as BSF layer to single-sided passivated HIT. PCE increases to 27.57% with  $V_{OC}$  of 660.2 mV,  $J_{SC}$  of 51.79 mA/cm², and FF of 80.65%, as shown in Fig. 7.6 (c). Finally, employing both full passivation and BSF layer, the structure Gr/n-Dn/a-Si:H(i)/p-cSi/a-Si:H(i)/p-Dn/Au was examined, as shown in Fig. 7.6 (d). This fully passivated HIT cell with diamane-based BSF layer has an overall PCE of 29.38%, with a  $V_{OC}$  of 683 mV,  $J_{SC}$  of 52.74 mA/cm², and FF of 81.5% [26]. These findings emphasise the significance of integrating diamane in emitter and BSF layers, as well as appropriate surface passivation, to improve the photovoltaic performance of the HIT solar cells.

Furthermore, to further advance the HIT cell performance, we introduced an additional passivation layer comprising Si<sub>3</sub>N<sub>4</sub> and SiO<sub>2</sub> over the emitter side. This approach was inspired by the success of commercial PERC technology, which effectively utilizes surface passivation to minimize recombination losses and boost cell efficiency. The resulting I-V curve of these improved structures are presented in Fig. 7.7 (a-d), demonstrating the positive impact of emitter passivation on device performance. In Fig. 7.7 (a), the structure Gr/Si<sub>3</sub>N<sub>4</sub>/SiO<sub>2</sub>/n-Dn/a-Si:H(i)/p-cSi/Au included extra passivation over the emitter layer (n-Dn) is simulated, yielding an efficiency of 26.94% with a Voc of 694.5 mV, J<sub>SC</sub> of 46.37 mA/cm<sup>2</sup>, and FF of 83.65%. Similarly, we have passivated the emitter of the fully passivated HIT cell Gr/Si<sub>3</sub>N<sub>4</sub>/SiO<sub>2</sub>/n-Dn/a-Si:H(i)/p-cSi/a-Si:H(i)/Au, reaching  $\eta$  of 28.15% with a  $V_{OC}$  of 691.4 mV,  $J_{SC}$  of 48.89 mA/cm<sup>2</sup>, and FF of 83.28%, shown in Fig. 7.7 (b). To suppress rear-side recombination and improve carrier selectivity, a p-type diamane layer was introduced as the back-surface field along with the passivation of Si<sub>3</sub>N<sub>4</sub>/SiO<sub>2</sub> on the emitter layer, resulting in the structure Gr/Si<sub>3</sub>N<sub>4</sub>/SiO<sub>2</sub>/n-Dn/a-Si:H(i)/p-cSi/p-Dn/Au. This configuration further boosted the PCE to 28.73% with a V<sub>OC</sub> of 678.9 mV, J<sub>SC</sub> of 51.95 mA/cm<sup>2</sup>, and FF of 81.45%, shown in Fig. 7.7 (c). Finally, the fully optimized HIT solar cell—combining a passivated emitter, double-sided passivation of the c-Si active layer, and addition of diamane as BSF layer was modelled as Gr/Si<sub>3</sub>N<sub>4</sub>/SiO<sub>2</sub>/n-Dn/a-Si:H(i)/p-cSi/a-Si:H(i)/p-Dn/Au, shown in Fig. 7.7 (d). This structure delivered the maximum ever efficiency of 30.69% with a  $V_{OC}$  of 683 mV,  $J_{SC}$  of 52.74 mA/cm<sup>2</sup>, and FF of 81.55%. These results demonstrate that integrating passivation at both emitter and rear interfaces, along with 2D carbon materials, significantly improves the performance of HIT solar cells.

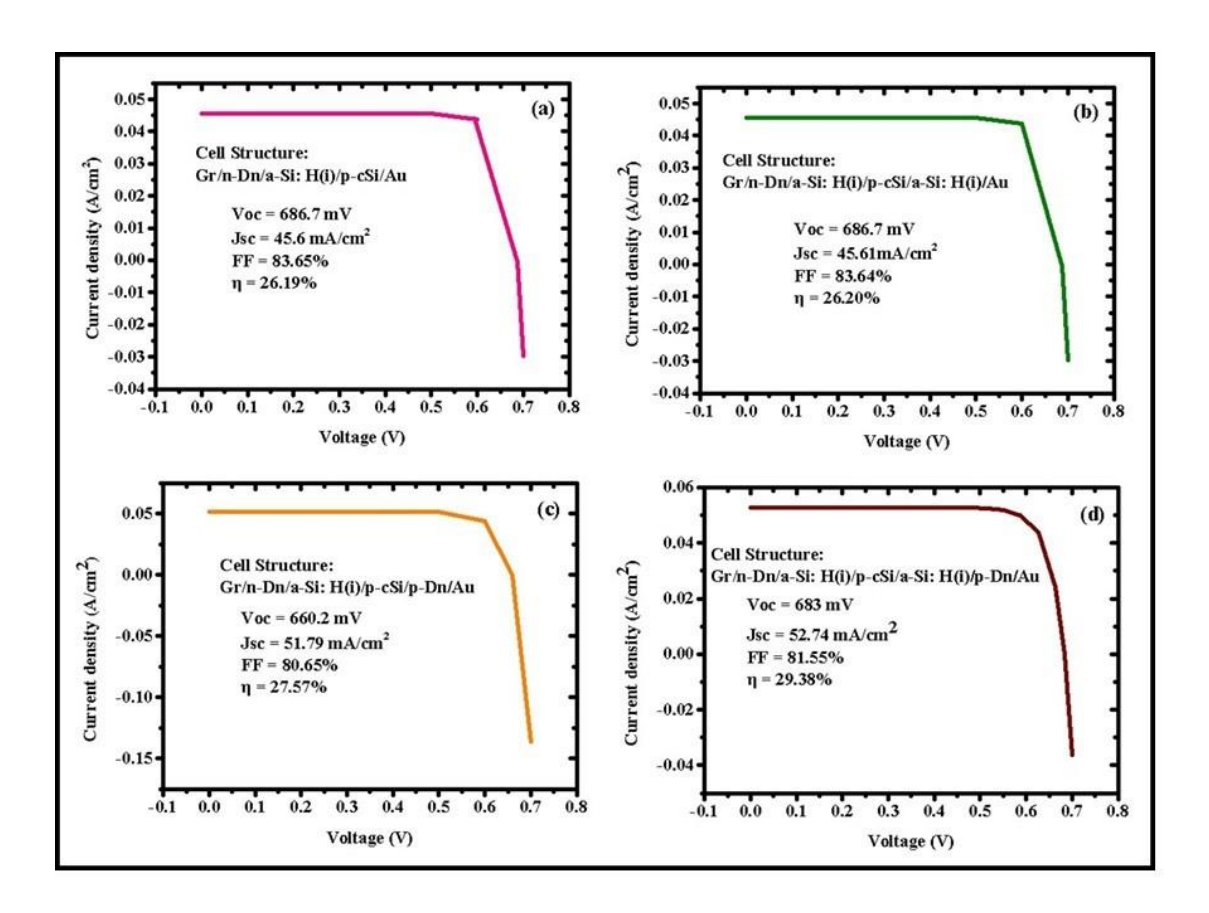


**Fig. 7.6** I-V characteristics of optimized HIT solar cells: **(a)** Gr/n-Dn/a-Si:H(i)/p-cSi/Au – Simple HIT design with single-sided passivation, achieving 26.19% PCE. **(b)** Gr/n-Dn/a-Si:H(i)/p-cSi/a-Si:H(i)/Au – Double-sided passivated c-Si layer slightly improves PCE to 26.20%. **(c)** Gr/n-Dn/a-Si:H(i)/p-cSi/p-Dn/Au – Adding a p-Dn BSF to single-sided passivated HIT boosts PCE to 27.57%. **(d)** Gr/n-Dn/a-Si:H(i)/p-cSi/a-Si:H(i)/p-Dn/Au – Fully passivated c-Si with BSF further increases PCE to 29.38% [17].

It is now plausible to review whether the Gr/Si<sub>3</sub>N<sub>4</sub>/SiO<sub>2</sub>/n-Dn/a-Si:H(i)/p-cSi/a-Si:H(i)/p-Dn/Au solar cell structure could be experimentally fabricated. The practicality of experimentally fabricating the Gr/Si<sub>3</sub>N<sub>4</sub>/SiO<sub>2</sub>/n-Dn/a-Si:H(i)/p-cSi/a-Si:H(i)/p-Dn/Au solar cell structure seems to be possible now by assessing the standard infrastructure available for 2D carbon material and silicon solar cells. The process begins with doping in p-type crystalline silicon (p-cSi) wafer either by thermal diffusion or ion implantation, which is then thoroughly cleaned to remove contaminants and native oxide. A thin intrinsic hydrogenated amorphous silicon (a-Si:H(i)) layer is deposited on both sides of the wafer using plasma-enhanced chemical vapor deposition (PECVD) or Hotwire chemical vapour deposition (HFCVD) to provide surface passivation.

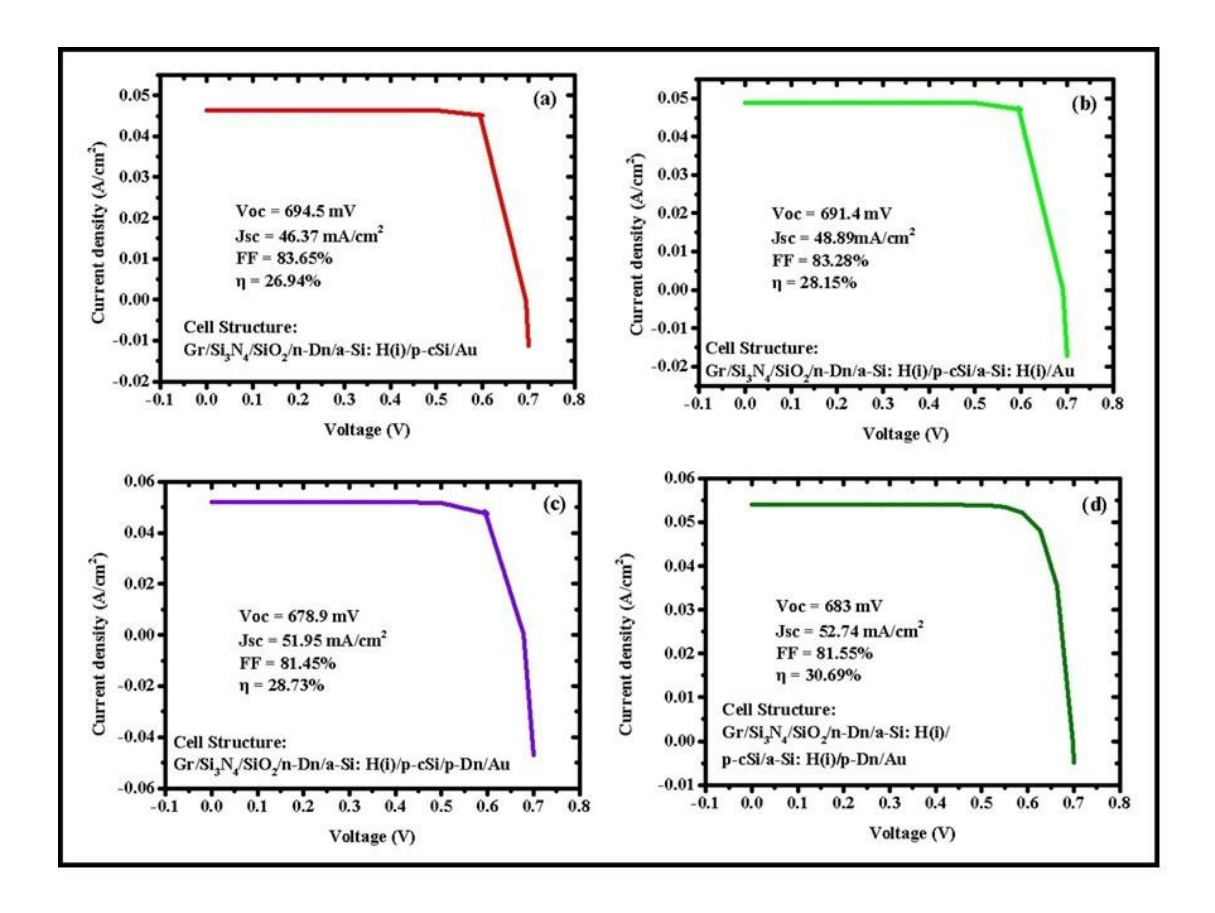


**Fig. 7.7** I-V characteristics of optimized HIT solar cells with passivated emitter: **(a)** Gr/Si<sub>3</sub>N<sub>4</sub>/SiO<sub>2</sub>/n-Dn/a-Si:H(i)/p-cSi/Au – Passivated emitter with Si<sub>3</sub>N<sub>4</sub>/SiO<sub>2</sub> enhances PCE to 26.94%. **(b)** Gr/Si<sub>3</sub>N<sub>4</sub>/SiO<sub>2</sub>/n-Dn/a-Si:H(i)/p-cSi/a-Si:H(i)/Au – Fully passivated c-Si layer with emitter passivation improves PCE to 28.15%. **(c)** Gr/Si<sub>3</sub>N<sub>4</sub>/SiO<sub>2</sub>/n-Dn/a-Si:H(i)/p-cSi/p-Dn/Au – Adding a p-Dn BSF to single-sided passivated HIT with emitter passivation boosts PCE to 28.73%. **(d)** Gr/Si<sub>3</sub>N<sub>4</sub>/SiO<sub>2</sub>/n-Dn/a-Si:H(i)/p-cSi/a-Si:H(i)/p-Dn/Au – Fully optimized HIT with passivated emitter achieves 30.69% PCE.

The challenge is to deposit or transfer the diamane on the front or rear side of the active layer of Si. But it is possible to synthesize diamane on a silicon substrate by first transferring bilayer graphene (BLG) onto a cleaned silicon wafer, typically using a well-known PMMA-assisted method. After transfer and annealing, the graphene is converted to diamane through hydrogen plasma treatment, or fluorination, which induces a transition from sp<sup>2</sup> to sp<sup>3</sup> carbon bonding.

In another way, first, polycrystalline/ nanocrystalline diamond films can be deposited on a silicon substrate using microwave plasma-enhanced chemical vapor deposition (MPCVD) or HFCVD, where a methane-hydrogen gas mixture is used at high temperatures to grow a diamond film. After deposition, the film has to be thinned down

to just a few manometers using standard techniques such as reactive ion etching (RIE), focused ion beam (FIB) milling, or chemical mechanical polishing (CMP). This thinning process has to be carefully controlled to reach a few atomic layers, creating a structure similar to diamane, a two-dimensional sp<sup>3</sup>-bonded carbon film. To preserve the diamond-like properties at this ultrathin scale, surface passivation typically with hydrogen or fluorine is applied to prevent graphitization. Furthermore, thinning up to the manometer scale can be achieved by high-power or prolonged hydrogen plasma treatment that can lead to graphitization of the top surface, especially in thin diamond films or near-surface layers. The energetic hydrogen species and elevated temperatures can break sp<sup>3</sup> carbon bonds, allowing the structure to convert into sp<sup>2</sup>-bonded graphitic carbon. After the graphitization of the top surface, low-power, short-duration hydrogen plasma in the presence of oxygen can safely passivate diamond surfaces and even stabilize ultrathin sp<sup>3</sup> layers like diamane. Precise control of treatment conditions is essential to avoid damaging the diamond structure. Next, a thin SiO<sub>2</sub> layer is grown by thermal oxidation or deposited using PECVD, followed by a Si<sub>3</sub>N<sub>4</sub> layer that acts as an anti-reflective and passivation coating. A monolayer or few-layer graphene sheet, grown via CVD, is transferred onto the Si<sub>3</sub>N<sub>4</sub> layer using a PMMA-assisted wet transfer process, then cleaned and annealed. Finally, a gold (Au) layer is deposited on the rear side by thermal evaporation or sputtering to serve as the back contact. The completed device is then characterized under standard solar illumination to measure performance parameters such as current-voltage (J-V) characteristics, external quantum efficiency (EQE), and contact resistance. This is very costly and extensive labours that need precise perfection and well-equipped infrastructure. We envision that the presented work will pave the way for researchers involved in the area of carbon materials and silicon solar cells.

# 7.5 Summary

An outstanding power conversion efficiency of 30.59% was achieved, corresponding to a current density of 54.53 mA/cm<sup>2</sup>. This result surpasses previously reported single-junction silicon solar cell efficiencies, which have reached up to 29.4% with  $J_{SC}$  of approximately 43 mA/cm<sup>2</sup>. We found that passivation significantly improved

performance. For instance, after passivation, the PCE of the BSFHJ cell improved from 26.66% to 30.59%. A similar effect was seen in the BSFHIT structure. These findings highlight not only the excellent performance potential of p-type silicon passivated emitter solar cells but also the effectiveness of SiO<sub>2</sub> and Si<sub>3</sub>N<sub>4</sub> based dielectric passivation in reducing surface recombination on lightly nitrogen-doped emitters. These findings demonstrate how novel materials like diamane can be utilized with proven passivation layers (SiO<sub>2</sub> and Si<sub>3</sub>N<sub>4</sub>) to enhance solar cell performance and facilitate further developments in silicon photovoltaics.

## REFERENCES

- [1] Lim, E.L., Yap, C.C., Jumali, M.H.H., Teridi, M.A.M. and The, C.H., 2018. A mini review: Can graphene be a novel material for perovskite solar cell applications? *Nano-Micro Letters*, 10, 1, pp.27.
- [2] Dada, M. and Popoola, P., 2023. Recent advances in solar photovoltaic materials and systems for energy storage applications: a review. *Beni-Suef University Journal of Basic and Applied Sciences*, 12, 1, pp.66.
- [3] Xiao, S. and Xu, S., 2014. High-efficiency silicon solar cells—Materials and devices physics. *Critical Reviews in Solid State and Materials Sciences*, 39, 4, pp.139–151.
- [4] Blakers, A., 2019. Development of the PERC solar cell. *IEEE Journal of Photovoltaics*, 9, 3, pp.629–635.
- [5] Boukortt, N., Patan, S. & Hadri, B., 2018. Development of high-efficiency PERC solar cells using Atlas Silvaco. *Silicon*, 11, 1, pp.145–152.
- [6] Min, B., Kwon, J., Kim, Y., Park, J., Kim, Y., Ahn, J., Lee, J., Kim, H., Kim, J., Kim, D., Yoon, K., Kim, H. and Park, S., 2017. A roadmap toward 24% efficient PERC solar cells in industrial mass production. *IEEE Journal of Photovoltaics*, 7, 6, pp.1540–1545.
- [7] Dullweber, T. and Schmidt, J., 2016. Industrial silicon solar cells applying the passivated emitter and rear cell (PERC) concept—A review. *IEEE Journal of Photovoltaics*, 6, 5, pp.1366–1381.
- [8] Benick, J., Hoex, B., van de Sanden, M.C.M., Schultz-Wittmann, O., Feldmann, F., Hofmann, T., Karg, D., Hovel, H., Hermle, M. and Glunz, S.W., 2008. High efficiency n-type Si solar cells on Al2O3-passivated boron emitters. *Applied Physics Letters*, 92, 25, pp.253504.
- [9] Phimu, K., Singh, K.J. and Dhar, R.S., 2022. Design of PERC cell using SiO<sub>2</sub>, Si<sub>3</sub>N<sub>4</sub>, and Al<sub>2</sub>O<sub>3</sub> with the novel technique for enhanced absorption of silicon selective emitter for solar cell processing. *IEEE International Conference on Nanoelectronics, Nanophotonics, Nanomaterials, Nanobioscience & Nanotechnology (5NANO)*, pp.1–4.
- [10] Beliaev, L.Y., Shkondin, E., Lavrinenko, A.V. and Takayama, O., 2022. Optical, structural and composition properties of silicon nitride films deposited by different methods. *Thin Solid Films*, 763, 1, pp.139568.
- [11] Tong, R., Zheng, Z., Zhu, Y., Yang, D., Sun, S., Zhang, X., Lu, M., Lu, Z., Li, J., Zhao, Y. and Chen, W., 2021. Tuning back side passivation for enhancing the performance of PERC solar cells. *Solar Energy Materials & Solar Cells*, 231, 1, pp.111319.

- [12] Descoeudres, A., Barraud, L., Wolf, S.D., Holman, Z.C., Ballif, C. and Boccard, M., 2013. >21% efficient silicon heterojunction solar cells on n- and p-type wafers compared. *IEEE Journal of Photovoltaics*, 3, 1, pp.83–89.
- [13] Seif, J.P., Taguchi, M., Yoshikawa, K., Kanematsu, M., Yamamoto, K., Descoeudres, A., Wolf, S.D. and Ballif, C., 2014. Amorphous silicon oxide window layers for higherficiency silicon heterojunction solar cells. *Journal of Applied Physics*, 115, 8, pp.084503.
- [14] Van Sark, W., 2016. Heterojunction silicon solar cells. In *Photovoltaic Solar Energy*. Wiley, pp.1–30.
- [15] Holman, Z.C., Descoeudres, A., Barraud, L., Wolf, S.D., Ballif, C. and Boccard, M., 2012. Current losses at the front of silicon heterojunction solar cells. *IEEE Journal of Photovoltaics*, 2, 1, pp.7–15.
- [16] Naima, Tyagi, P.K. and Singh, V., 2024. Doped diamane: An efficient electron/hole collection layer in HIT solar cell. *Materials Science and Engineering B*, 310, 1, pp.117754.
- [17] Naima, Tyagi, P.K. & Singh, V., 2024. Potential application of p-type diamane as back surface field layer in silicon-based heterojunction solar cells. *Semiconductor Science and Technology*, 39, 12, pp.125021.
- [18] Chernozatonskii, L.A., Sorokin, P.B., Kvashnin, A.G. and Kvashnin, D.G., 2009. Diamond-like C2H nanolayer, diamane: Simulation of the structure and properties. *JETP Letters*, 90, 2, pp.134–138.
- [19] Piazza, F., Jadczak, J., Rechciński, R., Kutrowska-Girzycka, J., Bożek, R., Korona, K.P., Strupiński, W., Borysiuk, J., Baranowski, J.M., Nowicki, P. and Kossacki, P., 2020. Raman evidence for the successful synthesis of diamane. *Carbon*, 169, 1, pp.129–133.
- [20] Qin, G., Wu, L. and Gou, H., 2021. Diamane: design, synthesis, properties, and challenges. *Functional Diamond*, 1, 1, pp.1–15.
- [21] Zhu, L., Li, W. and Ding, F., 2019. Giant thermal conductivity in diamane and influence of horizontal reflection symmetry on phonon scattering. *Nanoscale*, 11, 10, pp.4248–4257.
- [22] Cheng, T., Liu, Z. and Liu, Z., 2020. High elastic moduli, controllable bandgap and carrier mobility in single-layer diamond. *Journal of Materials Chemistry C*, 8, 44, pp.13819–13826.
- [23] Bouzidi, S., Barhoumi, M. and Said, M., 2021. Optical properties of Janus and non-Janus diamanes monolayers using ab-initio calculations. *Optik*, 235, 1, pp.166642.
- [24] Niu, C., Yan, H., Wang, Y., Zhang, S., Shi, L. and Liu, J., 2022. Configuration stability and electronic properties of diamane with boron and nitrogen dopants. *Physical Review B*, 105, 17, pp.174106.
- [25] Naima, Tyagi, P.K. and Singh, V., 2022. N-type diamane: An effective emitter layer in crystalline silicon heterojunction solar cell. *Carbon Trends*, 9, 1, pp.100209.
- [26] Naima, Tyagi, P.K. and Singh, V., 2023. Potential application of graphene/diamane interface in silicon-based heterojunction with intrinsic thin layer solar cell. *Computational Materials Science*, 226, 1, pp.112252.
- [27] Naima, Tyagi, P.K. and Singh, V., 2023. Affinity optimization of crystalline-silicon heterojunction solar cell using AFORS-HET software. In *Recent Advances in Nanotechnology*. Springer Proceedings in Materials, 28, pp.1-10.
- [28] Joonwichien, S., Phromdee, P., Kanjanaboos, P., Yimnirun, R. and Taweepreda, W., 2018. Assisted passivation by chemically grown SiO2 layer in selective emitter-passivated emitter and rear cells. *Solar Energy Materials and Solar Cells*, 186, 1, pp.84–91.

- [29] Zhuang, Y.F., Li, S.F., Chen, X., Zhang, X.X., Chen, L., Wang, D., Zhou, H.L., Liu, Z.X., Zhang, S., Zhao, Y. and Lu, L.F., 2019. Application of SiO2 passivation technique in mass production of silicon solar cells. *Solar Energy Materials and Solar Cells*, 193, 1, pp.379–386.
- [30] Glunz, S.W. and Feldmann, F., 2018. SiO2 surface passivation layers—a key technology for silicon solar cells. *Solar Energy Materials and Solar Cells*, 185, 1, pp.260–269.
- [31] El Amrani, A., Outzourhit, A., Fliyou, M. and Bennouna, A., 2008. Silicon nitride film for solar cells. *Renewable Energy*, 33, 10, pp.2289–2293.
- [32] Stang, R., Leendertz, C. and Haschke, J., 2010. Numerical simulation and characterization of solar cells using AFORS-HET. *Solar Energy*, 84, 3, pp.432.
- [33] Wen, H.C., Lee, S.Y., Wu, T.B., Chang, H.C. and Hu, Y.C., 2005. Systematic investigation of amorphous transition-metal-silicon-nitride electrodes. In *VLSI Technology Symposium*, pp.46–47.
- [34] Kluska, S., Swatowska, B., Kolodziejczyk, M., Kozlowski, M., Raczkowski, A. and Sitarek, P., 2022. Thermo-optical properties of non-stoichiometric silicon nitride layers. *Materials*, 15, 7, pp.2260.
- [35] Lee, B.H., Kim, H., Park, C., Park, H., Jeon, H., Lee, J.C., Han, M.J. and Ahn, J.H., 2005. Gate stack technology for nanoscale devices. *Materials Today*, 9, 6, pp.32–38.
- [36] Luan, H., Yang, J., Buchanan, D.A., Cartier, E.A., Dong, T., Lee, W.C., Ma, T.P., Rai, R., Samavedam, S.B. and White, B.E., 2006. Evaluation of titanium silicon nitride for CMOS. *Applied Physics Letters*, 88, 14, pp.142113.
- [37] LibreTexts, 2020. Work function values (Reference Table). *LibreTexts Chemistry*. [Online] Available at: https://chem.libretexts.org [Accessed July 2025].
- [38] Johnson, P.B. and Christy, R.W., 1972. Optical constants of noble metals. *Physical Review B*, 6, 12, pp.4370–4379.
- [39] Bae, S., Kim, H., Lee, Y., Xu, X., Park, J.S., Zheng, Y., Balakrishnan, J., Lei, T., Kim, H.R., Song, Y.I., Kim, Y.J., Kim, K.S., Özyilmaz, B., Ahn, J.H., Hong, B.H. and Iijima, S., 2010. Roll-to-roll production of graphene films for transparent electrodes. *Nature Nanotechnology*, 5, 8, pp.574–578.
- [40] Ullah, S., Anjum, D.H., Hussain, T., Hussain, S., Zhao, Y., Alshareef, H.N. and Butt, F.K., 2021. Graphene transfer methods: A review. *Nano Research*, 14, 11, pp.3756–3772.
- [41] Niu, C., Wu, L., Gou, H., Du, J., Lin, Y. and Pan, Y., 2020. Boron-dopant enhanced stability of diamane with tunable band gap. *Journal of Physics: Condensed Matter*, 32, 13, pp.135503.
- [42] Zhuang, Y.F., Li, S.F., Chen, X., Zhang, X.X., Chen, L., Wang, D., Zhou, H.L., Liu, Z.X., Zhang, S., Zhao, Y. and Lu, L.F., 2019. Application of SiO<sub>2</sub> passivation in mass production of silicon solar cells. *Solar Energy Materials and Solar Cells*, 193, 1, pp.379–386.
- [43] Yang, X., Li, H., Zhang, X., Ma, J., Zhang, Y., Li, Z., Shi, J. and Liu, G., 2018. HIT solar cells with N-type low-cost metallurgical silicon. *Advances in OptoElectronics*, 7368175, pp.5.
- [44] Van Sark, W.G.J.H.M., 2007. Teaching the relation between solar cell efficiency and annual energy yield. *European Journal of Physics*, 28, 3, pp.415–427.
- [45] Kazici, M., Soykan, M.E., Kurt, E., Yildirim, D. and Hepbasli, A., 2018. Solar cells. In *Comprehensive Energy Systems*, 4, pp.295–336.
- [46] Dizaj, M.H., 2020. Efficiency calculation and quality improvement of perovskite solar cells. *Energy Conversion*, 2, 7, pp.1–8.

- [47] Borah, C.K., Tyagi, P.K. and Kumar, S., 2018. Few-layer p-type phosphorene sheet as transparent electrode in silicon heterojunction solar cells. *Computational Materials Science*, 151, pp.65–72.
- [48] Bessler, R., Duerig, U. and Koren, E., 2019. Dielectric constant of bilayer graphene interface. *Nanoscale Advances*, 1, 5, pp.1702–1706.
- [49] Shen, W., Li, X., Cui, Y., Guo, X., Han, X., Lu, Q., Yang, Y., Zhou, J. and Chen, X., 2019. Electron affinity of boron-terminated diamond (001) surface. *Journal of Materials Chemistry C*, 7, 31, pp.9534–9540.
- [50] Rietwyk, K.J., Fischer, M., Hoffmann, D.M., Stutzmann, M. and Garrido, J.A., 2013. Work function and electron affinity of fluorine-terminated diamond surface. *Applied Physics Letters*, 102, 9, pp.091604.
- [51] Benda, V., 2018. Crystalline silicon solar cell and module technology. In *A Comprehensive Guide to Solar Energy Systems*. Academic Press, pp.63–93.
- [52] Saga, T., 2010. Advances in crystalline silicon solar cell technology. *NPG Asia Materials*, 2, 3, pp.96–102.
- [53] Choe, K.S., 2014. Simulation of back-surface field effect in silicon solar cells. *Solid State Sciences*, 29, pp.48–51.

# CHAPTER 8

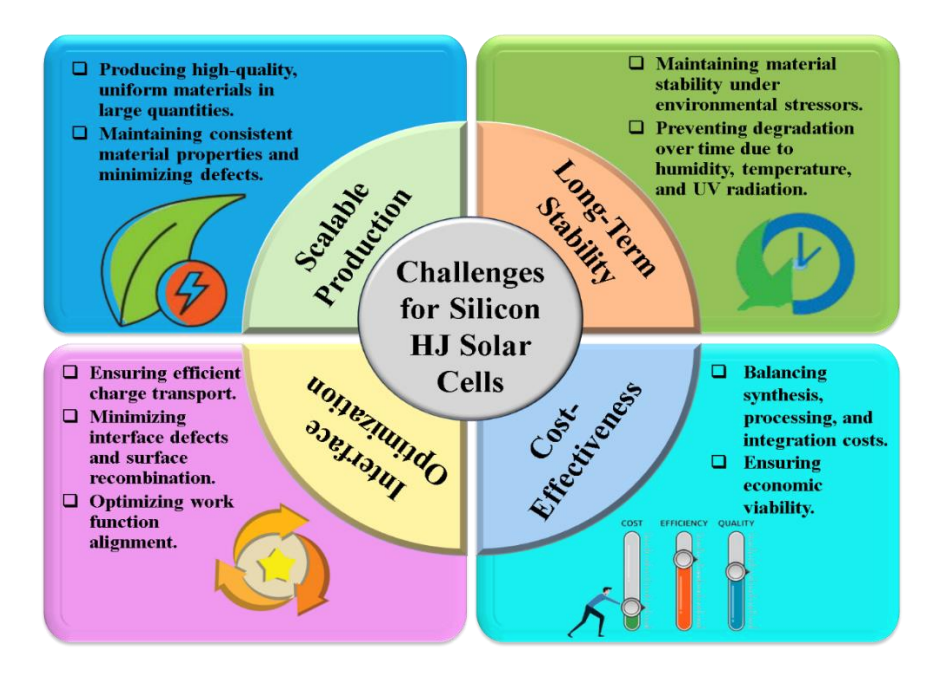
# CONCLUSION, FUTURE SCOPE, AND SOCIAL IMPACT

This chapter summarizes the key findings of the presented work and outlines the specific conclusions drawn from the investigation. It also highlights how the current research can be further advanced and utilized to fabricate highly efficient, cost-effective silicon-based solar cells by integrating diamane with other 2D materials. Such advancements have the potential to surpass existing theoretical efficiency limits. Progress in this direction could accelerate the global transition to renewable energy, enhance energy security by reducing dependence on imported fossil fuels, and make a meaningful contribution to sustainable development and economic growth. The insights gained from the presented research will contribute to the development of next-generation high-efficiency solar cells with enhanced industrial applicability. This detailed simulation and optimization approach underscores the potential of the c-Si solar cell structure, which provides maximum PCE in industrial applications.

## 8.1 Conclusion

In this thesis, comprehensively potential applications of diamane—a novel two-dimensional (2D) sp³-hybridized carbon material have been explored in silicon HJ and HIT solar cells. Through systematic modelling, simulation, and comparative analysis across five studies, diamane has been found as a promising alternative to conventional doped amorphous silicon layers for emitter, BSF, and carrier-selective contact applications.

In the initial investigation, the ITO/n-diamane/p-cSi/Ag device configuration was analysed to understand the impact of key physical parameters of n-type diamane on cell performance. It was found that, except for hole mobility, most parameters—including bandgap, electron affinity, and work function—directly influenced the photovoltaic behaviour. The formation of a Schottky junction at the n-Dn/p-cSi interface played a pivotal role in charge carrier transport. A maximum efficiency of 16.84% was achieved after optimization, and it was concluded that enhancing diamane's work function via chemical doping or other means could significantly improve its emitter performance in silicon heterojunction solar cells.



In this study, first, we have proposed the structure ITO/n- Dn/p-cSi/Ag. After optimizing the parameters of both diamane as well as silicon, the maximum efficiency of 16.84% was achieved. We also compared the optimized values with the reported experimental

values and found in well-agrement. It has been found that the thickness of front and back contacts does not play an important role on the performance of the modelled heterojunction cell. This finding demonstrated that n-type diamane might be used as an effective emitter layer in crystalline Si heterojunction solar cell.

The study further proceeded to examine the integration of a graphene as a TCE paired with n-diamane emitter and a-Si:H(i) as passivation layer graphene/diamane interface in HIT structures, marking the first reported comparison between ITO and graphene as TCOs in conjunction with diamane emitter layers. The structure modelled as: graphene/n-diamane/a-Si:H (i)/p-cSi/Ag was simulated and a theoretical efficiency of 31.2% achieved. The obtained results demonstrated that single-layer graphene and n-type diamane could effectively work as a TCO-emitter pair, improving efficiency from 25.61% to 31.2% in the ideal case. The commercially feasible configuration of silicon yielded an efficiency of 24.15%, validating the theoretical outcomes. These findings emphasized the dual potential of graphene and diamane as transparent and conductive contact layers for high-efficiency photovoltaic devices.

In further extended study, doped diamane layers were investigated as electron and hole collection layers. Novelty of the reported work is the use of doped diamane as an effective electron/hole collection layer to enhance the performance of the HIT solar cell. Here, n and p-type diamane layers are used as the electron/hole collection layers or the emitter and BSF layer, respectively. Considering the absorption loss at the front contact, the maximum efficiency for the fully optimized cell is found 27.88 % with  $V_{\rm OC}$  691.1 mV,  $J_{\rm SC}$  49.3 mA/cm², and FF 81.83 % whereas, in conventional HIT cell with  $J_{\rm SC}$  of 41.8 mA/cm² and  $\eta$  of 25.6 % reported. If zero absorption loss is considered, the efficiency could exceed its theoretical limit.

Now we have further made the comparative performance analysis of HJBSF (Gr/n-Diamane/p-cSi/p-Diamane/Au) and HITBSF (Gr/n-Diamane/a-Si:H(i)/p-cSi/a-Si:H(i)/p-Diamane/Au) structures revealed that p-type diamane can be used an effective BSF layer. The HITBSF cell showed a peak efficiency of 29.38% at only 35 µm of c-Si thickness, highlighting the suitability of thin wafers and the vital role of a-Si:H (i) layers in surface passivation. Despite technological handling challenges with ultra-thin wafers, the

reduced material usage significantly enhances cost-effectiveness while maintaining high performance.

In order to assess industrial viability of obtained results, a BSFHJ solar cell was designed using a SiO<sub>2</sub>/Si<sub>3</sub>N<sub>4</sub> passivation stack and diamane as both emitter and BSF layers. After optimizing doping, thickness, and carrier lifetimes, the cell achieved 30.59% efficiency, outperforming PERC (24.01%) and comparable to BSFHIT (30.69%) cells. The study underscores the potential of diamane-based, passivated architectures for high-efficiency solar technology, emphasizing the role of bandgap tuning, passivation, and thickness control.

# 8.2 Future Scope and Social Impact

This thesis provides useful insights into improving photovoltaic performance using diamane-based solar cell designs, as well as highlighting plenty of promising areas for further research. These crucial areas include experimental validation of computational findings, scalable and cost-effective synthesis of high-quality diamane films, and the development of sophisticated device structures, including tandem and multi-junction cells. Investigating long-term environmental stability, integrating with smart grid and energy storage systems, and exploring diamane's applications beyond photovoltaics, such as in photodetectors and electronics, are also important. Socially, the adoption of high-efficiency diamane-based solar cells can accelerate clean energy deployment, mitigate climate change, and improve electricity access in underprivileged areas. We anticipate that commercializing diamane-based technology may drive economic growth, foster technological independence, and support educational and research progress in 2D materials and renewable energy. These initiatives are aligned with global sustainability goals and represent a step forward toward a more equitable and environmentally responsible energy future.

# **DTU** (formerly Delhi college of engineering)

# Naima | Curriculum Vitae

**Naima** 

(Research Scholar - Solar Cells) Department of Applied & Engineering Physics, Nano-Fabrication Laboratory (NFL) Delhi Technological University, IN-110042 Phone: +91-8279545878

E-mail: naimatyagi1995@gmail.com

ResearchGate Link:

https://www.researchgate.net/profile/Naim

a? ev=hdr\_xprf

# **Education**

♣ Ph.D. in Physics (Solar Cells) – Delhi Technological University, 2020–2025
Thesis: Potential application of 2D carbon materials in silicon heterojunction solar cells

- ♣ M.Sc. in Physics (Electronics) Chaudhary Charan Singh University, 2015–2017 (71.55%)
- ♣ B.Sc. in Physical Sciences Chaudhary Charan Singh University, 2012–2015 (62.6%)

# **Research Focus**

- Design, simulation, and optimization of silicon-based heterojunction (HJ/HIT) solar cells
- ♣ Integration of 2D materials (diamane, graphene) for next-generation photovoltaics
- Device modelling with AFORS-HET, SCAPS-1D, and COMSOL
- High-efficiency and stable silicon-perovskite hybrid architectures

# **Key Achievements**

- ♣ Engineered high-efficiency HJ and HIT solar cells by incorporating diamane as an emitter, and back surface field (BSF) layer and graphene as transparent conducting electrode (TCE).
- ♣ Achieved a peak simulated power conversion efficiency of ~29% using doped diamane as electron/hole collection layers in HIT cell architectures or hole selective layer.
- Demonstrated the feasibility of graphene/diamane interfaces in HIT structures.
- Published in reputed journals and contributed novel insights into the use of 2D materials for improving solar cell efficiency, stability, and scalability.

# **Research Publications**

- **1. Naima**, P.K. Tyagi, V. Singh. *N-type diamane: An effective emitter layer in crystalline silicon heterojunction solar cell*, **Carbon Trends**, 9 (2022) 100209.
- **2.** Naima, P.K. Tyagi, V. Singh. *Potential application of novel graphene/diamane interface in silicon HIT solar cells*, **Computational Materials Science**, 226 (2023) 112252.
- **3.** Naima, P.K. Tyagi, V. Singh. *Doped diamane: An efficient electron/hole collection layer in HIT solar cells*, *Materials Science and Engineering B*, 310 (2024) 117754.
- **4.** Naima, P.K. Tyagi, V. Singh. *p-type diamane as back surface field layer in silicon heterojunction solar cells*, **Semiconductor Science and Technology**, 39 (2024) 125021.
- **5.** H. El-assib, **Naima**, et al. *High-performance optimization of*  $Cs_2CuSbCl_6$ -based lead-free double perovskite solar cells with >27% efficiency, **Renewable Energy**, 239 (2025) 122092.
- **6. Naima**, P. K. Tyagi, M. Alla, and V. Singh, Potential application of diamane and graphene in siliconbased
  - heterojunction solar cells, **Diamond & Related Materials** (Under Review).
- H. El-Assib, M. Alla, S. Tourougui, M. Mohammed, S. Dar, Y. Labghough, M. Alla, Naima, M. Rouchdi, B. Fares, Electron extraction layer-Driven performance enhancement in CaHfSe 3 Photovoltaics, RSC Advances (Accepted).

- **8. Naima**, P. K. Tyagi, and Vinod Singh "Affinity Optimization of Commercially Available Crystalline Silicon Heterojunction Solar Cell by Using AFORS-HET Software" **Springer Proceedings in Materials**.
- **9. Naima**, P. K. Tyagi, and Vinod Singh "Effect of temperature variation on the performance of HIT solar cell" **Springer's Proceedings in Physics** (Submitted)

# **Teaching Experience**

- **↓ Teaching Assistant (2020–2025), DTU –** Undergraduate & Postgraduate Labs:
- Physics Experimental Laboratory (2020–24)
- Condensed Matter Physics (M.Sc., 2022)
- Electronics & Microwave Experimental Labs (M.Sc., 2023–25)
- Engineering Physics Course (B.Tech, 2024)

# **Awards & Fellowships**

- Commendable Research Award DTU (2023–2025)
- Senior Research Fellowship (SRF) DTU (2022–2025)
- **↓** Junior Research Fellowship (JRF) DTU (2020–2022)

# **Professional Activities & Service**

- Organized invited talks and workshops at DTU (2023–2025)
- Ph.D. Coordinator, Applied Physics Department, DTU (2024)
- Represented DTU laboratories & documents handling during NBA accreditation visits

# **Technical Skills**

- Simulation: AFORS-HET, SCAPS-1D, COMSOL
- Data Analysis: Origin, MS Office
- Operating Systems: Linux, Windows

# Conferences, Seminars, and Workshops

- ♣ 2021 E-Workshop, DTU

  Orientation Session for All Students & F
  - Orientation Session for All Students & Faculties of Institute by Innovation Ambassador
- 4 2022 Technical Talk, DTU
  - Stronger Glass Products and an Overview of IYoG (International Year of Glass)
- **2022 Poster Presentation**, IUMRS-ICA, IIT Jodhpur Effect of optical band gap of the emitter layer on the efficiency of the silicon heterojunction photovoltaic cell
- 2022 Poster Presentation, ICNOC, Jamia Millia Islamia, Delhi Affinity Optimization of Commercially Available Crystalline Silicon Heterojunction Solar Cell by Using AFORS-HET Software
- **2023 National Seminar**, Institution's Innovation Council (IIC), DTU *Implementation of NEP-2020 in special reference to Innovation & Entrepreneurship*
- **2023 National Seminar**, Department of Applied Physics, DTU Recent Advancements in Semiconductor Devices and Materials (RASDM-2023)
- 2023 National Seminar, HRDC in association with IIC & DTU National Science Day – 2023
- 2023 National Workshop, DTU

- Ascertaining a Skill Centre for Glass and Glazing (ASCGG-2023) Bringing Industry and Academia Together
- **2023 Poster Presentation**, ICAMNOP, DTU Effect of temperature variation on the performance of HIT solar cell
- **2024 National Seminar**, SSB, DTU Recent Trends in Applied Physics and Engineering (RTAPE-2024)
- **4 2024 − National Workshop**, SERB, IIT Jammu

  High-End Workshop on Next Generation Materials for Energy Storage

# References

- ♣ Prof. Vinod Singh Professor (Ph.D. Advisor)
  Department of Applied Physics, DTU, New Delhi, India (110042) | ☑ vinodsingh@dtu.ac.in
- **Dr. Pawan Kumar Tyagi** Associate Professor (*Ph.D. Advisor*)

  Department of Applied Physics, DTU, New Delhi, India (110042) | ☑ pawantyagi@dtu.ac.in
- ♣ Dr. Kamlesh Patel Associate Professor
  Department of Electronic Science, University of Delhi, India (110042) | ☑ kpatel@south.du.ac.in
- ♣ Dr. Renuka Bokolia, Assistant Professor
  Department of Applied Physics, DTU, New Delhi, India (110042) | ☑ renukabokolia@dtu.ac.in
- ♣ Prof. Garima Jain Professor Department of Physics, D.A.V. College, Muzaffarnagar, U.P., India (251001) | ☑ garima@davcollegemzn.org
- ♣ Dr. Kailash Garg Assistant Professor Motilal Nehru College, University of Delhi, India (110021) | ☑ kailashgarg@mln.du.ac.in



Contents lists available at ScienceDirect

# **Carbon Trends**

journal homepage: www.elsevier.com/locate/cartre



# N-type diamane: An effective emitter layer in crystalline silicon heterojunction solar cell



Naima, Pawan K. Tyagi\*, Vinod Singh

Department of Applied Physics, Delhi Technological University, New Delhi 110042, India

#### ARTICLE INFO

Article history: Received 20 June 2022 Revised 9 August 2022 Accepted 27 August 2022

Keywords: 2D material Diamane Silicon heterojunction solar cell AFORS-HET v 2.5 software

#### ABSTRACT

In the presented work, cell's parameter of heterostructure silicon solar cell modelled as: ITO (front contact)/n-Dn/p-cSi/Ag under the illumination of monochromatic light at standard spectrum AM-1.5 G, has been optimized by using AFORS-HET v 2.5 software. We have used n-type diamane as an emitter layer and the nature of diamane has been considered 3D in spite of 2D as well as electronic nature of diamane is considered isotropic. To ensure that Schottky junction has been formed at interface, the electric contacts have been made along the c-axis so that maximum charge carriers get collected. To obtain the high efficiency, various parameters of n-type diamane as well as p-type c-Si layers have been optimized and the maximum efficiency of 16.84% has been obtained for single layer n-diamane at 100 µm thick silicon wafer. We also investigated the spectral response and dependency of temperature on the performance of exclusively designed solar cell and we obtained the best efficiency 16.84% at 300 K temperature. In order to check the performance on commercially available silicon we have optimized the same solar cell by considering the parameters of commercially available p-type crystalline silicon layer and maximum efficiency 10.41% was achieved. After getting the maximum efficiency 16.84% we further carried out the simulation by optimizing the layer numbers of n-diamane and found decrement in the efficiency up to 15.3% which indicates that, efficiency slightly decreases as layer number increases. We have demonstrated that n-type diamane might be used as an effective emitter layer in crystalline Si heterojunction solar cell.

This is an open access article under the CC BY license (http://creativecommons.org/licenses/by/4.0/)

#### 1. Introduction

Recently, a new allotrope of the carbon named as "Diamane" (Dn) possess sp<sup>3</sup> carbon bonding has been synthesized and reported to be two-dimensional (2D) being a physical analogue to "graphene-graphane" [1–4]. Recently, Bakharev et al. [5] confirmed that diamane exhibited 2 D electronic system. It was confirmed by estimating the optical band gap of diamane adopting the approach described in previous studies [6,7] for 2D electronic systems. They found that the experimental optical gap value of 3.3–3.4 eV is consistent with the calculated optical gap of 2.87 eV obtained for F-diamane. Furthermore, Raman spectroscopy was used to confirm the successful synthesis of 2D diamane and the characterization of its electronic structure has also been reported [8,9]. It has thermal conductivity of 1960 W/mK as high as to its bulk counterpart diamond (1000 W/mK), due to which it is considered as promising material for the high temperature electronic applica-

tions [1,10]. Furthermore, density functional theory (DFT) calculations reveal that 2D diamane has smaller effective mass (0.55m<sub>0</sub>) of conduction electrons in comparison of its bulk counterpart i.e., diamond (0.57m<sub>0</sub>), which is also very promising to use 2D diamane in various electronic applications such as solar cells [1]. 2D materials are best to use in electronic applications as they have large tunability in their bandgaps and they are flexible, strong and extremely thin. It was first predicted by Chernozatonskii et al., in 2009 [11], although its experimental synthesis was reported recently. The detailed verification of its bonding and electronic structure has also been probed by using various characterization techniques like: X-ray photoelectron spectroscopy (XPS), UV photoelectron, Raman, UV-Vis and electron energy loss spectroscopies, transmission electron microscopy and X-ray Diffraction (XRD) [5]. Formerly, the instability of diamane was marked as a big hurdle for its above-mentioned potential applications. Recently, the stability of diamane has been improved by the substitution of N atoms on its surface. The N atom has one more electron than C atom that form lone pair of electrons and behaves as the passivation, which stabilizes the structure and extends the band gap [2]. The first principal method has investigated the configuration

<sup>\*</sup> Corresponding author.

E-mail address: pawantyagi@dtu.ac.in (P.K. Tyagi).

ELSEVIER

Contents lists available at ScienceDirect

# Computational Materials Science

journal homepage: www.elsevier.com/locate/commatsci



#### Full Length Article



# Potential application of novel graphene/diamane interface in silicon-based heterojunction with intrinsic thin layer solar cell

Naima, Pawan K. Tyagi \*, Vinod Singh

Department of Applied Physics, Delhi Technological University, New Delhi 110042, India

#### ARTICLE INFO

# Keywords: HIT solar cell Transparent Conducting Electrode (TCE) Emitter layer 2D material Diamane Graphene AFORS-HET version 2.5 software

#### ABSTRACT

In this article, the patentability of novel graphene/diamane interface in HIT solar cell has been explored by simulated a structure modelled as: graphene (TCO) / n-diamane / a-Si: H (i) / p-cSi / Ag (back contact) with the help of software AFORS-HET version 2.5. Here, n-type diamane is used as an emitter layer and graphene as TCO. An efficiency of 31.2 % is achieved with this structure by varying various parameters of n-type diamane, p-crystalline silicon and hydrogenated intrinsic amorphous silicon layer which is pressed in between the two oppositely doped wafer (diamane and c-Si). Furthermore, when ITO is used as TCO then a comparatively low efficiency 27.15 % is achieved and when the commercially available values of silicon's parameters is used for the validation of results then an efficiency of 24.15 % is obtained. Some parameters of a-Si: H (i) has been further optimized and the optimum efficiency 31.2 % has been found at minimum thickness of 3 nm at bandgap 1.6 eV. Finally, we have demonstrated that only carbon material has an ability that its two-dimensional allotropes can be used as an emitter layer as well as efficient transparent conducting electrode.

#### 1. Introduction

The holy grail hurdle in the profitable expansion of photovoltaic solar cell is to make them cost effective as well as exhibits high efficiency. For this motive, a number of solar cells have been explored and fabricated with different materials in order to increase its efficiency [1,2]. Recently, a new 2D material called diamane (Dn) has been used as an emitter layer by Naima *et. al.* [3] and elaborated the significance of using diamane in silicon heterojunction solar cell for enhancing its efficiency to good extent. In order to further proceed the possibility of achieving higher efficiency, we have explored a HIT (heterojunction solar cell with intrinsic thin layer) module where 2D carbon material (diamane) is used as an emitter layer. It is reported that 26.6 % and more than 30 % efficiency can be achieved for different HIT modules [4,5].

Furthermore, to ease the movement of photons from the emitter layer to the external circuit a transparent conducting oxide (TCO) is needed which must be highly transparent as well as low sheet resistance and high carrier mobility. In this search graphene is found to be potential candidate which possess 97.4 % optical transparency with sheet resistance approximately,  $125\,\Omega\text{sq}^{-1}$  [6] for monolayer graphene and its work function can be manipulate in the range 3.10 eV to 5.57 eV [7,8]. It is reported that HIT module with graphene/MoS2 interface is

commendable for achieving higher efficiency 25.61 % [9]. Similarly, another HIT cell has also been simulated previously, in which up to 20.23 % efficiency has reached for the area of 156 mm  $\times$  156 mm active layer of silicon [2]. Therefore, it is plausible to use graphene/diamane interface in HIT solar cells with intention of improving efficiency.

Previously, numerous studies have been done on the excellent optoelectronic properties of various 2D materials and their heterojunctions [10-12]. In 2009, 2-D ultra-thin layer of diamond called diamane was predicted and studied [13,14]. The effective mass of conduction electron in diamane is very small  $(0.55 \text{ m}_0)$  and it has wide bandgap which is diverse ranging from 3.1 eV to 4.5 eV [14,15]. In addition, the carrier' mobility in diamane is also very high as 2732 cm<sup>2</sup>/Vs for electrons and 1565 cm<sup>2</sup>/Vs for holes for its different forms [15]. Its work function can also be tuned in range 6.78 eV to 7.24 eV by vacuum annealing at  $350\,^{0}$ C [16]. Doping of diamane with nitrogen makes it n-type as well as highly stable material which can be used in different electronic applications. Also, diamane is a  $sp^3$  hybridized  $C_2H$  based layered structure on the bilayer graphene which is also sp<sup>3</sup> hybridized and the neighbouring carbon atoms of both materials are covalently bonded with the hydrogen atoms located out there. In this way, we can state that the graphene/ diamane interface would be stable [13] and this heterostructure can find applications in electronic devices.

E-mail addresses: pawankumartyagi@gmail.com, pawantyagi@dtu.ac.in (P.K. Tyagi).

<sup>\*</sup> Corresponding author.

ELSEVIER

Contents lists available at ScienceDirect

# Materials Science & Engineering B

journal homepage: www.elsevier.com/locate/mseb



# Check for updates

# Doped diamane: An efficient electron/hole collection layer in HIT solar cell

Naima, Pawan K. Tyagi \*, Vinod Singh

Department of Applied Physics, Delhi Technological University, New Delhi 110042, India

ARTICLE INFO

Keywords:
2D materials
HIT solar cell
Power conversion efficiency
Texturing angle
Band alignment diagram

#### ABSTRACT

In this report, the optimization of various parameters of electron/hole collection layer, buffer layer and active layer of the HIT solar cell have been carried out by using AFORS-HET software. Novelty of the reported work is the use of doped diamane as an effective electron/hole collection layers for the enhanced performance of the HIT solar cell. Here, n and p-type diamane layers are used as the electron/hole collection layers or the emitter and back surface field (BSF) layer, respectively. Considering the absorption loss at the front contact, the maximum efficiency ( $\eta$ ) for the fully optimized cell is found 27.88 % with open circuit voltage ( $V_{OC}$ ) 691.1 mV, current density ( $J_{SC}$ ) 49.3 mA/cm² and fill factor (FF) 81.83 % whereas, in conventional HIT cell with  $\eta$  of 25.6 % and  $J_{SC}$  of 41.8 mA/cm² reported by Masuko et. al. [7]. If zero absorption loss is considered, the efficiency could exceed its theoretical limit. A detailed study has also been done on the role of texturing angle and absorption loss found at the front contact of the solar cell.

#### 1. Introduction

Photovoltaic solar cell is only the eco-friendly and constant energy source that has the capability of meeting the world's rising energy demand [1]. In this context, numerous research has been done to improve the efficiency of solar cells by using crystalline silicon as the active layer. It has been found that heterojunction with intrinsic thin layer (HIT) solar cells with back surface field (BSF) may provide higher conversion efficiency with comparably thin layer of crystalline silicon [1–6]. Previous research has demonstrated that crystalline silicon-based HIT solar cells can offer more than 25 % conversion efficiency [7]. An efficiency of 25.6 % has reportedly been attained on a cell area of 143.7 cm<sup>2</sup> with 1solar illumination. This might happen because of the passivation of the c-Si layer, which has lowered recombination losses at the interface. This passivation is carried out by inserting an extremely thin intrinsic hydrogenated amorphous silicon layer (a-Si: H (i)) over the crystalline silicon layer [7]. Also, an efficiency of 31.07 % was reported for 15  $\mu m$ thick crystalline silicon layer by optimizing the doping concentration as well as by passivating the rear surface on the optimized geometry of interdigitated back contacts (IBC) [8].

In conventional silicon heterojunction solar cells, the conversion efficiency was strongly manipulated by the electron/hole collection layers, where these layers were made of inversely doped amorphous silicon layers [9,10]. Due to the lower bandgap (approximately 1.7 eV) and high defect density of these layers the parasitic light absorption

occurs throughout the solar spectrum's ultraviolet and visible range [11]. This absorption deteriorates the efficiency of the cell. Therefore, alternative materials having wider bandgap and lower defects density are needed. These wider band gap layers will be beneficial for the electron/hole collection under illumination. Because, the high Schottky-barrier in the voltage range (>0.7 V) resulted in the formation of a significant space charge region or inversion layer between hole selective layer (MoO<sub>x</sub>) and c-Si interface. This barrier influenced how well photogenerated carriers were captured, resulting in good transverse transportation which enhanced the  $V_{\rm OC}$  and FF [12].

We believe that the development of HIT solar cell is not yet complete and cells' overall efficiency might still be increased. But the parasitic light absorption losses that occurs at interfaces is the main impediment to enhance the conversion efficiency of HIT solar cells. It was reported that the electron/hole collection layers of doped amorphous silicon can be replaced by wide-bandgap transition metal oxide to reduce the parasitic light absorption loss in HIT solar cells [13]. In this direction, it has been suggested that titanium dioxide (TiO<sub>2</sub>) and zinc oxide (ZnO) can be employed as hole transporting layers materials and copper (I) thiocyanate (CuSCN) as an electron transporting layer material and an efficiency of 25.02 % has been attained [14]. Furthermore, transition-metal dichalcogenides (TMDs) are reported to possess adequate work function with high optical transparency which is required for gathering charge carriers, so adding of TMDs layer between the p-type amorphous silicon and the TCO electrode as window layer may lead to better optical

E-mail address: pawantyagi@dtu.ac.in (P.K. Tyagi).

<sup>\*</sup> Corresponding author.

# Potential application of p-type diamane as back surface field layer in silicon-based heterojunction solar cells

Naima, Pawan K Tyagi\* and Vinod Singh

Department of Applied Physics, Delhi Technological University, New Delhi 110042, India

E-mail: pawantyagi@dtu.ac.in and pawankumartyagi@gmail.com

Received 28 August 2024, revised 25 October 2024 Accepted for publication 3 November 2024 Published 25 November 2024



#### **Abstract**

A higher efficiency of photovoltaic cells can be attained by optimizing their design, selecting the appropriate materials, and implementing of effective passivation process. The present study investigates the influence of the thickness and band gap of different layers of the solar cell and resuting opto-electric performance parameters of both single junction heterojunction (HJ) and heterojunction with intrinsic thin layer (HIT) cells. These cells are made up of a crystalline silicon (c-Si) active layer having back surafce field layer. The reported simulated work was conducted using AFORS-HET, an automated program specifically designed for simulating heterostructures. An efficiency of 26.86% has been attained for a HJ solar cell, this efficiency was further improved to 29.38% for the HIT solar cell by optimising all parameters. These cells require an emitter layer with a bandgap of around 1.4 eV. The optimal values of open-circuit voltage ( $V_{\rm OC}$ ), short-circuit current density ( $I_{\rm SC}$ ), and fill factor are determined and found to be: 631.2 mV, 51.16 mA cm<sup>-2</sup>, and 83.16% for HJ solar cell, and 683 mV, 52.74 mA cm<sup>-2</sup>, and 81.55% for HIT solar cell. Moreover, the J-V curve, spectral response and quantum efficiency analysis have also been studied.

Keywords: 2D carbon materials, photovoltaic cells, higher efficiency, BSF layer, energy band diagram

#### 1. Introduction

The greatest challenge in the world at present is to find a green energy source that can meet the world's growing energy needs and decrease its dependence on traditional energy sources, which are harmful to both human beings and the environment, especially fossil fuels [1]. To meet climate goals by the end of this century, we must move promptly to a green economy. This means transitioning the world economy from being dominated by the fossil-fuelled (brown) sector to being dominated by the low-emission (green) sector. By utilising photovoltaic (PV) technology, the sun, which is a prominent energy source across the globe, may be effectively utilised to generate electricity. This technology has the ability to fulfill the growing need

for power. As we know that primary renewable energy sources with zero operating carbon emissions is photovoltaic solar cells [2, 3]. Consequently, photovoltaic solar cell is acknowledged as an indispensable energy source and its viability is essentially evaluated by its power conversion efficiency, commonly referred to as PCE. Wafer-based crystalline silicon (c-Si) solar cell is the dominant technology in the global photovoltaic market due to their cost-effectiveness, robust stability, and high PCE [2]. The c-Si wafer accounts for around 20% of the overall production cost of the PV module [4]. Thus, the production cost of PV modules can be reduced by systematically decreasing the thickness of wafers and, consequently, the amount of crystalline material used will be lowered [4, 5].

Recently, there has been a major emphasis on to design and manufacture of the extremely efficient solar cells by utilising innovative materials and topologies. Various materials

<sup>\*</sup> Author to whom any correspondence should be addressed.

# **RSC Advances**



**PAPER** 

View Article Online
View Journal | View Issue



Cite this: RSC Adv., 2025, 15, 35859

# Electron extraction layer-driven performance enhancement in CaHfSe<sub>3</sub> photovoltaics

Hicham El-assib,<sup>a</sup> Mohamed Alla,<sup>ab</sup> Safae Tourougui,<sup>a</sup>
Mustafa K. A. Mohammed, <sup>©</sup>\*\* Shazia Akhtar Dar,<sup>e</sup> Yasmine Labghough,<sup>f</sup>
Malika Alla,<sup>a</sup> Naima,<sup>g</sup> Mustapha Rouchdi<sup>a</sup> and Boubker Fares<sup>a</sup>

Traditional solar cells – including those based on silicon or lead-halide perovskites – have a number of significant disadvantages, including long-term instability, costs, and toxicity. We demonstrate the suitability of CaHfSe<sub>3</sub> as a promising next-generation lead-free thermally stable absorber material. We performed a comprehensive numerical simulation study using SCAPS-1D to consider several device topologies of the type FTO/TiO<sub>2</sub> AZnO, WS<sub>2</sub>/CaHfSe<sub>3</sub>/MoO<sub>3</sub>/Au, and to investigate the different features of a system based on CaHfSe<sub>3</sub>. We conducted a full parametric study of the impacts of absorber thickness, defect density, acceptor doping and concentration, as well as carrier concentrations in the electron and hole transport layers. In addition, through experimentation we considered the operational characteristics of carrier generation-recombination methods, temperature and back contact effect current–voltage I-V characteristics, quantum efficiency, and the influence of series and shunt resistance. This allowed us to determine the optimized configuration. The top-performing structure, FTO/TiO<sub>2</sub>/CaHfSe<sub>3</sub>/MoO<sub>3</sub>/Au, had an outstanding PCE of 32.39%,  $V_{\rm OC} = 1.52~V$ ,  $J_{\rm SC} = 23.17~mA~cm^{-2}$ , and FF = 91.41%. This research offers both fundamental insights and practical guidance for developing stable, efficient, and environmentally friendly CaHfSe<sub>3</sub>-based solar cells. It paves the path for further experimental realization and commercial application.

Received 10th August 2025 Accepted 23rd September 2025

DOI: 10.1039/d5ra05879a

rsc.li/rsc-advances

# Introduction

Transition to renewable energy sources has emerged as a global imperative to address the challenges posed by climate change and rising electricity demand. Among energy conversion technologies, solar cells have experienced significant growth thanks to advances in developing new semiconductor materials. 1,2 Although silicon-based photovoltaic cells currently dominate the market, they have certain limitations regarding manufacturing cost, efficiency, and stability. In particular, crystalline silicon suffers from intrinsic constraints as an indirect band gap semiconductor, its low absorption coefficient requires a minimum thickness to ensure sufficient light harvesting. Still, increasing thickness inevitably raises the series

resistance.3 This trade-off between absorption and Joule losses fundamentally restricts the overall performance of silicon solar cells. These constraints have driven the exploration of alternative materials, especially perovskites, which are garnering increasing attention in this context due to their exceptional optical and electronic properties, cost-effectiveness, and sustainability for photovoltaic devices.4-6 Specifically, MAPbX3 or FABX<sub>3</sub> lead halide perovskites have demonstrated remarkable power conversion efficiency (PCE) of 27%.7 However, conventional PSCs are weak in resilience to heat and humidity, have a high concentration of defects, are unstable due to the instability of organic cations, and contain poisonous lead (Pb), all of which pose significant health and environmental dangers, preventing their widespread commercialization. The primary obstacle is the search for lead (Pb)-free, stable, and eco-friendly materials. This is achieved by replacing cations such as Ge<sup>2+</sup> or Sn<sup>2+</sup>, which have advantageous band gaps, for Pb<sup>2+</sup> ions.<sup>8,9</sup> However, the resultant perovskites are extremely unstable in air because of the strong oxidation propensity of Ge2+ and Sn2+ to Sn<sup>4+</sup> and Ge<sup>4+</sup>, respectively, which is linked to the increased energy levels of their respective 5s and 4s orbitals.10 However, a major obstacle still stands in the way of these promising solar materials, poor durability.

This study is aimed at identifying materials with the positive attributes of lead halide perovskites while eliminating their

<sup>&</sup>quot;(STCE)-Energy Research Centre (ERC), Faculty of Science, Mohammed V University, Rabat, Morocco

<sup>&</sup>lt;sup>b</sup>MANAPSE Lab, Faculty of Sciences, Mohammed V University in Rabat, Morocco <sup>c</sup>College of Remote Sensing and Geophysics, Al-Karkh University of Science, Baghdad 10011, Iraq. E-mail: dr.mustafa@ks.edu.iq

<sup>&</sup>lt;sup>d</sup>College of Science, University of Warith Al-Anbiyaa, Karbala 56001, Iraq

<sup>\*</sup>Department of Electronics and Communication Engineering, National Institute of Technology, Srinagar 190006, India

Laboratory of Information Processing (LTI), Faculty of Sciences Ben MSick, University Hassan II, Casablanca, Morocco

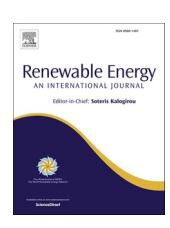
<sup>\*</sup>Department of Applied Physics, Delhi Technological Technology, Delhi 110042, India



Contents lists available at ScienceDirect

# Renewable Energy

journal homepage: www.elsevier.com/locate/renene



# High-performance optimization and analysis of Cs₂CuSbCl<sub>6</sub>-Based lead-free double perovskite solar cells with theoretical efficiency exceeding 27 %

Hicham El-assib <sup>a</sup>, Mohamed Alla <sup>a,\*</sup>, Safae Tourougui <sup>a</sup>, Malika Alla <sup>a</sup>, Fatima Elfatouaki <sup>b</sup>, Shazia Akhtar Dar <sup>c</sup>, Asha Chauhan <sup>d</sup>, Naima <sup>e</sup>, N. Chawki <sup>a</sup>, Nikhil Shrivastav <sup>f</sup>, Vishesh Manjunath <sup>g,h</sup>, Mustapha Rouchdi <sup>a</sup>, Boubker Fares <sup>a</sup>

- <sup>a</sup> (STCE)-Energy Research Centre (ERC), Faculty of Science, Mohammed V University, Rabat, Morocco
- <sup>b</sup> LaMEE, Department of Physics, Faculty of Sciences Semlalia, Cadi Ayyad University, Marrakech, Morocco
- <sup>c</sup> Department of Electronics and Communication Engineering, National Institute of Technology, Srinagar, 190006, India
- <sup>d</sup> Department of Physics, National Institute of Technology, Raipur, Chhattisgarh, 492010, India
- <sup>e</sup> Department of Applied Physics, Delhi Technological University, New Delhi, 110042, India
- f VLSI Centre of Excellence, Chitkara University Institute of Engineering and Technology Chitkara University, Puniab, India
- g Department of Metallurgy Engineering and Materials Science, Indian Institute of Technology Indore, Khandwa Road, Simrol, 453552, India
- h Department of Materials Science and Engineering and Optoelectronics Convergence Research Center, Chonnam National University, Gwangju, 61186, South Korea

#### ABSTRACT

The primary challenges in photovoltaic solar energy include toxicity, stability, and the cost of solar cells. To address these issues, we propose the use of noble metal halide double perovskites, which are lead-free.  $Cs_2CuSbCl_6$  stands out as a popular absorber due to its huge bandgap, high absorption coefficient, and affordable price. Our research analyzes and simulates solar cells with  $Cs_2CuSbCl_6$  as the absorber material, utilizing SCAPS-1D software. Along with AZnO for the electron transport layer (ETL), we assess the material's stability and suggest less expensive substitutes for hole transport materials (HTLs) such as Spiro-OMeTAD,  $MoO_3$ ,  $MiOO_3$ , MiO

#### 1. Introduction

The complete conversion of light energy into electrical energy is not achieved due to various losses that affect a cell's efficiency. These losses primarily stem from the characteristics of the material utilized and the chosen technology. The first generation consists of structures made of mono-crystalline or multi-crystalline silicon (Si), which currently dominate the market. However, their widespread adoption is hindered by the high processing cost of silicon wafers [1]. The second generation includes thin-film solar cells such as amorphous Si, CdTe, and CIGS. These have limited widespread use due to concerns over cadmium (Cd) toxicity in CdTe and the scarcity of Indium (In) in CIGS [1]. All other emerging technologies, such as perovskites and organic cells [2], belong to the third generation.

Third-generation perovskite solar cells are the most promising among all other generations, demonstrating rapid development and opening up new directions in photovoltaics, thanks to their low cost, strong absorbency, and high PCE [3]. Over the years, significant research efforts have been dedicated to studying these cells, resulting in a remarkable increase in efficiency from approximately 3.8 % to around 26.42 %. This progress has been documented in works published between 2009 and 2021 [4].

Much attention has been paid to the organic-inorganic hybrid halide perovskites MABX3 (MA = CH<sub>3</sub>NH<sub>3</sub>) or FABX<sub>3</sub> (FA = NH<sub>2</sub>CHNH<sub>2</sub>), and (B=Pb<sup>2+</sup>, X = Cl-, Br-, or I-) in high-efficiency solar cell exceeding 26.1 % [5,6]. Nevertheless, the instability of perovskites and concerns regarding lead toxicity have impeded the development of such solar cells [5]. The MABX<sub>3</sub> is extremely decomposed in light, heat, and humid environments [7]. The primary challenge is identifying stable, environmentally friendly, materials free from lead (Pb). This is accomplished by substituting cations like  $Ge^{2+}$  or  $Sn^{2+}$  ions for  $Pb^{2+}$  ions, attributed to their favorable band gap [8,9], However, the oxidation tendency of  $Sn^{2+}$  and  $Ge^{2+}$  cations is attributed to the high-energy levels of their 5s and 4s orbitals respectively, resulting in the corresponding perovskites being

E-mail address: mohamed.alla19021ma@gmail.com (M. Alla).

<sup>\*</sup> Corresponding author.